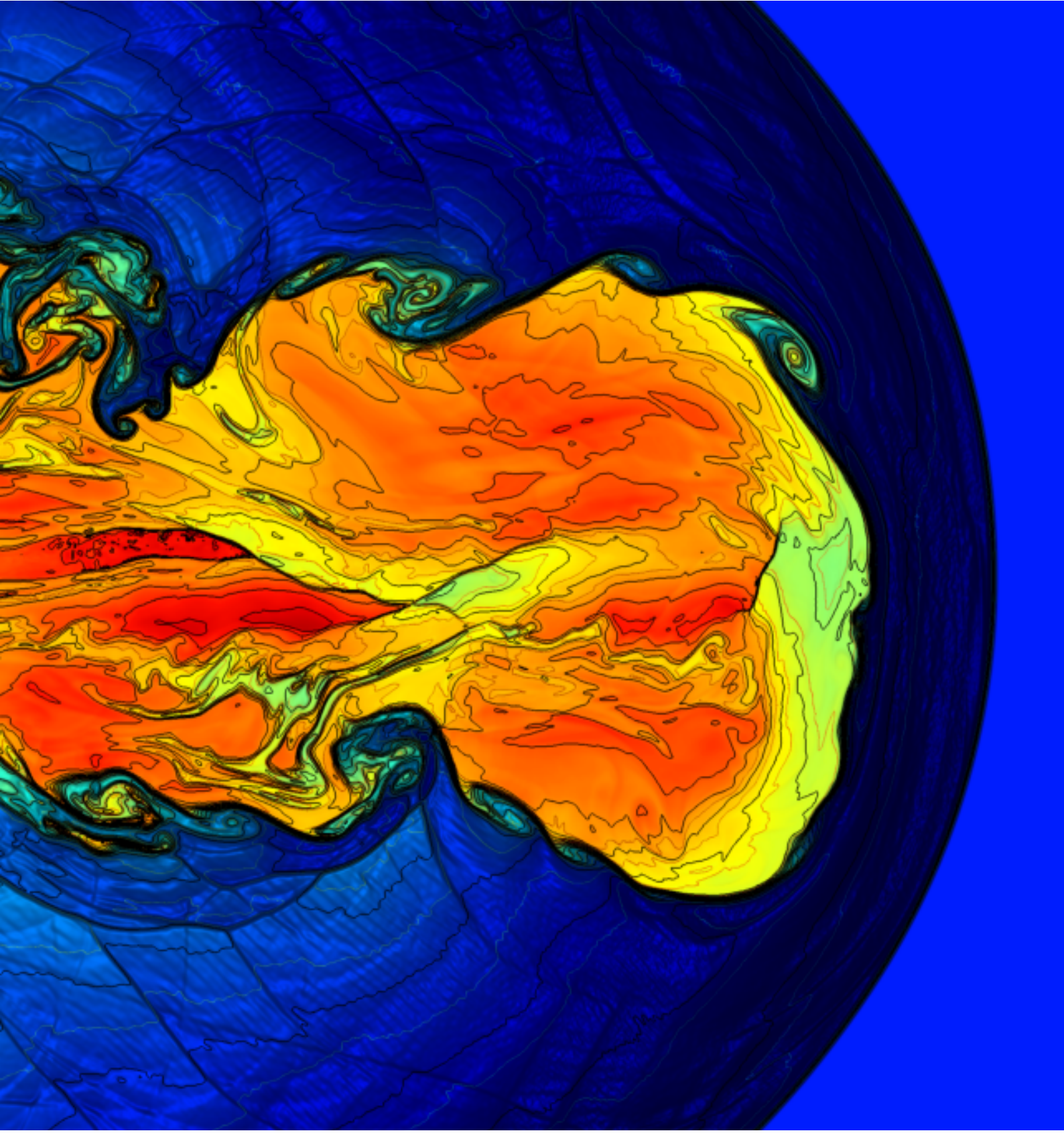

High-Order Methods for Computational Astrophysics

Jonatan Núñez-de la Rosa

High-Order Methods for Computational Astrophysics

A thesis accepted by the
Faculty of Aerospace Engineering and Geodesy of the University of Stuttgart
in partial fulfilment of the requirements for the degree of
Doctor of Engineering Sciences (Dr.-Ing.)

by

Jonatan Núñez-de la Rosa

born in Cartagena (Colombia)

Main-referee:	Prof. Dr. Claus-Dieter Munz
Co-referee:	Prof. Dr. Michael Dumbser
Date of defense:	4th December 2014

Institute of Aerodynamics and Gas Dynamics
University of Stuttgart

2015

Dedicado a mi Familia
especialmente a mis hijos
Ángel y Jonatan

Wirklich es ist nicht das Wissen, sondern das Lernen,
nicht das Besitzen, sondern das Erwerben,
nicht das Da-Sein, sondern das Hinkommen,
was den größten Genuss gewährt

JOHANN FRIEDRICH CARL GAUSS

Preface

This thesis was developed during my work as research assistant at the Institute of Aerodynamics and Gas Dynamics of the University of Stuttgart.

Many thanks to my doctoral supervisor Prof. Dr. Claus-Dieter Munz for the exceptional working conditions in his research group, especially for all the scientific freedom I was granted under his supervision. I thank to my co-referee Prof. Dr. Michael Dumbser for the very careful reading of the manuscript and all his valuable suggestions and comments. Furthermore, I thank to all my colleagues at the Institute of Aerodynamics and Gas Dynamics for the good working atmosphere and all the fruitful scientific discussions. A special thank to my colleagues Matthias Sonntag and Christoph Altmann.

I enormously benefited from the work of Andrea Mignone (main developer of the PLUTO CODE), and James Stone (main developer of the ATHENA CODE). They made freely available their codes together with an extensive documentation, which helped me a lot when the things were not going so-well with the development of my XTROEM CODE. I really appreciate all their effort, and offer my profoundest gratitude.

I thank my former astrophysics professors, Juan Manuel Tejeiro and Jean Fred Murillo, for all their support during my years as an astrophysics student in Colombia. Moreover, I thank my friends Dayro Rendón, Silvio Daguer, Julian Mora, Gabriele Ohla, Jakub Kaleta, Marta Kaleta, Balász Bokor, and Partho Upadhyay for sharing with me many nice moments during the last years. Also, many thanks to Jakub Kaleta for his corrections of the German version of the abstract of this dissertation. I am in debt with Silke Hamacher from DAAD for all her collaboration with the management of my scholarship.

I would like to thank my family for their continued encouragement, patience, love, and support through this long journey. For this reason, I dedicate this work to my father Boris, my mother María, my siblings Melisa, Yamid, Katerine, and Yeison, and especially my loving legendary warriors, Ángel and Jonatan.

This work was financed by the Deutscher Akademischer Austauschdienst (DAAD) and the Deutsche Forschungsgemeinschaft (DFG).

30th December 2014

Jonatan Núñez-de la Rosa
Stuttgart, Germany

Contents

Abstract

In computational fluid dynamics, high-order numerical methods have gained quite popularity in the last years due to the need of high fidelity predictions in the simulations. High-order methods are suitable for unsteady flow problems and long-term simulations because they are more efficient when obtaining higher accuracy than low-order methods, and because of their outstanding dissipation and dispersion properties. In the present work, the development and application of three high-order numerical methods, namely, the conservative finite difference (FD) method, the finite volume (FV) method, and the discontinuous Galerkin spectral element method (DGSEM), is presented. These methods are used here for solving three equations systems arising in computational astrophysics on flat spacetimes, specifically, the ideal magnetohydrodynamics (MHD), relativistic hydrodynamics (SRHD) and relativistic magnetohydrodynamics (SRMHD). Our computational framework has been subject to the standard testbench in computational astrophysics. Numerical results of problems having smooth flows, and problems with shock-dominated flows, are also reported.

Finite volume methods are numerical methods based on the weak solution of conservation laws in integral form. Unlike finite volume methods, where cell averages of the solution are evolved in time, in the conservative finite difference schemes only the solution at specific nodal points are considered. This difference offers a high efficiency of finite difference over finite volume methods in two and three dimensional high-order calculations because of the form of the utilized stencils in the reconstruction step. Recently, a lot of effort has been put into the development of efficient high-order accurate reconstruction procedures on structured and unstructured meshes. The most widely used procedure to achieve high-order spatial accuracy in finite volume and conservative finite difference methods is the WENO reconstruction. The basic idea of the WENO schemes is based on an adaptive reconstruction procedure to obtain a higher-order approximation on smooth regions while the scheme remains non-oscillatory near discontinuities. For this reason, the WENO formulation is particularly effective when solving conservation laws containing discontinuities. In this work, the FD and FV methods are extended to very high-order accuracy on regular Cartesian meshes by making use of the arbitrary high-order reconstruction WENO operator. The time discretization is carried out with a strong stability-preserving Runge-Kutta (SSPRK) method. The MHD, SRHD and SRMHD

equations are then solved with these two methods for problems having strong shock configurations.

Another numerical approach to achieve high-order accuracy is the discontinuous Galerkin (DG) method. The DG methods combine the ideas of the finite element (FE) and the finite volume methods. From the FE methods, the solution and test functions in the variational formulation of the conservation law are locally represented by polynomials, allowing to be discontinuous at element faces. In order to stabilize the scheme, from the FV methods are borrowed the ideas of using Riemann solvers, which permit to connect a given element with its direct neighboring ones. One special case in the family of DG methods is the DGSEM. In these methods, the domain is decomposed into quadrilateral/hexahedral elements, and the solution and the fluxes are represented by tensor-product basis functions (high-order Lagrangian interpolants). The integrals are approximated by quadrature, and the nodal points, where the solution is computed, are the Gauss-Legendre quadrature points. With these choices, the DG operator has a dimension-by-dimension splitting form, which yields more efficiency due to less operations and less memory consumption. In this work, the DGSEM has been also extended to the equations of computational astrophysics on flat spacetimes, but restricted only to the MHD and SRHD equations.

Because discontinuous solutions form part of the nature of the hyperbolic conservation laws, shock capturing strategies have to be devised, especially for the discontinuous Galerkin method. For the DGSEM, several shock capturing schemes were considered, like the moment limiter, the artificial viscosity, the WENO limiter, and a hybrid DG/FV approach. For robustness and efficiency reasons, only the latter is used as the main building block for stabilization of the solution when shocks take place. The hybrid DGSEM/FV is constructed in such a way that, in regions of smooth flows, the DGSEM method is employed, and those parts of the flow having shocks, the DGSEM elements are interpreted as quadrilateral/hexahedral subdomains. In each of these subdomains, the nodal DG solution values are used to build a new local domain composed now of finite volume subcells, which are evolved with a robust finite volume method with third order WENO reconstruction. This new numerical framework for computational astrophysics based on the hybridization of high-order methods brings very promising results.

Kurzfassung

In der numerischen Strömungsmechanik sind numerische Methoden hoher Ordnung, aufgrund der Notwendigkeit hochgenauer Vorhersagen in den Simulationen, in den letzten Jahren immer populärer geworden. Verfahren hoher Ordnung eignen sich für instationäre Strömungsprobleme und langfristige Simulationen, weil sie beim Erreichen höherer Genauigkeit effizienter sind als Methoden niedriger Ordnung und hervorragende Dissipations- und Dispersionseigenschaften besitzen. In dieser Arbeit wird die Entwicklung und Anwendung dreier numerischer Verfahren hoher Ordnung vorgestellt: der konservativen Finite-Differenzen-Methode (FD), der Finite-Volumen-Methode (FV) und der Discontinuous Galerkin-Spektral-Element-Methode (DGSEM). Diese Methoden werden zur Lösung von drei Gleichungssystemen aus der Computer-Astrophysik auf flachen Raumzeiten verwendet, nämlich der Magnetohydrodynamik (MHD), der relativistischen Hydrodynamik (SRHD) und der relativistischen Magnetohydrodynamik (SRMHD). Unser Berechnungsverfahren wurde den Standard-Testfällen der Computer-Astrophysik unterzogen. Numerische Berechnungen von Problemen mit glatten Strömungsverläufen und Problemen mit starken Stößen werden ebenfalls angegeben.

Finite-Volumen-Verfahren sind numerische Verfahren, die auf der schwachen Lösung der Erhaltungsgleichungen in integraler Form basieren. Im Gegensatz zu den Finite-Volumen-Verfahren, in denen die Mittelwerte der Lösung in der Zeit entwickelt werden, wird in den konservativen Finite-Differenzen-Verfahren nur die Lösung an bestimmten Knotenpunkten berücksichtigt. Dieser Unterschied führt, aufgrund der Form der im Rekonstruktionsschritt verwendeten Stencils, bei zwei- und dreidimensionalen Berechnungen hoher Ordnung zu einer höheren Effizienz der Finite-Differenzen-Verfahren gegenüber den Finite-Volumen-Verfahren. In letzter Zeit gab es viele Bemühungen in der Entwicklung effizienter Rekonstruktionsverfahren hoher Ordnung auf strukturierten und unstrukturierten Gittern. Das am weitesten verbreitete Verfahren, um räumliche Genauigkeit hoher Ordnung in Finite-Volumen- und konservativen Finite-Differenzen-Methoden zu erreichen ist die WENO-Rekonstruktion. Die Grundidee des WENO-Schemas basiert auf einem adaptiven Rekonstruktionsverfahren, um eine Näherung höherer Ordnung in glatten Gebieten zu erhalten, während das Schema in der Nähe von Unstetigkeiten oszillationsfrei bleibt. Aus diesem Grund ist die WENO-Formulierung besonders wirksam bei der Lösung von Erhaltungsgleichungen mit auftretenden Un-

stetigkeiten. In dieser Arbeit werden die FD- und FV-Methoden durch die Nutzung des WENO-Rekonstruktions-Operators beliebiger Ordnung auf regulären kartesischen Gittern zu einer Genauigkeit sehr hoher Ordnung erweitert. Die Zeitdiskretisierung erfolgt mit einer "Strong Stability-Preserving Runge-Kutta"-Methode (SSPRK). Die MHD-, SRHD- und SRMHD-Gleichungen werden mit diesen beiden Methoden gelöst und es werden numerische Berechnungen von Problemen mit Stößen angegeben.

Ein weiteres numerisches Verfahren hoher Ordnung ist die Discontinuous Galerkin-Methode (DG). Die DG-Verfahren kombinieren die Ideen der Finite-Elemente- (FE) und der Finite-Volumen-Methoden. Wie im FE-Verfahren werden die Lösung und die Testfunktionen in der Variationsformulierung der Erhaltungsgleichung durch Polynome dargestellt, aber mit Zulassung von Unstetigkeiten an Elementgrenzen. Zur Stabilisierung des Schemas, wird von den FV-Methoden die Verwendung von Riemann-Lösern entliehen, welche die Verbindung eines gegebenen Elements mit seinen direkten Nachbarn ermöglichen. Ein Sonderfall in der Familie der DG-Methoden ist die DGSEM. Bei diesen Verfahren wird das Rechengebiet in Vierecks/Hexaeder-Elemente zerlegt, während die Lösung und die Flüsse von Tensorprodukt-Basisfunktionen (Lagrange-Interpolanten hoher Ordnung) dargestellt werden. Die Integrale werden durch Quadratur approximiert und die Knotenpunkte, an denen die Lösung berechnet wird, sind Gauß-Legendre-Quadraturpunkte. Durch diese Wahl hat der DG-Operator eine "Dimension-by-Dimension"-Form, die mehr Effizienz durch weniger Operationen und weniger Speicherbedarf ergibt. In dieser Arbeit wurde die DGSEM auch für die Gleichungen der Computer-Astrophysik auf flachen Raumzeiten erweitert, aber mit Einschränkung auf die MHD- und die SRHD-Gleichungen.

Da diskontinuierliche Lösungen ein Teil der Natur von hyperbolischen Erhaltungsgleichungen sind, müssen Shock-Capturing-Strategien entwickelt werden, insbesondere für das Discontinuous Galerkin-Verfahren. Für die DGSEM wurden mehrere Shock-Capturing-Schemen betrachtet, wie zum Beispiel der Moment-Limiter, die künstliche Viskosität, der WENO-Limiter und ein hybrider DG/FV-Ansatz. Wegen Robustheit und Effizienzgründen wird nur letzteres als Hauptbaustein zur Stabilisierung der Lösung verwendet, wenn Stöße auftreten. Das Hybrid DGSEM/FV ist so aufgebaut, dass in Bereichen mit glattem Strömungsverlauf das DGSEM-Verfahren verwendet wird, während in Gebieten mit Stößen die DGSEM-Elemente als Vierecks/Hexahedral-Untergebiete interpretiert werden. In jedem dieser Untergebiete werden die nodalen DG-Lösungswerte verwendet, um ein neues lokales Gebiet aus Finite-Volumen-Unterzellen zu bauen, die mit einem robusten Finite-Volumen-Verfahren mit WENO-Rekonstruktion dritter Ordnung entwickelt werden. Dieses neue numerische Gerüst für die Computer-Astrophysik, das auf der Hybridisierung von Verfahren hoher Ordnung basiert, bringt sehr vielversprechende Ergebnisse.

Symbols

E	Reference element
∂E	Reference element boundary
Ω_{ijk}	Physical element
$\partial \Omega_{ijk}$	Physical element boundary
Ω	Physical domain
$\partial \Omega$	Physical domain boundary
$\mathcal{O}$	Order of the scheme
$\boldsymbol{u}$	Vector of conserved quantities
$\mathbf{f}$	Tensor of physical fluxes
$\boldsymbol{f}$	Physical flux in x-direction
$\boldsymbol{g}$	Physical flux in y-direction
$\boldsymbol{h}$	Physical flux in z-direction
$\hat{\boldsymbol{f}}$	Numerical flux in x-direction
$\hat{\boldsymbol{g}}$	Numerical flux in y-direction
$\hat{\boldsymbol{h}}$	Numerical flux in z-direction
N_{GP}	Number of Gaussian integration points
t	Time
$\boldsymbol{x}$	Position vector in physical space $\boldsymbol{x} = (x^1, x^2, x^3) = (x, y, z)$
$\boldsymbol{\xi}$	Position vector in reference space $\boldsymbol{\xi} = (\xi^1, \xi^2, \xi^3) = (\xi, \eta, \zeta)$
Δt	Timestep
Δx	Size of a rectangular element in x-direction
Δy	Size of a rectangular element in y-direction
Δz	Size of a rectangular element in z-direction
$\mathbf{A}_x$	Jacobian matrix $\mathbf{A}_x = \boldsymbol{f}'(\boldsymbol{u})$
$\mathbf{A}_y$	Jacobian matrix $\mathbf{A}_y = \boldsymbol{g}'(\boldsymbol{u})$
$\mathbf{A}_z$	Jacobian matrix $\mathbf{A}_z = \boldsymbol{h}'(\boldsymbol{u})$
$\mathbf{L}_x$	Matrix of left eigenvectors of the Jacobian matrix $\mathbf{A}_x$
$\mathbf{L}_y$	Matrix of left eigenvectors of the Jacobian matrix $\mathbf{A}_y$
$\mathbf{L}_z$	Matrix of left eigenvectors of the Jacobian matrix $\mathbf{A}_z$

$\mathbf{R}_x$	Matrix of right eigenvectors of the Jacobian matrix $\mathbf{A}_x$
$\mathbf{R}_y$	Matrix of right eigenvectors of the Jacobian matrix $\mathbf{A}_y$
$\mathbf{R}_z$	Matrix of right eigenvectors of the Jacobian matrix $\mathbf{A}_z$
$\mathbf{J}$	Jacobian matrix of the coordinate transformation $\boldsymbol{x} = \boldsymbol{X}(\xi)$
$\mathcal{J}$	Jacobian determinant
ρ	Mass-density
D	Mass-density (relativistic case)
ρ	Rest-mass density (relativistic case)
p	Pressure
E	Total energy density
h	Specific enthalpy
$\boldsymbol{v}$	Velocity vector
$\boldsymbol{S}$	Momentum vector
$\boldsymbol{B}$	Magnetig field vector
v_x	Velocity component in x-direction
v_y	Velocity component in y-direction
v_z	Velocity component in z-direction
S_x	Momentum component in x-direction
S_y	Momentum component in y-direction
S_z	Momentum component in z-direction
B_x	Magnetig field component in x-direction
B_y	Magnetig field component in y-direction
B_z	Magnetig field component in z-direction
c_s	Speed of sound
γ	Adiabatic index, also ratio of specific heats
Γ	Lorentz factor

Abbreviations

ADER	Arbitrary High Order Using Derivatives
AGN	Active Galactic Nuclei
CFD	Computational Fluid Dynamics
CFL	Courant-Friedrichs-Lewy
DG	Discontinuous Galerkin
DGSEM	Discontinuous Galerkin Spectral Element Method
DNS	Direct Numerical Simulation
DOF	Degree(s) of Freedom
ENO	Essentially Non-Oscillatory
FD	Finite Differences
FV	Finite Volume
GLM	Generalized Lagrange Multiplier (divergence cleaning)
GRB	Gamma Ray Bursts
HLL	Approximate Riemann solver after Harten, Lax, & van Leer
HLLE	Approximate Riemann solver after Harten, Lax, van Leer, & Einfeldt
HLLC	HLL Riemann solver with resolution of the contact discontinuity
HPC	High Performance Computing
HRSC	High-Resolution Shock-Capturing
HWENO	Hermite Weighted Essentially Non-Oscillatory
LSERK	Low Storage Explicit Runge-Kutta
LSERK3	LSERK 3rd order (ODE solver)
LSERK4	LSERK 4rd order (ODE solver)
MHD	Magnetohydrodynamics
MP5	Monotonicity Preserving 5th order
MPI	Message-Passing-Interface
MUSCL	Monotonic Upstream-Centered Scheme for Conservation Laws
ODE	Ordinary Differential Equation
PDE	Partial Differential Equation
PPM	Piecewise Parabolic Method

RK	Runge-Kutta
RKDG	Discontinuous Galerkin Method with Runge-Kutta time discretization
RKFD	Finite Difference Method with Runge-Kutta time discretization
RKFV	Finite Volume Method with Runge-Kutta time discretization
SEM	Spectral Element Method
SRHD	Special Relativistic Hydrodynamics
SRMHD	Special Relativistic Magnetohydrodynamics
SSPRK	Strong Stability-Preserving Runge-Kutta
SSPRK3	SSPRK 3rd order (ODE solver)
SSPRK4	SSPRK 4rd order (ODE solver)
STE	Space-Time-Expansion
TV	Total Variation
TVB	Total Variation Bounded
TVD	Total Variation Diminishing
WENO	Weighted Essentially Non-Oscillatory
WENO3	WENO 3rd order (reconstruction/interpolation)
WENO5	WENO 5th order (reconstruction/interpolation)
WENO7	WENO 7th order (reconstruction/interpolation)

Chapter 1

Introduction

High-energy astrophysical phenomena involve, in many cases, magnetohydrodynamic and relativistic flows. Typical examples are superluminal motion of relativistic jets in extragalactic radio sources, accretion flows around massive compact objects, pulsar winds and gamma-ray bursts (GRB), and thus understanding magnetohydrodynamic and relativistic flows is important for interpreting the astrophysical phenomena correctly. Multi-wavelength observation of extragalactic jets performed in radio, optical and X-ray bands have dramatically extended our knowledge about the complex phenomenology of these objects. By means of these observations, different kinds of objects that can house these jets have been characterized, at the moment we can classify distinctly these sources as radio galaxies and quasars. A deeper analysis of these and other related objects led us to the idea of Active Galactic Nuclei (AGN). The images obtained from Hubble Space Telescope revealed a new detail in gas flow and shock wave patterns involving astrophysical jets and colliding interstellar winds of particles.

Astrophysical jets are defined as highly collimated outflows in the form of high velocity mass flows. The outflows are observed in young stellar objects, proto-planetary nebula, compact objects, AGN, and GRB. The jets have usually high Mach number and interact with surrounding ambient gas. For instance, intrinsic beam velocities typically larger than $0.9c$ are required to explain the apparent superluminal motions observed in relativistic jets in microquasars in Galaxies as well as in extragalactic radio sources associated with AGN. The shocks created during these phenomena accelerate particles which emit the observed radiation. In particular, it is widely accepted that the recently discovered GRB afterglow results from an emission by relativistic shocks, created by the interaction between an initial ejecta and the interstellar medium. The recent observations of GRB afterglow have led to numerous attempts to model these phenomena.

General relativistic effects must be considered when strong gravitational fields are encountered, for example, in the case of coalescing neutron stars or near black holes. The significant gravitational wave signal produced by some of these phenomena can also only be understood in the framework of the theory of general relativity. Another field of research, where special relativistic flows are encountered, is heavy-ion collision experiments performed with large particle accelerators (Ollitrault 2008; Wilson & Mathews 2003). The heavy-ions are accelerated up to ultra-relativistic velocities to study various

aspects of heavy-ion collision physics (e.g., multi-particle production, the occurrence of nuclear shock waves, collective flow phenomena, or dissipative processes) to explore the equation of state for hot dense nuclear matter, and to find evidence for the existence of the quark-gluon plasma.

Another interesting astrophysical phenomenon involving magnetohydrodynamic and/or relativistic flows is the accretion onto a compact object. The accretion disk consists of a highly conducting plasmas which slowly spiral down onto a central gravitating body, e.g., a proto-star in proto-planetary systems, black holes in active galactic nuclei, white dwarfs in cataclysmic binaries, etc. The accretion process leads to the formation of disk-like structures, since the falling-in matter will have too much angular momentum to fall inward radially, and in this manner, because of angular momentum conservation, tends to rotate about the center of gravity. The combination of a magnetic field and the outwardly decreasing differential rotation generates magnetohydrodynamic vorticity, known as magneto-rotational instability (MRI), which is very effective in transporting angular momentum and crucial for the existence of these astrophysical objects (Balbus & Hawley 1991a; Balbus & Hawley 1991b; Balbus & Hawley 1998; Balbus & Hawley 2002). For the numerical simulation of astrophysical accretion processes, two methodologies are generally used: the global and the local approaches. In the first one, large-scale global models are employed to investigate the overall structure of the disk and the gas flows that form it. But there are some difficulties with global accretion disk simulations due to the wide range of both spatial and temporal scales. In the local approach for the simulation of an accretion disk, the focus is on a small local region within the disk, called the "shearing-box". Here, the local disk physics is represented by a Cartesian box that includes the velocity shear, tidal and Coriolis forces associated with differentially rotating flow.

1.1. Computational Astrophysics

The modeling of the phenomena mentioned above has prompted the search for efficient and accurate numerical formulations of the magnetohydrodynamics and relativistic magnetohydrodynamics equations (Martí & Müller 2003; Font 2008). Simulating the fluid flow and shock wave patterns by implementing theoretical models in a gas dynamics simulator will help in analyzing the processes taking place in these astrophysical phenomena. There is now a strong consensus that the so-called High-Resolution Shock-Capturing (HRSC) schemes provide the necessary tools in developing stable and robust relativistic fluid dynamical codes (Dolezal & Wong 1995; Martí et al. 1996; Mignone & Bodo 2005; Choi & Ryu 2005). One of the fundamental ingredients of such schemes is the exact or approximate solution to the Riemann problem (Chung 2002; LeVeque 2002; Blazek 2005; Toro 2009). The solution to the Riemann problem has been extensively studied in the literature, and an exact solution can be found within high degree of accuracy by iterative techniques, see, for instance, for the magnetohydrodynamics (MHD) equations

(Ryu & Jones 1995b; Torrilhon 2003), for the special relativistic hydrodynamics (SRHD) equations (Martí & Müller 1994; Pons et al. 2000; Rezzolla & Zanotti 2001; Rezzolla et al. 2003), and for the special relativistic magnetohydrodynamics (SRMHD) equations (Giacomazzo & Rezzolla 2006). In the relativistic cases, one of the major differences with the classical counterpart is the velocity coupling introduced by the Lorentz factor and the coupling of the latter with the specific enthalpy. This increases the computational cost, making the use of an exact solver code prohibitive in a multidimensional Godunov-type code (LeVeque et al. 1998; LeVeque 2002; Toro 2001; Toro 2009).

At present, many codes have been developed for solving the equations of the computational astrophysics on flat spacetimes. Most of these codes are still widely used by the astrophysics community. The numerical method chosen to be the main building block of these codes is mainly the second order finite difference (Ryu & Jones 1995b; Ryu & Jones 1995a; Ryu et al. 1998), and finite volume methods (Zachary & Colella 1992; Zachary et al. 1994; Dai & Woodward 1994a; Dai & Woodward 1994b; Balsara & Spicer 1999b; Tóth 2000; Janhunen 2000; Dedner et al. 2002; Ziegler 2004; Balsara 2004). Numerical frameworks solving the magnetohydrodynamics equations with applications in astrophysics include the PLUTO CODE (Mignone et al. 2007), and the ATHENA CODE (Stone et al. 2008). They make use of different reconstruction procedures, especially the PLUTO CODE, allowing in this manner high-order accuracy. In Jiang & Wu (1999), for the first time, a high-order finite difference method for MHD based on weighted essentially non-oscillatory (WENO) reconstruction operators was presented. In that work, the authors were able to achieve fifth order of accuracy on multidimensional smooth flows. Taube et al. (2007), and Dumbser et al. (2008) have also achieved very high-order accurate solutions by using the discontinuous Galerkin method, but for problems with shocks, they reduce the polynomial degree of the interpolation in the so-called troubled cells.

Regarding the relativistic hydrodynamics and relativistic magnetohydrodynamics, only a few attempts with high-order methods have been done so far. High-order finite difference schemes for relativistic magnetohydrodynamics were discussed in del Zanna et al. (2007), and in Tchekhovskoy et al. (2007), high-order finite volume WENO schemes for relativistic hydrodynamics in general relativity have been presented. Recently, Radice & Rezzolla (2012) developed a new code for relativistic hydrodynamics emphasizing in turbulence computations. The first very high-order discontinuous Galerkin method for the equations of the relativistic hydrodynamics in general relativity was extensively treated in Radice & Rezzolla (2011). Dumbser et al. (2008) have tackled the SRHD and SRMHD equations, giving excellent results on smooth flows, but changing to the finite volume with WENO3 reconstruction when the problem involves discontinuities. Beckwith & Stone (2011) extended the ATHENA CODE to cover SRMHD, but using a second order finite volume method. They noted that the use of methods with orders larger than second order is not always the best approach to improve the overall accuracy of the solution.

1.2. High-Order Numerical Methods

In computational fluid dynamics, high-order numerical methods have gained quite popularity in the last years due to the need of high fidelity predictions in the simulations. Low-order methods show a considerable amount of numerical dissipation, meanwhile for high-order methods, the dissipation is very low (see figure 1.1 for a simple comparison with three different numerical schemes, namely the Runge-Kutta finite difference (RKFD), the Runge-Kutta finite volume (RKFV), and the Runge-Kutta discontinuous Galerkin (RKDG) methods). Examples of high-order numerical methods for conservation laws are the conservative finite difference methods (Shu & Osher 1988; Shu & Osher 1989) and the finite volume methods (Godunov 1959; van Leer 1979; Woodward & Colella 1984; Dumbser & Käser 2007; Dumbser et al. 2007; Shu 2009). Both methods make use of a high-order reconstruction operator in order to achieve high-order accuracy. The finite volume methods have the advantage of working also on unstructured meshes, although the reconstruction operator is more complicated. The finite difference methods require structured grids.

Another high-order method is the family of discontinuous Galerkin schemes. These methods are in discussion as future solvers in hydrodynamic flow problems because of their excellent properties and efficiency for complex flows and geometries (Cockburn & Shu 2001; Canuto et al. 2006; Hesthaven & Warburton 2008; Kopriva 2009). The discontinuous Galerkin schemes are playing a central role because the very attractive properties they possess, making of them the most suitable for solving the equations of fluid dynamics on complex geometries, and in general, nonlinear hyperbolic systems of conservation laws. In the discontinuous Galerkin method high-order accuracy is obtained through the approximation of the solution with a higher degree polynomial. The method has the capacity to handle complicated geometries, and due to its locality, it is highly parallelizable.

High-order methods are less robust than lower-order methods. In fact, the shock capturing methods used by the high-order methods are very difficult to develop and implement. But an advantage of high-order methods over lower-order methods is the need of less number of computational cells in order to get a solution with the same accuracy. This ables high-order methods to use coarse meshes, in comparison with the lower-order methods (Wang et al. 2013).

1.3. Shock Capturing for High-Order Methods

Conservation laws allow in their solution discontinuities. It is well known that these discontinuities will produce spurious oscillations, the so-called Gibbs phenomenon (Gibbs 1898; Gibbs 1899). These oscillations can cause unphysical states (negative density or pressure, or superluminal velocities in relativistic flows), making the code to fail. Therefore, a stabilization mechanism has to be constructed in order to get a well behaved

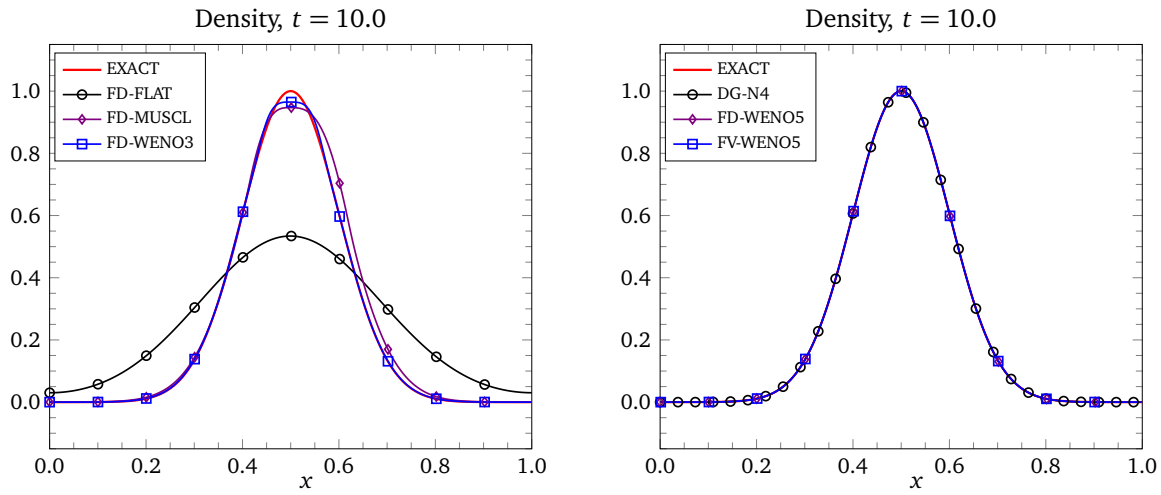

Figure 1.1: Low-Order vs. High-Order Methods: Advection of a Gaussian pulse over 10 periods. Using the RKFD with low-order reconstructions on a grid made of 400 points (left). Using the RKFD method with the high-order reconstruction procedure WENO5 on a grid composed of 400 points, using the RKFV method with the high-order reconstruction procedure WENO5 on a mesh made of 400 cells, and using the RKDG method with a polynomial of degree $N = 4$ on a mesh with only 100 elements (right).

numerical solution (see figure 1.2). For finite volume and finite difference methods, this is achieved by using the slope/flux limiters (Harten et al. 1983; Harten 1983), or by using an adaptive reconstruction operator, like the WENO reconstruction (Jiang & Shu 1996; Shu 2009). For some problems, the reconstruction can even produce these oscillations, hence it is advisable to perform the reconstruction on characteristic variables. For the discontinuous Galerkin methods, the situation is much more difficult, and several approaches have been devised. Among them, the most used by the CFD community are the *Generalized Slope Limiter* (Cockburn & Shu 1989), the *Moment Limiter* (Biswas et al. 1994; Krivodonova 2007), the *Artificial Diffusion* (Persson & Peraire 2006; Casoni et al. 2012; Casoni et al. 2013). The family of WENO reconstruction methods used as limiters in the discontinuous Galerkin method has been well studied in the last years (Shu & Osher 1988; Harten et al. 1987; Qiu & Shu 2005b; Qiu & Shu 2005a; Zhu et al. 2008; Zhong & Shu 2013; Zhu et al. 2013). The main drawback of the like-WENO limiters is that they have a huge computational overhead when high-order approximations are used.

A very promising approach consists in hybridize numerical schemes in such a way that we take advantage of the best features of each of them. For instance, a hybrid discontinuous Galerkin/finite volume scheme would be an excellent approach to tackle complex flows with shocks (Sonntag & Munz 2014; Dumbser et al. 2014). The idea is then to use the discontinuous Galerkin scheme on flow regions where shocks and discontinuities are absent, and using a robust finite volume in flow regions with such shocks/discontinuities. A more complete strategy consists in efficiently detecting troubled regions (with shocks, discontinuities, violation of positivity of some quantities of interest like pressure and den-

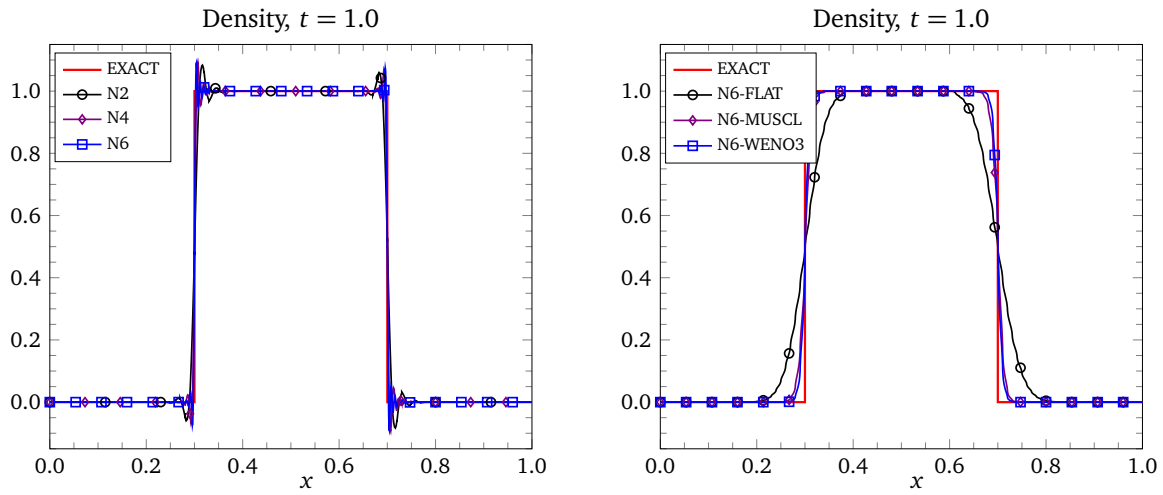

Figure 1.2: Low-Order vs. High-Order Methods: Advection of a square profile over 1 period. Using the RKDG method with polynomials of degree $N = 2, 4, 6$ on a mesh made of only 100 elements, without a shock capturing method (left). Using the RKDG method with a polynomial of degree $N = 6$ on a mesh made of 100 elements, with the hybrid DG/FV shock capturing strategy; solutions obtained with different reconstruction operators are depicted (right).

sity) and then apply an adaptive mesh refinement algorithm in those regions along with a robust finite volume scheme. Additionally, the robust finite volume can also have an adaptive reconstruction operator that lower its order at the same time it cannot obtain a physical and reasonable solution. The last step of this adaptation would be the use of the first order Godunov scheme (Titarev & Toro 2004; Dumbser et al. 2014).

1.4. XTROEM: A new Code for Computational Astrophysics

XTROEM is a new framework for computational astrophysics based on very high-order numerical methods. **XTROEM** is divided into three branches, depending on the base numerical scheme. Namely

- **XTROEM-FV** Based on high-order finite volume methods.
- **XTROEM-FD** Based on high-order conservative finite difference methods.
- **XTROEM-DG** Based on high-order discontinuous Galerkin spectral element methods.

XTROEM solves multidimensional hyperbolic systems of conservations laws, mainly those taken from the astrophysical fluid dynamics on flat spacetimes, like the hydrodynamics and magnetohydrodynamics equations, and their special relativistic counterparts. **XTROEM** has been written in Fortran 90 and it is parallelized with the Message Passing Interface (MPI) library. Currently, **XTROEM** only solves conservation laws on structured meshes.

Table 1.1: Outline of the capabilities of the **XTROEM-FV** and **XTROEM-FD** codes.

Feature	**Implemented in XTROEM-FV and XTROEM-FD**	
Equations Systems	Advection	
	Burgers	
	Hydrodynamics	
	Magnetohydrodynamics	
	Relativistic Hydrodynamics	
	Relativistic Magnetohydrodynamics	
Reconstruction Operator	FLAT	MUSCL
	WENO3	WENO5
	WENO7	MP5
Time Discretization	LSERK3	LSERK4
	SSPRK3	SSPRK4
Shock Capturing	MUSCL	WENO3
Data Output and Visualization	HDF5	VTK
	TECPLOT	MATPLOTLIB

Regarding how the high-order of accuracy is achieved, in **XTROEM-FV** and **XTROEM-FD** are implemented several reconstruction operators. These are used in a dimension-by-dimension fashion in order to have a very efficient algorithm. The **XTROEM-DG** branch makes use of the local polynomial data representation in order to achieve very high-order accurate solutions on smooth flows. All codes implement efficient and robust algorithms for tackling shock flow problems. As mentioned in the last section, shock waves require an special treatment by the numerical framework. When high-order schemes are built, these oscillations appear because of the nature of the reconstruction/interpolation. A strategy able to solve this problem needs to locate the position of the shock wave or the discontinuities, and then change the reconstruction/polynomial order to a lower and oscillation-free one, and if refinement is implemented, then the shock is captured with a very good resolution.

It is very important to save the data output in a very effective way. The HDF5 library was used as main output format because its advantages and features. The solution is then post-processed and exported to several formats which can be then visualized by specialized software, like Tecplot, Paraview, Matplotlib, etc. The post-processing tools are also parallelized with the MPI library. In the tables 1.1 and 1.2 are outlined the main features of the **XTROEM** framework.

Table 1.2: Outline of the capabilities of the **XTROEM-DG** code.

Feature	**Implemented in XTROEM-DG**	
Equations Systems	Advection Burgers Hydrodynamics Magnetohydrodynamics Relativistic Hydrodynamics	
Time Discretization	LSERK3 SSPRK3	LSERK4 SSPRK4
Shock Capturing	Hybrid DG/FV-MUSCL	Hybrid DG/FV-WENO3
Data Output and Visualization	HDF5 TECPLOT	VTK MATPLOTLIB

1.5. Objectives of this Work

The **XTROEM** framework has been developed in order to achieve the objectives of this dissertation. The three main goals of this work are the following

- Devise a numerical framework based on very high-order methods for solving the equations of the computational astrophysics on flat spacetimes. The equations of Magnetohydrodynamics, Relativistic Hydrodynamics and Relativistic Magnetohydrodynamics will be solved by using high-order numerical methods on structured meshes. The efficiency of the scheme has to be kept in mind in order to use the code for large scale calculations.

- Develop and implement robust shock capturing strategies for the high-order finite difference, finite volume and discontinuous Galerkin spectral element methods. The hyperbolic systems of conservations laws to be solved with these numerical methods, allow in their solution shocks, and it is typical to find in many astrophysical problems, complex-flow features, such as those present in the shock interaction with vortices. The shock capturing method has to be cheap and accurate enough in order to maintain and take advantage of the main numerical method of the framework.

- Perform numerical simulations of academic problems for the magnetohydrodynamics, relativistic hydrodynamics, and relativistic magnetohydrodynamics equations in order to assess all capabilities of high-order schemes for computational astrophysics. Simulate astrophysical flow problems, with special attention to astrophysical jets and accretion disks. Only simple configurations are taken into account, avoiding parameter studies.

1.6. Outline

The structure of this dissertation is as follows. In chapter 2, we start with an exhaustive treatment of the numerical methods for hyperbolic conservation laws. The fundamental concepts of finite volume methods, conservative finite differences methods and discontinuous Galerkin spectral element methods are explained. We focus on the derivation of the schemes on Cartesian meshes for the RKFD and RKFV, and hexahedral elements for the DGSEM case. Additionally, the time discretization based on Runge-Kutta methods is discussed. In chapter 3, more specific topics are explained, namely, the WENO reconstruction procedure employed in the conservative high-order finite difference method and the high-order finite volume method. Furthermore, the shock capturing strategies used in the context of the finite difference/volume methods and the discontinuous Galerkin methods are explained in detail. Last, the generalized Lagrange multiplier method as divergence cleaning strategy is described.

In chapters 4 to 6, the systems of equations (MHD, SRHD and SRMHD) solved with the high-order methods discussed in chapter 2 are outlined. In these chapters, all the relevant information regarding each equation system is shown, namely, the equations, the eigenvalues and the eigenvectors (only for the MHD and SRHD equations) of the Jacobian matrices of the physical fluxes, and the algorithms for the conversion between conservative and primitive variables. An extensive discussion of the standard one- and two-dimensional testbench for every equation system is given. This includes convergence tests on smooth flows, one-dimensional Riemann problems, and two-dimensional configurations with shock-dominated flows. Simulations of the two-dimensional Kelvin-Helmholtz instability are also taken into consideration for all equation systems. In addition, some simulations of relevant astrophysical flow problems are performed and discussed. At last, the conclusions and prospects are discussed in chapter 7.

CHAPTER 2

High-Order Methods: Foundations

In this chapter we are going to discuss the numerical methods employed along this work for solving the equations of computational astrophysics on flat space-times. We start with the basic notions in the theory of hyperbolic conservation laws, and afterwards three high-order conservative methods will be presented. The general framework of the finite volume and the conservative finite difference schemes are explained (see section 2.2 and section 2.3), but special attention is paid to the WENO reconstruction procedure in one and two space dimensions, giving all needed numerical ingredients for a successful implementation. In section 2.4 the discontinuous Galerkin method is shown and the discretization in three space dimensions is given in full detail for the DGSEM. Finally, in the section 2.5 the total variation diminishing Runge-Kutta schemes of third and fourth order are discussed.

2.1. Conservation Laws

In mathematics, a conservation law is defined as a time-dependent hyperbolic partial differential equation. Systems of conservation laws constitute a mathematical model for a huge spectrum of physical phenomena, like they are present in astrophysics, plasma physics, fluid dynamics, meteorology, acoustics, aerodynamics, optics, etc.. In this work, we are interested in the systems of conservation laws of the astrophysical fluid dynamics on flat space-times. These equations are the magnetohydrodynamics, the relativistic hydrodynamics and the relativistic magnetohydrodynamics. In the same way as in fluid dynamics, the relativistic Euler equations describe the behavior of compressible inviscid fluids, but subject to relativistic conditions (e.g., velocities close to the speed of light). Because of the most of astrophysical systems involve plasmas, a better approach for their modeling consists in using the equations of the relativistic magnetohydrodynamics. We refer to the literature on conservation laws for an overview of another relevant equation systems in physics and other subjects (Zel'dovich & Raizer 1967; LeVeque 1992; Kröner 1997; Meister & Struckmeier 2002; Toro 2009). We pretend to discuss the basic notions of hyperbolic partial differential equations that will be used along this work when we deal with its numerical treatment.

2.1.1. Hyperbolic Partial Differential Equations

Let us consider the following partial differential equation

$$\frac{\partial \boldsymbol{u}}{\partial t} + \frac{\partial \boldsymbol{f}(\boldsymbol{u})}{\partial x} + \frac{\partial \boldsymbol{g}(\boldsymbol{u})}{\partial y} + \frac{\partial \boldsymbol{h}(\boldsymbol{u})}{\partial z} = \boldsymbol{0}, \quad \text{in } \mathbb{R}^3 \times \mathbb{R}^+, \tag{2.1}$$

where $\boldsymbol{u} : \mathbb{R}^3 \times \mathbb{R}^+ \to \mathbb{R}^m$ is the vector of *conserved* quantities, $\boldsymbol{f}, \boldsymbol{g}, \boldsymbol{h} : \mathbb{R}^3 \to \mathbb{R}^m$ are the *flux functions*, and $\boldsymbol{u}_0(\boldsymbol{x}) : \mathbb{R}^3 \to \mathbb{R}^m$ denotes the initial data.

The system (2.1) is said to be hyperbolic at a point $(\boldsymbol{x}, t)$ if for all $\alpha_1, \alpha_2, \alpha_3 \in \mathbb{R}$ with at least one of them being different from zero, the matrix

$$\boldsymbol{A}(\boldsymbol{u}) \equiv \alpha_1 \frac{\partial \boldsymbol{f}}{\partial \boldsymbol{u}} + \alpha_1 \frac{\partial \boldsymbol{g}}{\partial \boldsymbol{u}} + \alpha_1 \frac{\partial \boldsymbol{h}}{\partial \boldsymbol{u}} \tag{2.2}$$

has m real eigenvalues $\lambda_1, \ldots, \lambda_m$ and a corresponding set of m linearly independent right eigenvectors $\boldsymbol{R}^{(1)}, \ldots, \boldsymbol{R}^{(m)}$. The system (2.1) is said to be strictly hyperbolic if the eigenvalues λ_i are all distinct (Toro 2009).

2.1.2. Weak Solutions

For simplicity, let us consider the following Cauchy initial value problem

$$\frac{\partial \boldsymbol{u}}{\partial t} + \frac{\partial \boldsymbol{f}(\boldsymbol{u})}{\partial x} = \boldsymbol{0}, \qquad \text{in } \mathbb{R} \times \mathbb{R}^+, \tag{2.3a}$$

$$\boldsymbol{u}(x, 0) = \boldsymbol{u}_0(x) \quad \text{in } \mathbb{R}. \tag{2.3b}$$

A classical solution of the equation (2.3a) is a function $\boldsymbol{u} \in \mathcal{C}^1(\mathbb{R} \times \mathbb{R}^+)$ that satisfies equations (2.3a-2.3b) pointwise. Even if smooth initial and boundary conditions are given, in nonlinear hyperbolic conservation laws can appear shock waves. In presence of this shock, beyond some critical time t_0, the classical solution of (2.3a-2.3b) does not exist. By introducing the notion of weak solutions of (2.3a-2.3b) together with an entropy condition, it then becomes possible to define a class of solutions where existence and uniqueness is guaranteed for times greater than t_0.

Let $\boldsymbol{u}_0 \in \mathcal{L}^\infty(\mathbb{R}^n)$. Then, $\boldsymbol{u}$ is a weak solution of (2.3a-2.3b) if $\boldsymbol{u} \in \mathcal{L}^\infty(\mathbb{R}^n \times \mathbb{R}^+)$ and (2.3a-2.3b) hold in the distributional sense, i.e.,

$$\int_{\mathbb{R}^n} \int_{\mathbb{R}^+} \left(\boldsymbol{u} \frac{\partial \phi}{\partial t} + \boldsymbol{f}(\boldsymbol{u}) \cdot \nabla \phi \right) \mathrm{d}t \, \mathrm{d}\boldsymbol{x} + \int_{\mathbb{R}^n} \boldsymbol{u}_0 \phi(\boldsymbol{x}, 0) \, \mathrm{d}\boldsymbol{x} = 0, \tag{2.4}$$

for all $\phi \in \mathcal{C}_0^1(\mathbb{R}^n \times \mathbb{R}^+)$. Note that classical solutions are weak solutions and weak solutions that lie in $\mathcal{C}^1(\mathbb{R}^n \times \mathbb{R}^+)$ satisfy (2.3a-2.3b) in the classical sense. It can be shown that there always exists at least one weak solution to (2.3a-2.3b) if the flux function $\boldsymbol{f}$ is at least Lipschitz continuous (Bressan 2000).

2.2. Finite Volume Methods

Finite volume methods are numerical methods based on the weak solution of conservation laws in integral form. In comparison with standard finite difference methods, these methods admit in a natural way discontinuous solutions because the integral formulation requires less smoothness of the solution (LeVeque 2002; Toro 2009). The mathematical theory of the finite volume methods has been developed in the last 30-40 years, reaching a very mature stage. Most of the codes used in astrophysics and the CFD codes used in the aerospace industry are based on second order finite volume methods. Recently, the development of efficient very high-order accurate reconstruction procedures has occupied an important place in research institutes around the world, giving as result the WENO procedures for structured and unstructured meshes (Liu et al. 1994; Jiang & Shu 1996; Meister & Struckmeier 2002; Shu 2009; Dumbser & Käser 2007; Dumbser et al. 2007).

The basic idea behind the finite volume scheme consists in subdividing the computational domain in non-overlapping control volumes. In each one of these control volumes, the solution is represented by the cell average of the conserved quantity. Eventually, every control volume can have an arbitrary form, but typically they are triangles and rectangles in 2D and tetrahedra and hexahedra in 3D. Finally, in each control volume, an integral conservation law statement is then imposed (LeVeque 1992; Bressan 2000; LeVeque 2002; Toro 2009).

In this section we will first define the integral conservation laws and conservative methods. Next, we will present the basic idea of Godunov's method and the Total Variation Diminishing (TVD) schemes. Last, the general principles of the high-order WENO reconstruction procedure on structured grids will be outlined.

2.2.1. Integral Conservation Laws

Conservation laws can be written either in differential form or integral form. The differential form was presented when we defined hyperbolic conservation laws. In this section we will show the integral form and explain its importance in the development of numerical methods.

Let us start by defining an integral conservation law. Following (Lax 1973), an integral conservation law asseverates that the rate of change of the total amount of a substance with density u in a fixed control volume Ω is equal to the total flux of the substance through the boundary $\partial\Omega$

$$\frac{\mathrm{d}}{\mathrm{d}t}\int_{\Omega} u \,\mathrm{d}\Omega + \int_{\partial\Omega} \mathbf{f}\cdot\boldsymbol{n}\,\mathrm{d}\sigma = 0. \tag{2.5}$$

Applying the divergence theorem to the equation (2.5) we get

$$\int_{\Omega}\left(\frac{\partial u}{\partial t} + \nabla\cdot\mathbf{f}(u)\right)\mathrm{d}\Omega = 0,$$

From the latter equation we obtain the conservation law in differential form by dividing it by the volume of Ω and shrinking Ω to a point where the partial derivatives of u and $\mathbf{f}$ are continuous (Lax 1973; Godlewski & Raviart 1996), that is

$$\frac{\partial u}{\partial t} + \nabla \cdot \mathbf{f}(u) = 0. \tag{2.6}$$

Systems of conservation laws are written as

$$\frac{\partial \boldsymbol{u}}{\partial t} + \nabla \cdot \mathbf{f}(\boldsymbol{u}) = \mathbf{0}, \tag{2.7}$$

where, again, $\boldsymbol{u}$ is the vector of conserved quantities, and $\mathbf{f} = [\boldsymbol{f}, \boldsymbol{g}, \boldsymbol{h}]$ is the tensor of physical fluxes.

2.2.2. Conservative Methods

Once defined an integral conservation law, we proceed to define a conservative scheme for the conservation law. We emphasize that although the definition shown below is given assuming a Cartesian mesh, this is also valid in unstructured meshes, where the control volume is defined by the triangulation used in the discretization. For a presentation of the finite volume method in general triangulations, see (Kröner 1997).

Let Ω_{ijk} a control volume obtained after the triangulation of the physical domain Ω by using rectangular cells. In this way, Ω_{ijk} is the cell

$$\Omega_{ijk} = \left[x_{i-\frac{1}{2}}, x_{i+\frac{1}{2}}\right] \times \left[y_{j-\frac{1}{2}}, y_{j+\frac{1}{2}}\right] \times \left[z_{k-\frac{1}{2}}, z_{k+\frac{1}{2}}\right].$$

A conservative numerical scheme for the system of hyperbolic conservation laws (2.7) is defined as a numerical method of the form

$$\frac{\mathrm{d}\boldsymbol{u}_{ijk}}{\mathrm{d}t} = \frac{\hat{\boldsymbol{f}}_{i-\frac{1}{2},jk} - \hat{\boldsymbol{f}}_{i+\frac{1}{2},jk}}{\Delta x} + \frac{\hat{\boldsymbol{g}}_{i,j-\frac{1}{2},k} - \hat{\boldsymbol{g}}_{i,j+\frac{1}{2},k}}{\Delta y} + \frac{\hat{\boldsymbol{h}}_{ij,k-\frac{1}{2}} - \hat{\boldsymbol{h}}_{ij,k+\frac{1}{2}}}{\Delta z}, \tag{2.8}$$

where the numerical fluxes

$$\begin{aligned} \hat{\boldsymbol{f}}_{i+\frac{1}{2},jk} &= \hat{\boldsymbol{f}}(\boldsymbol{u}_{i-p,jk}, \ldots, \boldsymbol{u}_{i+q,jk}), \\ \hat{\boldsymbol{g}}_{i,j+\frac{1}{2},k} &= \hat{\boldsymbol{g}}(\boldsymbol{u}_{i,j-p,k}, \ldots, \boldsymbol{u}_{i,j+q,k}), \\ \hat{\boldsymbol{h}}_{ij,k+\frac{1}{2}} &= \hat{\boldsymbol{h}}(\boldsymbol{u}_{ij,k-p}, \ldots, \boldsymbol{u}_{ij,k+q}), \end{aligned} \tag{2.9}$$

are an approximation of the physical fluxes and are consistent with them in the sense that $\hat{\boldsymbol{f}}(\boldsymbol{u}, \ldots, \boldsymbol{u}) = \boldsymbol{f}(\boldsymbol{u})$, $\hat{\boldsymbol{g}}(\boldsymbol{u}, \ldots, \boldsymbol{u}) = \boldsymbol{g}(\boldsymbol{u})$, and $\hat{\boldsymbol{h}}(\boldsymbol{u}, \ldots, \boldsymbol{u}) = \boldsymbol{h}(\boldsymbol{u})$.

When solving hyperbolic conservation laws, maybe the most important requirement on the numerical method is that it should be a conservative scheme. In fact, the Lax-Wendroff theorem guarantees that for such numerical methods, if they are convergent, they converge to the weak solution (Lax & Wendroff 1960). Another important result

related to conservative methods is the obtained by Hou & LeFloch (1994). They showed that a non-conservative numerical scheme does not converge to the correct solution if shock waves are present in the solution. Because of discontinuities are inherent to conservation laws, it is necessary to use conservative methods and those non-conservative should be avoided.

2.2.3. Finite Volume Formulation

Given the system of conservation laws (2.7)

$$\frac{\partial \boldsymbol{u}}{\partial t} + \frac{\partial \boldsymbol{f}(\boldsymbol{u})}{\partial x} + \frac{\partial \boldsymbol{g}(\boldsymbol{u})}{\partial y} + \frac{\partial \boldsymbol{h}(\boldsymbol{u})}{\partial z} = \boldsymbol{0}, \tag{2.10}$$

by integrating it over the cell Ω_{ijk}, we get the semi-discrete scheme[1]

$$\frac{\mathrm{d}\boldsymbol{u}_{ijk}}{\mathrm{d}t} = \frac{\hat{\boldsymbol{f}}_{i-\frac{1}{2},jk} - \hat{\boldsymbol{f}}_{i+\frac{1}{2},jk}}{\Delta x} + \frac{\hat{\boldsymbol{g}}_{i,j-\frac{1}{2},k} - \hat{\boldsymbol{g}}_{i,j+\frac{1}{2},k}}{\Delta y} + \frac{\hat{\boldsymbol{h}}_{ij,k-\frac{1}{2}} - \hat{\boldsymbol{h}}_{ij,k+\frac{1}{2}}}{\Delta z}, \tag{2.11}$$

where, in the context of finite volume methods, $\boldsymbol{u}_{ijk}$ is the spatial average of $\boldsymbol{u}$ in the cell Ω_{ijk} at time t

$$\boldsymbol{u}_{ijk} = \frac{1}{\Delta x}\frac{1}{\Delta y}\frac{1}{\Delta z}\int_{x_{i-\frac{1}{2}}}^{x_{i+\frac{1}{2}}}\int_{y_{j-\frac{1}{2}}}^{y_{j+\frac{1}{2}}}\int_{z_{k-\frac{1}{2}}}^{z_{k+\frac{1}{2}}} \boldsymbol{u}(x,y,z)\,\mathrm{d}z\,\mathrm{d}y\,\mathrm{d}x, \tag{2.12}$$

and $\hat{\boldsymbol{f}}_{i\pm\frac{1}{2},jk}$, $\hat{\boldsymbol{g}}_{i,j\pm\frac{1}{2},k}$, and $\hat{\boldsymbol{h}}_{ij,k\pm\frac{1}{2}}$ are spatial averages of the physical fluxes over the cell faces $x_{i\pm\frac{1}{2}}$, $y_{j\pm\frac{1}{2}}$, and $z_{k\pm\frac{1}{2}}$, respectively, at time t

$$\begin{aligned}
\hat{\boldsymbol{f}}_{i\pm\frac{1}{2},jk} &= \frac{1}{\Delta y}\frac{1}{\Delta z}\int_{y_{j-\frac{1}{2}}}^{y_{j+\frac{1}{2}}}\int_{z_{k-\frac{1}{2}}}^{z_{k+\frac{1}{2}}} \boldsymbol{f}\big(\boldsymbol{u}(x_{i\pm\frac{1}{2}},y,z)\big)\,\mathrm{d}z\,\mathrm{d}y,\\
\hat{\boldsymbol{g}}_{i,j\pm\frac{1}{2},k} &= \frac{1}{\Delta x}\frac{1}{\Delta z}\int_{x_{i-\frac{1}{2}}}^{x_{i+\frac{1}{2}}}\int_{z_{k-\frac{1}{2}}}^{z_{k+\frac{1}{2}}} \boldsymbol{g}\big(\boldsymbol{u}(x,y_{j\pm\frac{1}{2}},z)\big)\,\mathrm{d}z\,\mathrm{d}x,\\
\hat{\boldsymbol{h}}_{ij,k\pm\frac{1}{2}} &= \frac{1}{\Delta x}\frac{1}{\Delta y}\int_{x_{i-\frac{1}{2}}}^{x_{i+\frac{1}{2}}}\int_{y_{j-\frac{1}{2}}}^{y_{j+\frac{1}{2}}} \boldsymbol{h}\big(\boldsymbol{u}(x,y,z_{k\pm\frac{1}{2}})\big)\,\mathrm{d}y\,\mathrm{d}x.
\end{aligned} \tag{2.13}$$

So far, no approximation has been done. In fact, the semi-discrete scheme (2.11) is an exact relation as well as the averaged quantities (2.12) and (2.13). We need to find a high-order approximation of the fluxes (2.13) in order to have a high-order accurate solution of (2.11). The integrals of the fluxes given in the equation (2.13) are discretized by means of a high-order Gaussian quadrature with suitable Gaussian integration points

[1] It is not surprising that the semi-discrete scheme (2.11) has the conservative form (2.8).

over the faces of the control volume; in the case of the present work, for Cartesian meshes, this is written as

$$\begin{aligned}
\hat{\boldsymbol{f}}_{i\pm\frac{1}{2},jk} &= \frac{1}{\Delta y}\frac{1}{\Delta z}\sum_{\alpha=1}^{N_{GP}}\sum_{\beta=1}^{N_{GP}}\boldsymbol{f}\big(\boldsymbol{u}(x_{i\pm\frac{1}{2}},y_\alpha,z_\beta)\big)\omega_\alpha\omega_\beta,\\
\hat{\boldsymbol{g}}_{i,j\pm\frac{1}{2},k} &= \frac{1}{\Delta x}\frac{1}{\Delta z}\sum_{\alpha=1}^{N_{GP}}\sum_{\beta=1}^{N_{GP}}\boldsymbol{g}\big(\boldsymbol{u}(x_\alpha,y_{j\pm\frac{1}{2}},z_\beta)\big)\omega_\alpha\omega_\beta,\\
\hat{\boldsymbol{h}}_{ij,k\pm\frac{1}{2}} &= \frac{1}{\Delta x}\frac{1}{\Delta y}\sum_{\alpha=1}^{N_{GP}}\sum_{\beta=1}^{N_{GP}}\boldsymbol{h}\big(\boldsymbol{u}(x_\alpha,y_\beta,z_{k\pm\frac{1}{2}})\big)\omega_\alpha\omega_\beta.
\end{aligned} \tag{2.14}$$

Because only the cell averages $\boldsymbol{u}_{ijk}$ are known, we require a high-order accurate numerical procedure to reconstruct the point-wise values of $\boldsymbol{u}$ at the Gaussian integration points at the faces. By evaluating the fluxes at these points, we note that there are two sets of reconstructed values at a given face: those obtained through the use of the cell Ω_{ijk} as the main cell in the reconstruction procedure and those associated with the neighboring cell. These are known as the left and right values at the face interface: $\boldsymbol{u}_L$ and $\boldsymbol{u}_R$. Finally the fluxes are evaluated by replacing $\boldsymbol{f}$, $\boldsymbol{g}$, and $\boldsymbol{h}$ by a monotone flux, the so-called Riemann solver. Almost for every conservation law of interest there is a Riemann solver (exact or approximate). A detailed description of Riemann solvers and their application in fluid dynamics can be found in the book of Toro (2009).

Before we go into the details of the reconstruction procedure, we will next present the basic ideas of the Godunov's method and high-order schemes. We recommend the reviews by Wang (2007) and Wang et al. (2013) and the books by Barth & Deconinck (1999) and Wang (2011) for a more exhaustive explanation of high-order methods and their applications in computational physics.

2.2.4. Godunov's Method

The numerical treatment for conservation laws received a fundamental boost thanks to the ideas of Sergei Godunov. In 1959 Godunov published a paper in which he proposed the use of the Riemann problem solution as a building block for a finite volume scheme for conservation laws (Godunov 1959). By employing the solution of a Riemann problem (see figure 2.1), he was able to compute the numerical fluxes at cell interfaces. His scheme is characterized by the use of a piecewise constant data representation, being first-order accurate and monotone. Thanks to his work, a new family of numerical methods for conservation laws emerged and today it constitutes a very active research field. It was (van Leer 1999) whom defined Godunov type methods as *non-oscillatory finite-volume schemes that incorporate the solution (exact or approximate) to Riemann's initial-value problem, or a generalization of it*.

One of the most important results of Godunov's work is his famous theorem, also known as *Godunov's order barrier theorem*. This states that *monotonicity preserving con-*

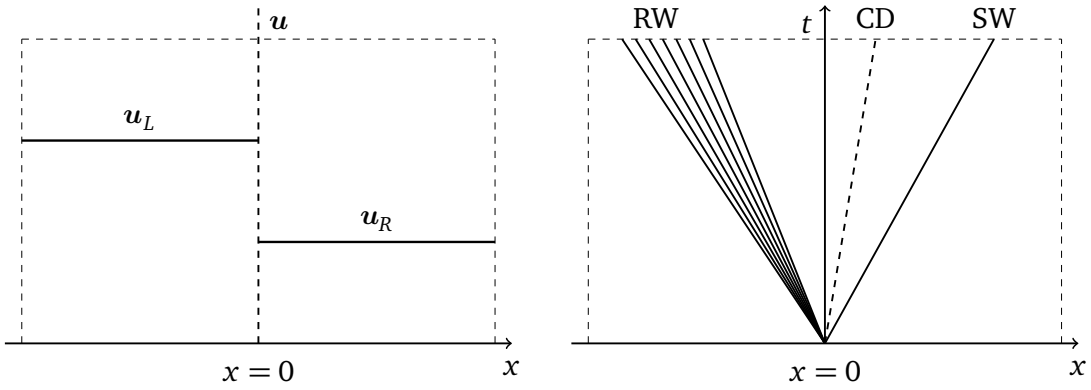

Figure 2.1: Initial data for a generic Riemann problem (left). Riemann fan for the one-dimensional Euler equations (right). Here RW stands for rarefaction wave, CD for contact discontinuity and SW for shock wave. In general, a Riemann problem consists of a conservation law together with piecewise constant data separated by a discontinuity as initial condition (Lax 1973).

stant coefficient schemes can be at most first order accurate. As a consequence of it, it is only through the use of *nonlinear schemes* that high-order accuracy and monotonicity can be achieved (Toro 2001). Because of that, high-order extensions of the Godunov's method have appeared by changing the way the data are represented. As examples of high-order finite volume schemes we have the MUSCL scheme of van Leer (1979), the piecewise parabolic method (PPM) of Woodward & Colella (1984), the essentially non-oscillatory schemes of Harten et al. (1987), or the weighted essentially non-oscillatory schemes of Jiang & Shu (1996). In the original work of Godunov, he used the exact solution of the Riemann problem, but other researchers have employed approximations to the solution of the Riemann problem because the computing of the exact solution is very expensive. A large family of approximate Riemann solvers have risen for different conservation laws, but the main effort has been put in the Euler equations. For instance, the most used Riemann solvers for the Euler equations are the Roe Riemann solver (Roe 1981), the Osher Riemann solver (Osher & Solomon 1982), the HLL Riemann solver (Harten et al. 1983), the HLLE (Einfeldt 1988), and the HLLC Riemann solver (Toro et al. 1994).

In the following we are going to describe with an example the basic ideas of the Godunov's method. We do not pretend to describe exactly the original work of Godunov as it is presented in his paper. Let us start by considering the one-dimensional scalar conservation law

$$\frac{\partial u}{\partial t} + \frac{\partial f(u)}{\partial x} = 0. \tag{2.15}$$

For seek of simplicity, we assume that the mesh is uniform. In the Godunov's method, the values u_i^n are assumed to be the cell averages of the solution $u(x,t)$ at time t^n, that

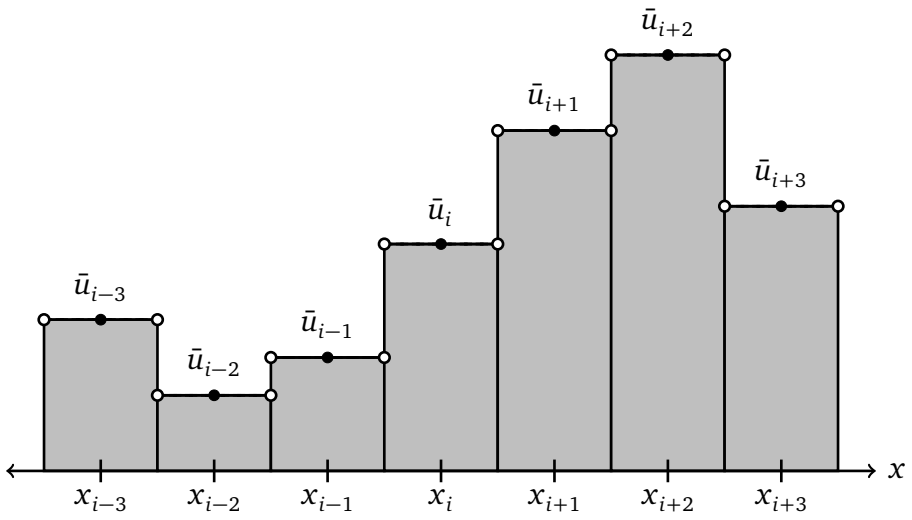

Figure 2.2: Piecewise constant data representation in the finite volume Godunov's scheme (Godunov 1959). Riemann problems are solved in the cell interfaces $x_{i\pm\frac{1}{2}}$, namely $RP_i^-(u_{i-1},u_i)$, and $RP_i^+(u_i,u_{i+1})$.

is the solution has a piecewise constant data representation (see figure 2.2)

$$u_i^n = \frac{1}{\Delta x}\int_{x_{i-\frac{1}{2}}}^{x_{i+\frac{1}{2}}} u(x,t^n)\,\mathrm{d}x. \tag{2.16}$$

At cell interfaces a Riemann problem is solved, and later on they are used to update the numerical solution.

After integrating integrate the conservation law (2.15) over the space-time cell $\left[x_{i-\frac{1}{2}},x_{i+\frac{1}{2}}\right]\times\left[t^n,t^{n+1}\right]$, we get

$$\int_{t^n}^{t^{n+1}}\int_{x_{i-\frac{1}{2}}}^{x_{i+\frac{1}{2}}}\frac{\partial u}{\partial t}(x,t)\,\mathrm{d}x\,\mathrm{d}t = -\int_{t^n}^{t^{n+1}}\int_{x_{i-\frac{1}{2}}}^{x_{i+\frac{1}{2}}}\frac{\partial f(u)}{\partial x}(x,t)\,\mathrm{d}x\,\mathrm{d}t, \tag{2.17}$$

from where

$$\int_{x_{i-\frac{1}{2}}}^{x_{i+\frac{1}{2}}}\Big[u(x,t^{n+1})-u(x,t^n)\Big]\mathrm{d}x = -\int_{t^n}^{t^{n+1}}\Big[f\big(u(x_{i+\frac{1}{2}},t)\big)-f\big(u(x_{i-\frac{1}{2}},t)\big)\Big]\mathrm{d}t. \tag{2.18}$$

Using the definition of cell average of u given above, we can then write the Godunov's method in conservation form

$$u_i^n = u_i^{n+1} - \frac{\Delta t}{\Delta x}\Big(f_{i+\frac{1}{2}}^n - f_{i-\frac{1}{2}}^n\Big), \tag{2.19}$$

where we have introduced the numerical fluxes

$$
\begin{aligned}
f^n_{i-\frac{1}{2}} &= f(u^n_{i-1}, u^n_i) = \frac{1}{\Delta t}\int_{t^n}^{t^{n+1}} f\big(u(x_{i-\frac{1}{2}}, t)\big)\,\mathrm{d}t,\\
f^n_{i+\frac{1}{2}} &= f(u^n_i, u^n_{i+1}) = \frac{1}{\Delta t}\int_{t^n}^{t^{n+1}} f\big(u(x_{i+\frac{1}{2}}, t)\big)\,\mathrm{d}t.
\end{aligned}
\tag{2.20}
$$

From these definitions of numerical fluxes we see that they do depend only of the state at cell interfaces, $u(x_{x\pm\frac{1}{2}})$, i.e., $f^n_{i\pm\frac{1}{2}} = f(u^n_{i\pm\frac{1}{2}})$. Godunov used the exact solution of the Riemann problem, but approximate solutions can also be employed.

2.2.5. Total-Variation-Diminishing Schemes

In spite of the great success of the Godunov's method, it is first-order accurate and it is too diffusive. As a result, when a discontinuity or shock appears, it is smeared. This has motivated the development of high-resolution shock-capturing numerical methods for hyperbolic problems. The main drawback of high-order schemes is basically the presentation of spurious oscillations around discontinuities. This phenomenon is inevitable for linear schemes, which could not be both monotonicity preserving and higher than first order accurate, as Godunov proved in his seminal paper (Godunov 1959). For this reason, research has turn into the construction of nonlinear high-order schemes, starting with the works of Boris & Book (1973), and van Leer (1973), van Leer (1974), van Leer (1977a), van Leer (1977b), and van Leer (1979). On the other hand, to achieve high-order accuracy we must change the data representation. In fact, one of the most popular high-order schemes in computational fluid dynamics, the MUSCL scheme, make use of a piecewise linear reconstruction inside every computational cell (see figure 2.3). The idea of using a piecewise linear data representation was initially developed in Kolgan (1972), and developed further in van Leer (1979).

With the introduction of high-order schemes and their inevitable spurious oscillations, it was necessary to construct a monitor for them. The *total variation* was utilized for this purpose. The reason was that, for the scalar conservation law, the analytic total variation,

$$
\mathrm{TV}(u) = \int \left|\frac{\partial u}{\partial x}\right| \mathrm{d}x, \tag{2.21}
$$

does not increase (and only does decrease across shocks (Lax 1973)). Harten et al. (1983) proposed that the numerical schemes should imitate this behavior at a discrete level

$$
\mathrm{TV}(u^n) = \sum_i \left|u^n_i - u^n_{i-1}\right|, \tag{2.22}
$$

that is,

$$
\mathrm{TV}(u^{n+1}) \leq \mathrm{TV}(u^n). \tag{2.23}
$$

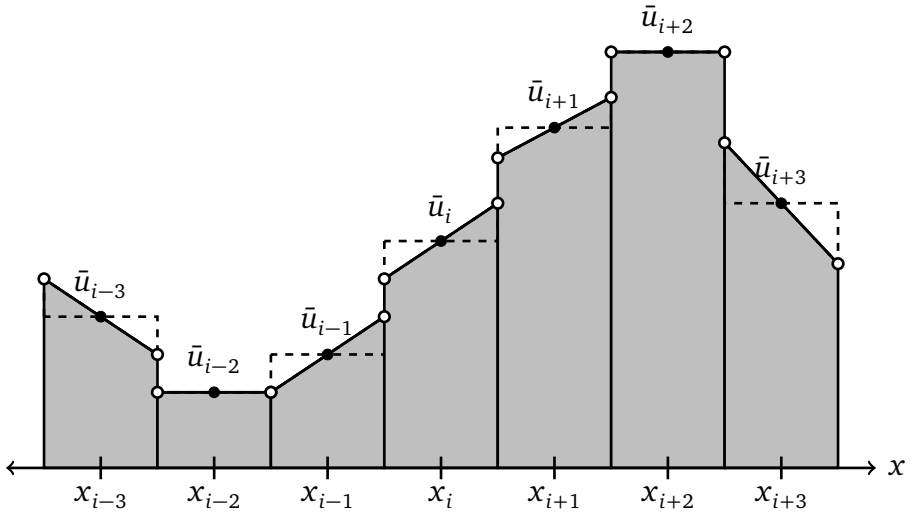

Figure 2.3: Piecewise linear data representation in the finite volume MUSCL scheme (van Leer 1979). Riemann problems are solved in the cell interfaces $x_{i\pm\frac{1}{2}}$, namely $RP_i^-(u_{i-1},u_i)$, and $RP_i^+(u_i,u_{i+1})$.

The schemes that obey this relation are called Total Variation Diminishing (TVD). If a conservative scheme is TVD, then it converges to the weak solution. The piecewise data representation was constructed to maintain conservation by defining the cell representation to be

$$u_i(x) = u_i^n + \frac{\Delta_i u}{\Delta x}(x - x_i), \tag{2.24}$$

where u_i^n is the Godunov cell average and the slope $\frac{\Delta_i u}{\Delta x}$ must be defined. The quantity $\Delta_i u$ is defined through central differencing of the piecewise constant cell averages $\Delta_i u = \frac{1}{2}(u_{i+1} - u_i)$. At the cell interfaces of the piecewise linear data representation, we have a set of so-called generalized Riemann problems. Here, a discontinuity separates two piecewise linear states. These are not as easily solved as the basic Riemann problem and the wave paths are now curves rather than straight lines in the $x-t$ space (Artzi & Falcovitz 1984; LeFloch & Raviart 1988; Titarev & Toro 2002).

2.2.6. WENO Reconstruction

The most widely used procedure to achieve high-order spatial accuracy in finite volume and conservative finite difference methods is the WENO reconstruction. WENO stands for weighted essentially non-oscillatory and is based on the ENO schemes (Harten et al. 1987). The WENO schemes were introduced in Liu et al. (1994), and in Jiang & Shu (1996) and Balsara & Shu (2000) a general framework to construct arbitrary order accurate together with new smoothness indicators was provided. Smoothness indicators and interpolated values are reported up to seventh order of accuracy in Balsara & Shu

(2000). Very high-order WENO schemes are reported, up to 17th order of accuracy in Gerolymos et al. (2009) .

The basic idea of the WENO schemes is based on an adaptive reconstruction procedure to obtain a higher-order approximation on smooth regions while the scheme remains non-oscillatory near discontinuities (Shu 2009). In each stencil, a polynomial is reconstructed from the cell averages of the solution and later a weighted combination of all these polynomials is constructed. The nonlinear weights are computed taking into account the smoothness of every polynomial in its respective stencil.

In this section we are going to outline the dimension-by-dimension reconstruction algorithm used in this work for three-dimensional conservation laws and we let for the section 3.1 the description of the main aspects of the WENO reconstruction operator, as the computation of the oscillation indicators, and the linear and nonlinear weights for the WENO3, WENO5 and WENO7 schemes. The dimension-by-dimension reconstruction was introduced by Casper & Atkins (1993) in the ENO framework for two-dimensional conservation laws. Titarev & Toro (2004) extended it to three-dimensional domains. We emphasize that the dimension-by-dimension reconstruction is only valid for structured meshes, and at the same time, it is the less computationally expensive among all reconstructions (although a new methodology for finite volume methods in Cartesian meshes has been introduced by Buchmüller & Helzel (2014), making the reconstruction process as simple as for finite difference methods). For unstructured grids (and they are also valid in Cartesian grids) there are another strategies, for example, the genuine multidimensional reconstruction of Hu & Shu (1999), but they will not be considered in this work.

The aim of the reconstruction is the following: From the cell averages of the solution, points values of the function at appropriate points (that is, the Gaussian integration points) are interpolated (or *reconstructed*), which will be used in the finite-volume methodology to calculate the numerical fluxes via a Riemann solver. This means, given the cell averages of the function $u(x,y,z)$ in the cell Ω_{ijk}

$$\begin{aligned} u_{ijk} &= \frac{1}{\left|\Omega_{ijk}\right|}\int_{\Omega_{ijk}} u(x,y,z)\,\mathrm{d}z\,\mathrm{d}y\,\mathrm{d}x \\ &= \frac{1}{\Delta x}\frac{1}{\Delta y}\frac{1}{\Delta z}\int_{x_{i-\frac{1}{2}}}^{x_{i+\frac{1}{2}}}\int_{y_{j-\frac{1}{2}}}^{y_{j+\frac{1}{2}}}\int_{z_{k-\frac{1}{2}}}^{z_{k+\frac{1}{2}}} u(x,y,z)\,\mathrm{d}z\,\mathrm{d}y\,\mathrm{d}x, \end{aligned} \tag{2.25}$$

we reconstruct point values of u at the Gaussian integration points $(x_{i\pm\frac{1}{2}}, y_{j+\alpha}, z_{k+\beta})$, $(x_{i+\alpha}, y_{j\pm\frac{1}{2}}, z_{k+\beta})$, $(x_{i+\alpha}, y_{j+\beta}, z_{i\pm\frac{1}{2}})$. In this work we make use of the two points Gaussian quadrature rule

$$\int_{-1}^{+1} f(x)\,\mathrm{d}x \approx \sum_{i=1}^{2} w_i f(x_i) = f\left(-\frac{1}{\sqrt{3}}\right) + f\left(+\frac{1}{\sqrt{3}}\right), \tag{2.26}$$

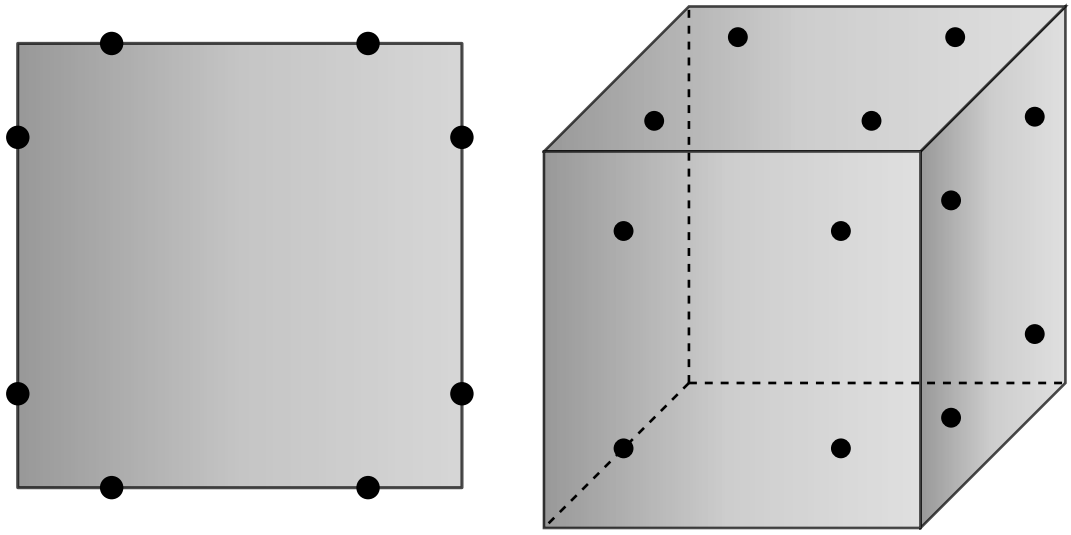

Figure 2.4: Gaussian integration points in a control volume where the WENO reconstruction is performed. At cell edges in the two-dimensional case, they are given by $(x_{i\pm\frac{1}{2}}, y_{j+\alpha})$ and $(x_{i+\alpha}, y_{j\pm\frac{1}{2}})$ (left). At cell faces in the three-dimensional case, they are given by $(x_{i\pm\frac{1}{2}}, y_{j+\alpha}, z_{k+\beta})$, $(x_{i+\alpha}, y_{j\pm\frac{1}{2}}, z_{k+\beta})$, and $(x_{i+\alpha}, y_{j+\beta}, z_{i\pm\frac{1}{2}})$ (right). In both cases $\alpha, \beta = \pm 1/2\sqrt{3}$.

for calculating the surface integral appearing in the finite volume formulation just as it is reported in the work of Titarev & Toro (2004) and Titarev & Toro (2005). In the figure 2.4 these Gaussian integration points are depicted. They are given by $(x_{i\pm\frac{1}{2}}, y_{j+\alpha})$ and $(x_{i+\alpha}, y_{j\pm\frac{1}{2}})$ in 2D and $(x_{i\pm\frac{1}{2}}, y_{j+\alpha}, z_{k+\beta})$, $(x_{i+\alpha}, y_{j\pm\frac{1}{2}}, z_{k+\beta})$, $(x_{i+\alpha}, y_{j+\beta}, z_{i\pm\frac{1}{2}})$ in 3D, with $\alpha, \beta = \pm 1/2\sqrt{3}$. A higher-order Gaussian quadrature gives as result negatives linear weights in the point-wise WENO reconstruction. Although there is an strategy to deal with such negatives weights (Shi et al. 2002), we prefer to follow the recommendations given in Titarev & Toro (2004). We stress that the high-order accuracy of the scheme is provided by the high-order reconstruction of the function values at the Gaussian integration points.

In the following, we are going to show the dimension-by-dimension algorithm only for the reconstruction at the Gaussian integration points $(x_{i\pm\frac{1}{2}}, y_{j+\alpha}, z_{k+\beta})$, i.e., the points at faces $x_{i\pm\frac{1}{2}}$. In an analog way we can reconstruct the point values of the function $u(x, y, z)$ at points $(x_{i+\alpha}, y_{j\pm\frac{1}{2}}, z_{k+\beta})$, and $(x_{i+\alpha}, y_{j+\beta}, z_{i\pm\frac{1}{2}})$, corresponding to the faces $y_{j\pm\frac{1}{2}}$ and $z_{k\pm\frac{1}{2}}$. The algorithm consists of three sweeps in the 3D case and two sweeps in the 2D case. Let us start defining the stencils, and adopting the notation given in Titarev & Toro (2004). In order to reconstruct $u_{i\pm\frac{1}{2},j+\alpha,k+\beta}$ with a WENO scheme of $(2N+1)$th order (where the polynomials used in every stencil are of degree N), we require the stencil to be formed by the cells $\Omega_{i_x i_y i_z}$, with i_x, i_y, and i_z satisfying

$$i - N \leq i_x \leq i + N, \quad j - N \leq i_y \leq j + N, \quad k - N \leq i_z \leq k + N. \tag{2.27}$$

As an example, the stencils for the WENO5 reconstruction procedure are depicted in the figure 2.5 for the two- and three-dimensional cases. Once the stencils are defined, we

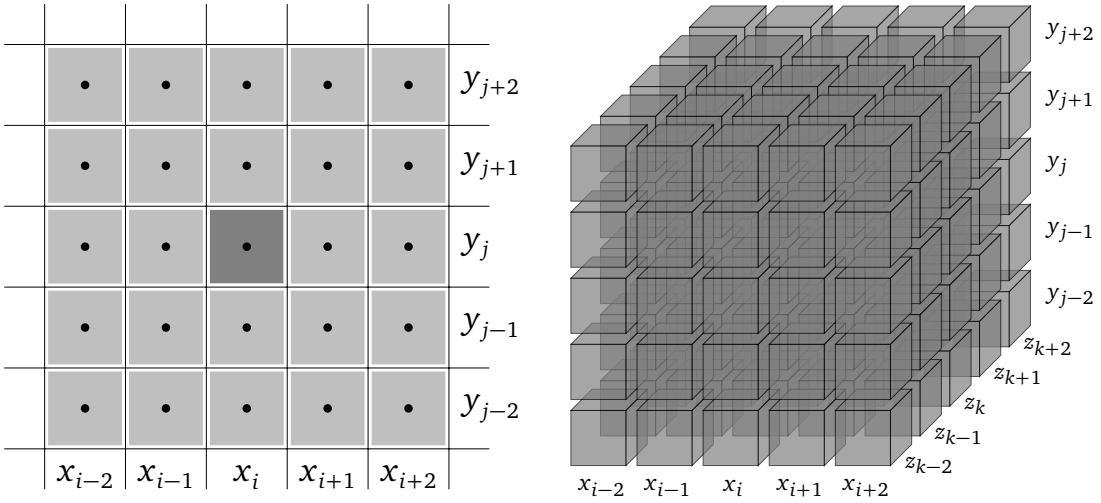

Figure 2.5: Stencil for the high-order WENO5 reconstruction for finite volume methods. The state is reconstructed in the Gaussian integration points depicted in the figure 2.4. For the cell Ω_{ij} in 2D (left). For the cell Ω_{ijk} in 3D (right).

proceed with the description of the sweeps:

- **First Sweep**: From the cell averages u_{ijk}, a one-dimensional reconstruction in the x-direction is carried out for all values of the indexes i_y, i_z from the stencil. Two-dimensional averages at faces $x_{i\pm\frac{1}{2}}$ are obtained from this procedure

$$\bar{\bar{u}}_{i_y i_z}\Big|_{x_{i\pm\frac{1}{2}}} = \frac{1}{\Delta y}\frac{1}{\Delta z}\int_{y_{i_y-\frac{1}{2}}}^{y_{i_y+\frac{1}{2}}}\int_{z_{i_z-\frac{1}{2}}}^{z_{i_z+\frac{1}{2}}} u(x_{i\pm\frac{1}{2}}, y, z)\,\mathrm{d}z\,\mathrm{d}y.$$

- **Second Sweep**: From the obtained two-dimensional averages $\bar{\bar{u}}_{i_y i_z}$, a one-dimensional reconstruction in the y-direction is carried out for all values of the index i_z from the stencil. One-dimensional averages at lines $y_{j\pm\frac{1}{2\sqrt{3}}}$ on the faces $x_{i\pm\frac{1}{2}}$ are obtained from this procedure

$$\bar{u}_{i_z}\Big|_{\substack{x_{i\pm\frac{1}{2}} \\ y_{j\pm\frac{1}{2\sqrt{3}}}}} = \frac{1}{\Delta z}\int_{z_{i_z-\frac{1}{2}}}^{z_{i_z+\frac{1}{2}}} u(x_{i\pm\frac{1}{2}}, y_{j\pm\frac{1}{2\sqrt{3}}}, z)\,\mathrm{d}z.$$

- **Third Sweep**: In the last sweep, a one-dimensional reconstruction in the z-direction is carried out from all line averages $\bar{u}$ of every line $(x = x_{i\pm\frac{1}{2}}, y = y_{j\pm\frac{1}{2\sqrt{3}}})$. In this step are reconstructed all point-wise values $u(x_{i\pm\frac{1}{2}}, y_{j\pm\frac{1}{2\sqrt{3}}}, z_{k\pm\frac{1}{2\sqrt{3}}})$.

The dimension-by-dimension WENO reconstruction can be summarized as follows (for the two-dimensional case, see Figure 2.6)

$$\begin{aligned}
&\text{2D:} \quad \{u_{ij}\} \longrightarrow \left\{\bar{u}_{i\pm\frac{1}{2},i_y}\right\} \longrightarrow \left\{u_{i\pm\frac{1}{2},j\pm\frac{1}{2\sqrt{3}}}\right\}, \\
&\text{3D:} \quad \{u_{ijk}\} \longrightarrow \left\{\bar{\bar{u}}_{i\pm\frac{1}{2},i_y i_z}\right\} \longrightarrow \left\{\bar{u}_{i\pm\frac{1}{2},j\pm\frac{1}{2\sqrt{3}},i_z}\right\} \longrightarrow \left\{u_{i\pm\frac{1}{2},j\pm\frac{1}{2\sqrt{3}},k\pm\frac{1}{2\sqrt{3}}}\right\}.
\end{aligned} \tag{2.28}$$

A flow diagram for the finite volume method is depicted in the figure 2.7.

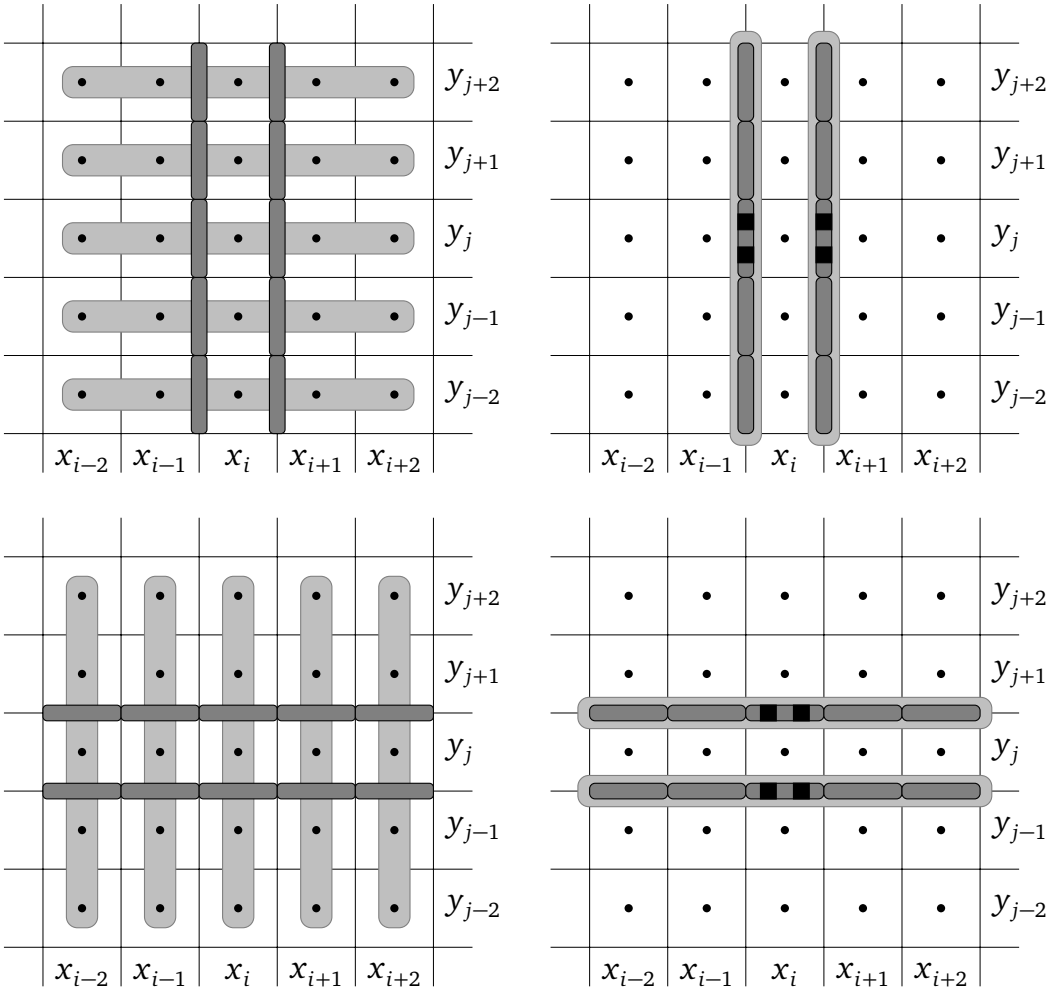

Figure 2.6: Stencils for the two-dimensional WENO5 reconstruction procedure.

2.3. Finite Difference Methods

In this section we are going to consider conservative finite difference methods for solving hyperbolic conservation laws. These schemes were first devised in Shu & Osher (1988) and Shu & Osher (1989). Unlike finite volume methods, where cell averages of the solution are evolved in time, in the conservative finite difference schemes only the point values of the solution are considered. This difference offers a high efficiency of finite difference over finite volume methods in two and three dimensional high-order calculations. Although both methods can use the same high-order reconstruction, the finite volume schemes perform more operations in order to reconstruct the function point values at the Gaussian interpolation points, even in the dimension-by-dimension way. The reason is that in the finite volume framework, we have to reconstruct from cell averages the edge averages, and from these we can interpolate at Gaussian integration points, where the fluxes are calculated with the help of Riemann solvers (Shi et al. 2002). A disadvantage of the high-order conservative finite difference methods is that they can only

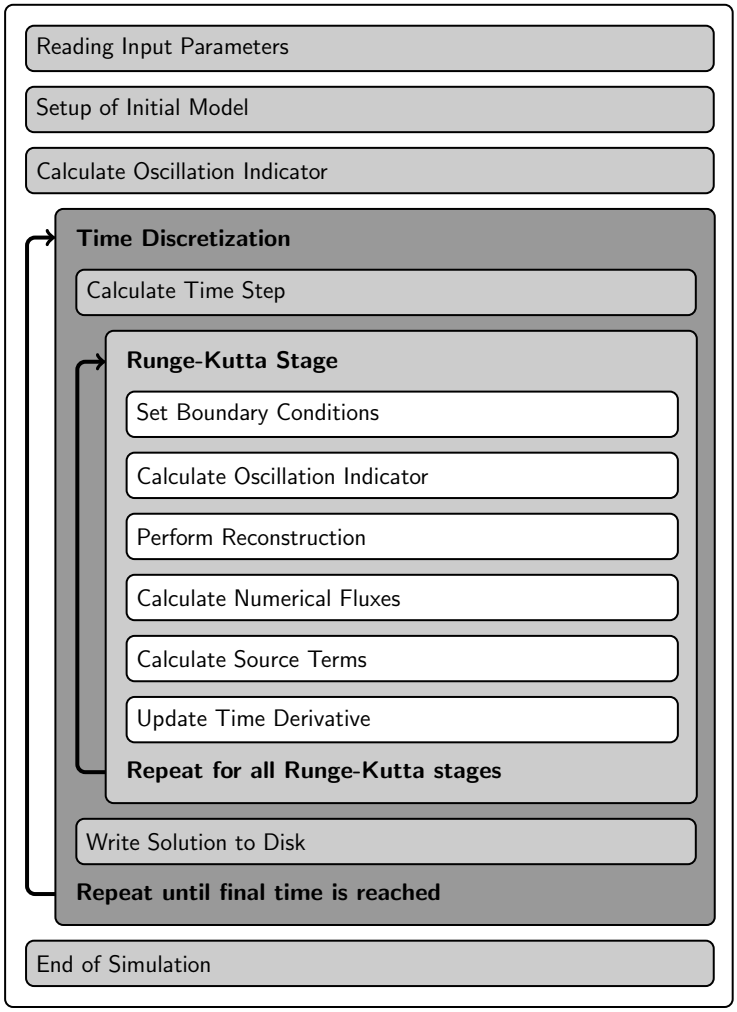

Figure 2.7: Flow diagram for the finite volume method.

be applied in uniform structured grids. A detailed explanation of this fact can be found in the work of Merriman (2003). If complex geometries are considered, a way to circumvent this issue is, for example, by using block-structured conservative finite differences WENO schemes (Sebastian & Shu 2003; Shen et al. 2011).

2.3.1. Formulation

Let us consider the following hyperbolic system of conservation laws

$$\frac{\partial \boldsymbol{u}}{\partial t} + \frac{\partial \boldsymbol{f}(\boldsymbol{u})}{\partial x} + \frac{\partial \boldsymbol{g}(\boldsymbol{u})}{\partial y} + \frac{\partial \boldsymbol{h}(\boldsymbol{u})}{\partial z} = \boldsymbol{0}. \tag{2.29}$$

In order to solve equation (2.29) with a conservative finite difference scheme, we have to discretize the physical domain employing an *uniform* Cartesian mesh, where every cell has size $\Delta x \Delta y \Delta z$. As in standard finite difference methods, the solution $\boldsymbol{u}_{ijk}$ is calculated in the center $(x_i, y_j, z_k) = (i\Delta x, j\Delta y, k\Delta z)$ of the cell. Because of the Lax-Wendroff

theorem (LeVeque 2002), it is required that the scheme is written in conservation form, otherwise the computed solution would not converge to the weak solution. As a consequence, the shock position will not be determined correctly. We start by writing the spatial derivatives in the equation (2.29) as

$$\frac{\mathrm{d}\boldsymbol{u}_{ijk}}{\mathrm{d}t} = \frac{\hat{\boldsymbol{f}}_{i-\frac{1}{2},jk} - \hat{\boldsymbol{f}}_{i+\frac{1}{2},jk}}{\Delta x} + \frac{\hat{\boldsymbol{g}}_{i,j-\frac{1}{2},k} - \hat{\boldsymbol{g}}_{i,j+\frac{1}{2},k}}{\Delta y} + \frac{\hat{\boldsymbol{h}}_{ij,k-\frac{1}{2}} - \hat{\boldsymbol{h}}_{ij,k+\frac{1}{2}}}{\Delta z}. \tag{2.30}$$

Note that the conservation law still is written in differential form and the right hand side should be interpreted as a continuous function of time (Rezzolla & Zanotti 2013). The numerical fluxes

$$\begin{aligned}
\hat{\boldsymbol{f}}_{i+\frac{1}{2},jk} &= \hat{\boldsymbol{f}}(\boldsymbol{u}_{i-p,jk}, \ldots, \boldsymbol{u}_{i+q,jk}), \\
\hat{\boldsymbol{g}}_{i,j+\frac{1}{2},k} &= \hat{\boldsymbol{g}}(\boldsymbol{u}_{i,j-p,k}, \ldots, \boldsymbol{u}_{i,j+q,k}), \\
\hat{\boldsymbol{h}}_{ij,k+\frac{1}{2}} &= \hat{\boldsymbol{h}}(\boldsymbol{u}_{ij,k-p}, \ldots, \boldsymbol{u}_{ij,k+q}),
\end{aligned} \tag{2.31}$$

are consistent with the physical fluxes in the sense that $\hat{\boldsymbol{f}}(\boldsymbol{u}, \ldots, \boldsymbol{u}) = \boldsymbol{f}(\boldsymbol{u})$, $\hat{\boldsymbol{g}}(\boldsymbol{u}, \ldots, \boldsymbol{u}) = \boldsymbol{g}(\boldsymbol{u})$, and $\hat{\boldsymbol{h}}(\boldsymbol{u}, \ldots, \boldsymbol{u}) = \boldsymbol{h}(\boldsymbol{u})$. The scheme is rth order accurate if the solution $\boldsymbol{u}$ is smooth and the following conditions are satisfied

$$\begin{aligned}
\frac{1}{\Delta x}\left(\hat{\boldsymbol{f}}_{i+\frac{1}{2},jk} - \hat{\boldsymbol{f}}_{i-\frac{1}{2},jk}\right) &= \left.\frac{\partial \boldsymbol{f}(\boldsymbol{u})}{\partial x}\right|_{x=x_i} + \mathcal{O}(\Delta x^r), \\
\frac{1}{\Delta y}\left(\hat{\boldsymbol{g}}_{i,j+\frac{1}{2},k} - \hat{\boldsymbol{g}}_{i,j-\frac{1}{2},k}\right) &= \left.\frac{\partial \boldsymbol{g}(\boldsymbol{u})}{\partial y}\right|_{y=y_j} + \mathcal{O}(\Delta y^r), \\
\frac{1}{\Delta z}\left(\hat{\boldsymbol{h}}_{ij,k+\frac{1}{2}} - \hat{\boldsymbol{h}}_{ij,k-\frac{1}{2}}\right) &= \left.\frac{\partial \boldsymbol{h}(\boldsymbol{u})}{\partial z}\right|_{z=z_k} + \mathcal{O}(\Delta z^r).
\end{aligned} \tag{2.32}$$

These equations represent an appropriate high-order approximation of the partial derivatives of the fluxes at the points x_i, y_j, and z_k. Next, we present the way of approximating these derivatives with a higher order of accuracy as it was devised by Shu & Osher (1988). Let us define $\boldsymbol{F}(x)$, $\boldsymbol{G}(y)$, and $\boldsymbol{H}(z)$ implicitly as

$$\begin{aligned}
\boldsymbol{f}\big(\boldsymbol{u}(x)\big) &= \frac{1}{\Delta x}\int_{x-\frac{\Delta x}{2}}^{x+\frac{\Delta x}{2}} \boldsymbol{F}(\zeta)\,\mathrm{d}\zeta, \\
\boldsymbol{g}\big(\boldsymbol{u}(y)\big) &= \frac{1}{\Delta y}\int_{y-\frac{\Delta y}{2}}^{y+\frac{\Delta y}{2}} \boldsymbol{G}(\zeta)\,\mathrm{d}\zeta, \\
\boldsymbol{h}\big(\boldsymbol{u}(z)\big) &= \frac{1}{\Delta z}\int_{z-\frac{\Delta z}{2}}^{z+\frac{\Delta z}{2}} \boldsymbol{H}(\zeta)\,\mathrm{d}\zeta,
\end{aligned} \tag{2.33}$$

then we have

$$\begin{aligned}
\left.\frac{\partial \boldsymbol{f}(\boldsymbol{u})}{\partial x}\right|_{x=x_i} &= \frac{1}{\Delta x}\left(\boldsymbol{F}\left(x_{i+\frac{1}{2}}\right)-\boldsymbol{F}\left(x_{i-\frac{1}{2}}\right)\right),\\
\left.\frac{\partial \boldsymbol{g}(\boldsymbol{u})}{\partial y}\right|_{y=y_j} &= \frac{1}{\Delta y}\left(\boldsymbol{G}\left(y_{j+\frac{1}{2}}\right)-\boldsymbol{G}\left(y_{j-\frac{1}{2}}\right)\right),\\
\left.\frac{\partial \boldsymbol{h}(\boldsymbol{u})}{\partial z}\right|_{z=z_k} &= \frac{1}{\Delta z}\left(\boldsymbol{H}\left(z_{k+\frac{1}{2}}\right)-\boldsymbol{H}\left(z_{k-\frac{1}{2}}\right)\right).
\end{aligned} \tag{2.34}$$

This means that we can identify the numerical fluxes in the equation (2.30) as

$$\begin{aligned}
\hat{\boldsymbol{f}}_{i\pm\frac{1}{2}} &= \boldsymbol{F}\left(x_{i\pm\frac{1}{2}}\right)+\mathcal{O}(\Delta x^r),\\
\hat{\boldsymbol{g}}_{j\pm\frac{1}{2}} &= \boldsymbol{G}\left(y_{j\pm\frac{1}{2}}\right)+\mathcal{O}(\Delta y^r),\\
\hat{\boldsymbol{h}}_{k\pm\frac{1}{2}} &= \boldsymbol{H}\left(z_{k\pm\frac{1}{2}}\right)+\mathcal{O}(\Delta z^r),
\end{aligned} \tag{2.35}$$

to ensure rth order of accuracy, if the functions $\boldsymbol{F}(x)$, $\boldsymbol{G}(y)$, and $\boldsymbol{H}(z)$ are computed with rth order of accuracy. Taking a closer look to the definitions given in (2.33), we can see that

$$\begin{aligned}
\boldsymbol{f}\left(\boldsymbol{u}(x_i)\right) &= \frac{1}{\Delta x}\int_{x_{i-\frac{1}{2}}}^{x_{i+\frac{1}{2}}} \boldsymbol{F}(\zeta)\,\mathrm{d}\zeta \equiv \bar{\boldsymbol{F}}_i,\\
\boldsymbol{g}\left(\boldsymbol{u}(y_j)\right) &= \frac{1}{\Delta y}\int_{y_{j-\frac{1}{2}}}^{y_{j+\frac{1}{2}}} \boldsymbol{G}(\zeta)\,\mathrm{d}\zeta \equiv \bar{\boldsymbol{G}}_j,\\
\boldsymbol{h}\left(\boldsymbol{u}(z_k)\right) &= \frac{1}{\Delta z}\int_{z_{k-\frac{1}{2}}}^{z_{k+\frac{1}{2}}} \boldsymbol{H}(\zeta)\,\mathrm{d}\zeta \equiv \bar{\boldsymbol{H}}_k.
\end{aligned} \tag{2.36}$$

That is, knowing the averages $\bar{\boldsymbol{F}}_i = \boldsymbol{f}\left(\boldsymbol{u}(x_i)\right)$, $\bar{\boldsymbol{G}}_i = \boldsymbol{g}\left(\boldsymbol{u}(y_j)\right)$, and $\bar{\boldsymbol{H}}_i = \boldsymbol{h}\left(\boldsymbol{u}(z_k)\right)$, we can reconstruct the values $\boldsymbol{F}_{i\pm\frac{1}{2}} = \hat{\boldsymbol{f}}_{i\pm\frac{1}{2}}$, $\boldsymbol{G}_{j\pm\frac{1}{2}} = \hat{\boldsymbol{g}}_{j\pm\frac{1}{2}}$, and $\boldsymbol{H}_{k\pm\frac{1}{2}} = \hat{\boldsymbol{h}}_{k\pm\frac{1}{2}}$ with the help of a high-order reconstruction procedure, like WENO (Liu et al. 1994; Jiang & Shu 1996; Shi et al. 2002; Borges et al. 2008) or MP5 (Suresh & Huynh 1997).

2.3.2. Lax-Friedrichs Flux Splitting

In the introduced numerical framework it is important to guarantee upwinding in the flux reconstruction in order to stabilize the scheme. For hyperbolic partial differential equations, the stability of a numerical approximation is related to the propagation of information in the correct direction. This direction is found by performing an analysis of the characteristics of the system. Let us introduce a global flux splitting

$$\begin{aligned}
\boldsymbol{f}(\boldsymbol{u}) &= \boldsymbol{f}^+(\boldsymbol{u})+\boldsymbol{f}^-(\boldsymbol{u}),\\
\boldsymbol{g}(\boldsymbol{u}) &= \boldsymbol{g}^+(\boldsymbol{u})+\boldsymbol{g}^-(\boldsymbol{u}),\\
\boldsymbol{h}(\boldsymbol{u}) &= \boldsymbol{h}^+(\boldsymbol{u})+\boldsymbol{h}^-(\boldsymbol{u}),
\end{aligned} \tag{2.37}$$

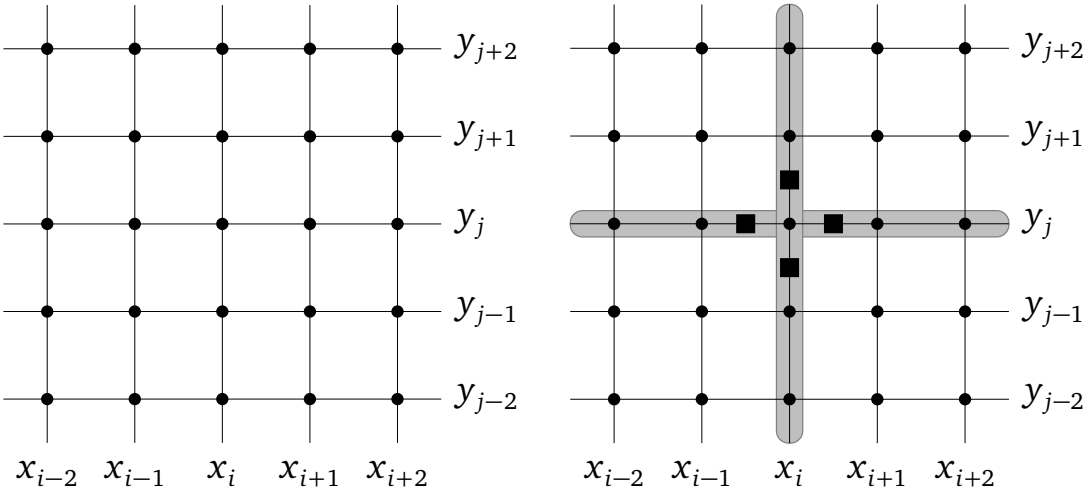

Figure 2.8: WENO reconstruction. Gaussian integration points for the cell I_{ij} (left). Stencils for the two-dimensional WENO5 reconstruction (right).

with

$$\begin{aligned}
&\frac{\mathrm{d}\boldsymbol{f}^{+}(\boldsymbol{u})}{\mathrm{d}\boldsymbol{u}} \geq \mathbf{0}, \quad \frac{\mathrm{d}\boldsymbol{f}^{-}(\boldsymbol{u})}{\mathrm{d}\boldsymbol{u}} \leq \mathbf{0}, \\
&\frac{\mathrm{d}\boldsymbol{g}^{+}(\boldsymbol{u})}{\mathrm{d}\boldsymbol{u}} \geq \mathbf{0}, \quad \frac{\mathrm{d}\boldsymbol{g}^{-}(\boldsymbol{u})}{\mathrm{d}\boldsymbol{u}} \leq \mathbf{0}, \\
&\frac{\mathrm{d}\boldsymbol{h}^{+}(\boldsymbol{u})}{\mathrm{d}\boldsymbol{u}} \geq \mathbf{0}, \quad \frac{\mathrm{d}\boldsymbol{h}^{-}(\boldsymbol{u})}{\mathrm{d}\boldsymbol{u}} \leq \mathbf{0}.
\end{aligned} \tag{2.38}$$

Among the numerical schemes that maintain stability, we use the local Lax-Friedrichs splitting approach. This scheme is based on splitting the flux into two different terms: each term propagates information in the opposite direction from the other.

Here we derive the local Lax-Friedrichs splitting. Let us start by considering the following one-dimensional hyperbolic system

$$\frac{\partial \boldsymbol{u}}{\partial t} + \frac{\partial \boldsymbol{f}(\boldsymbol{u})}{\partial x} = \mathbf{0}. \tag{2.39}$$

Applying the chain rule, we get

$$\frac{\partial \boldsymbol{u}}{\partial t} + \mathbf{A}_x \frac{\partial \boldsymbol{u}}{\partial x} = \mathbf{0}, \quad \text{with } \mathbf{A}_x \equiv \frac{\partial \boldsymbol{f}}{\partial \boldsymbol{u}}. \tag{2.40}$$

The eigenvalues of the Jacobian matrix $\mathbf{A}_x$ represent the wave speeds. Because the system is hyperbolic, the diagonalization of the matrix $\mathbf{A}_x$ yields $\boldsymbol{\Lambda}$. The matrix $\boldsymbol{\Lambda}$ is a diagonal matrix containing the eigenvalues of the system. The sign of each eigenvalues determines whether the corresponding characteristic information propagates in the $\pm x$ direction.

Let $\alpha = \max|\mathbf{A}_x|$ be the fastest wave speed of the system. Rewriting the flux as

$$\frac{\partial \boldsymbol{u}}{\partial t} + \frac{\partial}{\partial x}\left[\frac{1}{2}(\boldsymbol{f} + \alpha \boldsymbol{u} + \boldsymbol{f} - \alpha \boldsymbol{u})\right] = \mathbf{0}, \tag{2.41}$$

allows us to split the flux in the following manner

$$\frac{\partial \boldsymbol{u}}{\partial t} + \frac{1}{2}\left(\frac{\partial \boldsymbol{f}^{+}}{\partial x} + \frac{\partial \boldsymbol{f}^{-}}{\partial x}\right) = \boldsymbol{0}, \quad \text{where } \boldsymbol{f}^{\pm} = \boldsymbol{f} \pm \alpha \boldsymbol{u}. \tag{2.42}$$

The Jacobians of the split flux matrices are then given by

$$\frac{\partial \boldsymbol{f}^{\pm}}{\partial \boldsymbol{u}} = \frac{\partial \boldsymbol{f}}{\partial \boldsymbol{u}} \pm \mathbf{I}\alpha, \tag{2.43}$$

where $\mathbf{I}$ is the identity matrix. The diagonalization of these Jacobian matrices gives

$$\boldsymbol{\Lambda}^{+} = \boldsymbol{\Lambda} + \mathbf{I}\alpha \geq 0, \quad \boldsymbol{\Lambda}^{-} = \boldsymbol{\Lambda} - \mathbf{I}\alpha \leq 0, \tag{2.44}$$

which means that the $\boldsymbol{f}^{\pm}$ fluxes correspond to waves traveling in the $\pm x$ directions.

The conservative numerical implementation of this flux splitting technique is known as the local Lax-Friedrichs flux splitting. The spatial derivative of the flux is discretized as

$$\begin{aligned}
\left.\frac{\partial \boldsymbol{f}}{\partial x}\right|_{x=x_i} &\approx \frac{1}{2}\left(\frac{\hat{\boldsymbol{f}}^{+}_{i+\frac{1}{2}} - \hat{\boldsymbol{f}}^{+}_{i-\frac{1}{2}}}{\Delta x} + \frac{\hat{\boldsymbol{f}}^{-}_{i+\frac{1}{2}} - \hat{\boldsymbol{f}}^{-}_{i-\frac{1}{2}}}{\Delta x}\right) \\
&\approx \frac{1}{\Delta x}\left(\frac{\hat{\boldsymbol{f}}^{+}_{i+\frac{1}{2}} + \hat{\boldsymbol{f}}^{-}_{i+\frac{1}{2}}}{2} - \frac{\hat{\boldsymbol{f}}^{+}_{i-\frac{1}{2}} + \hat{\boldsymbol{f}}^{-}_{i-\frac{1}{2}}}{2}\right) \\
&\approx \frac{\hat{\boldsymbol{f}}_{i+\frac{1}{2}} - \hat{\boldsymbol{f}}_{i-\frac{1}{2}}}{\Delta x},
\end{aligned} \tag{2.45}$$

where

$$\hat{\boldsymbol{f}}_{i+\frac{1}{2}} = \frac{1}{2}\left(\hat{\boldsymbol{f}}^{+}_{i+\frac{1}{2}} + \hat{\boldsymbol{f}}^{-}_{i+\frac{1}{2}}\right) \tag{2.46}$$

is the total flux at each $x_{i+\frac{1}{2}}$ cell boundary. The Lax-Friedrichs fluxes around the $x_{i+\frac{1}{2}}$ interface are

$$\boldsymbol{f}^{\pm} = \boldsymbol{f} \pm \alpha_{i+\frac{1}{2}} \boldsymbol{u}, \tag{2.47}$$

where the local maximum wave speed is approximated by

$$\alpha_{i+\frac{1}{2}} = \max\left(\left|\frac{\partial \boldsymbol{f}}{\partial \boldsymbol{u}}\right|_{i}, \left|\frac{\partial \boldsymbol{f}}{\partial \boldsymbol{u}}\right|_{i+1}\right). \tag{2.48}$$

Summarizing, the Lax-Friedrichs splitting for the (2.29) is

$$\begin{aligned}
\boldsymbol{f}^{\pm}(\boldsymbol{u}) &= \frac{1}{2}\left(\boldsymbol{f}(\boldsymbol{u}) \pm \alpha_x \boldsymbol{u}\right), \\
\boldsymbol{g}^{\pm}(\boldsymbol{u}) &= \frac{1}{2}\left(\boldsymbol{g}(\boldsymbol{u}) \pm \alpha_y \boldsymbol{u}\right), \\
\boldsymbol{h}^{\pm}(\boldsymbol{u}) &= \frac{1}{2}\left(\boldsymbol{h}(\boldsymbol{u}) \pm \alpha_z \boldsymbol{u}\right),
\end{aligned} \tag{2.49}$$

where

$$\begin{aligned}\alpha_x &= \max_{\boldsymbol{u}} \left|\boldsymbol{f}'(\boldsymbol{u})\right|,\\ \alpha_y &= \max_{\boldsymbol{u}} \left|\boldsymbol{g}'(\boldsymbol{u})\right|,\\ \alpha_z &= \max_{\boldsymbol{u}} \left|\boldsymbol{h}'(\boldsymbol{u})\right|,\end{aligned} \tag{2.50}$$

are fastest characteristic speeds associated to the physical fluxes in every coordinate direction. Other flux splitting approaches can be employed, for instance, the Roe flux-splitting. This is less dissipative than the Lax-Friedrichs and it is less expensive. The Roe flux-splitting has the inconvenient that it can create entropy-violating shocks and also it can suffer the carbuncle phenomenon (Quirk 1994).

2.3.3. Reconstruction for Systems of Conservation Laws

Until now we have shown the complete formulation of high-order conservative finite difference methods in 3D for systems of conservation laws. In order to avoid spurious oscillations, the reconstruction procedure should be performed in local characteristic variables instead of the primitive or conservative ones (Harten et al. 1987; Shu & Osher 1988), although for the scalar case this is not necessary. In the characteristic reconstruction one first has to transform to the local characteristic variables and then applies the reconstruction operator to each component of these variables. The final reconstructed flux is obtained by transforming back to conservative variables. That is, given the matrices of left $\mathbf{L}_\alpha$ and right $\mathbf{R}_\alpha$ eigenvectors of the Jacobian matrices $\mathbf{A}_\alpha$ (with $\alpha = x, y, z$)

$$\begin{aligned}\mathbf{A}_x &= \boldsymbol{f}'(\boldsymbol{u}),\\ \mathbf{A}_y &= \boldsymbol{g}'(\boldsymbol{u}),\\ \mathbf{A}_z &= \boldsymbol{h}'(\boldsymbol{u}),\end{aligned} \tag{2.51}$$

we perform the reconstruction on the characteristic variables

$$\begin{aligned}\tilde{\boldsymbol{u}}_x &= \mathbf{L}_x \boldsymbol{u}, \quad \tilde{\boldsymbol{f}} = \mathbf{L}_x \boldsymbol{f},\\ \tilde{\boldsymbol{u}}_y &= \mathbf{L}_y \boldsymbol{u}, \quad \tilde{\boldsymbol{g}} = \mathbf{L}_y \boldsymbol{g},\\ \tilde{\boldsymbol{u}}_z &= \mathbf{L}_z \boldsymbol{u}, \quad \tilde{\boldsymbol{h}} = \mathbf{L}_z \boldsymbol{h},\end{aligned} \tag{2.52}$$

and after that we switch back to the conservative variables

$$\begin{aligned}\hat{\boldsymbol{f}}_{1\pm1/2} &= \mathbf{R}_x \tilde{\boldsymbol{f}}_{1\pm1/2},\\ \hat{\boldsymbol{g}}_{1\pm1/2} &= \mathbf{R}_y \tilde{\boldsymbol{g}}_{1\pm1/2},\\ \hat{\boldsymbol{h}}_{1\pm1/2} &= \mathbf{R}_z \tilde{\boldsymbol{h}}_{1\pm1/2}.\end{aligned} \tag{2.53}$$

A flow diagram for the finite difference method is depicted in the figure 2.9.

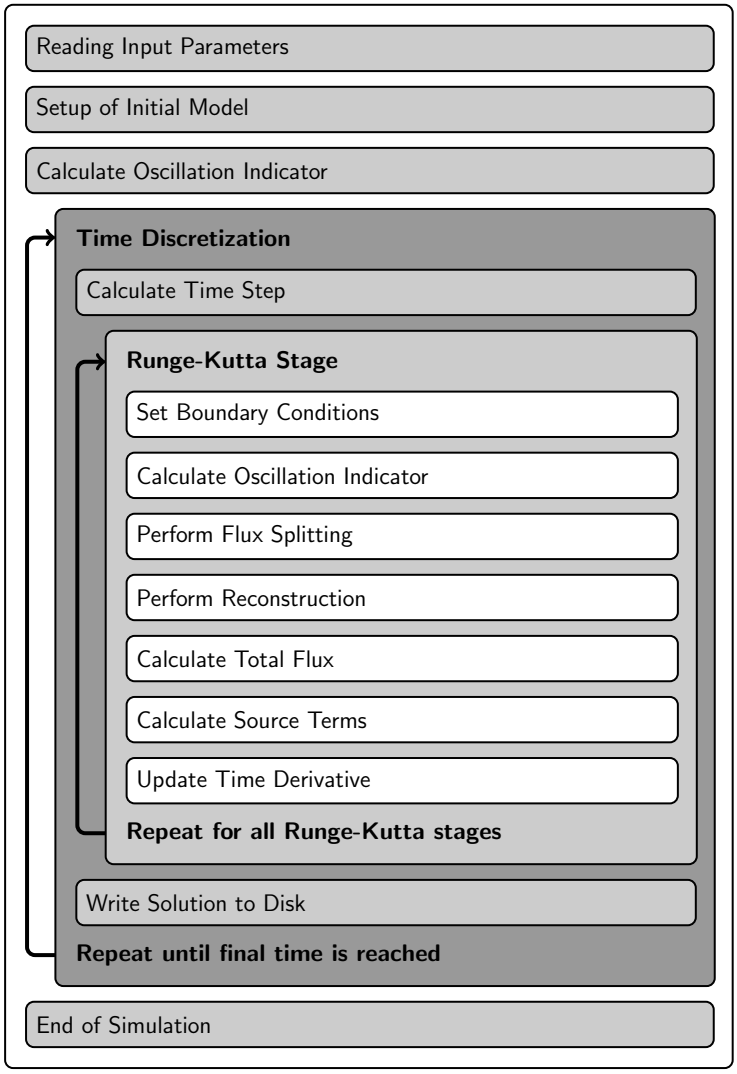

Figure 2.9: Flow diagram for the finite difference method.

2.4. Discontinuous Galerkin Methods

Using high-order numerical methods is becoming the new standard in computational science and engineering because of the advantages provided by this family of numerical schemes. Among the high-order methods, the discontinuous Galerkin schemes are the most renowned candidates and are playing a central role because of all the attractive properties they possess, making of them the most suitable for solving the equations of fluid dynamics on complex geometries, and in general, nonlinear hyperbolic systems of conservation laws.

In the discontinuous Galerkin method high-order accuracy is obtained through the approximation of the solution with a higher degree polynomial. The method has the capacity to handle complicated geometries, and due to its locality, the it is highly parallelizable.

The discontinuous Galerkin method was originally proposed by Reed & Hill (1973) in 1973 for the numerical solution of the steady-state neutron transport equation

$$\sigma u + \nabla \cdot (au) = f, \tag{2.54}$$

where σ is a real constant, a is piecewise constant, and u is the unknown. We stress that a two years before the work of Reed & Hill, Nitsche (1971) introduced in 1971 the discontinuous Galerkin method for the approximation of elliptic equations. The method was recovered by Cockburn & Shu (1989) to solve time dependent non-linear conservation laws. In the subsequent years, in a series of papers, the general framework of the discontinuous Galerkin for nonlinear systems of conservation laws, even in multiple space dimensions was established (Cockburn et al. 1989; Cockburn et al. 1990; Cockburn & Shu 1998).

2.4.1. Discontinuous Galerkin Formulation

Let us consider the following system of conservation laws

$$\frac{\partial \boldsymbol{u}}{\partial t} + \frac{\partial \boldsymbol{f}(\boldsymbol{u})}{\partial x} + \frac{\partial \boldsymbol{g}(\boldsymbol{u})}{\partial y} + \frac{\partial \boldsymbol{h}(\boldsymbol{u})}{\partial z} = \boldsymbol{0}, \tag{2.55}$$

also written as

$$\frac{\partial \boldsymbol{u}}{\partial t} + \nabla \cdot \mathbf{f}(\boldsymbol{u}) = \boldsymbol{0}, \tag{2.56}$$

where $\boldsymbol{u} \in \mathbb{R}^m$ is the vector of *conserved* quantities, and $\mathbf{f} = \left[\boldsymbol{f}, \boldsymbol{g}, \boldsymbol{h}\right]$ is the tensor of physical fluxes, with $\boldsymbol{f}, \boldsymbol{g}, \boldsymbol{h} \in \mathbb{R}^m$ being the *flux functions* in the directions x, y, and z, respectively. Next let us consider the test function $\phi = \phi(\boldsymbol{x}) = \phi(x, y, z)$, which is an arbitrary differentiable function defined in a subset $\Omega_k \subset \Omega \subset \mathbb{R}^3$. We assume that the subset Ω_k corresponds to a cell in the discontinuous Galerkin scheme. The variational formulation consists in projecting the residual of the partial differential equation (2.56) on the test function $\phi(\boldsymbol{x})$ and demand that this projection is zero, that is

$$\int_{\Omega_k} \left(\frac{\partial \boldsymbol{u}}{\partial t} + \nabla \cdot \mathbf{f}(\boldsymbol{u}) \right) \phi(\boldsymbol{x}) \, \mathrm{d}\boldsymbol{x} = \boldsymbol{0}. \tag{2.57}$$

The weak formulation of the equation (2.56) is obtained by integrating by parts the flux term in the equation (2.57)

$$\int_{\Omega_k} \frac{\partial \boldsymbol{u}}{\partial t} \phi(\boldsymbol{x}) \, \mathrm{d}\boldsymbol{x} + \oint_{\partial \Omega_k} \mathbf{f} \cdot \boldsymbol{n} \, \phi(\boldsymbol{x}) \, \mathrm{d}s - \int_{\Omega_k} \mathbf{f} \cdot \nabla \phi(\boldsymbol{x}) \, \mathrm{d}\boldsymbol{x} = \boldsymbol{0}. \tag{2.58}$$

So far, no approximation has been done on the vector $\boldsymbol{u}$ or the fluxes $\boldsymbol{f}$, $\boldsymbol{g}$, $\boldsymbol{h}$. Depending in the discretization ansatz on these functions, we have different *flavors* of the discontinuous Galerkin method. In this work we will focus on the very efficient discontinuous Galerkin spectral element method developed by Kopriva & Kolias (1996) and Kopriva (1996). For an outstanding description and derivation of the method and how it is implemented, we recommend the book by Kopriva (2009).

2.4.2. Discontinuous Galerkin Spectral Element Methods

We are interested in solving numerically the equation system (2.56) with appropriate initial and boundary conditions by using the discontinuous Galerkin spectral element method. In this framework, a mapping from the *physical* domain, where we want the solution, to the *reference* domain, where actually the *equation* is solved, is constructed. With the help of this transformation, we transform the equation to the reference domain and finally we solve the transformed equation in the reference domain. We stress that in the general formulation of the discontinuous Galerkin, it is usual to solve the original equation in the physical space, where the involved integrals are mapped to the reference element. What we here pretend is to map first the equation to the reference element and then solve it there. Therefore, we apply the discontinuous Galerkin formulation (2.58) not to the original equation (2.56), but onto the mapped equation.

Before we derive the discontinuous Galerkin formulation for the conservation law in the reference element, we have to know how are transformed the derivative operators under a mapping from the physical to the reference domain. In the following we will discuss such derivation.

Derivative Operators under Mappings

Let us start by considering the domain $\Omega \subset \mathbb{R}^3$ with boundary $\partial\Omega$. We decompose Ω in K non-overlapping hexahedral elements Ω_k, which are further mapped onto the reference element $[-1,1]^3$ (see figure 2.10 for an example where a cylinder has been decomposed in several hexahedral elements (top), and how one from these elements is mapped into the reference element (bottom)). A point in the physical space is described by $\boldsymbol{x} = (x,y,z) = (x_1,x_2,x_3)$, and a point in the reference element by $\boldsymbol{\xi} = (\xi,\eta,\zeta) = (\xi^1,\xi^2,\xi^3)$. The mapping between the physical and the reference element is defined as $\boldsymbol{x} = \boldsymbol{X}(\boldsymbol{\xi})$. Let us see the effect of a coordinate transformation on the derivative of a function $f(\boldsymbol{x}) = (x,y,z)$ on the reference space. Applying the chain rule we get

$$\begin{aligned}
\frac{\partial f}{\partial \xi} &= \frac{\partial f}{\partial x}\frac{\partial x}{\partial \xi} + \frac{\partial f}{\partial y}\frac{\partial y}{\partial \xi} + \frac{\partial f}{\partial z}\frac{\partial z}{\partial \xi},\\
\frac{\partial f}{\partial \eta} &= \frac{\partial f}{\partial x}\frac{\partial x}{\partial \eta} + \frac{\partial f}{\partial y}\frac{\partial y}{\partial \eta} + \frac{\partial f}{\partial z}\frac{\partial z}{\partial \eta},\\
\frac{\partial f}{\partial \zeta} &= \frac{\partial f}{\partial x}\frac{\partial x}{\partial \zeta} + \frac{\partial f}{\partial y}\frac{\partial y}{\partial \zeta} + \frac{\partial f}{\partial z}\frac{\partial z}{\partial \zeta},
\end{aligned} \tag{2.59}$$

which we can write in matrix form

$$\begin{pmatrix} \frac{\partial f}{\partial \xi} \\ \frac{\partial f}{\partial \eta} \\ \frac{\partial f}{\partial \zeta} \end{pmatrix} = \begin{pmatrix} \frac{\partial x}{\partial \xi} & \frac{\partial y}{\partial \xi} & \frac{\partial z}{\partial \xi} \\ \frac{\partial x}{\partial \eta} & \frac{\partial y}{\partial \eta} & \frac{\partial z}{\partial \eta} \\ \frac{\partial x}{\partial \zeta} & \frac{\partial y}{\partial \zeta} & \frac{\partial z}{\partial \zeta} \end{pmatrix} \begin{pmatrix} \frac{\partial f}{\partial x} \\ \frac{\partial f}{\partial y} \\ \frac{\partial f}{\partial z} \end{pmatrix}, \tag{2.60}$$

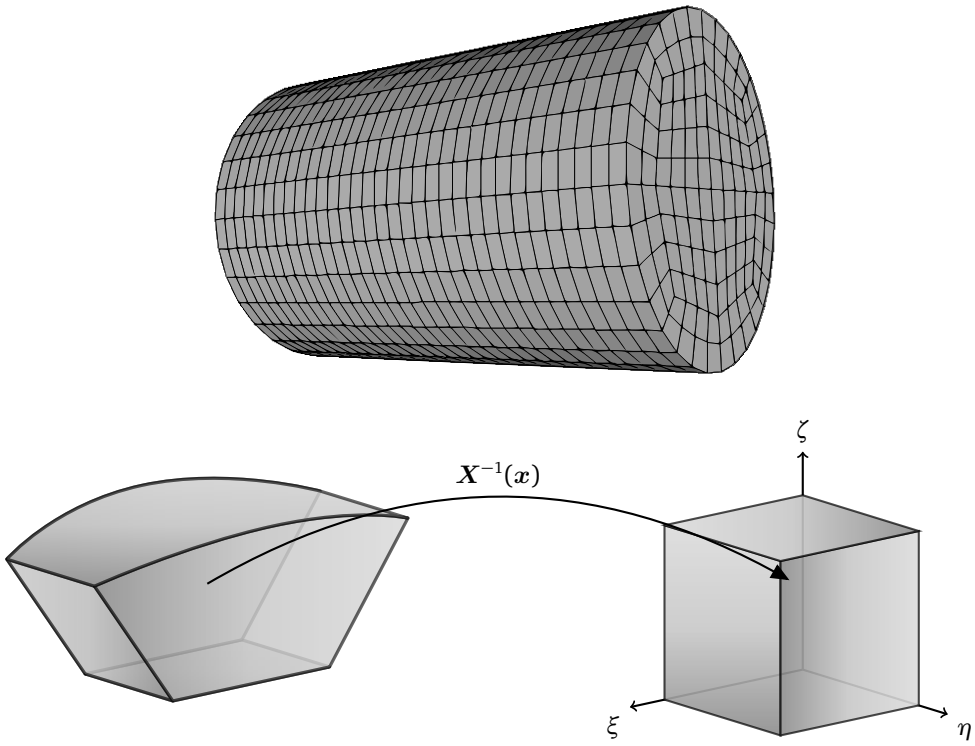

Figure 2.10: Triangulation of a cylinder using hexahedral elements (left). Mapping from the physical element Ω_i to the reference element $[-1,1]^3$ (right).

that is, $\nabla_\xi f = \mathbf{J}\nabla_{\boldsymbol{x}} f$, where $\mathbf{J}$ is the Jacobi matrix of the transformation $\boldsymbol{x} = \boldsymbol{X}(\boldsymbol{\xi})$. Because we want to map the equations from the physical space to the reference space, in practice, the coordinate transformation we need is the inverse, namely, $\boldsymbol{\xi} = \boldsymbol{X}^{-1}(\boldsymbol{x})$, which is represented in matrix form by $\mathbf{J}^{-1}$.

Before we write down the inverse of the Jacobi matrix, we will introduce some fundamental concepts taken from the differential geometry. Any point in the physical space can be represented by using two different basis vectors: The *covariant* basis vectors $\boldsymbol{e}_i$, for $i = 1,2,3$, and the *contravariant* basis vectors $\boldsymbol{e}^i$, for $i = 1,2,3$. By definition, the covariant vectors are tangent to the coordinate lines, while the contravariant are normal the coordinate lines. That is, they are defined by the following expressions

$$\boldsymbol{e}_i = \frac{\partial \boldsymbol{x}}{\partial \xi^i}, \quad i = 1,2,3, \quad \text{(Covariant vectors)}, \tag{2.61a}$$

$$\boldsymbol{e}^i = \nabla \xi^i, \quad i = 1,2,3, \quad \text{(Contravariant vectors)}. \tag{2.61b}$$

Vectors can be written either in covariant basis or in contravariant basis. That is possible because these bases form a base of the three-dimensional space. For example, given the vector $\boldsymbol{f}$, we know that it is not yet written in any basis. For that, we have to find its components in the given basis. We achieve that by projecting onto the basis vectors. Using the covariant basis vectors, we obtain the *covariant components* of the vector $\boldsymbol{f}$,

namely

$$f_i = \boldsymbol{e}_i \cdot \boldsymbol{f}, \tag{2.62}$$

and by projecting onto the contravariant basis vectors, we get the *contravariant components* of the vector $\boldsymbol{f}$,

$$f^i = \boldsymbol{e}^i \cdot \boldsymbol{f}, \tag{2.63}$$

and in this way, the vector $\boldsymbol{f}$ can be expressed in both basis

$$\boldsymbol{f} = \sum_{i=1}^{3} f_i \boldsymbol{e}_i = \sum_{i=1}^{3} f^i \boldsymbol{e}^i. \tag{2.64}$$

Now, coming back to the inverse of the Jacobi matrix, we use the definition of covariant basis vectors and we then introduce them in the expression for $\mathbf{J}$, yielding

$$\mathbf{J} = \begin{pmatrix} \dfrac{\partial x}{\partial \xi} & \dfrac{\partial y}{\partial \xi} & \dfrac{\partial z}{\partial \xi} \\ \dfrac{\partial x}{\partial \eta} & \dfrac{\partial y}{\partial \eta} & \dfrac{\partial z}{\partial \eta} \\ \dfrac{\partial x}{\partial \zeta} & \dfrac{\partial y}{\partial \zeta} & \dfrac{\partial z}{\partial \zeta} \end{pmatrix} = \left(\boldsymbol{e}_1, \boldsymbol{e}_2, \boldsymbol{e}_3\right)^{\intercal}. \tag{2.65}$$

Using the general formula for the inverse of a 3×3 matrix expressed in terms of the cross product and triple product, we get

$$\mathbf{J}^{-1} = \frac{1}{\det(\mathbf{J})} \begin{pmatrix} \left(\boldsymbol{e}_2 \times \boldsymbol{e}_3\right)^{\intercal} \\ \left(\boldsymbol{e}_3 \times \boldsymbol{e}_1\right)^{\intercal} \\ \left(\boldsymbol{e}_1 \times \boldsymbol{e}_2\right)^{\intercal} \end{pmatrix}, \tag{2.66}$$

where the Jacobian $\mathcal{J} = \det(\mathbf{J})$ is given by

$$\mathcal{J} = \det(\mathbf{J}) = \boldsymbol{e}_i \cdot \left(\boldsymbol{e}_j \times \boldsymbol{e}_k\right). \tag{2.67}$$

In any basic text on classical differential geometry and tensor analysis, we can find the following definitions for the differential element, the surface element and the volume element (Reddy & Rasmussen 1982; Apostol 1969b). The differential element written in terms of the covariant basis vectors is defined by

$$\mathrm{d}\boldsymbol{x} = \sum_{i=1}^{3} \frac{\partial \boldsymbol{x}}{\partial \xi^i} \mathrm{d}\xi^i = \sum_{i=1}^{3} \boldsymbol{e}_i \, \mathrm{d}\xi^i, \tag{2.68}$$

The surface element is defined as follows

$$\mathrm{d}\boldsymbol{S}^i = \boldsymbol{e}_j \, \mathrm{d}\xi^j \times \boldsymbol{e}_k \, \mathrm{d}\xi^k = \left(\boldsymbol{e}_j \times \boldsymbol{e}_k\right) \mathrm{d}\xi^j \, \mathrm{d}\xi^k, \tag{2.69}$$

where the indices i, j, k are cyclic. The volume element is finally defined as

$$\mathrm{d}V = \boldsymbol{e}_i \cdot \big(\boldsymbol{e}_j \times \boldsymbol{e}_k\big)\,\mathrm{d}\xi^i\,\mathrm{d}\xi^j\,\mathrm{d}\xi^k = \mathcal{J}\,\mathrm{d}\xi^i\,\mathrm{d}\xi^j\,\mathrm{d}\xi^k, \quad i, j, k \text{ are cyclic.} \tag{2.70}$$

Once these quantities are defined, we proceed to write down different derivative operators under a coordinate transformation. We refer to the book by Kopriva (2009) for more details. The divergence of a vector field can be defined by (Apostol 1969a)

$$\nabla \cdot \boldsymbol{f} = \lim_{\Delta V \to 0} \frac{1}{\Delta V} \int_{\partial \Delta V} \boldsymbol{f} \cdot \mathrm{d}\boldsymbol{S}. \tag{2.71}$$

From this, we get the *conservative form* of the divergence operator

$$\nabla_{\boldsymbol{x}} \cdot \boldsymbol{f} = \frac{1}{\mathcal{J}} \sum_{i=1}^{3} \frac{\partial}{\partial \xi^i} \big(\boldsymbol{f} \cdot (\boldsymbol{e}_j \times \boldsymbol{e}_k)\big). \tag{2.72}$$

It is possible to write the divergence operator in a *nonconservative form* if the following conditions on the basis covariant vectors are satisfied

$$\sum_{i=1}^{3} \frac{\partial}{\partial \xi^i} (\boldsymbol{e}_j \times \boldsymbol{e}_k) = 0. \tag{2.73}$$

This conditions, called *metric identities*, are obtained from the invariance under transformation of the divergence of a vector field. The *nonconservative form* of the divergence operator is then (Kopriva 2009)

$$\nabla_{\boldsymbol{x}} \cdot \boldsymbol{f} = \frac{1}{\mathcal{J}} \sum_{i=1}^{3} (\boldsymbol{e}_j \times \boldsymbol{e}_k) \frac{\partial \boldsymbol{f}}{\partial \xi^i}. \tag{2.74}$$

The gradient operator, subject to a coordinate transformation, acting on a scalar field f, is given in conservative form as

$$\nabla_{\boldsymbol{x}} f = \frac{1}{\mathcal{J}} \sum_{i=1}^{3} \frac{\partial}{\partial \xi^i} \big((\boldsymbol{e}_j \times \boldsymbol{e}_k) f\big), \tag{2.75}$$

and in nonconservative form as

$$\nabla_{\boldsymbol{x}} f = \frac{1}{\mathcal{J}} \sum_{i=1}^{3} (\boldsymbol{e}_j \times \boldsymbol{e}_k) \frac{\partial f}{\partial \xi^i}. \tag{2.76}$$

From this last equation, we can easily see that the contravariant vectors $\boldsymbol{e}^i = \nabla \xi^i$ are related with the covariant vectors $\boldsymbol{e}_i = \dfrac{\partial \boldsymbol{x}}{\partial \xi^i}$ through

$$\nabla \xi^i = \boldsymbol{e}^i = \frac{1}{\mathcal{J}} (\boldsymbol{e}_j \times \boldsymbol{e}_k), \quad i, j, k \text{ are cyclic,} \tag{2.77}$$

also

$$\mathcal{J}\boldsymbol{e}^i = \boldsymbol{e}_j \times \boldsymbol{e}_k, \quad i,j,k \text{ are cyclic.} \tag{2.78}$$

These quantities are called the *metric terms*. We can simplify the derivative operators by using this metric identities. The divergence operator is then

$$\nabla_x \cdot \boldsymbol{f} = \frac{1}{\mathcal{J}} \sum_{i=1}^{3} \frac{\partial}{\partial \xi^i}\big(\mathcal{J}\boldsymbol{e}^i \cdot \boldsymbol{f}\big), \quad \text{(Conservative form)}. \tag{2.79}$$

The gradient operator takes the form

$$\nabla_x f = \frac{1}{\mathcal{J}} \sum_{i=1}^{3} \frac{\partial}{\partial \xi^i}\big(\mathcal{J}\boldsymbol{e}^i f\big), \quad \text{(Conservative form)}, \tag{2.80}$$

and the metric identities

$$\sum_{i=1}^{3} \frac{\partial\big(\mathcal{J}\boldsymbol{e}^i\big)}{\partial \xi^i} = 0. \tag{2.81}$$

Conservation Laws under Mappings

The divergence operator present in the conservation law (2.56) has been applied in the physical space, namely

$$\frac{\partial \boldsymbol{u}}{\partial t} + \nabla_x \cdot \mathbf{f}(\boldsymbol{u}) = \mathbf{0}, \tag{2.82}$$

where $\boldsymbol{u} = \boldsymbol{u}(\boldsymbol{x}, t)$ is the vector of conserved quantities, and $\mathbf{f} = \big[\boldsymbol{f}_1, \boldsymbol{f}_2, \boldsymbol{f}_3\big] = \big[\boldsymbol{f}, \boldsymbol{g}, \boldsymbol{h}\big]$ the tensor of fluxes. Previously, we derived the divergence operator under a coordinate transformation

$$\nabla_x \cdot \mathbf{f} = \frac{1}{\mathcal{J}} \sum_{i=1}^{3} \frac{\partial}{\partial \xi^i}\big(\mathcal{J}\boldsymbol{e}^i \cdot \mathbf{f}\big) := \frac{1}{\mathcal{J}} \nabla_\xi \cdot \tilde{\mathbf{f}}, \tag{2.83}$$

with $\tilde{\mathbf{f}} = \big[\boldsymbol{f}^1, \boldsymbol{f}^2, \boldsymbol{f}^3\big]$ the tensor of contravariant fluxes and it is defined through its components by $\boldsymbol{f}^i \equiv \big(\mathcal{J}\boldsymbol{e}^i \cdot \mathbf{f}\big)$. The conservation law in the reference element takes the form

$$\frac{\partial \boldsymbol{u}}{\partial t} + \frac{1}{\mathcal{J}} \nabla_\xi \cdot \tilde{\mathbf{f}} = \mathbf{0}. \tag{2.84}$$

Observe that $\boldsymbol{u} = \boldsymbol{u}(\xi, t)$, $\tilde{\mathbf{f}} = \tilde{\mathbf{f}}\big(\boldsymbol{u}(\xi, t)\big)$, and $\mathcal{J} = \mathcal{J}(\xi)$. The variational formulation of the transformed conservation law is, after multiplying with a test function $\phi = \phi(\xi)$,

$$\int_\Omega \left(\frac{\partial \boldsymbol{u}}{\partial t} + \frac{1}{\mathcal{J}} \nabla_\xi \cdot \tilde{\mathbf{f}} \right) \phi \, \mathrm{d}\boldsymbol{x} = \mathbf{0}. \tag{2.85}$$

Transforming the integral to the reference element $E = [-1,1]^3$, and reminding that $\mathrm{d}\boldsymbol{x} = \mathcal{J}(\xi)\,\mathrm{d}\xi$, we obtain the variational formulation of the transformed equation on the reference element

$$\int_E \left(\mathcal{J}(\xi)\frac{\partial \boldsymbol{u}}{\partial t} + \nabla_\xi \cdot \tilde{\mathbf{f}} \right) \phi(\xi)\,\mathrm{d}\xi = \mathbf{0}. \tag{2.86}$$

Finally, the weak formulation of the equation (2.84) is obtained by integrating by parts the flux term in the equation (2.86)

$$\int_E \mathcal{J}(\xi)\frac{\partial \boldsymbol{u}}{\partial t}\phi(\xi)\,\mathrm{d}\xi - \int_E \tilde{\mathbf{f}} \cdot \nabla_\xi \phi(\xi)\,\mathrm{d}\xi + \oint_{\partial E} \left[\tilde{\mathbf{f}} \cdot \tilde{\boldsymbol{n}}\right]^* \phi(\xi)\,\mathrm{d}\boldsymbol{\sigma} = \mathbf{0}, \tag{2.87}$$

where $\tilde{\boldsymbol{n}}$ is the unit normal vector to the surface at the faces of the reference element. Observe that for a given direction in the reference space (e.g. $\tilde{\boldsymbol{n}}$ can be the normal unit vector at the face of the reference element in the direction $+\xi^i$) we have that

$$\begin{aligned} \tilde{\mathbf{f}} \cdot \tilde{\boldsymbol{n}} &= \sum_{i=1}^{3} \boldsymbol{f}^i \tilde{n}^i = \sum_{i=1}^{3} \left(\mathcal{J}\boldsymbol{e}^i \cdot \mathbf{f}\right)\tilde{n}^i = \sum_{i=1}^{3}\sum_{l=1}^{3} \left(\mathcal{J} e_l^i \boldsymbol{f}_l\right)\tilde{n}^i = \sum_{l=1}^{3}\left(\sum_{i=1}^{3} \mathcal{J} e_l^i \tilde{n}^i\right)\boldsymbol{f}_l \\ &= \sum_{l=1}^{3} \boldsymbol{f}_l n_l = \mathbf{f} \cdot \boldsymbol{n} = (\mathbf{f} \cdot \hat{\boldsymbol{n}})\|\boldsymbol{n}\|, \end{aligned} \tag{2.88}$$

where $\boldsymbol{n}$ is the normal vector at the surface in the physical space, which is computed from the metric terms evaluated at the surfaces, and $\hat{\boldsymbol{n}}$ is the unit normal vector $\hat{\boldsymbol{n}} = \boldsymbol{n}/\|\boldsymbol{n}\|$; the components of the vector $\boldsymbol{n}$ are calculated from

$$n_l = \sum_{i=1}^{3} \mathcal{J} e_l^i \tilde{n}^i, \quad l = 1,2,3. \tag{2.89}$$

Its norm represents the area of the face element in the physical space and it is given by

$$\sigma = \|\boldsymbol{n}\| = \sqrt{\sum_{l=1}^{3} \left(\mathcal{J} e_l^i\right)^2}. \tag{2.90}$$

The superindex i means that $\boldsymbol{n}$ is associated with $\tilde{\boldsymbol{n}}$ in the direction of the coordinate ξ^i as we pointed out before. We will not use indices for this denomination and henceforth it will understood from the context which direction it corresponds. Therefore

$$\left[\tilde{\mathbf{f}} \cdot \tilde{\boldsymbol{n}}\right]^* = \left[\mathbf{f} \cdot \boldsymbol{n}\right]^* = \left[\mathbf{f} \cdot \hat{\boldsymbol{n}}\right]^* \sigma. \tag{2.91}$$

At cell interfaces the solution is double-valued (one value is obtained from the data inside the current cell and the other value corresponds to the value calculated by the neighboring cell), just like the in the finite volume method. This discontinuity at cell interfaces implies that the flux has to be calculated by introducing the so-called *numerical flux*, and

we write that in the variational formulation as $\left[\mathbf{f}\cdot\hat{\boldsymbol{n}}\right]^*$. In the finite volume community these numerical fluxes are computed usually with a Riemann solver. There is a large variety of Riemann solvers available for different systems of conservation laws, see for example the book by Toro (2009) for an exhaustive treatment of this topic. We have to mention that the numerical flux in the normal direction is defined as a function of the left and right states at the element interface: $\boldsymbol{f}^* = \boldsymbol{f}^*(\boldsymbol{u}_L, \boldsymbol{u}_R; \hat{\boldsymbol{n}}) = \left[\mathbf{f}\cdot\hat{\boldsymbol{n}}\right]^*$, and it is computed by solving a *one-dimensional* Riemann problem for the states in the Legendre-Gauss quadrature points on the surface of the element. Finally, the weak form of the equation (2.84) reads

$$\underbrace{\int_E \mathcal{J}(\xi)\frac{\partial \boldsymbol{u}}{\partial t}\phi(\xi)\,\mathrm{d}\xi}_{\text{Time Derivative Integral}} - \underbrace{\int_E \tilde{\mathbf{f}}\cdot\nabla_\xi\phi(\xi)\,\mathrm{d}\xi}_{\text{Volume Integral}} + \underbrace{\oint_{\partial E}\left[\mathbf{f}\cdot\hat{\boldsymbol{n}}\right]^*\sigma\phi(\xi)\,\mathrm{d}\boldsymbol{\sigma}}_{\text{Surface Integral}} = \mathbf{0}. \tag{2.92}$$

Discretization on Hexahedral Elements

The discontinuous Galerkin spectral element method is a discretization method specially designed for the approximate solution of conservation laws on quadrilateral/hexahedral computational domains. The partial differential equation is expressed in weak form and the solution and fluxes are approximated by using high-order Lagrangian interpolants. We stress that the polynomials are represented in a nodal form. The integrals are approximated by quadrature (in our case, Gauss quadrature), and the nodal points, where the solution is computed, are the Gauss-Legendre quadrature points. Along the boundaries, the nodes are chosen to be also Gauss-Legendre quadrature in order to compute the boundary integrals. In the Figure 2.11 these nodal points are depicted for the two-dimensional case. The ansatz discussed before will be used in the following for the purpose of discretizing each integral in the equation (2.92).

In every hexahedral element, we approximate the vector of conserved variables and the contravariant fluxes by polynomials, which basis are tensor products of one-dimensional Lagrange polynomials of degree N. The state is given by

$$\boldsymbol{u} = \sum_{i,j,k=0}^{N} \hat{\boldsymbol{u}}_{ijk}\psi_{ijk}(\xi), \tag{2.93}$$

with $\hat{\boldsymbol{u}}_{ijk}$ the nodal degrees of freedom. The components of the contravariant fluxes are written as

$$\boldsymbol{f}^m\big(\boldsymbol{u}(\xi)\big) = \sum_{i,j,k=0}^{N} \hat{\boldsymbol{f}}^m_{ijk}\psi_{ijk}(\xi), \quad m = 1,2,3. \tag{2.94}$$

The coefficients $\hat{\boldsymbol{f}}^m_{ijk}$ are computed in terms of the covariant fluxes, as it was pointed out before

$$\hat{\boldsymbol{f}}^m_{ijk} = \hat{\boldsymbol{f}}^m_{ijk}\big(\boldsymbol{u}(\xi_{ijk})\big) = \sum_{l=1}^{3} \mathcal{J}e^m_l(\xi_{ijk})\boldsymbol{f}_l\big(\boldsymbol{u}(\xi_{ijk})\big). \tag{2.95}$$

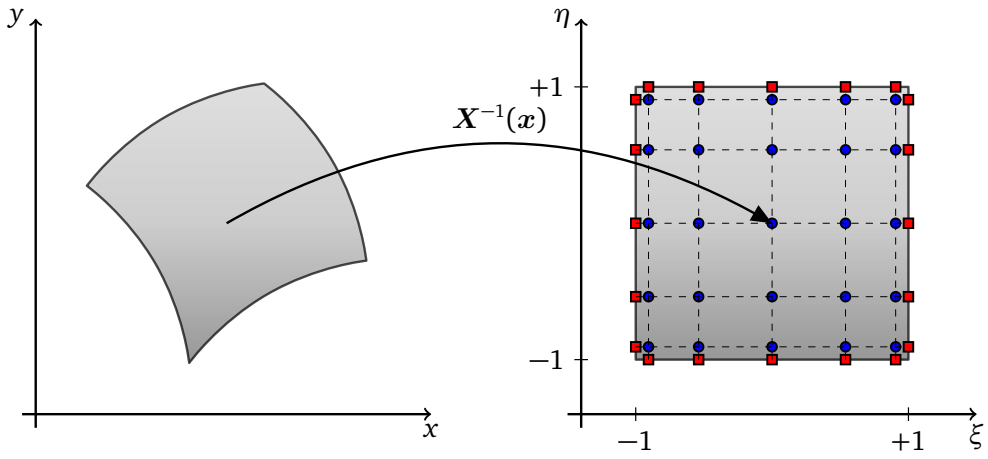

Figure 2.11: Mapping from the physical element Ω_i to the reference element $[-1,1]^2$ in a two-dimensional domain. The black-filled circles depict the two-dimensional Legendre-Gauss quadrature points in the reference element, where the solution is computed, and the black-filled squares represent the nodes where the boundary fluxes are calculated, and they are located at Legendre-Gauss quadrature points along the boundary.

The basis functions $\psi_{ijk}(\boldsymbol{\xi})$ used before have a tensor-product form

$$\psi_{ijk}(\boldsymbol{\xi}) = \ell_i(\xi^1)\ell_j(\xi^2)\ell_k(\xi^3), \tag{2.96}$$

with ℓ_i the Lagrange polynomials

$$\ell_j(\xi) = \prod_{\substack{i=0 \\ i\neq j}}^{N} \frac{(\xi - \xi_i)}{(\xi_j - \xi_i)}, \tag{2.97}$$

with the property

$$\ell_j(\xi_i) = \delta_{ij}, \quad i,j = 0,\ldots,N. \tag{2.98}$$

Time Derivative Integral

In the time derivative integral in the equation (2.92), we insert the approximation for $\boldsymbol{u}$ given in (2.93). Additionally, we assume that the test function is the same as the basis functions, $\phi = \psi_{ijk}$ (this is the Galerkin ansatz), and finally we approximate the integrals by Gaussian quadrature. Let us define I_{TD} by

$$\mathrm{I}_{\mathrm{TD}} \equiv \frac{\partial}{\partial t}\int_E \mathcal{J}(\xi)\,\boldsymbol{u}(\xi)\,\phi(\xi)\,\mathrm{d}\xi, \tag{2.99}$$

then

$$\mathrm{I}_{\mathrm{TD}} = \frac{\partial}{\partial t}\int_{-1}^{1}\int_{-1}^{1}\int_{-1}^{1} \mathcal{J}(\xi)\left(\sum_{l,m,n=0}^{N} \hat{\boldsymbol{u}}_{lmn}\psi_{lmn}(\xi)\right)\psi_{ijk}(\xi)\,\mathrm{d}\xi$$

$$
\begin{aligned}
&= \frac{\partial}{\partial t} \sum_{\lambda,\mu,\nu=0}^{N} \mathcal{J}(\xi_{\lambda\mu\nu}) \left(\sum_{l,m,n=0}^{N} \hat{\boldsymbol{u}}_{lmn} \psi_{lmn}(\xi_{\lambda\mu\nu}) \right) \psi_{ijk}(\xi_{\lambda\mu\nu}) \omega_\lambda \omega_\mu \omega_\nu \\
&= \frac{\partial}{\partial t} \sum_{\lambda,\mu,\nu=0}^{N} \mathcal{J}(\xi_{\lambda\mu\nu}) \left(\sum_{l,m,n=0}^{N} \hat{\boldsymbol{u}}_{lmn} \delta_{l\lambda} \delta_{m\mu} \delta_{n\nu} \right) \delta_{i\lambda} \delta_{j\mu} \delta_{k\nu} \omega_\lambda \omega_\mu \omega_\nu \\
&= \omega_i \omega_j \omega_k \mathcal{J}(\xi_{ijk}) \frac{\mathrm{d}\hat{\boldsymbol{u}}_{ijk}}{\mathrm{d}t},
\end{aligned}
$$

where we have made use of the property (2.98) of the Lagrange interpolating polynomials. Therefore

$$
\mathrm{I}_{\mathrm{TD}} = \frac{\partial}{\partial t} \int_E \mathcal{J}(\xi)\, \boldsymbol{u}(\xi)\, \phi(\xi)\, \mathrm{d}\xi = \omega_i \omega_j \omega_k \mathcal{J}(\xi_{ijk}) \frac{\mathrm{d}\hat{\boldsymbol{u}}_{ijk}}{\mathrm{d}t}. \tag{2.100}
$$

Volume Integral

The volume integral in the equation (2.92) involves the tensor $\tilde{\mathbf{f}}$. This integral can be written as

$$
\int_E \tilde{\mathbf{f}} \cdot \nabla_\xi \phi(\xi)\, \mathrm{d}\xi = \sum_{d=1}^{3} \int_E \boldsymbol{f}^d\big(\boldsymbol{u}(\xi)\big) \frac{\partial \phi(\xi)}{\partial \xi^d}\, \mathrm{d}\xi. \tag{2.101}
$$

We will show only the derivation for the contravariant component $\boldsymbol{f}^1$, and the other two components are obtained in an analogue manner. First, we approximate the first component of the contravariant flux $\boldsymbol{f}^1$ as it is given in the equation (2.94). Next, we assume that the test function is the same as the basis functions, e.g., $\phi = \psi_{ijk}$, and finally we approximate the integrals by Gaussian quadrature. Let us define I_{V1} by

$$
\mathrm{I}_{\mathrm{V1}} \equiv \int_E \boldsymbol{f}^1\big(\boldsymbol{u}(\xi)\big) \frac{\partial \phi(\xi)}{\partial \xi^1}\, \mathrm{d}\xi, \tag{2.102}
$$

then

$$
\begin{aligned}
\mathrm{I}_{\mathrm{V1}} &= \int_{-1}^{1}\int_{-1}^{1}\int_{-1}^{1} \left(\sum_{l,m,n=0}^{N} \hat{\boldsymbol{f}}^1_{lmn} \psi_{lmn}(\xi) \right) \frac{\partial \psi_{ijk}(\xi)}{\partial \xi^1}\, \mathrm{d}\xi \\
&= \sum_{\lambda,\mu,\nu=0}^{N} \left(\sum_{l,m,n=0}^{N} \hat{\boldsymbol{f}}^1_{lmn} \psi_{lmn}(\xi_{\lambda\mu\nu}) \right) \left. \frac{\partial \psi_{ijk}(\xi)}{\partial \xi^1} \right|_{\xi^1=\xi_\lambda} \omega_\lambda \omega_\mu \omega_\nu \\
&= \sum_{\lambda,\mu,\nu=0}^{N} \left(\sum_{l,m,n=0}^{N} \hat{\boldsymbol{f}}^1_{lmn} \delta_{l\lambda} \delta_{m\mu} \delta_{n\nu} \right) \left. \frac{\mathrm{d}\ell_i(\xi^1)}{\mathrm{d}\xi^1} \right|_{\xi^1=\xi_\lambda} \delta_{j\mu} \delta_{k\nu} \omega_\lambda \omega_\mu \omega_\nu \\
&= \sum_{\lambda=0}^{N} \hat{\boldsymbol{f}}^1_{\lambda jk} \left. \frac{\mathrm{d}\ell_i(\xi^1)}{\mathrm{d}\xi^1} \right|_{\xi^1=\xi_\lambda} \omega_\lambda \omega_j \omega_k \\
&= \omega_j \omega_k \sum_{\lambda=0}^{N} D_{\lambda i} \hat{\boldsymbol{f}}^1_{\lambda jk}\, \omega_\lambda,
\end{aligned}
$$

where we have introduced the differentiation matrix $D_{\lambda i}$, which is defined as

$$D_{ij} = \left.\frac{\mathrm{d}\ell_j(\xi)}{\mathrm{d}\xi}\right|_{\xi=\xi_i}, \quad i,j = 0,\ldots,N. \tag{2.103}$$

In this way, we get the integrals I_{V1}, I_{V2} and I_{V3}

$$\mathrm{I}_{\mathrm{V1}} = \int_E \boldsymbol{f}^1\big(\boldsymbol{u}(\xi)\big)\frac{\partial\phi(\xi)}{\partial\xi^1}\,\mathrm{d}\xi = \omega_j\omega_k\sum_{\lambda=0}^{N} D_{\lambda i}\hat{\boldsymbol{f}}^1_{\lambda jk}\,\omega_\lambda, \tag{2.104}$$

$$\mathrm{I}_{\mathrm{V2}} = \int_E \boldsymbol{f}^2\big(\boldsymbol{u}(\xi)\big)\frac{\partial\phi(\xi)}{\partial\xi^2}\,\mathrm{d}\xi = \omega_i\omega_k\sum_{\mu=0}^{N} D_{\mu j}\hat{\boldsymbol{f}}^2_{i\mu k}\,\omega_\mu, \tag{2.105}$$

$$\mathrm{I}_{\mathrm{V3}} = \int_E \boldsymbol{f}^3\big(\boldsymbol{u}(\xi)\big)\frac{\partial\phi(\xi)}{\partial\xi^3}\,\mathrm{d}\xi = \omega_i\omega_j\sum_{\nu=0}^{N} D_{\nu k}\hat{\boldsymbol{f}}^3_{ij\nu}\,\omega_\nu. \tag{2.106}$$

Finally, the volume integral is given by the sum of the three volume integrals

$$\mathrm{I}_{\mathrm{V}} = \omega_j\omega_k\sum_{\lambda=0}^{N} D_{\lambda i}\hat{\boldsymbol{f}}^1_{\lambda jk}\,\omega_\lambda + \omega_i\omega_k\sum_{\mu=0}^{N} D_{\mu j}\hat{\boldsymbol{f}}^2_{i\mu k}\,\omega_\mu + \omega_i\omega_j\sum_{\nu=0}^{N} D_{\nu k}\hat{\boldsymbol{f}}^3_{ij\nu}\,\omega_\nu. \tag{2.107}$$

Surface Integral

The last integral we will compute is the surface integral in the equation (2.92). Observe that this surface integral is the sum of the surface integrals over each face of the reference element

$$\oint_{\partial E}\big[\mathbf{f}\cdot\hat{\boldsymbol{n}}\big]^*\sigma\phi(\xi)\,\mathrm{d}\boldsymbol{\sigma} = \sum_{l=1}^{6}\int_{\partial E_l}\big[\mathbf{f}\cdot\hat{\boldsymbol{n}}_l\big]^*\sigma_l\,\phi(\xi_l)\,\mathrm{d}\boldsymbol{\sigma}_l. \tag{2.108}$$

The vector ξ_l means that the points are on the surface ∂E_l, and σ_l is the area of the element face l. We will compute only the integrals in the direction $\pm\xi^1$. Remember that the sign in the directions is included in the normal vector. The numerical flux $\boldsymbol{f}^* = \big[\mathbf{f}\cdot\hat{\boldsymbol{n}}\big]^*$ on the faces $\pm\xi^1$ of the reference element E, as we pointed out before, are calculated by using the states $\boldsymbol{u}_L$ and $\boldsymbol{u}_R$. The state $\boldsymbol{u}_L$ is obtained from the extrapolation of the inner state to the element boundaries and the state $\boldsymbol{u}_R$ from the extrapolation in the neighboring element (or in the case that the face to be evaluated is located on the physical boundary, from the boundary conditions imposed in the problem). This extrapolation is carried out on the Legendre-Gauss quadrature points on the face of the reference element. Therefore, the numerical fluxes on the faces $\pm\xi^1$ (i.e. the faces at $\xi^1 = \pm 1$) are approximated by

$$\big[\mathbf{f}\cdot\hat{\boldsymbol{n}}_l\big]^*\sigma_l\Big|_{l=\pm\xi^1} = \boldsymbol{f}^*(\pm1,\xi^2,\xi^3)\,\sigma_{\pm\xi^1} = \sum_{j,k=0}^{N}\big[\boldsymbol{f}^*\sigma\big]^{\pm\xi^1}_{jk}\,\ell_j(\xi^2)\ell_k(\xi^3). \tag{2.109}$$

Let us define I_{S1} by

$$\mathrm{I}_{\mathrm{S1}} \equiv \int_{\partial E_l} \left[\mathbf{f}\cdot\hat{\boldsymbol{n}}_l\right]^* \sigma_l\, \phi(\boldsymbol{\xi}_l)\, \mathrm{d}\boldsymbol{\sigma}_l \Big|_{l=-\xi^1}. \tag{2.110}$$

Using the previous result for the numerical flux and employing $\phi = \psi_{ijk}$ as test function, we can see that

$$\begin{aligned}
\mathrm{I}_{\mathrm{S1}} &= \int_{-1}^{1}\int_{-1}^{1}\left(\sum_{m,n=0}^{N}\left[\boldsymbol{f}^*\sigma\right]_{mn}^{-\xi^1}\ell_m(\xi^2)\ell_n(\xi^3)\right)\ell_i(-1)\ell_j(\xi^2)\ell_k(\xi^3)\,\mathrm{d}\xi^2\,\mathrm{d}\xi^3 \\
&= \sum_{\mu,\nu=0}^{N}\left(\sum_{m,n=0}^{N}\left[\boldsymbol{f}^*\sigma\right]_{mn}^{-\xi^1}\ell_m(\xi^2_\mu)\ell_n(\xi^3_\nu)\right)\ell_i(-1)\ell_j(\xi^2_\mu)\ell_k(\xi^3_\nu)\omega_\mu\omega_\nu \\
&= \sum_{\mu,\nu=0}^{N}\left(\sum_{m,n=0}^{N}\left[\boldsymbol{f}^*\sigma\right]_{mn}^{-\xi^1}\delta_{m\mu}\delta_{n\nu}\right)\ell_i(-1)\delta_{j\mu}\delta_{k\nu}\omega_\mu\omega_\nu \\
&= \omega_j\omega_k\left[\boldsymbol{f}^*\sigma\right]_{jk}^{-\xi^1}\ell_i(-1).
\end{aligned}$$

In the same way, we compute the integrals I_{S2}, I_{S3}, I_{S4}, I_{S5}, and I_{S6} and get

$$\mathrm{I}_{\mathrm{S1}} = \int_{\partial E_l} \left[\mathbf{f}\cdot\hat{\boldsymbol{n}}_l\right]^* \sigma_l\, \phi(\boldsymbol{\xi}_l)\, \mathrm{d}\boldsymbol{\sigma}_l \Big|_{l=-\xi^1} = \omega_j\omega_k\left[\boldsymbol{f}^*\sigma\right]_{jk}^{-\xi^1}\ell_i(-1), \tag{2.111}$$

$$\mathrm{I}_{\mathrm{S2}} = \int_{\partial E_l} \left[\mathbf{f}\cdot\hat{\boldsymbol{n}}_l\right]^* \sigma_l\, \phi(\boldsymbol{\xi}_l)\, \mathrm{d}\boldsymbol{\sigma}_l \Big|_{l=+\xi^1} = \omega_j\omega_k\left[\boldsymbol{f}^*\sigma\right]_{jk}^{+\xi^1}\ell_i(+1), \tag{2.112}$$

$$\mathrm{I}_{\mathrm{S3}} = \int_{\partial E_l} \left[\mathbf{f}\cdot\hat{\boldsymbol{n}}_l\right]^* \sigma_l\, \phi(\boldsymbol{\xi}_l)\, \mathrm{d}\boldsymbol{\sigma}_l \Big|_{l=-\xi^2} = \omega_i\omega_k\left[\boldsymbol{f}^*\sigma\right]_{ik}^{-\xi^2}\ell_j(-1), \tag{2.113}$$

$$\mathrm{I}_{\mathrm{S4}} = \int_{\partial E_l} \left[\mathbf{f}\cdot\hat{\boldsymbol{n}}_l\right]^* \sigma_l\, \phi(\boldsymbol{\xi}_l)\, \mathrm{d}\boldsymbol{\sigma}_l \Big|_{l=+\xi^2} = \omega_i\omega_k\left[\boldsymbol{f}^*\sigma\right]_{ik}^{+\xi^2}\ell_j(+1), \tag{2.114}$$

$$\mathrm{I}_{\mathrm{S5}} = \int_{\partial E_l} \left[\mathbf{f}\cdot\hat{\boldsymbol{n}}_l\right]^* \sigma_l\, \phi(\boldsymbol{\xi}_l)\, \mathrm{d}\boldsymbol{\sigma}_l \Big|_{l=-\xi^3} = \omega_i\omega_j\left[\boldsymbol{f}^*\sigma\right]_{ij}^{-\xi^3}\ell_k(-1), \tag{2.115}$$

$$\mathrm{I}_{\mathrm{S6}} = \int_{\partial E_l} \left[\mathbf{f}\cdot\hat{\boldsymbol{n}}_l\right]^* \sigma_l\, \phi(\boldsymbol{\xi}_l)\, \mathrm{d}\boldsymbol{\sigma}_l \Big|_{l=+\xi^3} = \omega_i\omega_j\left[\boldsymbol{f}^*\sigma\right]_{ij}^{+\xi^3}\ell_k(+1). \tag{2.116}$$

Finally, the surface integral is given by the sum of the six surface integrals

$$\begin{aligned}
\mathrm{I}_{\mathrm{S}} = &+ \omega_j\omega_k\Big(\left[\boldsymbol{f}^*\sigma\right]_{jk}^{+\xi^1}\ell_i(+1) + \left[\boldsymbol{f}^*\sigma\right]_{jk}^{-\xi^1}\ell_i(-1)\Big) \\
&+ \omega_i\omega_k\Big(\left[\boldsymbol{f}^*\sigma\right]_{ik}^{+\xi^2}\ell_j(+1) + \left[\boldsymbol{f}^*\sigma\right]_{ik}^{-\xi^2}\ell_j(-1)\Big) \\
&+ \omega_i\omega_j\Big(\left[\boldsymbol{f}^*\sigma\right]_{ij}^{+\xi^3}\ell_k(+1) + \left[\boldsymbol{f}^*\sigma\right]_{ij}^{-\xi^3}\ell_k(-1)\Big).
\end{aligned} \tag{2.117}$$

Semi-discrete Formulation

Once discretized all integrals appearing in the equation (2.92), we are able to write down the semi-discrete formulation of the discontinuous Galerkin spectral element method on

hexahedral elements. Before we write the final equation, we define some useful quantities, which can be precomputed and stored in memory. The operators to be defined are

$$\hat{D}_{ij} = -D_{ji}\frac{\omega_j}{\omega_i}, \quad \hat{\ell}_i(\pm 1) = \frac{\ell_i(\pm 1)}{\omega_i}, \quad i,j = 0,\ldots,N. \tag{2.118}$$

The semi-discrete formulation has the following form

$$\begin{aligned}\frac{\mathrm{d}\hat{\boldsymbol{u}}_{ijk}}{\mathrm{d}t} = &-\frac{1}{\mathcal{J}_{ijk}}\left[\sum_{\lambda=0}^{N}\hat{D}_{i\lambda}\hat{\boldsymbol{f}}^{1}_{\lambda jk} + \left(\left[\boldsymbol{f}^{*}\sigma\right]^{+\xi^1}_{jk}\hat{\ell}_i(+1) + \left[\boldsymbol{f}^{*}\sigma\right]^{-\xi^1}_{jk}\hat{\ell}_i(-1)\right)\right] \\ &-\frac{1}{\mathcal{J}_{ijk}}\left[\sum_{\mu=0}^{N}\hat{D}_{j\mu}\hat{\boldsymbol{f}}^{2}_{i\mu k} + \left(\left[\boldsymbol{f}^{*}\sigma\right]^{+\xi^2}_{ik}\hat{\ell}_j(+1) + \left[\boldsymbol{f}^{*}\sigma\right]^{-\xi^2}_{ik}\hat{\ell}_j(-1)\right)\right] \\ &-\frac{1}{\mathcal{J}_{ijk}}\left[\sum_{\nu=0}^{N}\hat{D}_{k\nu}\hat{\boldsymbol{f}}^{3}_{ij\nu} + \left(\left[\boldsymbol{f}^{*}\sigma\right]^{+\xi^3}_{ij}\hat{\ell}_k(+1) + \left[\boldsymbol{f}^{*}\sigma\right]^{-\xi^3}_{ij}\hat{\ell}_k(-1)\right)\right].\end{aligned} \tag{2.119}$$

The semi-discrete formulation given by equation (2.119) consists of one-dimensional DGSEM operators (the quantities in square brackets), each of them applied along a direction. A flow diagram for the discontinuous Galerkin spectral element method is depicted in the figure 2.12.

2.5. Time Discretization with Runge-Kutta Schemes

So far we have spoken about numerical methods for solving systems of conservation laws, but we never mentioned the time discretization, but only the spatial one. In fact, for all three methods discussed we got a *semi-discrete scheme*, meaning that the obtained set of equations are continuous in time and discretized in space. This kind of technique, called the *method of lines*, is used very often for solving partial differential equations, especially those of hyperbolic nature (see for example the book by Schiesser (1991)). As we can see from the semi-discrete form of the numerical schemes under consideration in this work, the method of lines has led to a system of ordinary differential equations. The method of lines acquires the accuracy order of the integrator used to solve the system of ordinary differential equations, on the condition that the spatial discretization is of the same order of accuracy or higher. There is a large variety of numerical methods to solve ordinary differential equations, see for example the books by Hairer et al. (1993) and Hairer & Wanner (1996), but we will only focus on the class of explicit schemes most widely used for conservation laws, namely, the explicit Runge-Kutta methods. Implicit schemes or the so-called implicit/explicit approaches (Ascher et al. 1997; Pareschi & Russo 2005) will not be discussed, as well as the family of one-step ADER schemes by Titarev & Toro (2002) and by Dumbser & Munz (2006) for finite volume methods and for the discontinuous Galerkin methods, respectively.

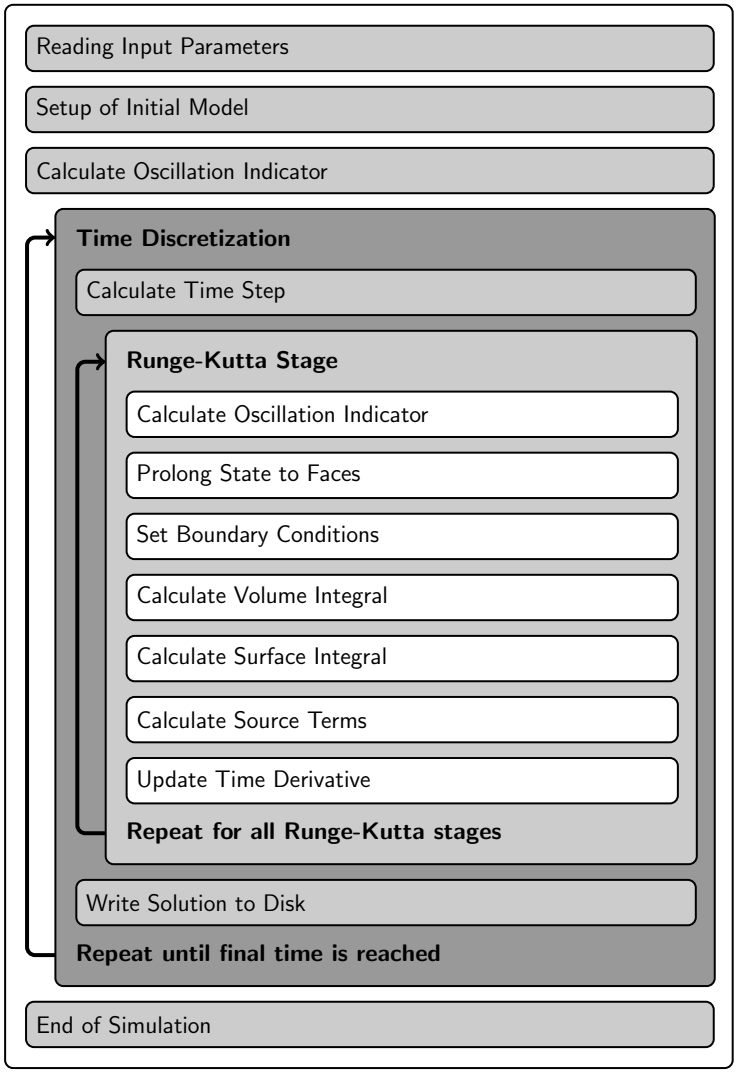

Figure 2.12: Flow diagram for the discontinuous Galerkin spectral element method.

Going back to the system of hyperbolic conservation laws

$$\frac{\partial \boldsymbol{u}}{\partial t} + \frac{\partial \boldsymbol{f}(\boldsymbol{u})}{\partial x} + \frac{\partial \boldsymbol{g}(\boldsymbol{u})}{\partial y} + \frac{\partial \boldsymbol{h}(\boldsymbol{u})}{\partial z} = \boldsymbol{0}, \tag{2.120}$$

with given initial and boundary conditions, we got the following semi-discrete scheme for the finite volume and for the finite difference methods on structured grids/meshes

$$\frac{\mathrm{d}\boldsymbol{u}_{ijk}}{\mathrm{d}t} = -\left[\frac{\hat{\boldsymbol{f}}_{i+\frac{1}{2},jk} - \hat{\boldsymbol{f}}_{i-\frac{1}{2},jk}}{\Delta x}\right] - \left[\frac{\hat{\boldsymbol{g}}_{i,j+\frac{1}{2},k} - \hat{\boldsymbol{g}}_{i,j-\frac{1}{2},k}}{\Delta y}\right] - \left[\frac{\hat{\boldsymbol{h}}_{ij,k+\frac{1}{2}} - \hat{\boldsymbol{h}}_{ij,k-\frac{1}{2}}}{\Delta z}\right]. \tag{2.121}$$

For the discontinuous Galerkin spectral element method, we got the semi-discrete scheme

given by

$$\begin{aligned}\frac{\mathrm{d}\hat{\boldsymbol{u}}_{ijk}}{\mathrm{d}t} =& -\frac{1}{\mathcal{J}_{ijk}}\left[\sum_{\lambda=0}^{N}\hat{D}_{i\lambda}\hat{\boldsymbol{f}}^{1}_{\lambda jk}+\left(\left[\boldsymbol{f}^{*}\sigma\right]^{+\xi^1}_{jk}\hat{\ell}_i(+1)+\left[\boldsymbol{f}^{*}\sigma\right]^{-\xi^1}_{jk}\hat{\ell}_i(-1)\right)\right]\\ &-\frac{1}{\mathcal{J}_{ijk}}\left[\sum_{\mu=0}^{N}\hat{D}_{j\mu}\hat{\boldsymbol{f}}^{2}_{i\mu k}+\left(\left[\boldsymbol{f}^{*}\sigma\right]^{+\xi^2}_{ik}\hat{\ell}_j(+1)+\left[\boldsymbol{f}^{*}\sigma\right]^{-\xi^2}_{ik}\hat{\ell}_j(-1)\right)\right]\\ &-\frac{1}{\mathcal{J}_{ijk}}\left[\sum_{\nu=0}^{N}\hat{D}_{k\nu}\hat{\boldsymbol{f}}^{3}_{ij\nu}+\left(\left[\boldsymbol{f}^{*}\sigma\right]^{+\xi^3}_{ij}\hat{\ell}_k(+1)+\left[\boldsymbol{f}^{*}\sigma\right]^{-\xi^3}_{ij}\hat{\ell}_k(-1)\right)\right].\end{aligned} \tag{2.122}$$

The meaning of all quantities involved in the equations (2.121) and (2.122) can be found in the sections dedicated to the numerical method used in its derivation. In this section we present two numerical methods for solving the systems of ordinary differential equations (2.121) and (2.122). The first one is the *strong stability preserving Runge-Kutta* method of Shu & Osher (1988), and the second one is the *low-storage explicit Runge-Kutta* method of Williamson (1980). Methods obtained by combining *low-storage* and *strong stability-preserving* schemes are reviewed in Ketcheson (2008) and Ketcheson (2010).

2.5.1. Strong Stability-Preserving Runge-Kutta Methods

In this section we will discuss the family of high-order strong stability preserving Runge-Kutta (SSPRK) methods for systems of ordinary differential equations obtained from the application of the method of lines to hyperbolic partial differential equations. The present discussion is based on the review by Gottlieb et al. (2001). The class of SSPRK methods was first developed by Shu & Osher (1988) and Shu (1988), where they called them TVD (Total Variation Diminishing) time discretizations, and further by Gottlieb & Shu (1998). New developments have been reported in Hundsdorfer et al. (2003), Ruuth & Spiteri (2002), Spiteri & Ruuth (2002), Spiteri & Ruuth (2003), Gottlieb (2005), and Gottlieb et al. (2009). The main idea of these methods resides in assuming that the first-order forward Euler method is strongly stable under the total variation norm (and in general, any given norm) and a suitable time step restriction. From this, the aim is to construct a higher-order time discretization that preserves strong stability under the TVD norm, and maybe, with a different time step restriction (Shu & Osher 1988).

The systems of ordinary differential equations (2.121) and (2.122) can be recast as

$$\frac{\mathrm{d}\boldsymbol{u}}{\mathrm{d}t} = \boldsymbol{L}(\boldsymbol{u},t), \quad \boldsymbol{u}(t_0)=\boldsymbol{u}_0, \quad t\in[t_0,t_f], \tag{2.123}$$

where $-\boldsymbol{L}(\boldsymbol{u},t)$ is the spatial discretization operator. In Shu (1988), it is assumed that the spatial discretization $-\boldsymbol{L}(\boldsymbol{u},t)$ in the system of ordinary differential equations (2.123) when is combined with the first-order forward Euler scheme

$$\boldsymbol{u}^{n+1} = \boldsymbol{u}^{n} + \Delta t\boldsymbol{L}(\boldsymbol{u}^{n},t^{n}) \tag{2.124}$$

is total variation diminishing, that is, the total variation of the one-dimensional discrete solution does not increase in time

$$\mathrm{TV}(\boldsymbol{u}^{n+1}) \leq \mathrm{TV}(\boldsymbol{u}^n), \quad \mathrm{TV}(\boldsymbol{u}^n) = \sum_i \left| \boldsymbol{u}_{i+1}^n - \boldsymbol{u}_i^n \right|, \tag{2.125}$$

for a time step restricted by the Courant-Friedrichs-Levy (CFL) condition,

$$\Delta t \leq \Delta t_E. \tag{2.126}$$

When a high-order strong stability-preserving Runge-Kutta method is constructed for the equations (2.123), the goal is to maintain the TVD property (2.125), maybe with a restricted CFL condition

$$\Delta t \leq c \Delta t_E, \tag{2.127}$$

where c is the SSP coefficient of the method. Let us consider the general m-stages Runge-Kutta method of the Shu-Osher form (Shu & Osher 1988)

$$\begin{aligned} \boldsymbol{u}^{(0)} &= \boldsymbol{u}^n, \\ \boldsymbol{u}^{(i)} &= \sum_{k=0}^{i-1} \Big(\alpha_{ik} \boldsymbol{u}^{(k)} + \Delta t \beta_{ik} \boldsymbol{L}\big(\boldsymbol{u}^{(k)}, t^n + \gamma_k \Delta t\big) \Big), \quad \alpha_{ik} \geq 0, \quad i = 1, \ldots, m, \\ \boldsymbol{u}^{n+1} &= \boldsymbol{u}^{(m)}. \end{aligned} \tag{2.128}$$

Clearly, the coefficients α_{ik}, β_{ik}, and γ_k have to be found such that the order conditions are satisfied (see the books by Hairer et al. (1993) and Hairer & Wanner (1996)). If any additional degree of freedom is available, the scheme can be optimized in some way. For consistency, we must have that

$$\sum_{k=0}^{i-1} \alpha_{ik} = 1. \tag{2.129}$$

If all β_{ik} are nonnegative, then the Runge-Kutta method (2.128) is a convex combination of forward Euler steps, provided the following CFL restriction

$$\Delta t \leq c \Delta t_E, \quad c = \min_{i,k} \frac{\alpha_{ik}}{\beta_{ik}}. \tag{2.130}$$

This is clearly visible in the following equation, where we have rewritten the stages in the equation (2.128)

$$\boldsymbol{u}^{(i)} = \sum_{k=0}^{i-1} \alpha_{ik} \Big(\boldsymbol{u}^{(k)} + \frac{\beta_{ik}}{\alpha_{ik}} \Delta t \boldsymbol{L}\big(\boldsymbol{u}^{(k)}, t^n + \gamma_k \Delta t\big) \Big). \tag{2.131}$$

When designing SSPRK methods, an additional goal is to optimize the number c in order to minimize the cost of the time integration. The strong stability-preserving Runge-Kutta methods are desirable in problems with discontinuities and strong shocks, because they guarantee that, as part of the time-integration process, no additional oscillations are introduced (Hesthaven & Warburton 2008).

SSPRK3 Method

The third-order SSPRK with three stages is given by

$$\begin{aligned}
\boldsymbol{u}^{(0)} &= \boldsymbol{u}^n \\
\boldsymbol{u}^{(1)} &= \boldsymbol{u}^{(0)} + \Delta t \boldsymbol{L}\big(\boldsymbol{u}^{(0)}, t^n\big) \\
\boldsymbol{u}^{(2)} &= \frac{1}{4}\Big(3\boldsymbol{u}^{(0)} + \boldsymbol{u}^{(1)} + \Delta t \boldsymbol{L}\big(\boldsymbol{u}^{(1)}, t^n + \Delta t\big)\Big) \\
\boldsymbol{u}^{(3)} &= \frac{1}{3}\Big(\boldsymbol{u}^{(0)} + 2\boldsymbol{u}^{(2)} + 2\Delta t \boldsymbol{L}\big(\boldsymbol{u}^{(2)}, t^n + 0.5\Delta t\big)\Big) \\
\boldsymbol{u}^{n+1} &= \boldsymbol{u}^{(3)}.
\end{aligned} \tag{2.132}$$

This scheme has an SSP coefficient $c \equiv \min_{i,k} \frac{\alpha_{ik}}{\beta_{ik}} = 1.0$. The SSP coefficient satisfies $\Delta t \leq c\Delta t_E$, where Δt_E is the time step restricted by the Courant-Friedrichs-Levy (CFL) condition for the first-order forward Euler method. This means that the maximum time step is the same as that of the forward Euler method (Spiteri & Ruuth 2002).

SSPRK4 Method

The fourth-order SSPRK with five stages derived in Spiteri & Ruuth (2002) is given by

$$\begin{aligned}
\boldsymbol{u}^{(0)} &= \boldsymbol{u}^n \\
\boldsymbol{u}^{(1)} &= \boldsymbol{u}^{(0)} + 0.39175222700392\,\Delta t \boldsymbol{L}\big(\boldsymbol{u}^{(0)}, t^n\big) \\
\boldsymbol{u}^{(2)} &= 0.44437049406734\,\boldsymbol{u}^{(0)} + 0.55562950593266\,\boldsymbol{u}^{(1)} \\
&\quad + 0.36841059262959\,\Delta t \boldsymbol{L}\big(\boldsymbol{u}^{(1)}, t^n + 0.39175222700392\,\Delta t\big) \\
\boldsymbol{u}^{(3)} &= 0.62010185138540\,\boldsymbol{u}^{(0)} + 0.37989814861460\,\boldsymbol{u}^{(2)} \\
&\quad + 0.25189177424738\,\Delta t \boldsymbol{L}\big(\boldsymbol{u}^{(2)}, t^n + 0.58607968896780\,\Delta t\big) \\
\boldsymbol{u}^{(4)} &= 0.17807995410773\,\boldsymbol{u}^{(0)} + 0.82192004589227\,\boldsymbol{u}^{(3)} \\
&\quad + 0.54497475021237\,\Delta t \boldsymbol{L}\big(\boldsymbol{u}^{(3)}, t^n + 0.47454236302687\,\Delta t\big) \\
\boldsymbol{u}^{(5)} &= 0.00683325884039\,\boldsymbol{u}^{(0)} + 0.51723167208978\,\boldsymbol{u}^{(2)} \\
&\quad + 0.12759831133288\,\boldsymbol{u}^{(3)} + 0.34833675773694\,\boldsymbol{u}^{(4)} \\
&\quad + 0.08460416338212\,\Delta t \boldsymbol{L}\big(\boldsymbol{u}^{(3)}, t^n + 0.47454236302687\,\Delta t\big) \\
&\quad + 0.22600748319395\,\Delta t \boldsymbol{L}\big(\boldsymbol{u}^{(4)}, t^n + 0.93501063100924\,\Delta t\big) \\
\boldsymbol{u}^{n+1} &= \boldsymbol{u}^{(5)}.
\end{aligned} \tag{2.133}$$

This scheme has an SSP coefficient $c \equiv \min_{i,k} \frac{\alpha_{ik}}{\beta_{ik}} = 1.50818004975927$. The SSP coefficient satisfies $\Delta t \leq c\Delta t_E$, where Δt_E is the time step restricted by the Courant-Friedrichs-Levy (CFL) condition for the first-order forward Euler method.

2.5.2. Low Storage Explicit Runge-Kutta Methods

Direct numerical simulations in computational fluid dynamics and computational plasma physics usually require a huge amount of grid points/mesh elements in order to nu-

Table 2.1: Coefficients for the low-storage three-stage third-order Runge-Kutta method (Williamson 1980).

i	α_i	β_i	γ_i
1	0	$\frac{1}{3}$	0
2	$-\frac{5}{9}$	$\frac{15}{16}$	$\frac{1}{3}$
3	$-\frac{153}{128}$	$\frac{8}{15}$	$\frac{3}{4}$

merically study the behavior of the fluid at different scales. Therefore, the number of ordinary differential equations obtained after applying the *method-of-lines* to the conservation laws is considerable large. In this kind of computation, one has to consider the memory requirements for the simulation for a desired accuracy, specially if high-order methods are taken into consideration. Actually, the CFD community is contemplating that in the simulation for such problems, high-order spatial *and* temporal discretizations are a must. High-order time discretizations performed through the integration of ordinary differential equations with low-storage methods have received a lot of effort the last years, even combining them with the strong stability-preserving methods discussed before (Williamson 1980; Carpenter & Kennedy 1994; Kennedy et al. 2000; Ketcheson 2008; Ketcheson 2010). The idea of these methods is to reduce computer memory usage during numerical integration of the ordinary differential equations while maintaining higher-order accuracy. In some cases, because of method's efficiency, the scheme may require more stages than its counterpart explicit Runge-Kutta method (Ketcheson 2008). For a more detailed survey of this family of ODE integrators, we suggest the work by Ketcheson (2010).

In this work, two LSERK schemes requiring only two memory registers were used. The s-stages low-storage explicit Runge-Kutta method considered and taken from Williamson (1980) and Carpenter & Kennedy (1994), have the following general form

$$\begin{aligned}
\boldsymbol{u}^{(0)} &= \boldsymbol{u}^n \\
\boldsymbol{k}^{(i)} &= \alpha_i \boldsymbol{k}^{(i-1)} + \Delta t \boldsymbol{L}\big(\boldsymbol{u}^{(i-1)}, t^n + \gamma_i \Delta t\big), \quad \text{for } i \in [1,\ldots,s] \\
\boldsymbol{u}^{(i)} &= \boldsymbol{u}^{(i-1)} + \beta_i \boldsymbol{k}^{(i)}, \quad \text{for } i \in [1,\ldots,s] \\
\boldsymbol{u}^{n+1} &= \boldsymbol{u}^{(s)},
\end{aligned} \tag{2.134}$$

where α_i, β_i are the $2N$-storage variables. These coefficients for the third order and fourth order LSERK are found in the Table 2.1 and Table 2.2.

Table 2.2: Coefficients for the low-storage five-stage fourth-order Runge-Kutta method (Carpenter & Kennedy 1994).

i	α_i	β_i	γ_i
1	0	$\frac{1432997174477}{9575080441755}$	0
2	$-\frac{567301805773}{1357537059087}$	$\frac{5161836677717}{13612068292357}$	$\frac{1432997174477}{9575080441755}$
3	$-\frac{2404267990393}{2016746695238}$	$\frac{1720146321549}{2090206949498}$	$\frac{2526269341429}{6820363962896}$
4	$-\frac{3550918686646}{2091501179385}$	$\frac{3134564353537}{4481467310338}$	$\frac{2006345519317}{3224310063776}$
5	$-\frac{1275806237668}{842570457699}$	$\frac{2277821191437}{14882151754819}$	$\frac{2802321613138}{2924317926251}$

2.5.3. Courant-Friedrichs-Lewy Condition

For hyperbolic partial differential equations, the Courant-Friedrichs-Lewy (CFL) condition is a necessary condition for stability of any explicit one-level numerical scheme (Courant et al. 1928). It establishes that the domain of dependence of the solution is contained in the numerical domain of dependence of the numerical method. From a physical point of view, this condition guarantees that the propagation speed of any traveling wave is always smaller than the numerical speed $c_N \equiv \Delta x/\Delta t$. In other words, the time step should be equal to or smaller than the time necessary for a wave to travel across the stencil of the spatial discretization scheme (Blazek 2005). This condition is applied to constraint the time step, and in the one-dimensional case is given by

$$\Delta t = \mathrm{CFL} \min_k \left(\frac{\Delta x}{|\lambda_{k,x}|} \right), \tag{2.135}$$

with λ_k the maximum eigenvalue of the physical x-flux Jacobian over all computational cells. The number CFL satisfies $\mathrm{CFL} \leq 1$, and depends on the spatial discretization and on the time-stepping scheme used for solving the conservation law. In the multidimensional case, only approximated values of the CFL condition are available for nonlinear equations. In Titarev & Toro (2005), the following value is considered

$$\Delta t = \frac{\mathrm{CFL}}{D} \min_k \left(\frac{\Delta x}{|\lambda_{k,x}|}, \frac{\Delta y}{|\lambda_{k,y}|}, \frac{\Delta z}{|\lambda_{k,z}|} \right). \tag{2.136}$$

For the discontinuous Galerkin method, Cockburn & Shu (2001) gave an approximate CFL condition for linear stability, and it has the following form

$$\Delta t = \mathrm{CFL} \frac{\Delta x}{|\lambda_{\max}|} \frac{1}{2N+1}, \tag{2.137}$$

where N is the polynomial degree used in the spatial discretization. In Kubatko et al. (2008), CFL conditions were derived for several different strong-stability-preserving Runge-Kutta time discretization methods.

CHAPTER 3

High-Order Methods: Special Topics

In order to achieve very high-order of accuracy, the finite volume and finite difference methods require a high-order conservative reconstruction operator. Moreover, all three numerical methods used in this work for the spatial discretization of the hyperbolic conservation laws demand a *shock capturing* procedure, that combined with the base scheme, provides a sort of stabilization to the solution when strong rarefaction waves, discontinuities (like shock waves) are involved. In this chapter we present in a very detailed fashion the WENO reconstruction procedure for Cartesian meshes (see section 3.1). In section 3.2 is discussed the general methodology for shock capturing in the three numerical methods employed in this dissertation. Finally, in the section 3.3, we present the general approach for maintaining the divergence constraint $\nabla \cdot \boldsymbol{B} = 0$.

3.1. WENO Reconstruction Procedure

Hyperbolic conservation laws have as main feature the appearance of shock waves in their solution. This constitutes the most difficult task when designing numerical methods for this kind of partial differential equations. Low order numerical methods, like the Godunov scheme (Godunov 1959), can resolve the discontinuities monotonically without generating spurious oscillations, but they often smear some of these discontinuities excessively. They also contain relatively large numerical dissipation in the smooth part of the solution. In the 1970s and 1980s were developed the high resolution schemes represented by the MUSCL schemes (van Leer 1979), the TVD schemes (Harten et al. 1983), and the PPM schemes (Colella & Woodward 1984), are usually second order accurate in smooth regions and can resolve discontinuities monotonically with a sharper transition than first order schemes.

In this section we are going to consider the WENO reconstruction procedure used for solving hyperbolic conservation laws. WENO schemes are an excellent candidate for solving problems containing complex-flow features, such as those present in the shock interaction with vortices, because they are higher-order of accuracy and can resolve shocks in an essentially non-oscillatory fashion. In the following, explicit formulae for the WENO reconstruction WENO3, WENO5 and WENO7 will be presented. For a more detailed description of the scheme and also other applications besides the solution of partial differ-

ential equations, we refer to the review of Shu (2009).

3.1.1. Basic Idea

In this section we are going to present the WENO reconstruction of third, fifth, and seventh order for the following interpolation points:

$$x = x_{i-\frac{1}{2}}, \quad x = x_{i+\frac{1}{2}}, \quad x = x_{i-\frac{1}{2\sqrt{3}}}, \quad x = x_{i+\frac{1}{2\sqrt{3}}}. \tag{3.1}$$

The general idea will be described in the following for the interpolation point $x = x_{i+\frac{1}{2}}$, but the procedure is completely similar for the other points.

Let be $I = [a, b]$. Let $a < \cdots < x_{i-1} < x_i < x_{i+1} < \cdots < b$ be a partition of I. Let us assume that the mesh is uniform, i.e., $\Delta x = x_{i+1} - x_i = \text{constant}$. Therefore we can take $x_i = i\Delta x$. Let $u(x)$ be a function. Let us assume that all cell averages

$$\bar{u}_i = \frac{1}{\Delta x} \int_{x_{i-\frac{1}{2}}}^{x_{i+\frac{1}{2}}} u(x)\,\mathrm{d}x \tag{3.2}$$

over the intervals $I_i = \left(x_{i-\frac{1}{2}}, x_{i+\frac{1}{2}}\right)$ are given. As an example, let us find an approximation of the function $u(x)$ at a point other than the cell barycenter x_i, for instance, the point $x = x_{i+\frac{1}{2}}$. Defining the primitive function $u(x)$ by

$$U(x) = \int_{x_{-\frac{1}{2}}}^{x} u(\zeta)\,\mathrm{d}\zeta, \tag{3.3}$$

where the lower limit is irrelevant and can be replaced for any fixed point, then clearly we have

$$U\left(x_{i+\frac{1}{2}}\right) = \int_{x_{-\frac{1}{2}}}^{x_{i+\frac{1}{2}}} u(\zeta)\,\mathrm{d}\zeta = \sum_{l=0}^{i} \int_{x_{l-\frac{1}{2}}}^{x_{l+\frac{1}{2}}} u(\zeta)\,\mathrm{d}\zeta = \sum_{l=0}^{i} \Delta x\, \bar{u}_l. \tag{3.4}$$

That is, knowing all the cell averages $\bar{u}_l$, we also know the point values of the primitive function $U\left(x_{i+\frac{1}{2}}\right)$ at all half nodes. Therefore, interpolation polynomials can be constructed for the primitive function $U(x)$. The derivative of such an interpolation polynomial for $U(x)$ can then be used as an approximation to $u(x) = U'(x)$.

Let $P_k(x)$ be the polynomials of degree at most $N+1$ which interpolates the function $U(x)$ at the $N+2$ points $x_{j+\frac{1}{2}}$, for $j = i-N-3+k+l$, with $l = 1, \ldots, N+2$. Let us approximate the value of the function $u(x)$ at $x_{i+\frac{1}{2}}$, $u_{i+\frac{1}{2}}$ by using polynomials of degree N. For that, we can use $N+1$ possible stencils S_k containing the interval I_i and build unique interpolation polynomials of degree at most N, $p_k(x) = P_k'(x)$ that reconstruct the function $u(x)$ over the stencil $S_k = \left\{ I_j \,\middle|\, j = i-N-2+k+l, \text{ with } l = 1, \ldots, N+1 \right\}$ in the sense that

$$(\bar{p}_k)_j = \frac{1}{\Delta x} \int_{x_{j-\frac{1}{2}}}^{x_{j+\frac{1}{2}}} p_k(x)\,\mathrm{d}x = \bar{u}_j, \quad j = i-N-2+k+l, \text{ with } l = 1, \ldots, N+1 \tag{3.5}$$

approximates the value $u^{(k)}_{i+\frac{1}{2}} \equiv p_k(x_{i+\frac{1}{2}})$. All these polynomials satisfy $p_k(x_i) = u_i$.

3.1.2. WENO3 scheme

Let us approximate the value of the function $u(x)$ at the points $x_{i-\frac{1}{2}}$, $x_{i+\frac{1}{2}}$, $x_{i-\frac{1}{2\sqrt{3}}}$ and $x_{i+\frac{1}{2\sqrt{3}}}$ by using polynomials of degree $N = 1$. For the stencil S_k we get the corresponding values $u^{(k)}_{i-\frac{1}{2}}$, $u^{(k)}_{i+\frac{1}{2}}$, $u^{(k)}_{i-\frac{1}{2\sqrt{3}}}$ and $u^{(k)}_{i+\frac{1}{2\sqrt{3}}}$. Let us write down the stencils (see figure 3.1)

$$S_1 = \{I_{i-1}, I_i\}, \quad S_2 = \{I_i, I_{i+1}\}. \tag{3.6}$$

The corresponding interpolated values for the point $x_{i-\frac{1}{2}}$ are

$$u^{(1)}_{i-\frac{1}{2}} = \frac{1}{2}\big(\bar{u}_{i-1} + \bar{u}_i\big), \tag{3.7}$$

$$u^{(2)}_{i-\frac{1}{2}} = \frac{1}{2}\big(3\bar{u}_i - \bar{u}_{i+1}\big), \tag{3.8}$$

and the corresponding interpolated values for the point $x_{i+\frac{1}{2}}$ are

$$u^{(1)}_{i+\frac{1}{2}} = \frac{1}{2}\big(-\bar{u}_{i-1} + 3\bar{u}_i\big), \tag{3.9}$$

$$u^{(2)}_{i+\frac{1}{2}} = \frac{1}{2}\big(\bar{u}_i + \bar{u}_{i+1}\big). \tag{3.10}$$

In the same way as before, the corresponding interpolated values for the point $x_{i-\frac{1}{2\sqrt{3}}}$ are

$$u^{(1)}_{i-\frac{1}{2\sqrt{3}}} = \frac{1}{6}\big(\sqrt{3}\bar{u}_{i-1} + 6\bar{u}_i - \sqrt{3}\bar{u}_i\big), \tag{3.11}$$

$$u^{(2)}_{i-\frac{1}{2\sqrt{3}}} = \frac{1}{6}\big(\sqrt{3}\bar{u}_i + 6\bar{u}_i - \sqrt{3}\bar{u}_{i+1}\big), \tag{3.12}$$

and the corresponding interpolated values for the point $x_{i+\frac{1}{2\sqrt{3}}}$ are

$$u^{(1)}_{i+\frac{1}{2\sqrt{3}}} = \frac{1}{6}\big(-\sqrt{3}\bar{u}_{i-1} + 6\bar{u}_i + \sqrt{3}\bar{u}_i\big), \tag{3.13}$$

$$u^{(2)}_{i+\frac{1}{2\sqrt{3}}} = \frac{1}{6}\big(-\sqrt{3}\bar{u}_i + 6\bar{u}_i + \sqrt{3}\bar{u}_{i+1}\big). \tag{3.14}$$

If we choose the large stencil

$$S = \{I_{i-1}, I_i, I_{i+1}\}, \tag{3.15}$$

which is the union of all 2 stencils S_k, then we are able to find an interpolation polynomial $p(x)$ of degree at most 2, satisfying $p(x_j) = u_j$ for $i - N \le j \le i + N$ and giving the approximations $u_{i-\frac{1}{2}} \equiv p(x_{i-\frac{1}{2}})$, $u_{i+\frac{1}{2}} \equiv p(x_{i+\frac{1}{2}})$,

$$u_{i-\frac{1}{2}} = \frac{1}{6}\big(2\bar{u}_{i-1} + 5\bar{u}_i - \bar{u}_{i+1}\big), \tag{3.16}$$

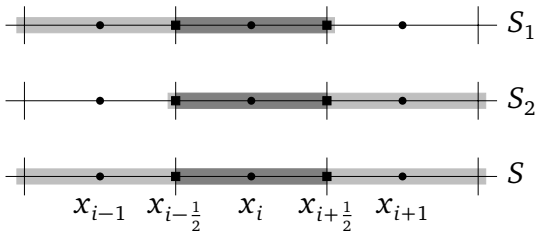

Figure 3.1: Stencils for the third order WENO reconstruction procedure.

$$u_{i+\frac{1}{2}} = \frac{1}{6}\big(-\bar{u}_{i-1} + 5\bar{u}_i + 2\bar{u}_{i+1}\big), \tag{3.17}$$

and the approximations $u_{i-\frac{1}{2\sqrt{3}}} \equiv p(x_{i-\frac{1}{2\sqrt{3}}})$ and $u_{i+\frac{1}{2\sqrt{3}}} \equiv p(x_{i+\frac{1}{2\sqrt{3}}})$

$$u_{i-\frac{1}{2\sqrt{3}}} = \frac{1}{12}\big(\sqrt{3}\bar{u}_{i-1} + 12\bar{u}_i - \sqrt{3}\bar{u}_{i+1}\big), \tag{3.18}$$

$$u_{i+\frac{1}{2\sqrt{3}}} = \frac{1}{12}\big(-\sqrt{3}\bar{u}_{i-1} + 12\bar{u}_i + \sqrt{3}\bar{u}_{i+1}\big), \tag{3.19}$$

provided that the function is smooth in the large stencil S.

3.1.3. WENO5 scheme

Let us approximate the value of the function $u(x)$ at the points $x_{i-\frac{1}{2}}$, $x_{i+\frac{1}{2}}$, $x_{i-\frac{1}{2\sqrt{3}}}$ and $x_{i+\frac{1}{2\sqrt{3}}}$ by using polynomials of degree $N = 2$. For the stencil S_k we get the corresponding values $u^{(k)}_{i-\frac{1}{2}}$, $u^{(k)}_{i+\frac{1}{2}}$, $u^{(k)}_{i-\frac{1}{2\sqrt{3}}}$ and $u^{(k)}_{i+\frac{1}{2\sqrt{3}}}$. Let us write down the stencils (See figure 3.2)

$$S_1 = \{I_{i-2}, I_{i-1}, I_i\}, \quad S_2 = \{I_{i-1}, I_i, I_{i+1}\}, \quad S_3 = \{I_i, I_{i+1}, I_{i+2}\}. \tag{3.20}$$

The corresponding interpolated values for the point $x_{i-\frac{1}{2}}$ are

$$u^{(1)}_{i-\frac{1}{2}} = \frac{1}{6}\big(-\bar{u}_{i-2} + 5\bar{u}_{i-1} + 2\bar{u}_i\big), \tag{3.21}$$

$$u^{(2)}_{i-\frac{1}{2}} = \frac{1}{6}\big(2\bar{u}_{i-1} + 5\bar{u}_i - \bar{u}_{i+1}\big), \tag{3.22}$$

$$u^{(3)}_{i-\frac{1}{2}} = \frac{1}{6}\big(11\bar{u}_i - 7\bar{u}_{i+1} + 2\bar{u}_{i+2}\big), \tag{3.23}$$

and the corresponding interpolated values for the point $x_{i+\frac{1}{2}}$ are

$$u^{(1)}_{i+\frac{1}{2}} = \frac{1}{6}\big(2\bar{u}_{i-2} - 7\bar{u}_{i-1} + 11\bar{u}_i\big), \tag{3.24}$$

$$u^{(2)}_{i+\frac{1}{2}} = \frac{1}{6}\big(-\bar{u}_{i-1} + 5\bar{u}_i + 2\bar{u}_{i+1}\big), \tag{3.25}$$

$$u^{(3)}_{i+\frac{1}{2}} = \frac{1}{6}\big(2\bar{u}_i + 5\bar{u}_{i+1} - \bar{u}_{i+2}\big). \tag{3.26}$$

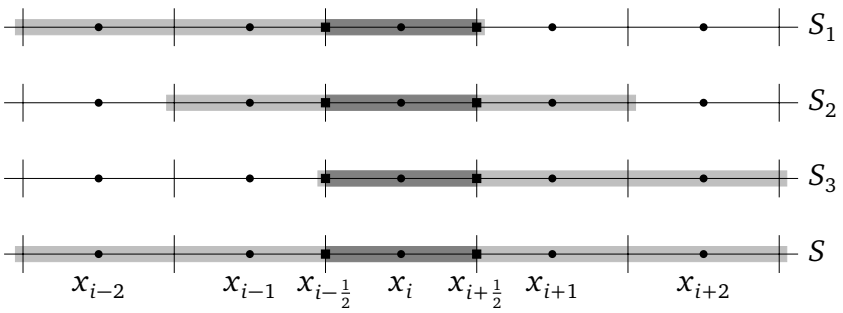

Figure 3.2: Stencils for the fifth order WENO reconstruction procedure.

In the same way as before, the corresponding interpolated values for the point $x_{i-\frac{1}{2\sqrt{3}}}$ are

$$u^{(1)}_{i-\frac{1}{2\sqrt{3}}} = \frac{1}{12}\big(-\sqrt{3}\bar{u}_{i-2} + 4\sqrt{3}\bar{u}_{i-1} + 12\bar{u}_i - 3\sqrt{3}\bar{u}_i\big), \tag{3.27}$$

$$u^{(2)}_{i-\frac{1}{2\sqrt{3}}} = \frac{1}{12}\big(\sqrt{3}\bar{u}_{i-1} + 12\bar{u}_i - \sqrt{3}\bar{u}_{i+1}\big), \tag{3.28}$$

$$u^{(3)}_{i-\frac{1}{2\sqrt{3}}} = \frac{1}{12}\big(12\bar{u}_i + 3\sqrt{3}\bar{u}_i - 4\sqrt{3}\bar{u}_{i+1} + \sqrt{3}\bar{u}_{i+2}\big), \tag{3.29}$$

and the corresponding interpolated values for the point $x_{i+\frac{1}{2\sqrt{3}}}$ are

$$u^{(1)}_{i+\frac{1}{2\sqrt{3}}} = \frac{1}{12}\big(\sqrt{3}\bar{u}_{i-2} - 4\sqrt{3}\bar{u}_{i-1} + 12\bar{u}_i + 3\sqrt{3}\bar{u}_i\big), \tag{3.30}$$

$$u^{(2)}_{i+\frac{1}{2\sqrt{3}}} = \frac{1}{12}\big(-\sqrt{3}\bar{u}_{i-1} + 12\bar{u}_i + \sqrt{3}\bar{u}_{i+1}\big), \tag{3.31}$$

$$u^{(3)}_{i+\frac{1}{2\sqrt{3}}} = \frac{1}{12}\big(12\bar{u}_i - 3\sqrt{3}\bar{u}_i + 4\sqrt{3}\bar{u}_{i+1} - \sqrt{3}\bar{u}_{i+2}\big). \tag{3.32}$$

If we choose the large stencil

$$S = \{I_{i-2}, I_{i-1}, I_i, I_{i+1}, I_{i+2}\}, \tag{3.33}$$

which is the union of all 3 stencils S_k, then we are able to find an interpolation polynomial $p(x)$ of degree at most 4, satisfying $p(x_j) = u_j$ for $i - N \le j \le i + N$ and giving the approximations $u_{i-\frac{1}{2}} \equiv p(x_{i-\frac{1}{2}})$, $u_{i+\frac{1}{2}} \equiv p(x_{i+\frac{1}{2}})$,

$$u_{i-\frac{1}{2}} = \frac{1}{60}\big(-3\bar{u}_{i-2} + 27\bar{u}_{i-1} + 47\bar{u}_i - 13\bar{u}_{i+1} + 2\bar{u}_{i+2}\big), \tag{3.34}$$

$$u_{i+\frac{1}{2}} = \frac{1}{60}\big(+2\bar{u}_{i-2} - 13\bar{u}_{i-1} + 47\bar{u}_i + 27\bar{u}_{i+1} - 3\bar{u}_{i+2}\big), \tag{3.35}$$

and the approximations $u_{i-\frac{1}{2\sqrt{3}}} \equiv p(x_{i-\frac{1}{2\sqrt{3}}})$ and $u_{i+\frac{1}{2\sqrt{3}}} \equiv p(x_{i+\frac{1}{2\sqrt{3}}})$

$$\begin{aligned} u_{i-\frac{1}{2\sqrt{3}}} = \frac{1}{4320}\big(&-70\sqrt{3}\bar{u}_{i-2} - \bar{u}_{i-2} + 500\sqrt{3}\bar{u}_{i-1} + 4\bar{u}_{i-1} + 4314\bar{u}_i \\ &- 500\sqrt{3}\bar{u}_{i+1} + 4\bar{u}_{i+1} + 70\sqrt{3}\bar{u}_{i+2} - \bar{u}_{i+2}\big), \end{aligned} \tag{3.36}$$

$$u_{i+\frac{1}{2\sqrt{3}}} = \frac{1}{4320}\big(+70\sqrt{3}\bar{u}_{i-2} - \bar{u}_{i-2} - 500\sqrt{3}\bar{u}_{i-1} + 4\bar{u}_{i-1} + 4314\bar{u}_i \\ + 500\sqrt{3}\bar{u}_{i+1} + 4\bar{u}_{i+1} - 70\sqrt{3}\bar{u}_{i+2} - \bar{u}_{i+2}\big), \tag{3.37}$$

provided that the function is smooth in the large stencil S.

3.1.4. WENO7 scheme

Let us approximate the value of the function $u(x)$ at the points $x_{i-\frac{1}{2}}$, $x_{i+\frac{1}{2}}$, $x_{i-\frac{1}{2\sqrt{3}}}$ and $x_{i+\frac{1}{2\sqrt{3}}}$ by using polynomials of degree $N = 3$. For the stencil S_k we get the corresponding values $u^{(k)}_{i-\frac{1}{2}}$, $u^{(k)}_{i+\frac{1}{2}}$, $u^{(k)}_{i-\frac{1}{2\sqrt{3}}}$ and $u^{(k)}_{i+\frac{1}{2\sqrt{3}}}$. Let us write down the stencils (See figure 3.3)

$$\begin{aligned} S_1 &= \{I_{i-3}, I_{i-2}, I_{i-1}, I_i\}, \quad S_2 = \{I_{i-2}, I_{i-1}, I_i, I_{i+1}\}, \\ S_3 &= \{I_{i-1}, I_i, I_{i+1}, I_{i+2}\}, \quad S_4 = \{I_i, I_{i+1}, I_{i+2}, I_{i+3}\}. \end{aligned} \tag{3.38}$$

The corresponding interpolated values for the point $x_{i-\frac{1}{2}}$ are

$$u^{(1)}_{i-\frac{1}{2}} = \frac{1}{12}\big(\bar{u}_{i-3} - 5\bar{u}_{i-2} + 13\bar{u}_{i-1} + 3\bar{u}_i\big), \tag{3.39}$$

$$u^{(2)}_{i-\frac{1}{2}} = \frac{1}{12}\big(-\bar{u}_{i-2} + 7\bar{u}_{i-1} + 7\bar{u}_i - \bar{u}_{i+1}\big), \tag{3.40}$$

$$u^{(3)}_{i-\frac{1}{2}} = \frac{1}{12}\big(3\bar{u}_{i-1} + 13\bar{u}_i - 5\bar{u}_{i+1} + \bar{u}_{i+2}\big), \tag{3.41}$$

$$u^{(4)}_{i-\frac{1}{2}} = \frac{1}{12}\big(25\bar{u}_i - 23\bar{u}_{i+1} + 13\bar{u}_{i+2} - 3\bar{u}_{i+3}\big), \tag{3.42}$$

and the corresponding interpolated values for the point $x_{i+\frac{1}{2}}$ are

$$u^{(1)}_{i+\frac{1}{2}} = \frac{1}{12}\big(-3\bar{u}_{i-3} + 13\bar{u}_{i-2} - 23\bar{u}_{i-1} + 25\bar{u}_i\big), \tag{3.43}$$

$$u^{(2)}_{i+\frac{1}{2}} = \frac{1}{12}\big(\bar{u}_{i-2} - 5\bar{u}_{i-1} + 13\bar{u}_i + 3\bar{u}_{i+1}\big), \tag{3.44}$$

$$u^{(3)}_{i+\frac{1}{2}} = \frac{1}{12}\big(-\bar{u}_{i-1} + 7\bar{u}_i + 7\bar{u}_{i+1} - \bar{u}_{i+2}\big), \tag{3.45}$$

$$u^{(4)}_{i+\frac{1}{2}} = \frac{1}{12}\big(3\bar{u}_i + 13\bar{u}_{i+1} - 5\bar{u}_{i+2} + \bar{u}_{i+3}\big). \tag{3.46}$$

In the same way as before, the corresponding interpolated values for the point $x_{i-\frac{1}{2\sqrt{3}}}$ are

$$u^{(1)}_{i-\frac{1}{2\sqrt{3}}} = \frac{1}{216}\big(11\sqrt{3}\bar{u}_{i-3} - 51\sqrt{3}\bar{u}_{i-2} + 105\sqrt{3}\bar{u}_{i-1} + 216\bar{u}_i - 65\sqrt{3}\bar{u}_i\big), \tag{3.47}$$

$$u^{(2)}_{i-\frac{1}{2\sqrt{3}}} = \frac{1}{216}\big(-7\sqrt{3}\bar{u}_{i-2} + 39\sqrt{3}\bar{u}_{i-1} + 216\bar{u}_i - 21\sqrt{3}\bar{u}_i - 11\sqrt{3}\bar{u}_{i+1}\big), \tag{3.48}$$

$$u^{(3)}_{i-\frac{1}{2\sqrt{3}}} = \frac{1}{216}\big(11\sqrt{3}\bar{u}_{i-1} + 216\bar{u}_i + 21\sqrt{3}\bar{u}_i - 39\sqrt{3}\bar{u}_{i+1} + 7\sqrt{3}\bar{u}_{i+2}\big), \tag{3.49}$$

$$u^{(4)}_{i-\frac{1}{2\sqrt{3}}} = \frac{1}{216}\big(216\bar{u}_i + 65\sqrt{3}\bar{u}_i - 105\sqrt{3}\bar{u}_{i+1} + 51\sqrt{3}\bar{u}_{i+2} - 11\sqrt{3}\bar{u}_{i+3}\big), \tag{3.50}$$

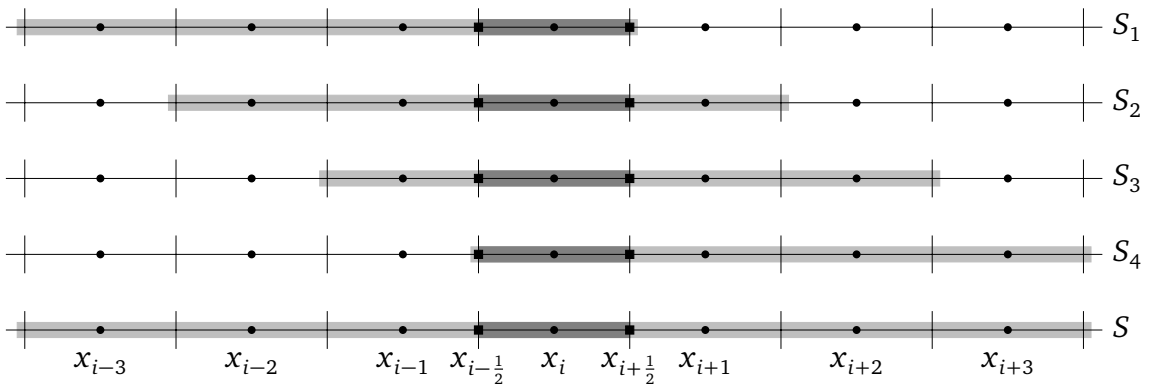

Figure 3.3: Stencils for the seventh order WENO7 reconstruction procedure.

and the corresponding interpolated values for the point $x_{i+\frac{1}{2\sqrt{3}}}$ are

$$u^{(1)}_{i+\frac{1}{2\sqrt{3}}} = \frac{1}{216}\big(-11\sqrt{3}\bar{u}_{i-3} + 51\sqrt{3}\bar{u}_{i-2} - 105\sqrt{3}\bar{u}_{i-1} + 216\bar{u}_i + 65\sqrt{3}\bar{u}_i\big), \tag{3.51}$$

$$u^{(2)}_{i+\frac{1}{2\sqrt{3}}} = \frac{1}{216}\big(7\sqrt{3}\bar{u}_{i-2} - 39\sqrt{3}\bar{u}_{i-1} + 216\bar{u}_i + 21\sqrt{3}\bar{u}_i + 11\sqrt{3}\bar{u}_{i+1}\big), \tag{3.52}$$

$$u^{(3)}_{i+\frac{1}{2\sqrt{3}}} = \frac{1}{216}\big(-11\sqrt{3}\bar{u}_{i-1} + 216\bar{u}_i - 21\sqrt{3}\bar{u}_i + 39\sqrt{3}\bar{u}_{i+1} - 7\sqrt{3}\bar{u}_{i+2}\big), \tag{3.53}$$

$$u^{(4)}_{i+\frac{1}{2\sqrt{3}}} = \frac{1}{216}\big(216\bar{u}_i - 65\sqrt{3}\bar{u}_i + 105\sqrt{3}\bar{u}_{i+1} - 51\sqrt{3}\bar{u}_{i+2} + 11\sqrt{3}\bar{u}_{i+3}\big). \tag{3.54}$$

If we choose the large stencil

$$S = \{I_{i-3}, I_{i-2}, I_{i-1}, I_i, I_{i+1}, I_{i+2}, I_{i+3}\}, \tag{3.55}$$

which is the union of all 4 stencils S_k, then we are able to find an interpolation polynomial $p(x)$ of degree at most 6, satisfying $p(x_j) = u_j$ for $i - N \le j \le i + N$ and giving the approximations $u_{i-\frac{1}{2}} \equiv p(x_{i-\frac{1}{2}})$ and $u_{i+\frac{1}{2}} \equiv p(x_{i+\frac{1}{2}})$

$$\begin{aligned} u_{i-\frac{1}{2}} = \frac{1}{420}\big(&+ 4\bar{u}_{i-3} - 38\bar{u}_{i-2} + 214\bar{u}_{i-1} + 319\bar{u}_i \\ &- 101\bar{u}_{i+1} + 25\bar{u}_{i+2} - 3\bar{u}_{i+3}\big), \end{aligned} \tag{3.56}$$

$$\begin{aligned} u_{i+\frac{1}{2}} = \frac{1}{420}\big(&- 3\bar{u}_{i-3} + 25\bar{u}_{i-2} - 101\bar{u}_{i-1} + 319\bar{u}_i \\ &+ 214\bar{u}_{i+1} - 38\bar{u}_{i+2} + 4\bar{u}_{i+3}\big), \end{aligned} \tag{3.57}$$

and the approximations $u_{i-\frac{1}{2\sqrt{3}}} \equiv p(x_{i-\frac{1}{2\sqrt{3}}})$ and $u_{i+\frac{1}{2\sqrt{3}}} \equiv p(x_{i+\frac{1}{2\sqrt{3}}})$

$$\begin{aligned} u_{i-\frac{1}{2\sqrt{3}}} = \frac{1}{1088640}\big(&+ 3717\sqrt{3}\bar{u}_{i-3} + 50\bar{u}_{i-3} - 32508\sqrt{3}\bar{u}_{i-2} - 552\bar{u}_{i-2} \\ &+ 144585\sqrt{3}\bar{u}_{i-1} + 1758\bar{u}_{i-1} + 1086128\bar{u}_i \\ &- 144585\sqrt{3}\bar{u}_{i+1} + 1758\bar{u}_{i+1} + 32508\sqrt{3}\bar{u}_{i+2} \\ &- 552\bar{u}_{i+2} - 3717\sqrt{3}\bar{u}_{i+3} + 50\bar{u}_{i+3}\big), \end{aligned} \tag{3.58}$$

Table 3.1: Linear weights for the WENO3, WENO5, and WENO7 schemes.

N	γ	$x_{i-\frac{1}{2}}$	$x_{i+\frac{1}{2}}$	$x_{i-\frac{1}{2\sqrt{3}}}$	$x_{i+\frac{1}{2\sqrt{3}}}$
1	γ_1	$\frac{2}{3}$	$\frac{1}{3}$	$\frac{1}{2}$	$\frac{1}{2}$
	γ_2	$\frac{1}{3}$	$\frac{2}{3}$	$\frac{1}{2}$	$\frac{1}{2}$
2	γ_1	$\frac{3}{10}$	$\frac{1}{10}$	$\frac{210+\sqrt{3}}{1080}$	$\frac{210-\sqrt{3}}{1080}$
	γ_2	$\frac{3}{5}$	$\frac{3}{5}$	$\frac{11}{18}$	$\frac{11}{18}$
	γ_3	$\frac{1}{10}$	$\frac{3}{10}$	$\frac{210-\sqrt{3}}{1080}$	$\frac{210+\sqrt{3}}{1080}$
3	γ_1	$\frac{4}{35}$	$\frac{1}{35}$	$\frac{11151+50\sqrt{3}}{166320}$	$\frac{11151-50\sqrt{3}}{166320}$
	γ_2	$\frac{18}{35}$	$\frac{12}{35}$	$\frac{168021+1174\sqrt{3}}{388080}$	$\frac{168021-1174\sqrt{3}}{388080}$
	γ_3	$\frac{12}{35}$	$\frac{18}{35}$	$\frac{168021-1174\sqrt{3}}{388080}$	$\frac{168021+1174\sqrt{3}}{388080}$
	γ_4	$\frac{1}{35}$	$\frac{4}{35}$	$\frac{11151-50\sqrt{3}}{166320}$	$\frac{11151+50\sqrt{3}}{166320}$

$$\begin{aligned} u_{i+\frac{1}{2\sqrt{3}}} = \frac{1}{1088640}\big(& -3717\sqrt{3}\bar{u}_{i-3} + 50\bar{u}_{i-3} + 32508\sqrt{3}\bar{u}_{i-2} - 552\bar{u}_{i-2} \\ & - 144585\sqrt{3}\bar{u}_{i-1} + 1758\bar{u}_{i-1} + 1086128\bar{u}_i \\ & + 144585\sqrt{3}\bar{u}_{i+1} + 1758\bar{u}_{i+1} - 32508\sqrt{3}\bar{u}_{i+2} \\ & - 552\bar{u}_{i+2} + 3717\sqrt{3}\bar{u}_{i+3} + 50\bar{u}_{i+3}\big), \end{aligned} \tag{3.59}$$

provided that the function is smooth in the large stencil S.

3.1.5. Linear weights

The approximations calculated by using the large stencils can be written as a *linear convex combination* of the approximations $u^{(k)}_{i+\frac{1}{2}}$ based on the small stencils S_i

$$u_{i+\frac{1}{2}} = \sum_{k=1}^{N+1} \gamma_k u^{(k)}_{i+\frac{1}{2}} \tag{3.60}$$

where the constants γ_j satisfy $\sum_{j=1}^{N+1} \gamma_j = 1$, are usually referred to as the *linear weights* in the WENO literature. We provide the linear weights for the points of interest considered before, namely, $x_{i-\frac{1}{2}}$, $x_{i+\frac{1}{2}}$, $x_{i-\frac{1}{2\sqrt{3}}}$, and $x_{i+\frac{1}{2\sqrt{3}}}$, in the table 3.1.

To find the linear weights, simply solve for γ_j in the following equation system

$$\sum_{i=1}^{N+1} \gamma_i p^{(i)}(x) = \sum_{k=i-N}^{i+N} \alpha_k u_k(x), \tag{3.61}$$

where the right hand side was determined with interpolation in the large stencil. This system is not always solvable, and for some cases, the linear weights are negative (see

Shi et al. (2002)). All this means that the WENO reconstruction procedure can only be applied for certain points in the interval $I_i = \left(x_{i-\frac{1}{2}}, x_{i+\frac{1}{2}}\right)$.

3.1.6. WENO algorithm

The WENO idea is to choose the final approximation as a convex combination of the approximations $u^{(k)}_{i+\frac{1}{2}}$

$$u_{i+\frac{1}{2}} = \sum_{k=1}^{N+1} w_k u^{(k)}_{i+\frac{1}{2}}, \tag{3.62}$$

where $w_k \geq 0$, $\sum_{k=1}^{N+1} w_k = 1$.

3.1.7. Nonlinear weights

The *nonlinear weights* w_k satisfy the following requirements

- $w_k \approx \gamma_k$ if $u(x)$ is smooth in the big stencil S;
- $w_k \approx 0$ if $u(x)$ has a discontinuity in the stencil S_k but is small in at least one of the other stencils.

It can be shown (Jiang & Shu 1996) that, as long as

$$w_k = \gamma_k + \mathcal{O}(\Delta x^N), \tag{3.63}$$

the WENO interpolation $u_{i+\frac{1}{2}}$ is $(2N+1)$th order accurate,

$$u_{i+\frac{1}{2}} - u(x_{i+\frac{1}{2}}) = \mathcal{O}(\Delta x^{2N+1}), \tag{3.64}$$

when the function $u(x)$ is smooth in the large stencil S. The second requirement above would guarantee a non-oscillatory, at least Nth order accurate WENO approximation $u_{i+\frac{1}{2}}$, since the contribution from any stencil containing the discontinuity of $u(x)$ has an essentially zero weight.

The choice of the nonlinear weights w_k relies on the *smoothness indicator* β_k, which measures the relative smoothness of the function $u(x)$ in the stencil S_k. The larger this smoothness indicator β_k, the less smooth the function $u(x)$ is in the stencil S_k. In the most of the WENO papers, the smoothness indicator is chosen as in Jiang & Shu (1996)

$$\beta_k = \sum_{l=1}^{N} \Delta x^{2l-1} \int_{x_{i-\frac{1}{2}}}^{x_{i+\frac{1}{2}}} \left(\frac{\mathrm{d}^l}{\mathrm{d}x^l} p_k(x)\right)^2 \mathrm{d}x, \tag{3.65}$$

where N is the polynomial degree of $p_k(x)$ (in our examples, $N = 1, 2, 3$). This is clearly just a scaled sum of the square L^2 norms of all the derivatives of the relevant interpolation

polynomial $p_k(x)$ in the relevant interval $[x_{i-\frac{1}{2}}, x_{i+\frac{1}{2}}]$, where the interpolating point is located. The scaling factor Δx^{2l-1} is to make sure that the final explicit formulae for the smoothness indicators do not depend on the mesh size Δx. Let us write the smoothness indicators for polynomials of degree $N = 1$

$$\beta_1 = (\bar{u}_{i-1} - \bar{u}_i)^2, \tag{3.66}$$
$$\beta_2 = (\bar{u}_i - \bar{u}_{i+1})^2, \tag{3.67}$$

and for polynomials of degree $N = 2$ we get

$$\beta_1 = \frac{1}{3}\left(4\bar{u}_{i-2}^2 - 19\bar{u}_{i-1}\bar{u}_{i-2} + 11\bar{u}_i\bar{u}_{i-2} + 25\bar{u}_{i-1}^2 + 10\bar{u}_i^2 - 31\bar{u}_{i-1}\bar{u}_i\right), \tag{3.68}$$
$$\beta_2 = \frac{1}{3}\left(4\bar{u}_{i-1}^2 - 13\bar{u}_i\bar{u}_{i-1} + 5\bar{u}_{i+1}\bar{u}_{i-1} + 13\bar{u}_i^2 + 4\bar{u}_{i+1}^2 - 13\bar{u}_i\bar{u}_{i+1}\right), \tag{3.69}$$
$$\beta_3 = \frac{1}{3}\left(10\bar{u}_i^2 - 31\bar{u}_{i+1}\bar{u}_i + 11\bar{u}_{i+2}\bar{u}_i + 25\bar{u}_{i+1}^2 + 4\bar{u}_{i+2}^2 - 19\bar{u}_{i+1}\bar{u}_{i+2}\right), \tag{3.70}$$

and for polynomials of degree $N = 3$ we get

$$\begin{aligned}\beta_1 = \frac{1}{240}\big(&+ 547\bar{u}_{i-3}^2 - 3882\bar{u}_{i-3}\bar{u}_{i-2} + 4642\bar{u}_{i-3}\bar{u}_{i-1} - 1854\bar{u}_{i-3}\bar{u}_i \\ &+ 7043\bar{u}_{i-2}^2 - 17246\bar{u}_{i-2}\bar{u}_{i-1} + 7042\bar{u}_{i-2}\bar{u}_i + 11003\bar{u}_{i-1}^2 \\ &- 9402\bar{u}_{i-1}\bar{u}_i + 2107\bar{u}_i^2\big),\end{aligned} \tag{3.71}$$
$$\begin{aligned}\beta_2 = \frac{1}{240}\big(&+ 267\bar{u}_{i-2}^2 - 1642\bar{u}_{i-2}\bar{u}_{i-1} + 1602\bar{u}_{i-2}\bar{u}_i - 494\bar{u}_{i-2}\bar{u}_{i+1} \\ &+ 2843\bar{u}_{i-1}^2 - 5966\bar{u}_{i-1}\bar{u}_i + 1922\bar{u}_{i-1}\bar{u}_{i+1} + 3443\bar{u}_i^2 \\ &- 2522\bar{u}_i\bar{u}_{i+1} + 547\bar{u}_{i+1}^2\big),\end{aligned} \tag{3.72}$$
$$\begin{aligned}\beta_3 = \frac{1}{240}\big(&+ 547\bar{u}_{i-1}^2 - 2522\bar{u}_{i-1}\bar{u}_i + 1922\bar{u}_{i-1}\bar{u}_{i+1} - 494\bar{u}_{i-1}\bar{u}_{i+2} \\ &+ 3443\bar{u}_i^2 - 5966\bar{u}_i\bar{u}_{i+1} + 1602\bar{u}_i\bar{u}_{i+2} + 2843\bar{u}_{i+1}^2 \\ &- 1642\bar{u}_{i+1}\bar{u}_{i+2} + 267\bar{u}_{i+2}^2\big),\end{aligned} \tag{3.73}$$
$$\begin{aligned}\beta_4 = \frac{1}{240}\big(&+ 2107\bar{u}_i^2 - 9402\bar{u}_i\bar{u}_{i+1} + 7042\bar{u}_i\bar{u}_{i+2} - 1854\bar{u}_i\bar{u}_{i+3} \\ &+ 11003\bar{u}_{i+1}^2 - 17246\bar{u}_{i+1}\bar{u}_{i+2} + 4642\bar{u}_{i+1}\bar{u}_{i+3} + 7043\bar{u}_{i+2}^2 \\ &- 3882\bar{u}_{i+2}\bar{u}_{i+3} + 547\bar{u}_{i+3}^2\big).\end{aligned} \tag{3.74}$$

Notice that these smoothness indicators are quadratic functions of the values of $u(x)$ in the relevant stencils. Equipped with these smoothness indicators, we can now define the nonlinear weights as

$$w_k = \frac{\tilde{w}_k}{\sum_{i=1}^N \tilde{w}_i}, \quad \text{with} \quad \tilde{w}_k = \frac{\gamma_k}{(\varepsilon + \beta_k)^2}. \tag{3.75}$$

Here ε is a small positive number used to avoid the denominator becoming zero and is typically chosen to be $\varepsilon = 10^{-6}$, but in our calculations we have used $\varepsilon = 10^{-24}$.

3.2. Shock Capturing for High-Order Methods

Before we discuss the shock-capturing strategies for the high-order methods used in this work, we would like to quote an extract of the paper on high-order numerical methods for computational fluid dynamics written by Wang (2007)

> *"Any shock-capturing method will degrade to first-order accuracy locally near a discontinuity because the error in the location of the shock is proportional to the mesh size (Harten et al. 1987). Methods which offer natural subcell resolution can make the error smaller, but cannot change the order. This argument suggests h-refinement near shock waves, coupling with a piece-wise constant reconstruction, which is the robust, first-order Godunov method, with p-refinement elsewhere. How a locally first-order scheme affects the solution elsewhere needs to be investigated, especially for unsteady flow problems."*

The approach stated in this text has been followed for many high-order methods-based codes when problems with shocks are taken into account. The way this strategy is implemented establishes different "flavors" of the shock capturing, but in principle, the ground idea is the shock detection and a further order reduction of the scheme in the vicinity of the shock, the so called *fallback approaches* (Mignone et al. 2007; Tchekhovskoy et al. 2007; Beckwith & Stone 2011; Radice & Rezzolla 2011; Radice & Rezzolla 2012). In the following we present and explain the methodology that we have employed to achieve the main goal of this work: *by using high-order numerical methods, perform simulations of flow problems containing strong shocks within the context of computational astrophysics in flat spacetimes*.

For all three methods subject of our research, namely, the Finite Difference, the Finite Volume and the Discontinuous Galerkin method, it is common that some unphysical states are produced in the intermediate stages of the simulation (e.g., during the reconstruction step, or the conservative to primitive variables conversion), especially when the flow involves shocks waves or strong rarefactions, and very high-order are used (reconstruction/interpolation order larger than second order). These unphysical states come from the loss of positivity of the density or the pressure, or the generation of super-luminal speeds. A general methodology to overcome this issue for very high-order methods consists basically in the three blocks outlined in the table 3.2.

3.2.1. Strategy for Finite Difference and Finite Volume Methods

The two methods of interest in this section are the finite difference and the finite volume method. In spite of their differences, they share the same procedure to achieve high-order accuracy: *The data reconstruction*. As it was explained in the section 2.3, in the one-dimensional case, for the finite difference method, reconstruction polynomials of the fluxes at points $x = x_{i\pm\frac{1}{2}}$ are built from the cell averages of the fluxes at points $x = x_i$,

Table 3.2: Shock capturing strategy for the higher-order finite difference, finite volume and discontinuous Galerkin methods discussed in this work (Mignone et al. 2007; Tchekhovskoy et al. 2007; Beckwith & Stone 2011; Radice & Rezzolla 2011; Radice & Rezzolla 2012).

Checking of physical quantities with restrictions	Positivity of density
	Positivity of pressure
	Maximum propagation speed (only in the relativistic case)
Detection of regions with strong shocks	Shocks indicators
	Oscillations indicators
	Marking of troubled points/cells and direct neighbors
Special treatment in troubled regions	Employment of robust Riemann solvers
	Employment of robust first-order Godunov scheme
	Employment of robust second/third order numerical scheme

and reconstruction polynomials at cell interfaces $x = x_{i\pm\frac{1}{2}}$ are constructed from the cell averages $\bar{u}_i$ in the finite volume method. This *reconstruction* is accomplished with the WENO reconstruction scheme (Jiang & Shu 1996; Shu 2009).

There are some cases in which the high-order WENO reconstruction fails when it is performed, that is, negative densities or pressure are obtained after the reconstruction step. This occurs especially in regions with severe shocks or when in the stencil several discontinuities are present. In such cases, the WENO algorithm cannot select an oscillation-free polynomial from all stencils. For that reason, we have to adopt the reconstruction-order-reduction strategy in those stencils containing more than one discontinuity or having a strong shock. That is, we first apply a shock indicator to every point/cell and then mark only those having a shock and their direct neighbors. For this purpose, we use the Jameson indicator in the pressure (Jameson et al. 1981)

$$\eta_i = \frac{\left|p_{i+1} - 2p_i + p_{i-1}\right|}{\left|p_{i+1}\right| + 2\left|p_i\right| + \left|p_{i-1}\right|}. \tag{3.76}$$

Next, in the marked cells we use a WENO3 reconstruction (or in severe cases, we switch to the second order MUSCL reconstruction). If these schemes fail to give a physical state, then we switch to the first-order Godunov scheme, where no reconstruction is performed. We remark that the use of the above strategy will never deteriorate the high order of accuracy of the method for smooth solutions, and the reason is that the indicator only flags the cell with discontinuities. We refer to the classical work of Harten et al. (1987) for more details.

We have to point out that this approach has provided very good results for a wide series of problems in one-dimensional and multidimensional Magnetohydrodynamics, Relativistic Hydrodynamics and Relativistic Magnetohydrodynamics. In fact, all calculations presented in this work have made use of WENO3 reconstruction in troubled points/cells

and higher-order WENO schemes in smooth parts of the flow. Only for two extreme cases we had to use the MUSCL scheme, and it was for two problems in Relativistic Magnetohydrodynamics. It is very important to mention that these equations are really complicated from the numerical point of view, and that the failure is mainly observed in the no convergence of the Newton iterative method in the Conservative-To-Primitive variables conversion.

3.2.2. Strategy for Discontinuous Galerkin Methods

Because discontinuous solutions form part of the nature of the hyperbolic conservation laws, shock capturing strategies have to be devised, especially for the discontinuous Galerkin method. For the DGSEM, several shock capturing schemes were considered, like the moment limiter (Biswas et al. 1994; Krivodonova 2007), the artificial viscosity (Persson & Peraire 2006; Casoni et al. 2012; Casoni et al. 2013), the WENO limiter (Shu & Osher 1988; Harten et al. 1987; Qiu & Shu 2005b; Qiu & Shu 2005a; Zhu et al. 2008; Zhong & Shu 2013; Qiu & Shu 2005a; Zhong & Shu 2013; Zhu et al. 2013), and a hybrid DGSEM/FV approach (Touil et al. 2007; Radice & Rezzolla 2011; Sonntag & Munz 2014). For robustness and efficiency reasons, only the latter is used as the main building block for the nonlinear stabilization of the solution when shocks take place. The hybrid DGSEM/FV is constructed in such a way that, in regions of smooth flows, the DGSEM method is employed, and those parts of the flow having shocks, the DGSEM elements are interpreted as quadrilateral/hexahedral subdomains. In each of these subdomains, the nodal DG solution values are used to build a new local domain composed now of finite volume subcells, which are evolved with a robust finite volume method with third order WENO reconstruction. In the following we will discuss with more detail the hybrid DGSEM/FV algorithm.

Hybrid DG/FV Shock Capturing

The hybrid DG/FV shock capturing method used in this works consists in basically in two steps: The first step is detecting the elements in the DG computational domain that contain oscillating polynomials, which cause instabilities in the computation and make the code to blow up. The second step is replacing the troubled elements with subdomains made of $(N+1)^d$ finite volume subcells each, with d the space dimension. Then the subdomains are evolved with a robust finite volume method which uses a second or third order reconstruction operator, typically MUSCL (second order) or WENO3 (third order).

Let us represent the solution in the DG element E_i at time level t^n by $\boldsymbol{u}_i^n$. In the context of DGSEM schemes, the element E_i has $(N+1)^d$ degrees of freedom. The DG solution is computed in the $(N+1)^d$ quadrature points. The element E_i is then decomposed into $(N+1)^d$ equidistant FV subcells, see figure 3.4. While in the DG element E_i the solution is represented by a polynomial, in the FV subdomain the solution at time level t^n is represented by piecewise constant subcell averages $\boldsymbol{\nu}_i^n$. These values are obtained

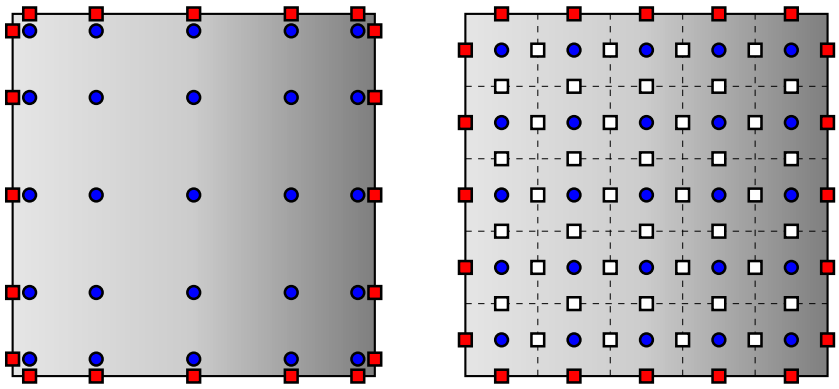

Figure 3.4: Hybrid DG/FV. DG element with $(N+1)^2$ inner nodal points (the blue filled circles) where the solution is computed, and which is approximated by a tensor-product of Lagrange polynomials of degree N (left). Corresponding FV subdomain made of $(N+1)^2$ equidistant subcells (right), with the barycenter of every subcell shown (the blue filled circles), and the points where the numerical fluxes are computed with the finite volume scheme (the white filled squares), and the borders of the subcells (dashed lines).

from the DG polynomial itself by using L_2 projection, that is $\boldsymbol{v}_i^n = \widehat{\mathbf{P}}_{\mathrm{FV}}\left(\boldsymbol{u}_i^n\right)$. Each of these piecewise constant subcell averages $\boldsymbol{v}_{ij}^n$ associated with the subcell $E_{i,j}$ are

$$\boldsymbol{v}_{i,j}^n = \frac{1}{\left|E_{i,j}\right|}\int_{E_{i,j}} \boldsymbol{u}_i^n(\boldsymbol{x}, t^n)\,\mathrm{d}\boldsymbol{x}. \tag{3.77}$$

Summarizing, given the DG state $\boldsymbol{u}_i^n$ at time level n, the oscillation indicator operator $\widehat{\mathbf{OI}}$ is applied to $\boldsymbol{u}_i^n$, $\forall i$, and only the troubled elements are flagged for shock capturing. For those not flagged elements, the state $\boldsymbol{u}^n$ is evolved with the DG solver operator $\widehat{\mathbf{DG}}$, but if the element is marked as a troubled cell, then we use the operator $\widehat{\mathbf{P}}_{\mathrm{FV}}$ to project the state $\boldsymbol{u}^n$ onto a FV subcells subdomain of piecewise cell averages, yielding $\boldsymbol{v}^n$; then we evolve the states $\boldsymbol{v}^n$ in the FV subdomain with the FV solver operator $\widehat{\mathbf{FV}}$, to get $\boldsymbol{v}^{n+1}$. The solution $\boldsymbol{v}^{n+1}$ is then projected back onto the DG element with the projection operator $\widehat{\mathbf{P}}_{\mathrm{DG}} = \widehat{\mathbf{P}}_{\mathrm{FV}}^{-1}$. In the figure 3.5 is depicted a flow diagram of the algorithm for the hybrid DG/FV shock capturing scheme. Since the stencil of the reconstruction operator used in the FV subdomain needs at least two neighboring cell data (one left and one right to the subcell of interest), those subcells at edges of the FV subdomain require boundary values, which are obtained from the neighboring elements (see figure 3.6).

Oscillation Indicators

In our *a priori* shock capturing strategy for discontinuous Galerkin methods, the first step consists in determining which elements contain oscillating polynomials, that is, those elements where shock waves or discontinuities are producing these kind of behavior in the approximating polynomials. The oscillation indicator is applied to every element at

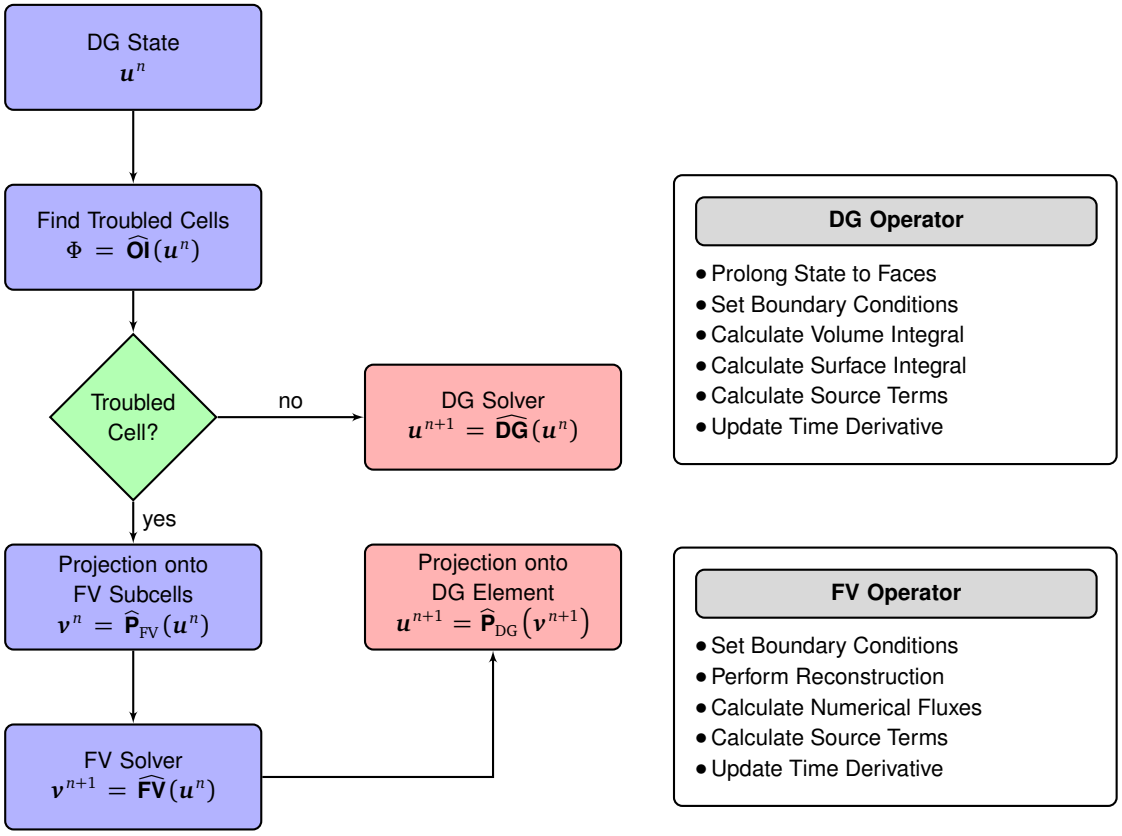

Figure 3.5: Flow diagram of the hybrid DG/FV. The DG state $\boldsymbol{u}^n$ at time level n. The oscillation indicator operator $\widehat{\mathbf{OI}}$ is applied to $\boldsymbol{u}^n$. The troubled elements are flagged. If the element is not flagged, then evolve the state $\boldsymbol{u}^n$ with the DG solver operator $\widehat{\mathbf{DG}}$, but if the element is marked as a troubled cell, then use the operator $\widehat{\mathbf{P}}_{\mathrm{FV}}$ to project the state $\boldsymbol{u}^n$ onto a FV subcells subdomain, yielding $\boldsymbol{v}^n$; then evolve the states $\boldsymbol{v}^n$ in the FV subdomain with the FV solver operator $\widehat{\mathbf{FV}}$, to get $\boldsymbol{v}^{n+1}$. The solution $\boldsymbol{v}^{n+1}$ is then projected back onto the DG element with the operator $\widehat{\mathbf{P}}_{\mathrm{DG}}$.

each stage of the explicit Runge-Kutta time discretization. Once the troubled element is flagged, the next step is to apply the hybrid DG/FV approach, where the DG element is used to build a new block made of finite volume subcells, and which is evolved using a robust second/third order finite volume scheme. In this work we use mainly two oscillation indicators: The Jameson indicator and the Persson indicator.

Jameson Indicator

The Jameson indicator was introduced by Jameson et al. (1981) within the context of finite volume methods, but has been used also in the finite difference community. The indicator is constructed from the approximation of a second order derivative in the pressure

$$\eta_i(p) = \frac{|p_{\min} - 2p_i + p_{\max}|}{|p_{\min} + 2p_i + p_{\max}|}. \tag{3.78}$$

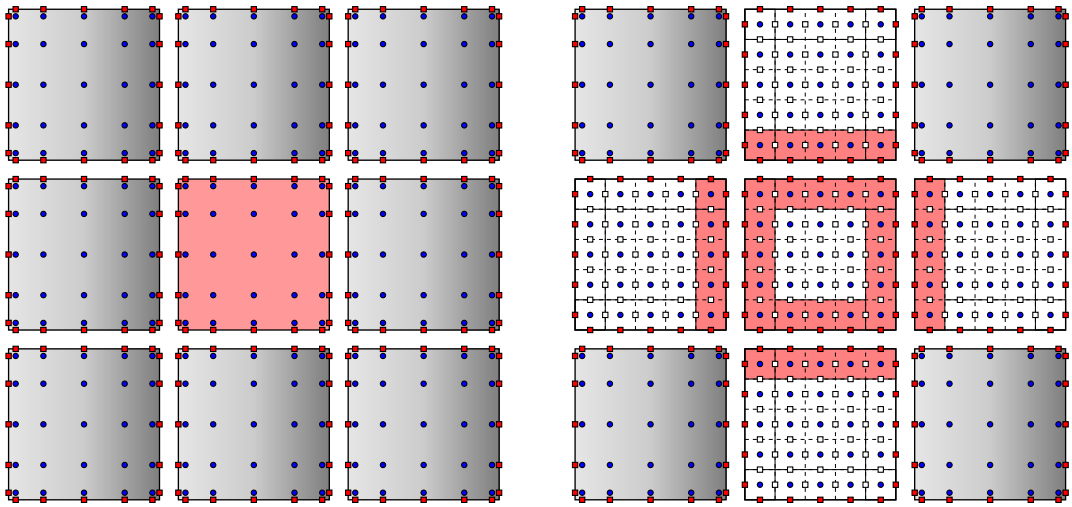

Figure 3.6: Hybrid DG/FV. Flagged element surrounded by DG elements (left). The DG polynomial in the troubled cell is then projected onto a FV subdomain made of $(N+1)^2$ subcells. For those subcells lying at the FV subdomain edges, neighboring elements are also projected onto a FV subdomain in order to use the cell averages at edges for computing the reconstructed values at subcell interfaces (right).

Here $p_{\min}$ and $p_{\max}$ are the minimum and maximum mean values of the pressure of all neighboring cells. Because of that, the Jameson indicator is not local like the Persson indicator.

Persson Indicator

The Persson indicator was developed by Persson & Peraire (2006), and it measures cell-wise the maximum energy decay in the highest and second highest degrees of freedom of the DG polynomial for the state variable u:

$$\eta(u) = \log_{10}\left\{ \max\left[\left(\frac{\sum_{j=N_{\mathrm{DOF}}(N-1)+1}^{N_{\mathrm{DOF}}(N)} \left(\hat{u}_j\right)^2}{\sum_{j=1}^{N_{\mathrm{DOF}}(N)} \left(\hat{u}_j\right)^2} \right), \left(\frac{\sum_{j=N_{\mathrm{DOF}}(N-2)+1}^{N_{\mathrm{DOF}}(N-1)} \left(\hat{u}_j\right)^2}{\sum_{j=1}^{N_{\mathrm{DOF}}(N-1)} \left(\hat{u}_j\right)^2} \right) \right] \right\}, \tag{3.79}$$

where $N_{\mathrm{DOF}}(N)$ denotes the number of degrees of freedom for a DG polynomial of degree N and $\hat{u}_j$ the j^{th} degree of freedom of the polynomial representation of u. Observe that this indicator takes into account the influence of odd/even order effects in the DG polynomial. The typical variable used by the Persson indicator in order to determine if a cell suffers of spurious oscillations is the pressure, since shock waves imply a jump in the pressure and not in the density. With this is distinguished shock waves and contact discontinuities.

3.3. Divergence Cleaning

In the underlying base numerical scheme, the constraint $\nabla \cdot \boldsymbol{B} = 0$ is not satisfied. In fact, due to the nonlinearities of the numerical discretization, errors in $\nabla \cdot \boldsymbol{B}$ are produced, which may grow with time, and may lead also to unphysical results (Brackbill & Barnes 1980; Powell 1994). For this reason, every MHD solver has to take into account a procedure to keep $\nabla \cdot \boldsymbol{B} = 0$.

There are basically two approaches to overcome this problem: The *divergence cleaning* and the *constrained transport* algorithms. In the divergence cleaning approach, numerical errors in $\nabla \cdot \boldsymbol{B}$ are removed. The most popular schemes of this class are the *Hodge projection* (Chorin 1967; Brackbill & Barnes 1980), the *8-wave formulation* (Powell 1994), and the *generalized Lagrange multiplier* (GLM) approach (Dedner et al. 2002).

In the **Hodge projection**, the main idea is to correct the $\boldsymbol{B}^*$ computed by a scheme with $\nabla \cdot \boldsymbol{B}^* \neq 0$, by projecting it on a subspace of zero divergence solutions. Therefore, $\boldsymbol{B}^*$ is modified by subtracting the gradient of a scalar field ϕ, to be computed from the Poisson equation

$$\nabla^2 \phi = \nabla \cdot \boldsymbol{B}^*. \tag{3.80}$$

From this, we see that the new magnetic field $\boldsymbol{B} = \boldsymbol{B}^* - \nabla\phi$ is solenoidal. In spite of maintaining the solenoidal constraint up to machine accuracy, this scheme requires a time consuming solution of a Poisson equation at each time step.

In the **8-wave formulation**, an additional non-physical wave is introduced into the MHD system, giving as result the appearance of source terms proportional to the divergence of the magnetic field

$$-\nabla \cdot \boldsymbol{B} \begin{pmatrix} 0 \\ \boldsymbol{B} \\ \boldsymbol{v} \cdot \boldsymbol{B} \\ \boldsymbol{v} \end{pmatrix}. \tag{3.81}$$

The resulting modified set of equations restores Galilean invariance. Because the method does not obey the strict conservation form of the equations, it can potentially introduce incorrect jumps across discontinuities.

In the **generalized Lagrange multiplier** approach, a new scalar field ψ is introduced. This variable couples the divergence constraint with the evolution equation of the magnetic field. Local divergence errors are propagated to the boundary of the computational domain by a wave equation. This approach is very simple and its implementation is straightforward, and at the same time, conservation of all physical variables is maintained.

From the other side, **constrained transport** algorithms exactly preserve the divergence constraint of the magnetic field, but with the price of introducing a staggered mesh (Evans & Hawley 1988). A requirement for this scheme is that the initial magnetic

field must be divergence-free, and the boundary conditions are set according to this. In the original idea of the constrained transport algorithms, the thermodynamic variables are defined at cell center, the components of the magnetic field at the cell interfaces, and the electric field vectors at cell vertices. After the magnetic field is updated by using the Stokes law, the solenoidal restriction of the magnetic field is maintained.

In this work we consider the GLM approach for controlling the solenoidal constraint of the magnetic field. In our algorithm we use the mixed hyperbolic/parabolic divergence cleaning as it is reported in Mignone et al. (2010).

3.3.1. Divergence Cleaning with the Generalized Lagrange Multiplier Method

The divergence-free constraint of the magnetic field has to be preserved also from the numerical point of view. The simplest and straightforward manner to do it is by means of the divergence cleaning of Munz et al. (1999) and Dedner et al. (2002). In this work we use the mixed hyperbolic/parabolic strategy first proposed in (Dedner et al. 2002). In this approach, the solenoidal constraint is coupled with the induction equation

$$\frac{\partial \boldsymbol{B}}{\partial t} + \nabla \cdot \left(\boldsymbol{B} \otimes \boldsymbol{v} - \boldsymbol{v} \otimes \boldsymbol{B} \right) = \boldsymbol{0}, \tag{3.82}$$

through the potential ψ. The induction equation and the solenoidal constraint take the following form

$$\frac{\partial \boldsymbol{B}}{\partial t} + \nabla \cdot \left(\boldsymbol{B} \otimes \boldsymbol{v} - \boldsymbol{v} \otimes \boldsymbol{B} + \psi \mathbb{I} \right) = \boldsymbol{0}, \tag{3.83a}$$

$$\frac{\partial \psi}{\partial t} + \nabla \cdot \left(c_h^2 \boldsymbol{B} \right) = -\frac{c_h^2}{c_p^2} \psi. \tag{3.83b}$$

3.3.2. Discretization of the GLM Divergence Cleaning

The equations for B_x and ψ are decoupled from the rest of the GLM-MHD system (see section 4.2.1 for further details). In fact, cleaning a vector quantity $\boldsymbol{B}$ with divergence errors results in the linear system

$$\frac{\partial}{\partial t} \begin{pmatrix} B_x \\ \psi \end{pmatrix} + \begin{pmatrix} 0 & 1 \\ c_h^2 & 0 \end{pmatrix} \frac{\partial}{\partial x} \begin{pmatrix} B_x \\ \psi \end{pmatrix} = \begin{pmatrix} 0 \\ -\frac{c_h^2}{c_p^2} \psi \end{pmatrix}. \tag{3.84}$$

The numerical flux is then derived as the solution of the local Riemann problem with left-hand state $(B_{x,l}, \psi_l)^T$ and right hand state $(B_{x,r}, \psi_r)^T$ as

$$B_{x,m} = \frac{1}{2}(B_{x,r} + B_{x,l}) - \frac{1}{2c_h}(\psi_r - \psi_l), \tag{3.85}$$

$$\psi_m = \frac{1}{2}(\psi_r + \psi_l) - \frac{c_h}{2}(B_{x,r} - B_{x,l}). \tag{3.86}$$

It is possible to employ for the quantities B_x and ψ the Riemann solver used in the full MHD system, but in this work we use the exact solution (3.85) of the linear Riemann problem (3.84). Dedner et al. (2002) suggest to use the solution (3.85) as input for the Riemann solver used in the solution of the other conserved quantities.

There are basically two possible ways to deal with the source term in equation (3.83b). The first one consists in simple add this source term to the hyperbolic update, that is to the semi-discrete scheme (2.11) (see Susanto et al. (2013)). The second one is based on an operator-splitting approach. Following the idea presented in Dedner et al. (2002), we first solve the homogeneous GLM-MHD system in a so-called *hyperbolic step*, and then we consider the source term in the *source step*. The scalar field ψ is then

$$\psi^{(\Delta t)} = \psi^{(0)} \exp\left(-\alpha_p \frac{c_h}{\Delta h/\Delta t}\right), \quad \text{with } \alpha_p = \Delta h \frac{c_h}{c_p^2}, \tag{3.87}$$

where $\psi^{(0)}$ has been computed in the hyperbolic step, and $\Delta h = \min(\Delta x, \Delta y, \Delta z)$ is the minimum mesh size. This approach is very simple to implement and is unconditionally stable (Dedner et al. 2002).

CHAPTER 4

Magnetohydrodynamics

In this chapter we report the numerical results obtained after solving the magnetohydrodynamics equations with higher-order numerical methods. We start by presenting the equations of the ideal magnetohydrodynamics, and their extension for dealing with the solenoidal constraint, the so-called GLM-MHD system. The eigenstructure of the GLM-MHD is also discussed. After this brief introduction of the governing equations, we proceed with a detailed discussion of the numerical benchmarking for the MHD equations: One- and two-dimensional shock-dominated test problems are solved with the finite difference, the finite volume and the discontinuous Galerkin spectral element methods.

4.1. Introduction

A plasma is a completely or partially ionized gas, consisting of electrons, ions, and neutral particles. Astrophysicists agree that more than the 95 % of the visible matter in the Universe is in plasma state. Depending on the kind of phenomenon we are interested in, there are basically three theoretical models for describing plasma processes, namely the *single particle motion under electromagnetic fields*, the *kinetic theory of plasmas* and the *fluid description of plasmas* (Goedbloed & Poedts 2004). It is in our interest to consider only the macroscopic dynamics of plasmas, where the appropriate scheme is the fluid approach of plasmas, also known as magnetohydrodynamics.

Magnetohydrodynamics model the physical phenomena involving electrically conducting fluid flow in which the electromagnetic forces can be of the same order or even greater than hydrodynamic ones. Contrasted with the kinetic theory of plasmas, in magnetohydrodynamics it is assumed that the electrons and ions are subject to frequent collisions, and therefore collisional relaxation times are shorter than the time scale on which the hydrodynamic description is applicable. In the special case of the ideal magnetohydrodynamics, it is also assumed that the resistivity due to these collisions is small. In fact, the plasma dynamics is considered on time scales shorter than the magnetic diffusion time scale. Another assumption in the fluid description of plasmas is that the length scales are much larger than the cyclotron radius of the charged particles, and time scales longer than the cyclotron frequencies. On these scales, the plasma behaves as a single fluid without distinguishing its individual species (electrons and ions) (Goedbloed

& Poedts 2004). The fundamental notions behind magnetohydrodynamics were introduced by the Swedish physicist Hannes Alfvén, for which he received the Nobel Prize in Physics in 1970. Alfvén made many contributions to plasma physics, playing a central role in the development of theories for describing the behavior of charged particle beams, physics of the terrestrial magnetosphere, and the interplanetary medium.

Computational magnetohydrodynamics has been intensively developed in the last 30 years. From the beginning, emphasis has been put in problems with shocks, because they are present in many astrophysical plasma phenomena of interest, as for example, astrophysical jets, accretion flows, supernovae explosions, etc. Second order numerical methods have been the standard in most of the astrophysical codes. In fact, conservative finite difference and finite volume method with high-resolution shock-capturing properties are the preferred methods for building robust and reliable astrophysical numerical laboratories. For instance, in the works of Ryu & Jones (1995b), Ryu & Jones (1995a), and Ryu et al. (1998), second order finite difference schemes with the TVD property have been employed. Second order finite volume methods have been also tested, as for example in Zachary & Colella (1992), Zachary et al. (1994), Dai & Woodward (1994a), Dai & Woodward (1994b), Balsara & Spicer (1999b), Tóth (2000), Janhunen (2000), Dedner et al. (2002), Ziegler (2004), and Balsara (2004).

Recently, new numerical platforms for solving the equations of the computational astrophysics has been developed, and are today very used in the astrophysical community. The PLUTO CODE by Mignone et al. (2007), the ZEUS CODE by Stone & Norman (1992a) and the ATHENA CODE by Stone et al. (2008), to cite some examples of these frameworks. These codes use the constrained transport algorithm for the numerical evolution of the components of the magnetic field for MHD simulations. In this manner, the numerically evolved field components satisfy the divergence-free constraint at all times. Besides, they make use of different reconstruction procedures, especially the PLUTO CODE, allowing in this way high-order accuracy. In Jiang & Wu (1999) and Mignone et al. (2010), a high-order finite difference method for MHD based on WENO reconstruction operators has been presented. In those work, the authors were able to achieve fifth order of accuracy on multidimensional smooth flows. Regarding another numerical techniques, Taube et al. (2007) and Dumbser et al. (2008) have also achieved also very high-order accurate solutions by using the discontinuous Galerkin method, but for problems with shocks, they reduce the polynomial degree of the interpolation, or make use of special limiters taken/adapted from finite volume methods.

4.2. Equations

Magnetohydrodynamics provides a powerful framework for describing the macroscopic behavior of plasmas, including both laboratory and space plasmas. The equations of the ideal magnetohydrodynamics, derived from the combination of Euler equations of the Hydrodynamics and the Maxwell equations of Electrodynamics, are given by the conser-

vation of mass, the conservation of momentum, the conservation of energy and induction equations:

$$\frac{\partial \rho}{\partial t} + \nabla \cdot \boldsymbol{S} = 0, \qquad \text{(Conservation of Mass)} \tag{4.1a}$$

$$\frac{\partial \boldsymbol{S}}{\partial t} + \nabla \cdot \left(\boldsymbol{S} \otimes \boldsymbol{v} + \mathbb{P}\right) = \boldsymbol{0}, \qquad \text{(Conservation of Momentum)} \tag{4.1b}$$

$$\frac{\partial E}{\partial t} + \nabla \cdot \left(E\boldsymbol{v} + \mathbb{P} \cdot \boldsymbol{v}\right) = 0, \qquad \text{(Conservation of Energy)} \tag{4.1c}$$

$$\frac{\partial \boldsymbol{B}}{\partial t} + \nabla \cdot \left(\boldsymbol{B} \otimes \boldsymbol{v} - \boldsymbol{v} \otimes \boldsymbol{B}\right) = \boldsymbol{0}, \qquad \text{(Induction Equations)} \tag{4.1d}$$

This system must satisfy an additional constraint: the solenoidal property of the magnetic field, which means that there are no magnetic monopoles (Jackson 1998)

$$\nabla \cdot \boldsymbol{B} = 0. \tag{4.2}$$

4.2.1. Magnetohydrodynamics Equations with Divergence Cleaning

Because of the solenoidal constraint of the magnetic field (4.2), a way to maintain this restriction from the numerical point of view has to be found. The simplest and straightforward manner to do it is by means of the divergence cleaning of Dedner et al. (2002). In this work we use the mixed approach explained in Dedner et al. (2002). Therefore, the equations of the magnetohydrodynamics together with the Generalized Lagrange Multiplier (GLM) method for the divergence correction are given by

$$\frac{\partial \rho}{\partial t} + \nabla \cdot \boldsymbol{S} = 0, \qquad \text{(Mass Conservation)} \tag{4.3a}$$

$$\frac{\partial \boldsymbol{S}}{\partial t} + \nabla \cdot \left(\boldsymbol{S} \otimes \boldsymbol{v} + \mathbb{P}\right) = \boldsymbol{0}, \qquad \text{(Momentum Conservation)} \tag{4.3b}$$

$$\frac{\partial E}{\partial t} + \nabla \cdot \left(E\boldsymbol{v} + \mathbb{P} \cdot \boldsymbol{v}\right) = 0, \qquad \text{(Energy Conservation)} \tag{4.3c}$$

$$\frac{\partial \boldsymbol{B}}{\partial t} + \nabla \cdot \left(\boldsymbol{B} \otimes \boldsymbol{v} - \boldsymbol{v} \otimes \boldsymbol{B} + \psi \mathbb{I}\right) = \boldsymbol{0}, \qquad \text{(Induction Equations)} \tag{4.3d}$$

$$\frac{\partial \psi}{\partial t} + \nabla \cdot \left(c_h^2 \boldsymbol{B}\right) = -\frac{c_h^2}{c_p^2}\psi. \qquad \text{(Divergence Cleaning)} \tag{4.3e}$$

The pressure tensor appearing in equations (4.3b) and (4.3c) combines the influence of the hydrodynamic and the magnetic pressure (the quantity in brackets is the total pressure)

$$\mathbb{P} = \left(p + \frac{1}{2}|\boldsymbol{B}|^2\right)\mathbb{I} - \boldsymbol{B} \otimes \boldsymbol{B}. \tag{4.4}$$

An equation of state (EOS) is used to close the system. In this work we make use of the ideal gas equation of state with adiabatic exponent γ

$$p = (\gamma - 1)\left(E - \frac{1}{2}\rho|\boldsymbol{v}|^2 - \frac{1}{2}|\boldsymbol{B}|^2\right). \tag{4.5}$$

4.2.2. Variables Transformations

The conservative variables (density ρ, momentum $\boldsymbol{S}$, total energy E and magnetic field $\boldsymbol{B}$) are related to the primitive variables (density ρ, velocity $\boldsymbol{v}$, pressure p and magnetic field $\boldsymbol{B}$) through the following equations

$$\rho = \rho \tag{4.6a}$$
$$\boldsymbol{S} = \rho \boldsymbol{v}, \tag{4.6b}$$
$$\boldsymbol{B} = \boldsymbol{B}, \tag{4.6c}$$
$$E = \frac{1}{\gamma - 1} p + \frac{1}{2}\rho \left|\boldsymbol{v}\right|^2 + \frac{1}{2}\left|\boldsymbol{B}\right|^2. \tag{4.6d}$$

Observe that these relations are rather simple! The inversion processes is quite direct and does not require an special treatment, as it occurs with the relativistic magnetohydrodynamics equations.

4.3. Spectral Decomposition

In this section we will present the spectral decomposition of the Jacobian matrices of the system, $\mathbf{A}_\alpha$, for the magnetohydrodynamics equations. These matrices are defined by

$$\mathbf{A}_i = \frac{\partial \mathbf{f}_i(\boldsymbol{u})}{\partial \boldsymbol{u}}, \quad (i = x, y, z), \tag{4.7}$$

where the state vector of conservative variables $\boldsymbol{u}$ and the components of the tensor of physical fluxes $\mathbf{f} = [\boldsymbol{f}, \boldsymbol{g}, \boldsymbol{h}]$ in the conservation law

$$\frac{\partial \boldsymbol{u}}{\partial t} + \frac{\partial \boldsymbol{f}(\boldsymbol{u})}{\partial x} + \frac{\partial \boldsymbol{g}(\boldsymbol{u})}{\partial y} + \frac{\partial \boldsymbol{h}(\boldsymbol{u})}{\partial z} = \mathbf{0}, \tag{4.8}$$

are defined as

$$\boldsymbol{u} = \begin{pmatrix} \rho \\ S_x \\ S_y \\ S_z \\ E \\ B_x \\ B_y \\ B_z \end{pmatrix}, \quad \mathbf{f}_i = \begin{pmatrix} S_i \\ S_x v_i + \mathbb{P}_{xi} \\ S_y v_i + \mathbb{P}_{yi} \\ S_z v_i + \mathbb{P}_{zi} \\ S_i \\ B_x v_i - v_x B_i \\ B_y v_i - v_y B_i \\ B_z v_i - v_z B_i \end{pmatrix}, \quad (i = x, y, z). \tag{4.9}$$

with

$$\mathbb{P}_{xi} = \left(p + \frac{1}{2}\left|\boldsymbol{B}\right|^2\right)\delta_{xi} - B_x B_i,$$
$$\mathbb{P}_{yi} = \left(p + \frac{1}{2}\left|\boldsymbol{B}\right|^2\right)\delta_{yi} - B_y B_i,$$

$$\mathbb{P}_{zi} = \left(p + \frac{1}{2}|\boldsymbol{B}|^2\right)\delta_{zi} - B_z B_i.$$

We present the spectral decomposition of the Jacobian matrices of the magnetohydrodynamics equations with an ideal gas equation of state in the x-direction, $\mathbf{A}_x$, whereas the cases y and z easily follows from symmetry. The eigenvalues of $\mathbf{A}_x$ in nondecreasing order are

$$\begin{aligned} &\lambda_1 = -c_h, && \lambda_2 = v_x - c_f, && \lambda_3 = v_x - c_a, \\ &\lambda_4 = v_x - c_s, && \lambda_5 = v_x, && \lambda_6 = v_x + c_s, \\ &\lambda_7 = v_x + c_a, && \lambda_8 = v_x + c_f, && \lambda_9 = c_h, \end{aligned} \tag{4.10}$$

where c_f, c_a, and c_s are the fast, Alfvén, and slow characteristic speeds. Observe that in the equation (4.10) there are three MHD waves families associated with the characteristic speeds and an entropy mode. The three characteristic speeds are given by

$$c_a = |b_1|, \tag{4.11}$$

$$c_s = \sqrt{\frac{1}{2}\left(a^2 + b^2 - \sqrt{(a^2+b^2)^2 - 4a^2 b_1^2}\right)}, \tag{4.12}$$

$$c_f = \sqrt{\frac{1}{2}\left(a^2 + b^2 + \sqrt{(a^2+b^2)^2 - 4a^2 b_1^2}\right)}, \tag{4.13}$$

where we have used the abbreviations

$$a^2 = \frac{\gamma p}{\rho}, \quad b^2 = \frac{|\boldsymbol{B}|^2}{\rho}, \quad b_1^2 = \frac{B_x^2}{\rho}. \tag{4.14}$$

Observe the two new eigenvalues from the GLM-MHD equations, namely $\lambda_{1,9} = \pm c_h$. These eigenmodes propagate the divergence errors to the boundaries at speed c_h; besides, these divergence errors are damped at a rate c_h^2/c_p^2. The magnitude of the wave speeds c_h is set to the maximum allowed speed in the pure MHD system and that is compatible with the CFL restriction in an explicit time discretization,

$$c_h = \max_i\big(\max\left(|\lambda_{2,i}|, |\lambda_{8,i}|\right)\big), \quad i = x, y, z. \tag{4.15}$$

The value of the constant c_p is chosen after setting $c_r \equiv c_p^2/c_h = 0.18$ (Dedner et al. 2002).

4.4. Numerical Benchmarking

4.4.1. Propagation of a smooth circular polarized Alfvén wave

This problem is characterized for being an exact nonlinear solution of the MHD equations. Because of the smoothness of this wave, it can be used for doing a convergence analysis. The test is run with the following simulation parameters (Tóth 2000). The dimensions of the computational domain satisfy $L_x = 2L_y$, and the discretization of it $N_x = 2N_y$. The

Table 4.1: Convergence rates for the MHD equations with initial condition given by the *smooth circularly polarized Alfvén wave*. The base numerical methods are the RKFD and the RKFV schemes. In these calculations we have employed the Rusanov Riemann solver. Results for L_2 norm error of the y-component of magnetic field are given, with reconstruction operator WENO3, WENO5 and WENO7. Simulation time was set to $t = 1.0$.

Reconstruction	Cells	L_2 error (FD)	L_2 order (FD)	L_2 error (FV)	L_2 order (FV)
WENO3	40×20	3.103×10^{-4}		3.218×10^{-4}	
	80×40	3.987×10^{-5}	2.960	4.120×10^{-5}	2.965
	160×80	4.828×10^{-6}	3.045	5.097×10^{-6}	3.015
	320×160	5.831×10^{-7}	3.049	6.275×10^{-7}	3.021
WENO5	40×20	1.917×10^{-6}		2.134×10^{-6}	
	80×40	6.147×10^{-8}	4.963	6.848×10^{-8}	4.961
	160×80	1.937×10^{-9}	4.987	2.158×10^{-9}	4.987
	320×160	6.073×10^{-11}	4.995	6.561×10^{-11}	5.039
WENO7	40×20	8.167×10^{-8}		8.285×10^{-8}	
	80×40	6.495×10^{-10}	6.974	7.984×10^{-10}	6.697
	160×80	5.121×10^{-12}	6.986	7.543×10^{-12}	6.725
	320×160	3.860×10^{-14}	7.051	6.308×10^{-14}	6.901

wave propagates along the diagonal of the grid, at an angle $\alpha = \arctan(0.5) \approx 26.6°$ with respect to the x-axis. Since the wave does not propagate along the diagonals of the grid cells, we guarantee the x- and y-fluxes are different; that is the problem is truly multi-dimensional. Following the description to this problem given by Tóth (2000), we set the density to $\rho = 1$, the pressure $p = 0.1$. Let be $v_0 = 0.1$ and $B_0 = 0.1$. Additionally let be $x_\parallel = (x\cos\alpha + y\sin\alpha)$, where α is the angle at which the wave propagates with respect to the grid. The components of velocity and magnetic field perpendicular to the wave vector are given by $v_\perp = v_0 \sin(2\pi x_\parallel)$ and $B_\perp = B_0 \sin(2\pi x_\parallel)$, and the velocity and magnetic field in z-direction are $v_z = v_0 \cos(2\pi x_\parallel)$ and $B_z = B_0 \cos(2\pi x_\parallel)$. The quantities $v_\perp$ and $B_\perp$ are related to B_x and B_y via $B_\perp = B_y \cos\alpha - B_x \sin\alpha$, and $B_\parallel = B_x \cos\alpha + B_y \sin\alpha$. An adiabatic equation of state with $\gamma = 5/3$ is considered. At the boundaries of the domain we consider periodic boundary conditions. The simulation time is $t = 1.0$. In the table 4.1 are shown the convergence rates when the MHD were solved with the RKFD and RKFV methods. In the table 4.2 are shown the convergence rates for the case when the MHD are solved with the RKDG scheme. All numerical methods (RKFD, RKFV, and RKDG) converge to the theoretical order of convergence. Observe that for the RKDG method only a few cells were enough to obtain the experimental order of convergence.

Table 4.2: Convergence rates for the MHD equations with initial condition given by the *smooth circular polarized Alfvén wave*. In these calculations we have employed the Rusanov Riemann solver. Results for L_2 norm error of the x-component of magnetic field are given, with polynomial degree $N = 1, 3, 5$, that is, for order of accuracy $\mathcal{O}(2)$, $\mathcal{O}(4)$ and $\mathcal{O}(6)$. Simulation time was set to $t = 1.0$.

Method	Elements	L_2 error	L_2 order
DGSEM $\mathcal{P}1$	4×4	1.09×10^{-1}	
	8×8	1.63×10^{-2}	2.75
	16×16	3.18×10^{-3}	2.35
	32×32	7.38×10^{-4}	2.11
DGSEM $\mathcal{P}3$	4×4	1.40×10^{-3}	
	8×8	6.04×10^{-5}	4.53
	16×16	3.58×10^{-6}	4.07
	32×32	2.22×10^{-7}	4.01
DGSEM $\mathcal{P}5$	2×2	6.62×10^{-4}	
	4×4	4.64×10^{-6}	7.16
	8×8	6.56×10^{-8}	6.14
	16×16	1.05×10^{-9}	5.96

4.4.2. One-dimensional Problems

In this section we present the calculation of one-dimensional Riemann problems, which feature different shocks configurations after the initial state is evolved to certain end time t. The study of shock tube problems constitutes the standard benchmark in computational magnetohydrodynamics because it is through these simple initial conditions that the robustness of the scheme is evaluated and also it is analyzed its capacity to resolve continuous and discontinuous flow structures (Mignone & Tzeferacos 2010). The considered tests are those discussed in Ryu & Jones (1995b), although some of them were first presented in Brio & Wu (1988) and in Dai & Woodward (1994b). For all these tests, we set the adiabatic index $\gamma = 5/3$ and transmissive boundary conditions. The CFL number is set to CFL $= 0.95$. The one-dimensional domain is the closed interval $[0, 1]$, and the membrane separating the left and right initial states is localized in the point $x = 0.5$. The left state will be represented by $\hat{\boldsymbol{u}}_L = \left(\rho, v_x, v_y, v_z, p, B_x, B_y, B_z\right)_L$ and the right state by $\hat{\boldsymbol{u}}_R = \left(\rho, v_x, v_y, v_z, p, B_x, B_y, B_z\right)_R$. Observe that left and right states are provided in primitive variables. The computational domain is decomposed into 500 grid points for the RKFD method, 500 cells for the RKFV method and 500 elements for the RKDG method. The numerical results discussed below were obtained with a high-order WENO7 reconstruction for the RKFD and RKFV methods, and with a polynomial $N = 6$ for the RKDG scheme. Moreover, all computations made use of the shock capturing

strategy outlined in section 3.2, that is, for the RKFD and the RKFV we use the WENO3 reconstruction operator for those regions with shocks, and for the RKDG scheme we use a hybrid DG/FV scheme with WENO3 reconstruction. The exact solution of the Riemann problems is plotted as red lines and they were obtained by solving the MHD equations with the second order MUSCL finite volume scheme with the MINMOD limiter, and in a very fine mesh made of 20.000 cells. The description of the flow patterns is presented below together with some comments regarding the capabilities of the **XTROEM-C**ode for solving such problems.

Riemann Problem 1

The initial condition is determined by the following left and right states

$$\begin{aligned} \hat{\boldsymbol{u}}_L &= \big(1, 10, 0, 0, 20, 5/\sqrt{4\pi}, 5/\sqrt{4\pi}, 0\big), \\ \hat{\boldsymbol{u}}_R &= \big(1, -10, 0, 0, 1, 5/\sqrt{4\pi}, 5/\sqrt{4\pi}, 0\big). \end{aligned} \tag{4.16}$$

This initial state will develop into two fast shocks, one weak slow shock, one slow rarefaction and one contact discontinuity. Plots of the density, thermal pressure, y-component of the velocity and the y-component of the magnetic field are depicted in the figure 4.1. The final simulation time is $t = 0.08$. Small oscillations are observed only for the RKFD and RKFV schemes with WENO7 reconstruction. The shocks are very well captured in around 3-4 cells with the WENO3 reconstruction operator for all three methods. The RKDG with $N = 6$ and hybrid DG/FV-WENO3 shock capturing has an outstanding resolution of the solution, with less oscillations than the RKFD and RKFV methods.

Riemann Problem 2

The initial condition is determined by the following left and right states

$$\begin{aligned} \boldsymbol{u}_L &= \big(1, 0, 0, 0, 1, 3/\sqrt{4\pi}, 5/\sqrt{4\pi}, 0\big), \\ \boldsymbol{u}_R &= \big(0.1, 0, 0, 0, 10, 3/\sqrt{4\pi}, 2/\sqrt{4\pi}, 0\big). \end{aligned} \tag{4.17}$$

This Riemann problem features one left-moving fast shock and one left-moving slow shock, one fast rarefaction and one slow rarefaction wave moving to the right, and one contact discontinuity. The z-component of the velocity and magnetic field is zero in all regions. Plots of the density, thermal pressure, y-component of the velocity and the y-component of the magnetic field at simulation time $t = 0.03$ are depicted in the figure 4.2. Small oscillations are observed only for the RKFD and RKFV schemes with WENO7 reconstruction. The shocks are very well captured in around 3-4 cells with the RKDG scheme with $N = 6$ and hybrid DG/FV-WENO3 shock capturing. In fact, the numerical solution with the RKDG scheme approximates much more better the “exact solution” than the RKFD and RKFV schemes. This is due to the subcell resolution of the DGSEM methods.

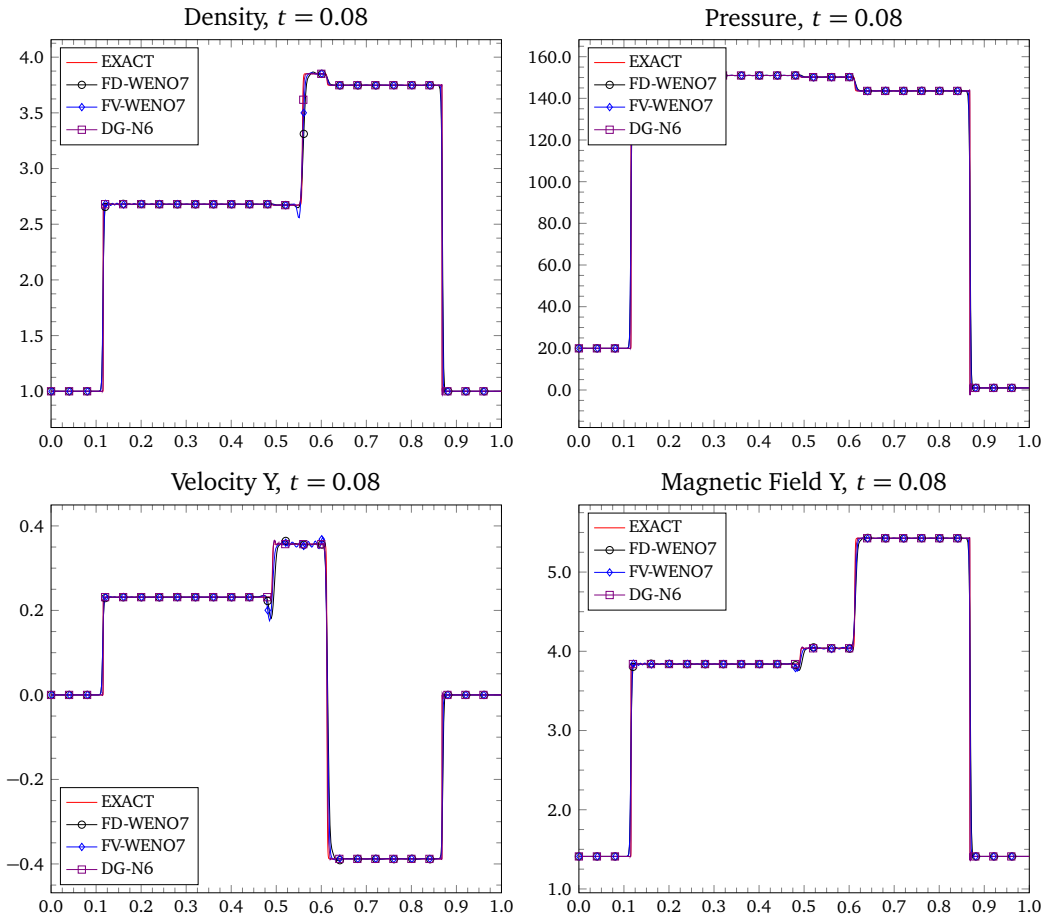

Figure 4.1: Riemann problem 1. The left and right states are given by equation (4.16). The final simulation time is $t = 0.08$. An ideal equation of state with adiabatic index $\gamma = 5/3$ is used. For the RKFD and RKFV, the WENO7 reconstruction is used in smooth parts of the flow and the WENO3 in regions with shocks. The RKDG is using a polynomial of degree $N = 6$ with the hybrid DG/FV-WENO3 as shock capturing.

Riemann Problem 3

The initial condition is determined by the following left and right states

$$\begin{aligned} \boldsymbol{u}_L &= \left(1.08, 1.2, 0.01, 0.5, 0.95, 2/\sqrt{4\pi}, 3.6/\sqrt{4\pi}, 2/\sqrt{4\pi}\right), \\ \boldsymbol{u}_R &= \left(1, 0, 0, 0, 1, 2/\sqrt{4\pi}, 4/\sqrt{4\pi}, 2/\sqrt{4\pi}\right). \end{aligned} \tag{4.18}$$

This problem is characterized by the appearance of multiple weak discontinuities, namely, two fast shocks, two slow shocks, two rotational discontinuities and one contact discontinuity. The shocks propagate from each side of the contact discontinuity. Plots of the density, thermal pressure, y-component of the velocity and the y-component of the magnetic field at time $t = 0.2$ are depicted in the figure 4.3. The shocks are very well captured in around 3-4 cells with all three methods, especially the RKDG scheme with $N = 6$ and hybrid DG/FV-WENO3 shock capturing. The solution computed with the RKFD and RKFV

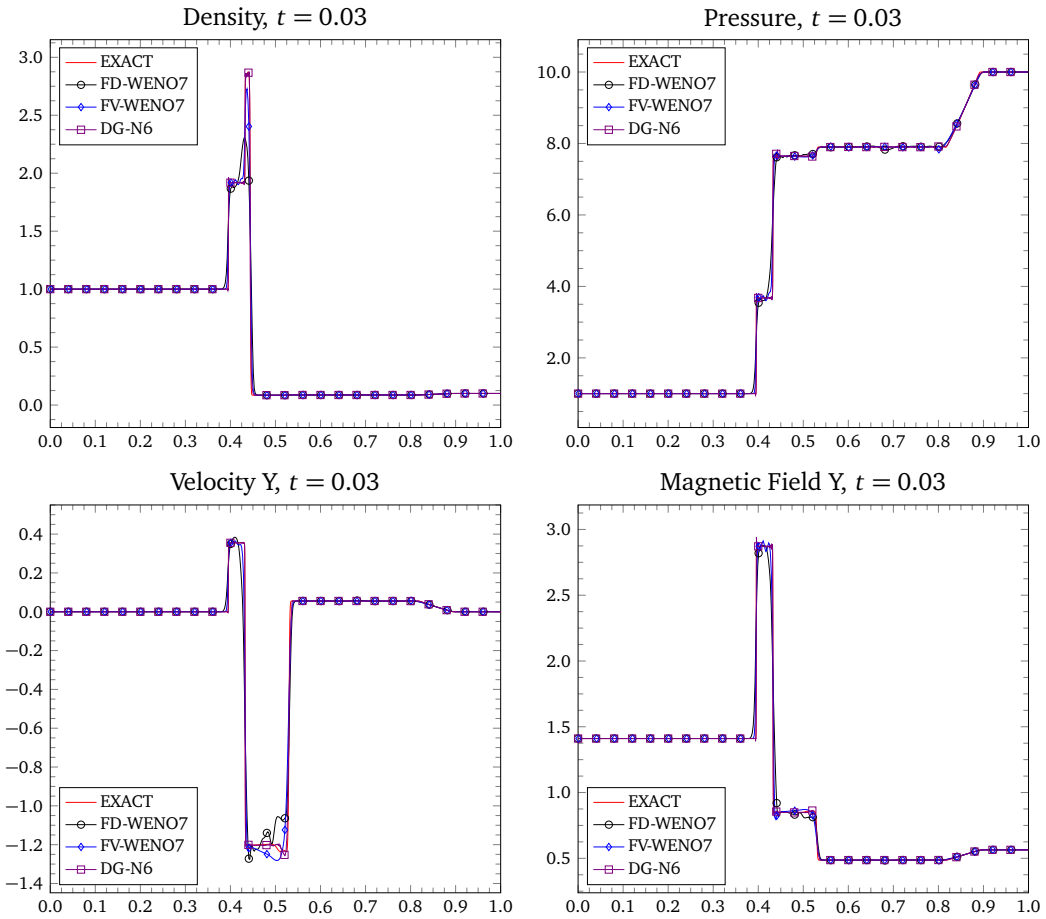

Figure 4.2: Riemann problem 2. The left and right states are given by equation (4.17). The final simulation time is $t = 0.03$. An ideal equation of state with adiabatic index $\gamma = 5/3$ is used. For the RKFD and RKFV, the WENO7 reconstruction is used in smooth parts of the flow and the WENO3 in regions with shocks. The RKDG is using a polynomial of degree $N = 6$ with the hybrid DG/FV-WENO3 as shock capturing.

schemes with WENO7 reconstruction shows some small oscillations, which are absent in the solution computed with the RKDG method.

Riemann Problem 4

The initial condition is determined by the following left and right states

$$\begin{aligned} \boldsymbol{u}_L &= \left(1, 0, 0, 0, 1, 3/\sqrt{4\pi}, 6/\sqrt{4\pi}, 0\right), \\ \boldsymbol{u}_R &= \left(0.10, 0, 2, 1, 10, 3/\sqrt{4\pi}, 1/\sqrt{4\pi}, 0\right). \end{aligned} \tag{4.19}$$

The solution to this Riemann problem features a fast shock, two rotational discontinuities, a slow shock, a contact discontinuity, a slow rarefaction, and a fast rarefaction. The rotation across the initial discontinuity of the magnetic field generates two rotational discontinuities. Plots of the density, thermal pressure, y-component of the velocity and

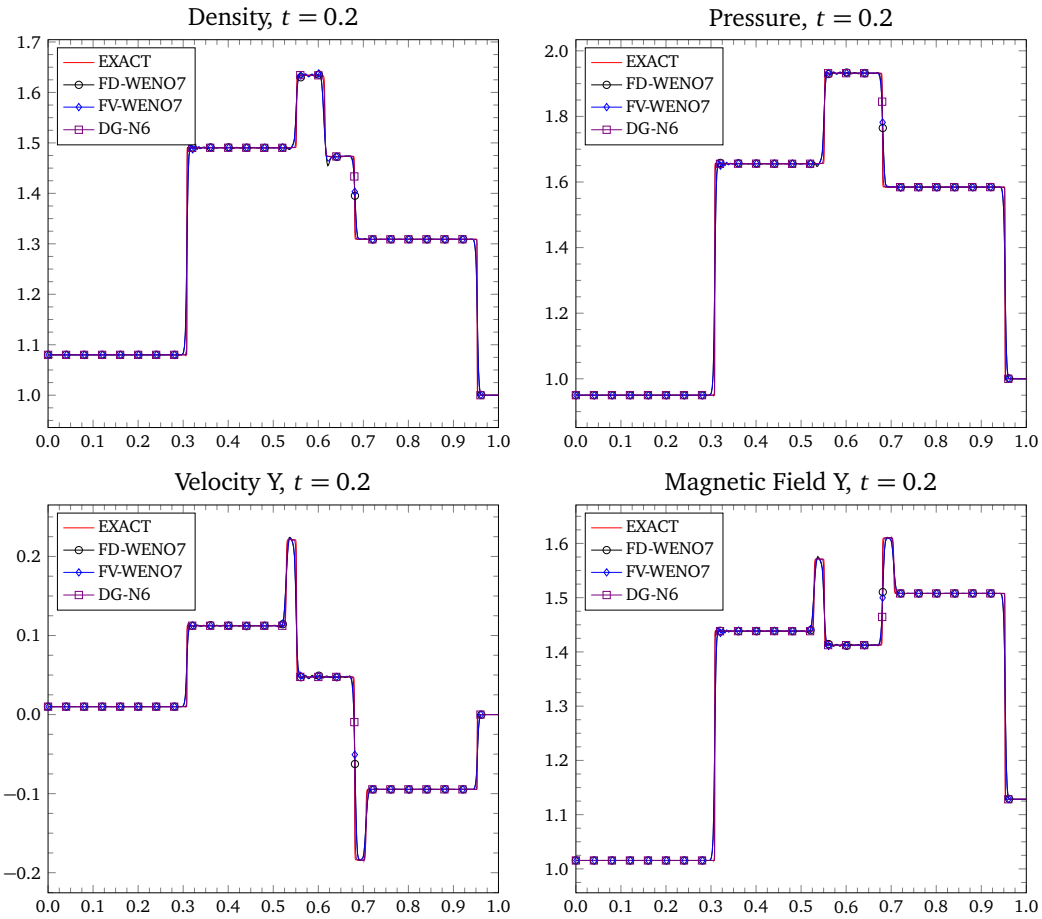

Figure 4.3: Riemann problem 3. The left and right states are given by equation (4.18). The final simulation time is $t = 0.20$. An ideal equation of state with adiabatic index $\gamma = 5/3$ is used. For the RKFD and RKFV, the WENO7 reconstruction is used in smooth parts of the flow and the WENO3 in regions with shocks. The RKDG is using a polynomial of degree $N = 6$ with the hybrid DG/FV-WENO3 as shock capturing.

the y-component of the magnetic field at simulation time $t = 0.035$ are depicted in the figure 4.4. The RKDG scheme with $N = 6$ and hybrid DG/FV-WENO3 shock capturing gets the best resolution among all three methods. The solution computed with the RKFD and RKFV schemes with WENO7 reconstruction is still very good, but some small oscillations are present.

Riemann Problem 5

The initial condition is determined by the following left and right states

$$\begin{aligned} \boldsymbol{u}_L &= \big(1, 0, 0, 0, 1, 1, 1, 0\big), \\ \boldsymbol{u}_R &= \big(0.2, 0, 0, 0, 0.1, 1, 0, 0\big). \end{aligned} \tag{4.20}$$

This test involves one of the so-called switch-on and switch-off structures, a switch-on

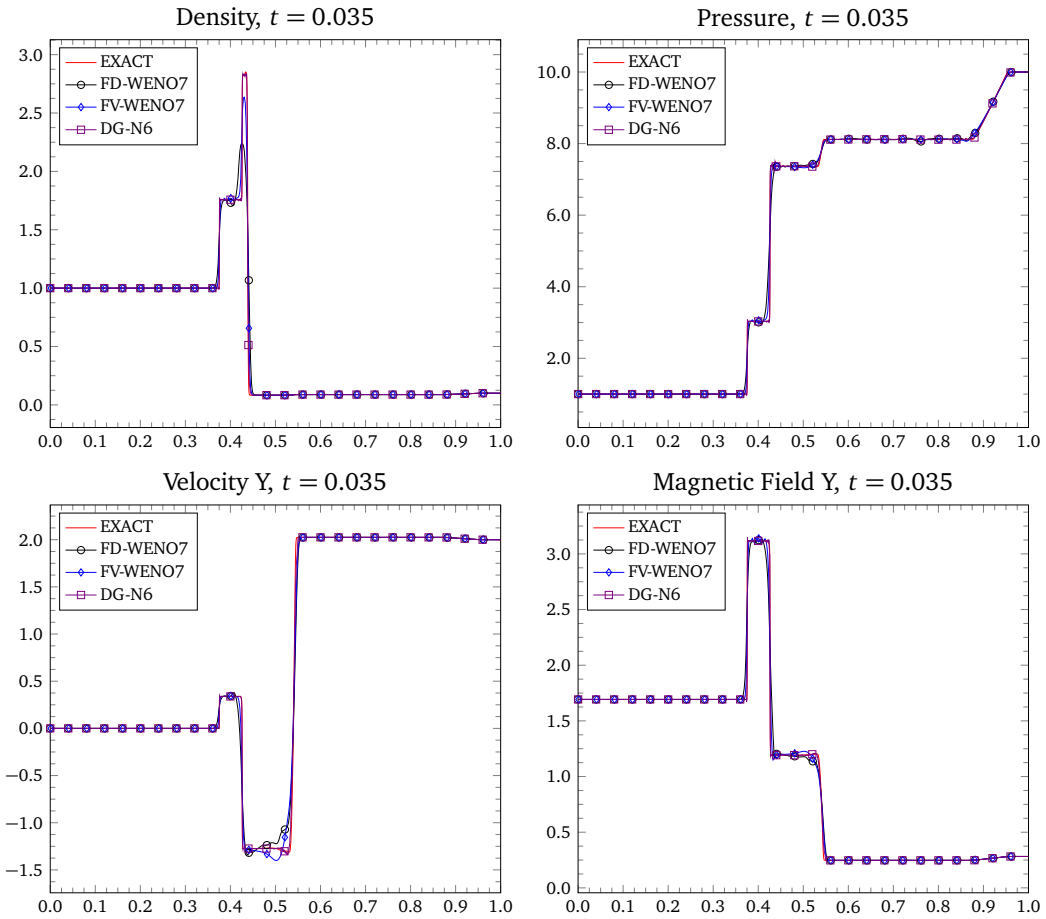

Figure 4.4: Riemann problem 4. The left and right states are given by equation (4.19). The final simulation time is $t = 0.035$. An ideal equation of state with adiabatic index $\gamma = 5/3$ is used. For the RKFD and RKFV, the WENO7 reconstruction is used in smooth parts of the flow and the WENO3 in regions with shocks. The RKDG is using a polynomial of degree $N = 6$ with the hybrid DG/FV-WENO3 as shock capturing.

fast shock. The main property of this problems is that the tangential magnetic field turns on in the region located behind the switch-on fast shocks and switch-on slow rarefactions waves. The switch-on fast shock is moving to the right. A fast rarefaction, a slow rarefaction, a contact discontinuity, and a slow shock are among the other structures developed in this problem. Plots of the density, thermal pressure, y-component of the velocity and the y-component of the magnetic field are shown in the figure 4.5 at the time $t = 0.15$. The solution computed with the RKFD and RKFV methods with WENO7 reconstruction are quite similar, and shows some oscillations around the discontinuities, which are resolved using only 3-4 cells. The solution computed with the RKDG method is very good, oscillation-free thanks to the hybrid DG/FV-WENO3 shock capturing scheme.

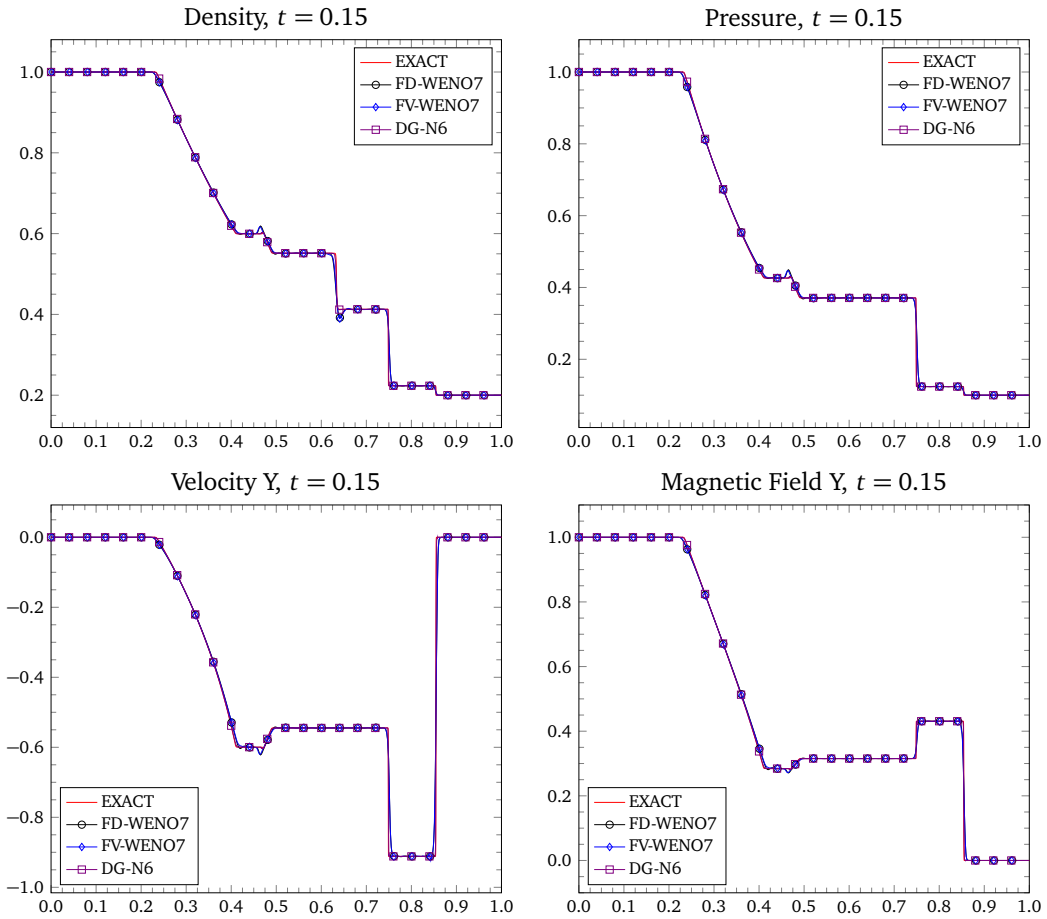

Figure 4.5: Riemann problem 5. The left and right states are given by equation (4.20). The final simulation time is $t = 0.15$. An ideal equation of state with adiabatic index $\gamma = 5/3$ is used. For the RKFD and RKFV, the WENO7 reconstruction is used in smooth parts of the flow and the WENO3 in regions with shocks. The RKDG is using a polynomial of degree $N = 6$ with the hybrid DG/FV-WENO3 as shock capturing.

Riemann Problem 6

The initial condition is determined by the following left and right states

$$\begin{aligned} \boldsymbol{u}_L &= \big(1, 0, 0, 0, 1, 0.7, 0, 0\big), \\ \boldsymbol{u}_R &= \big(0.3, 0, 0, 1, 0.2, 0.7, 1, 0\big). \end{aligned} \tag{4.21}$$

This problem comprises a switch-on slow rarefaction wave. In this case, the following structures are created: A hydrodynamic rarefaction, a switch-on slow rarefaction, a contact discontinuity, a slow shock, a rotational discontinuity, and a fast rarefaction. Plots of the density, thermal pressure, y-component of the velocity and the y-component of the magnetic field at time $t = 0.16$ are depicted in the figure 4.6. The structures mentioned before are showed in the figure, from left to right. The shocks have been very well captured using around 3-4 cells with the WENO3 reconstruction for both RKFD and RKDG

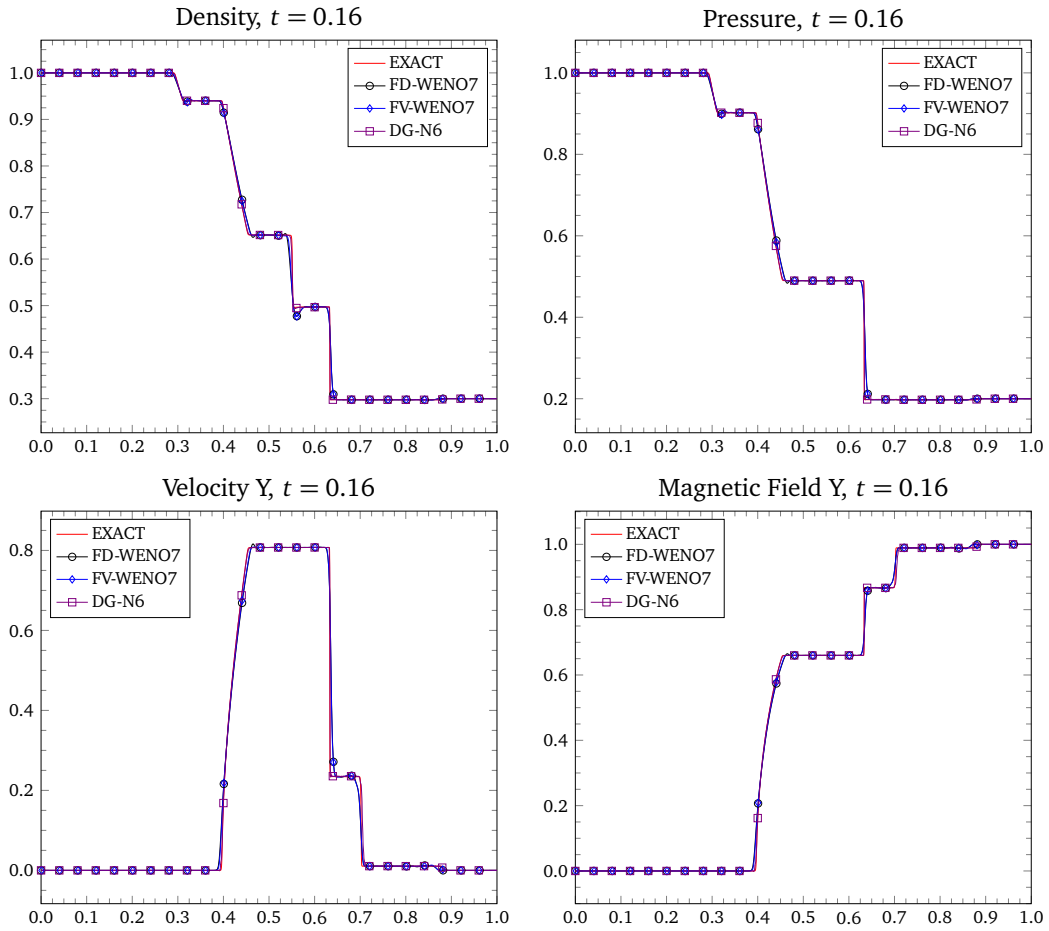

Figure 4.6: Riemann problem 6. The left and right states are given by equation (4.21). The final simulation time is $t = 0.16$. An ideal equation of state with adiabatic index $\gamma = 5/3$ is used. For the RKFD and RKFV, the WENO7 reconstruction is used in smooth parts of the flow and the WENO3 in regions with shocks. The RKDG is using a polynomial of degree $N = 6$ with the hybrid DG/FV-WENO3 as shock capturing.

schemes. The solution computed with the RKDG method fits almost with the exact solution, besides it is oscillation-free thanks to the hybrid DG/FV-WENO3 shock capturing scheme.

Riemann Problem 7

The initial condition is determined by the following left and right states

$$\begin{aligned} \boldsymbol{u}_L &= \big(1, 0, 0, 0, 1, 0.75, 1, 0\big), \\ \boldsymbol{u}_R &= \big(0.125, 0, 0, 0, 0.1, 0.75, -1, 0\big). \end{aligned} \tag{4.22}$$

This problem is similar to the Sod problem for the Euler equations. The test is characterized by the formation of the so-called compound structures. These structures involve a shock and a rarefaction wave traveling together. This kind of structures was first analyzed

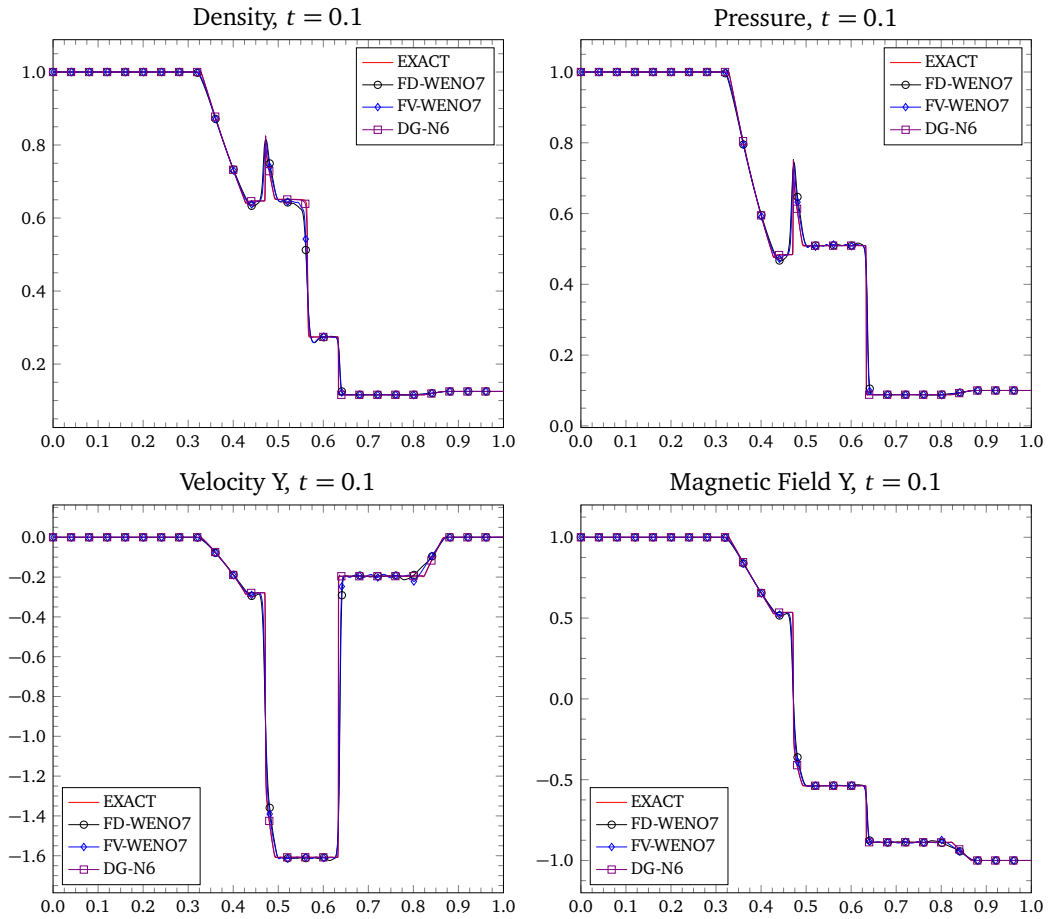

Figure 4.7: Riemann problem 7. The left and right states are given by equation (4.22). The final simulation time is $t = 0.1$. An ideal equation of state with adiabatic index $\gamma = 5/3$ is used. For the RKFD and RKFV, the WENO7 reconstruction is used in smooth parts of the flow and the WENO3 in regions with shocks. The RKDG is using a polynomial of degree $N = 6$ with the hybrid DG/FV-WENO3 as shock capturing.

in Brio & Wu (1988). This test involves a left-going slow compound wave. Plots of the density, thermal pressure, y-component of the velocity and the y-component of the magnetic field at time $t = 0.1$ are showed in the figure 4.7. The plots show the development (from left to right) of a left-going fast rarefaction, the left-going slow compound wave, a contact discontinuity, a right-going slow shock wave, and a right-going fast rarefaction wave. The WENO3 reconstruction operator used as shock capturing fro the RKFD and RKFV schemes resolves very well the shock wave and the contact discontinuity within just a few cells. The shocks are very well captured in around 3-4 cells with the RKDG scheme with $N = 6$ and hybrid DG/FV-WENO3 shock capturing. Observe the appearance of the compound structure for all schemes, even the reference solution computed with a RKFV-MUSCL scheme on a mesh of 20 000 cells.

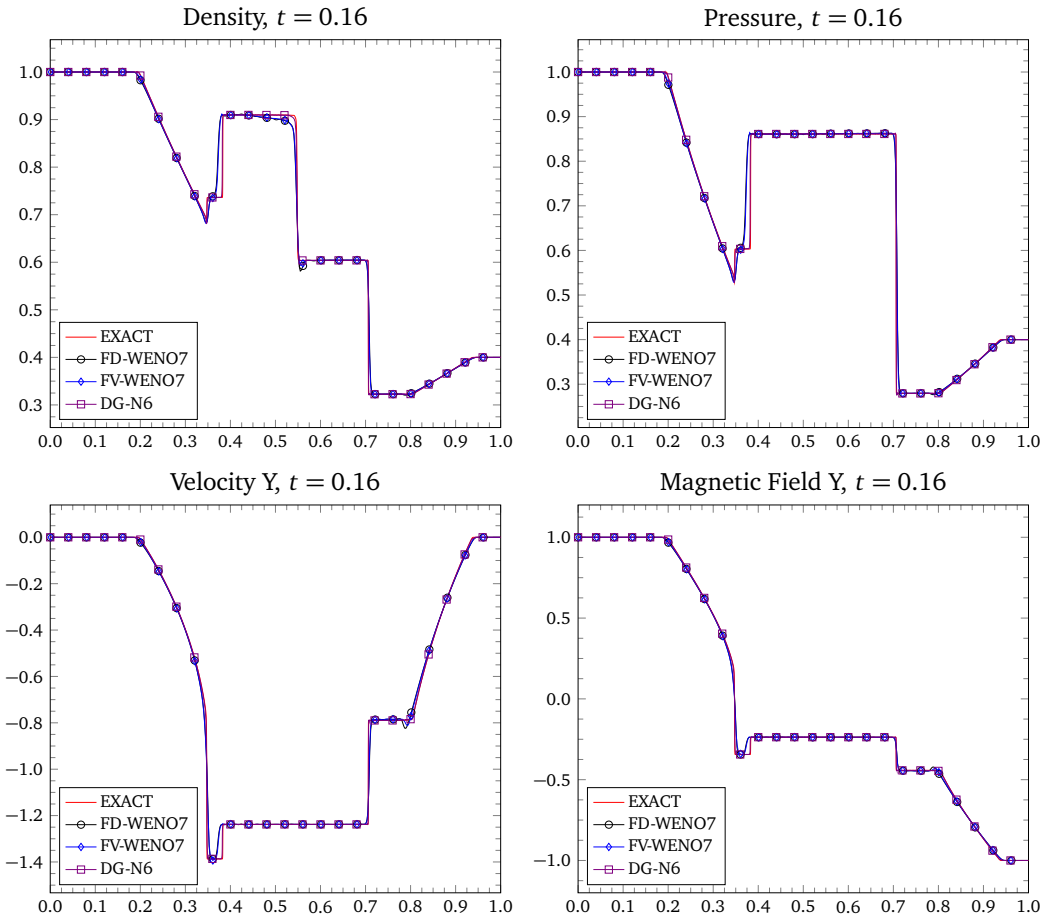

Figure 4.8: Riemann problem 8. The left and right states are given by equation (4.23). The final simulation time is $t = 0.16$. An ideal equation of state with adiabatic index $\gamma = 5/3$ is used. For the RKFD and RKFV, the WENO7 reconstruction is used in smooth parts of the flow and the WENO3 in regions with shocks. The RKDG is using a polynomial of degree $N = 6$ with the hybrid DG/FV-WENO3 as shock capturing.

Riemann Problem 8

The initial condition is determined by the following left and right states

$$\begin{aligned} \boldsymbol{u}_L &= \big(1, 0, 0, 0, 1, 1.3, 1, 0\big), \\ \boldsymbol{u}_R &= \big(0.4, 0, 0, 0, 0.4, 1.3, -1, 0\big). \end{aligned} \tag{4.23}$$

As the previous problem, this test involves the so-called compound structures, in fact, a fast compound structure. The analytic solution (has a rotational discontinuity and a fast rarefaction) is different from the numerical calculations. Other structures are the one fast rarefactions, two slow shocks, and a contact discontinuity. Plots of the density, thermal pressure, y-component of the velocity and the y-component of the magnetic field at the time $t = 0.16$. are depicted in the figure 4.8. The shocks are very well captured in around 3-4 cells with the WENO3 reconstruction operator for all three methods. The RKDG with

$N = 6$ and hybrid DG/FV-WENO3 shock capturing has an outstanding resolution of the solution, with less oscillations than the RKFD and RKFV methods. The DG solution fits better the reference solution.

4.4.3. Multidimensional Test Problems

Magnetic Field Loop Advection

The magnetic field loop advection is a very important test for multidimensional MHD because with it, one can observe whether the algorithm is able to preserve $\nabla \cdot \boldsymbol{B} = 0$. In this test, a cylindrical current distribution is advected along some direction of the computational domain. Because of the loop remains in magnetostatic balance, after some periods, its profile should be the same. With multidimensional MHD codes that do not include an algorithm for the treatment of the solenoidal constraint of the magnetic field, or if they use numerical methods too much diffusive, the magnetic loop will smear over the time. More details can be found in Tóth (2000), Stone et al. (2008), and Mignone & Tzeferacos (2010).

Following the description to this problem given in Tóth (2000), the computational domain is given by the box $[-1.0, +1.0] \times [-0.5, +0.5]$. We set the density to $\rho = 1$, and the pressure $p = 1$ in the whole domain. The initial velocity is given by

$$v_x = v_0 n_x, \quad v_y = v_0 n_y, \quad v_z = 0, \tag{4.24}$$

where v_0 is the magnitude of the velocity (we use $v_0 = \sqrt{5}$), n_x and n_y are the components of the unit vector in the direction of movement of the loop (we use $n_x = 2/\sqrt{5}$ and $n_y = 1/\sqrt{5}$). The magnetic field is constant everywhere, except for the loop structure of radius R (we use $R = 0.3$). In this way, for $r \leq R$ we have

$$B_x = -B_0 y/r, \quad B_y = +B_0 x/r, \quad B_z = 0, \tag{4.25}$$

where $r = \sqrt{x^2 + y^2}$, B_0 is the magnitude of the magnetic field and it should be small in such a way that the magnetic pressure is smaller than the gas pressure (we use $B_0 = 10^{-3}$). An adiabatic equation of state with $\gamma = 5/3$ is considered. At the boundaries of the domain we consider periodic boundary conditions. The simulation time is $t = 2.0$, and in the figure 4.9 is depicted the magnetic pressure at time $t = 2.0$ for all methods, with and without divergence cleaning. The computational domain is decomposed into 800×400 grid points for the RKFD-WENO7 scheme, 800×400 cells for the RKFV-WENO7 scheme, and 180×90 elements for the RKDG scheme, with $N = 5$. No shock capturing method was employed in this test. The divergence cleaning parameters used in the simulation are $c_r = 0.18$, and c_h determined by the maximum propagation speed in the system. The CFL condition was set to CFL $= 0.95$. We observe that the loop profile is only kept when the GLM is taken into account for all methods.

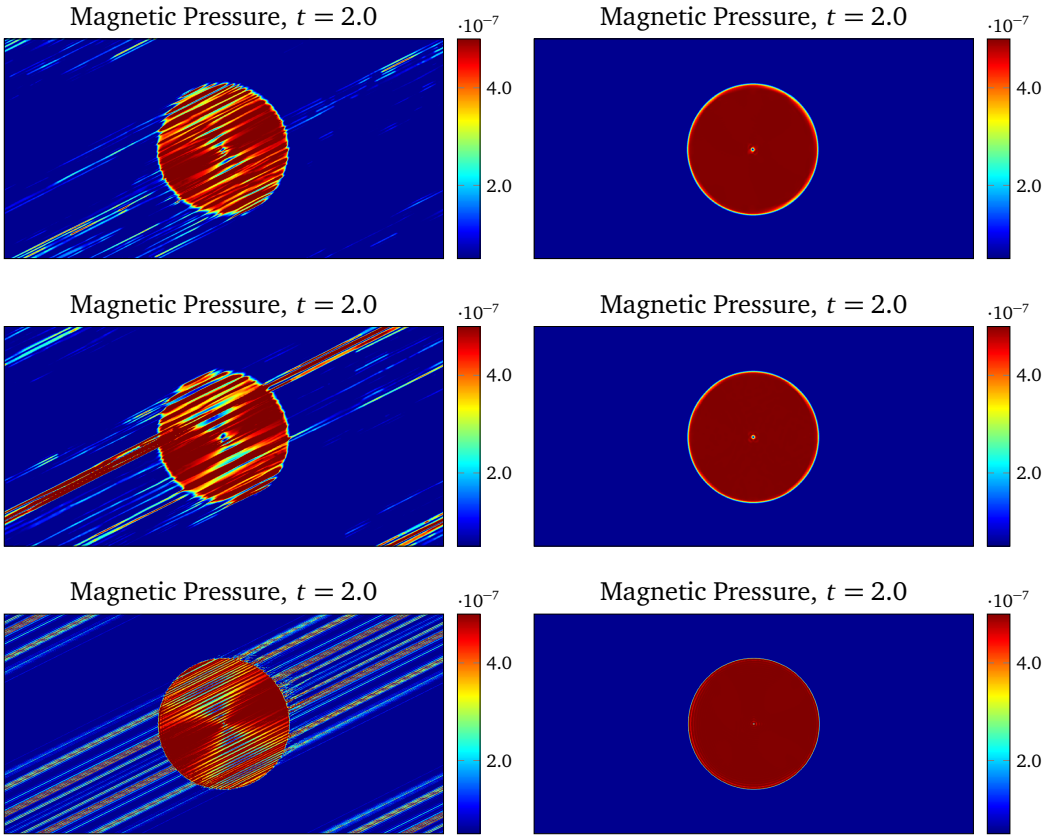

Figure 4.9: Magnetic field loop advection. Contour plots of the magnetic pressure at time $t = 2.00$ without divergence cleaning (left) and with divergence cleaning (right), for the RKFD-WENO7 scheme (top), the RKFV-WENO7 scheme (middle), and the RKDG scheme with $N = 5$.

Current Sheet

This problem was first discussed in Hawley & Stone (1995). Initially, a region is uniformly filled with a gas at rest. The magnetic field is initialized in such a way that this switches signs at the slices $x = +0.25$ and $x = -0.25$. Then we perturb the system with a sinusoidal velocity function in y, which generates nonlinear, linearly polarized Alfvén waves. Because the magnetic pressure does not remain constant, these Alfvén waves turn into magnetosonic waves. Magnetic reconnection occurs because of the two current sheets at $x = \pm 0.25$. Additionally, since the parameter $\beta < 1$, the magnetic reconnection drives highly over-pressurized regions, which launch magnetosonic waves transverse to the field, causing magnetic energy to be transformed into thermal energy (Hawley & Stone 1995). Large magnetic field gradients are produced close to the points where the magnetic reconnection take place. Because of that, this test problem is useful to check if the algorithm can handle these features.

For the simulation, we consider the computational domain to be the box $[-0.5, +0.5] \times [-0.5, +0.5]$. We set the density and pressure uniform in the whole domain, with $\rho = 1.0$, and $p = 0.5\beta$, where β is an input parameter which represents the

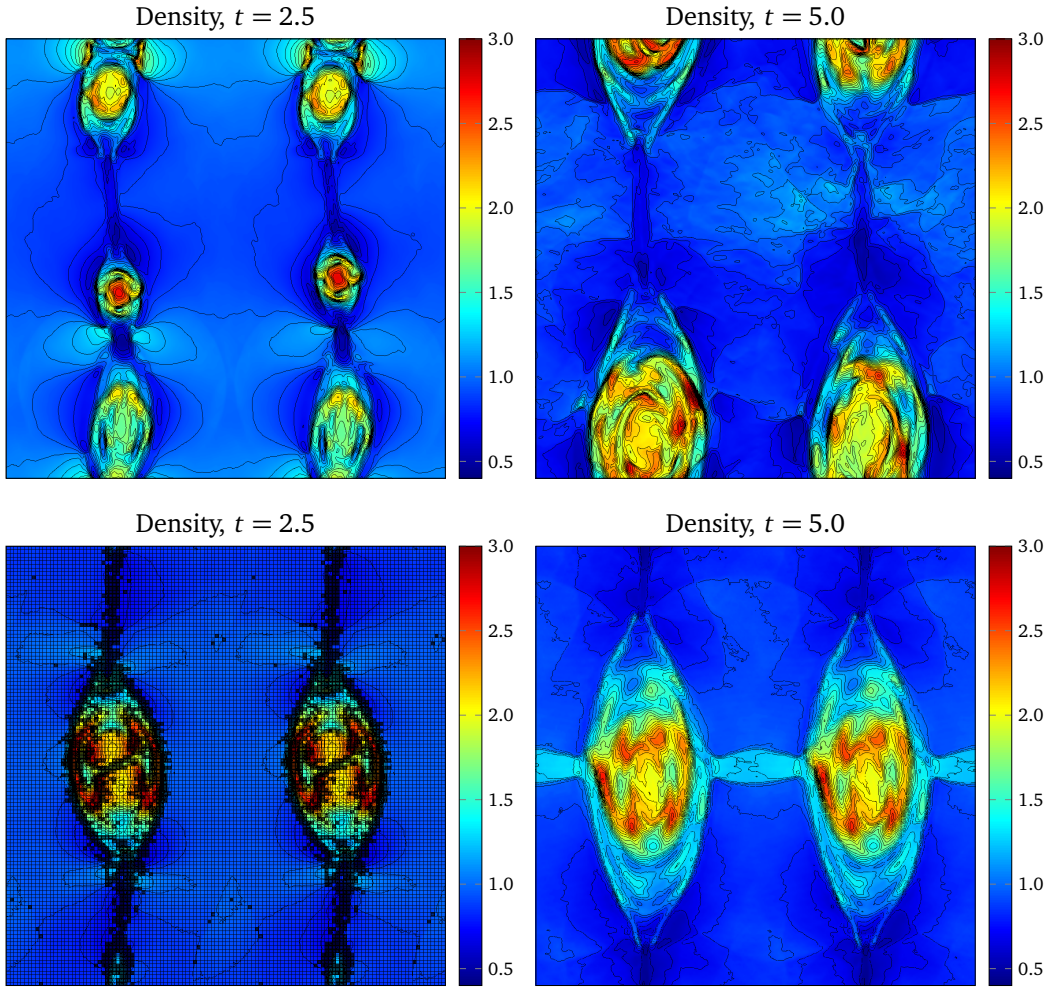

Figure 4.10: The current sheet problem. Contour plots of the density at times $t = 2.5$ (left) and $t = 5.0$ (right). The calculations were performed with a RKFD with WENO7 reconstruction scheme on a grid of 600×600 grid points (top), and a RKDG with $N = 4$ on a mesh made of 120×120 elements. The computational domain is the box $[-0.5, +0.5] \times [-0.5, +0.5]$.

ratio of gas pressure to magnetic energy density. We set $v_y = v_z = 0$, and $v_x = A\sin(2\pi y)$, where A is a parameter that is typically used to test the robustness of the algorithm. We set $B_x = B_z = 0$, and $B_y = 1$ for $|x| > 0.25$ and $B_y = -1$ otherwise. We employ $A = 0.1$ and $\beta = 0.1$ in our simulations. An adiabatic equation of state with $\gamma = 5/3$ is considered. At the boundaries of the domain we consider periodic boundary conditions. The end simulation time is $t = 10.0$. In the figure 4.10 is depicted the density at times $t \in \{2.5, 5.0\}$ obtained with the finite difference scheme with WENO7 reconstruction on a grid with 600×600 points (top), and the hybrid DG/FV-WENO3 method with $N = 4$ on a mesh made of 120×120 elements (bottom). In the figure 4.11 is also depicted the density at times $t \in \{7.5, 10.0\}$ obtained with the finite volume scheme with WENO7 reconstruction on a grid of 600×600 cells (top), and the hybrid DG/FV-WENO3 method with $N = 4$ (bottom). The CFL condition was set to CFL $= 0.95$. The results are quite similar to those

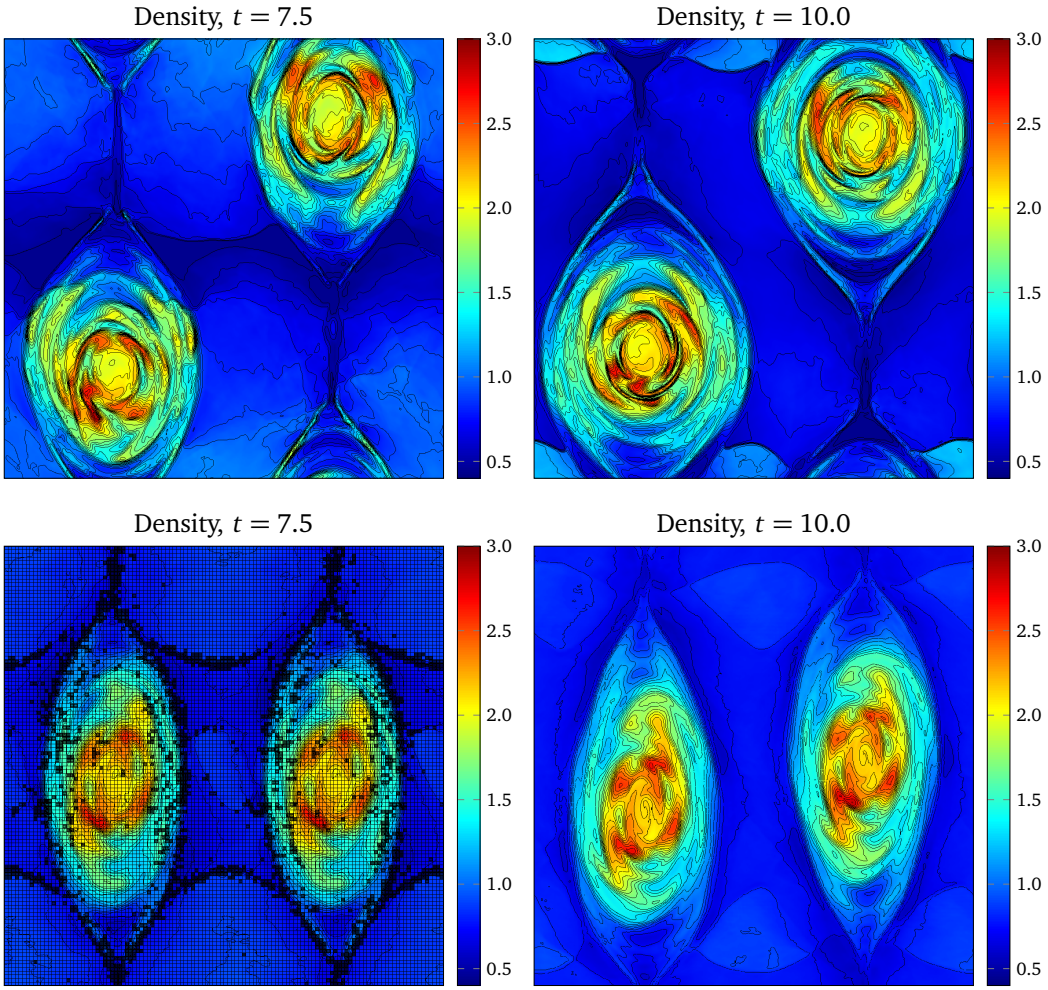

Figure 4.11: The current sheet problem. Contour plots of the density at times $t = 7.5$ (left) and $t = 10.0$ (right). The calculations were performed with a RKFV with WENO7 reconstruction scheme on a grid of 600×600 cells (top), and a RKDG with $N = 4$ on a mesh made of 120×120 elements. The computational domain is the box $[-0.5, +0.5] \times [-0.5, +0.5]$.

reported by Stone et al. (2008), but also they show the robustness of the code when tackling complex flow configurations with very high-order numerical schemes. For the RKDG scheme is also plotted the mesh and the FV subcells where the hybrid DG/FV-WENO3 acts for the shock capturing. Observe also the differences in all three methods for the solution of the same problem. Here the influence of the mesh resolution and dissipation properties of the scheme along with the shock capturing strategy employed has played an important role for such differences.

Orszag-Tang Vortex

This problem was first studied in Orszag & Tang (1979) for the incompressible MHD equations. Many authors have used the Orszag-Tang vortex for the compressible MHD

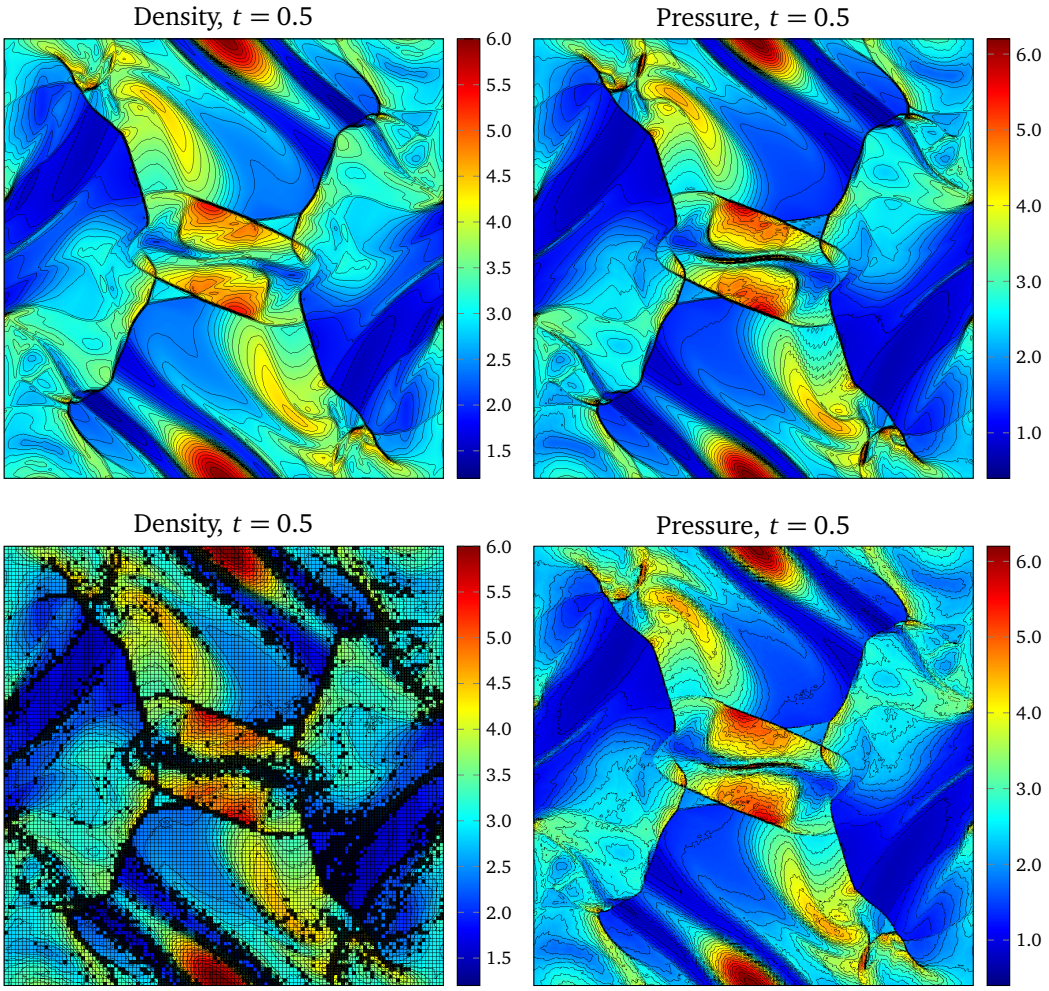

Figure 4.12: Orszag-Tang vortex problem. Contour plots of the density and pressure at time $t = 0.5$ for three high-order numerical methods, namely, RKFD with WENO7 reconstruction (top-left), RKFV with WENO7 reconstruction (top-right), and the RKDG with $N = 5$ and hybrid DG/FV-WENO3 shock capturing (bottom). The computational domain is given by the box $[0,1] \times [0,1]$.

equations as a test problem in order to know how robust is the employed numerical scheme at handling the formation and the interactions of MHD shocks (Zachary et al. 1994; Ryu & Jones 1995b; Ryu et al. 1998; Dai & Woodward 1998; Helzel et al. 2011; Jiang & Wu 1999; Tóth 2000; Londrillo & del Zanna 2000). The initial flow profile, which consists of smooth initial data, is obtained by the superposition of a velocity vortex with a magnetic vortex. Because of this highly unstable setup, a broad range of MHD waves are generated, interacting with each other, making a transition towards turbulence.

For this problem, the computational domain is given by the box $[0,1] \times [0,1]$. We set the density and pressure uniform in the whole domain, with $\rho = \gamma^2$ and $p = \gamma$. With this choice of the density and pressure we have a sound speed $c_s = 1$. For the 2D case of

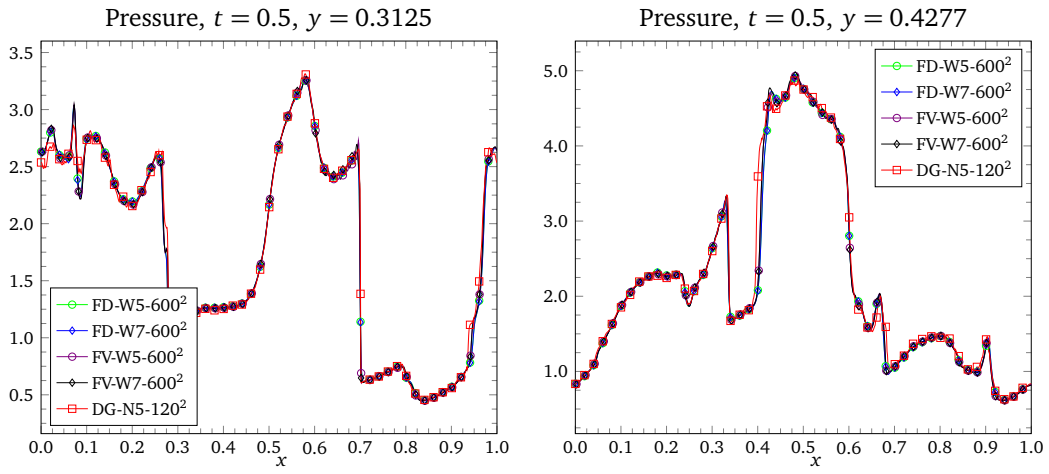

Figure 4.13: Orszag-Tang vortex problem. Slices of the pressure at $y = 0.3125$ and $y = 0.4277$ for the RKFD, RKFV, and RKDG schemes, with different mesh resolutions, and reconstruction operators.

the Orszag-Tang vortex, the velocity has the following profile

$$v_x = -\sin(2\pi y), \quad v_y = +\sin(2\pi x), \quad v_z = 0. \tag{4.26}$$

The magnetic field is given by

$$B_x = -\sin(2\pi y), \quad B_y = +\sin(4\pi x), \quad B_z = 0. \tag{4.27}$$

An adiabatic equation of state with $\gamma = 5/3$ is considered. At the boundaries of the domain we consider periodic boundary conditions. The simulation time is $t = 1.0$, and in the figure 4.12 are depicted the density and pressure at time $t = 0.5$. The solution was obtained with the finite difference scheme with WENO7 reconstruction on a grid with 600×600 points (top-left), finite volume scheme with WENO7 reconstruction on a grid of 600×600 cells (top-right), and the hybrid DG/FV-WENO3 method with $N = 5$ on a mesh made of 120×120 elements (bottom). The WENO7 reconstruction is used in smooth parts of the flow and the WENO3 in regions with shocks for the RKFD and RKFV schemes. For the RKDG scheme is also plotted the mesh and the FV subcells where the hybrid DG/FV-WENO3 is being used as shock capturing method. The divergence cleaning of Dedner et al. (2002) was used, with $c_r = 0.18$, and c_h determined by the maximum propagation speed in the system. We set the CFL condition to CFL $= 0.95$. For a more quantitative comparison, in the figure 4.13 are plotted slices of the pressure at $y = 0.3125$ and $y = 0.4277$ for different numerical methods (RKFD, RKFV, and RKDG), mesh resolutions (600×600 for the RKFD and RKFV schemes, and 120×120 for the RKDG scheme) and reconstruction operators (WENO5 and WENO7 for the RKFD and RKFV), or polynomial degree ($N = 5$ for the RKDG method). We observe the lack of oscillations in these contour plots, and also the very good agreement for all cases.

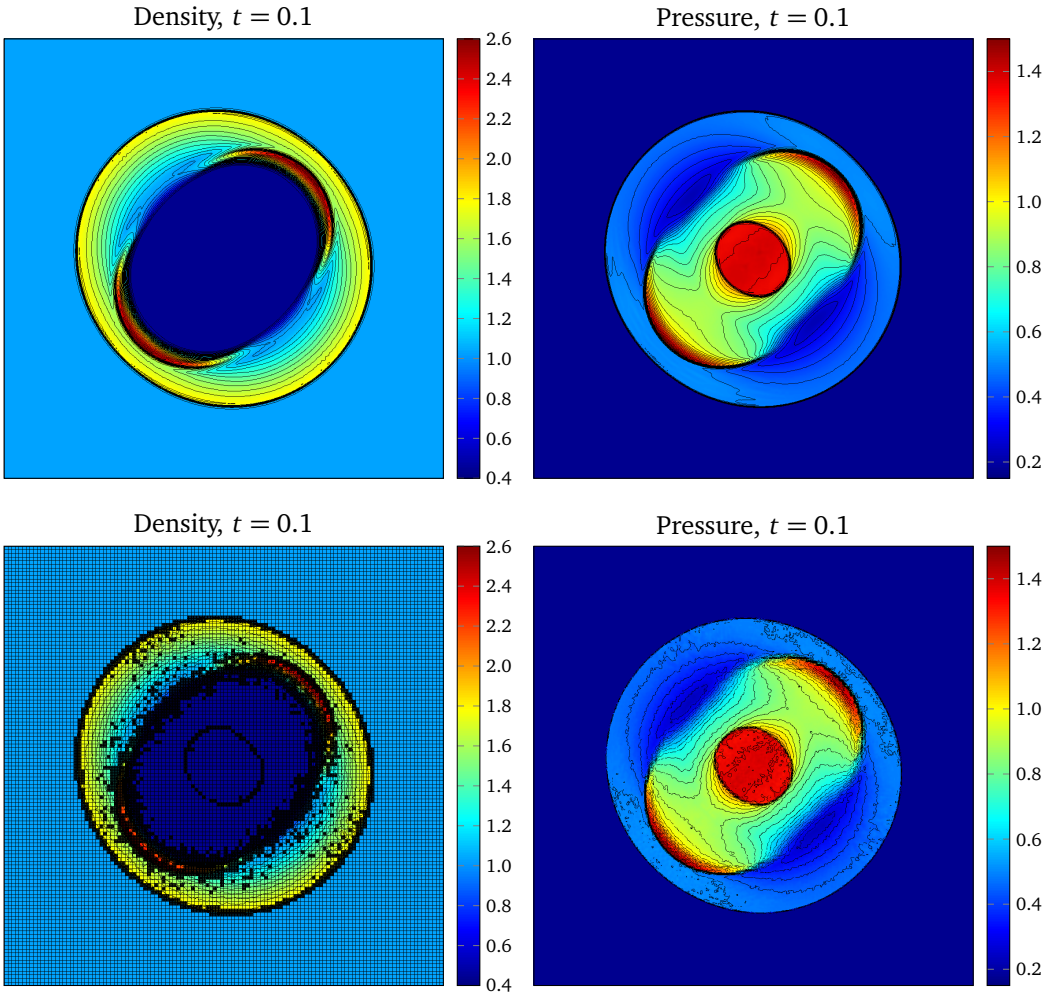

Figure 4.14: Cylindrical blast wave. Contour plots of the density and the pressure at time $t = 0.10$, obtained with a RKFD-WENO7 scheme (top-left), a RKFV-WENO7 scheme (top-right), and the RKDG with $N = 5$ and hybrid DG/FV-WENO3 shock capturing (bottom). The computational domain is given by the box $[0, 1] \times [0, 1]$.

Cylindrical Blast Wave

This problem concerns with the formation and propagation of strong shock waves in a highly magnetized medium (Zachary et al. 1994; Londrillo & del Zanna 2000; Stone et al. 2008; Mignone et al. 2010). Initially, a cylindrical region located in the center of a domain is filled with a magnetized overpressured gas. As result, a strong shock wave moving outwards is formed. This test is very difficult for any numerical method in the sense that the code can crash because of the formation of unphysical values in quantities like the density or the pressure. If periodic boundary conditions are used, then the interactions of the shock waves lead to very complex configurations.

For this problem, the computational domain is given by the box $[0, 1] \times [0, 1]$. We set the density and pressure uniform in the whole domain, with $\rho = 1$ and $p = 0.1$. The

pressure in the cylindrical region $(x-x_c)^2+(y-y_c)^2 < R$, with $(x_c, y_c) = (0.5, 0.5)$, and $R = 0.1$, is $p = 10.0$. Initially, the velocity is set to zero, that is $v_x = v_y = v_z = 0$. For the 2D case, the magnetic field is set to $B_x = B_y = B_z = 1/\sqrt{2}$. An adiabatic equation of state with $\gamma = 5/3$ is considered. At the boundaries of the domain we consider periodic boundary conditions. The simulation time is $t = 0.5$, and in the figure 4.14 are depicted the density and the pressure at time $t = 0.1$. The solution was obtained with the RKFD scheme with WENO7 reconstruction on a grid with 600×600 points (top-left), RKFV scheme with WENO7 reconstruction on a grid of 600×600 cells (top-right), and the hybrid DG/FV-WENO3 method with $N = 5$ on a mesh made of 120×120 elements (bottom). For the RKFD and RKFV methods we stress that the WENO7 reconstruction is used in smooth parts of the flow and the WENO3 in regions with shocks. The hybrid DG/FV-WENO3 scheme was used as shock capturing for the RKDG method, and the mesh of the FV subcells is also plotted. The divergence cleaning of Dedner et al. (2002) was used, with $c_r = 0.18$, and c_h determined by the maximum propagation speed in the system. We set the CFL condition to CFL $= 0.95$. We observe the appearance of some oscillations in the plot for the pressure computed with the RKDG scheme. The RKFD and the RKFV have an excellent agreement with the numerical results reported in the literature, and in fact, they effectively resolve the strong gradients arising after the release of the cylindrical region.

Rotor Problem

The rotor problem was first proposed in Balsara & Spicer (1999a), and also it was studied in Tóth (2000). It consists of a high-density, rapidly spinning fluid in a low-density fluid. Initially, both fluids are subject to an uniform magnetic field. Because of the rapidly rotating fluid, torsional Alfvén waves are launched into the fluid at rest. As a consequence the rotor suffers a decrease in its angular momentum.

The initial configuration of this problem is as follows: The computational domain is the box $[0,1] \times [0,1]$. We set the density and pressure uniform in the ambient medium, with $\rho = 1.0$ and $p = 1.0$. Inside the cylindrical rotor ($0.0 \leq (x-x_c)^2+(y-y_c)^2 \leq 0.1$, with $(x_c, y_c) = (0.5, 0.5)$) we set the density $\rho = 10.0$, and the pressure is the same as in the ambient fluid. The velocity in the ambient medium is initially set to zero, that is $v_x = v_y = v_z = 0$. The rotor has an angular velocity ω such that $v = \omega r = 1$ at $r = 0.1$. A linear taper is applied to the velocity and density field, however only in a very small range $0 \leq r \leq 1.115$ so that the density and the velocity match those of the ambient fluid at rest at a radius of $R = 1.115$. The magnetic field is set to $B_x = 5.0$, and $B_y = B_z = 0$ in the whole computational domain. An adiabatic equation of state with $\gamma = 7/5$ is considered. At the boundaries of the domain we consider transmissive boundary conditions. The divergence cleaning of (Dedner et al. 2002) was used, with $c_r = 0.18$, and c_h was determined by the maximum wave propagation speed in the system. We set the CFL condition to CFL $= 0.95$.

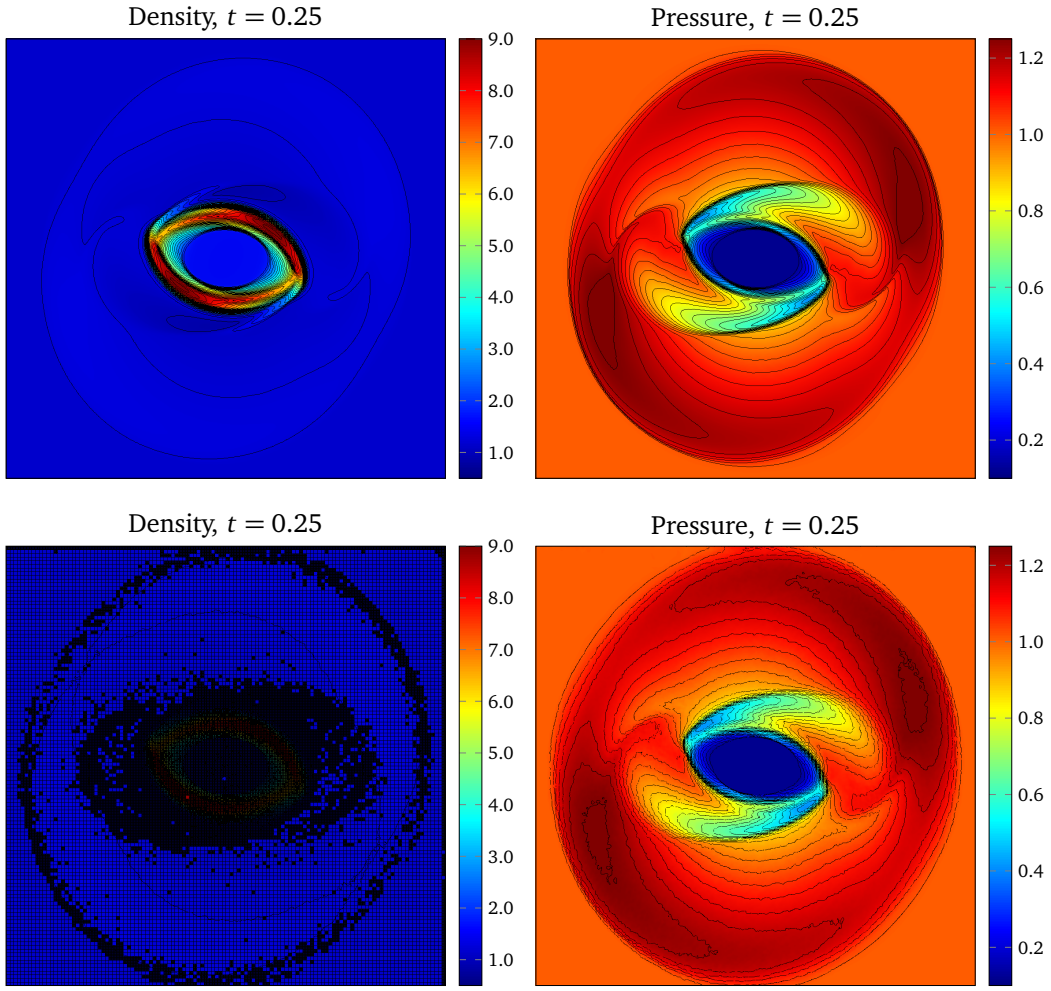

Figure 4.15: Rotor problem. Contour plots of the density and pressure at time $t = 0.25$. The computations were obtained with a RKFD-WENO7 scheme (top), and the RKDG with $N = 5$ and hybrid DG/FV-WENO3 shock capturing (bottom). The computational domain is given by the box $[0, 1] \times [0, 1]$.

This problem is extremely difficult for any numerical method, even for low-order schemes. A mechanism to preserve the positivity of the density and pressure has to be kept in mind for this problem, and efficiently combined with the shock capturing approach. The end simulation time is $t = 0.5$, and in the figure 4.15 are depicted the density, pressure at time $t = 0.25$ for the solutions computed with the RKFD scheme with WENO7 reconstruction on a grid with 600×600 points (top), and the hybrid DG/FV-WENO3 method with $N = 5$ on a mesh made of 120×120 elements (bottom). Also in the figure 4.16 are depicted the Mach number and the magnitude of the magnetic field at time $t = 0.25$ for the solutions computed with the RKFV scheme with WENO7 reconstruction on a grid with 600×600 cells (top), and the hybrid DG/FV-WENO3 method with $N = 5$ on a mesh made of 120×120 elements (bottom). In the plot for the Mach number is clearly visible that the fluid inside the rotor is still rotating with uniform an-

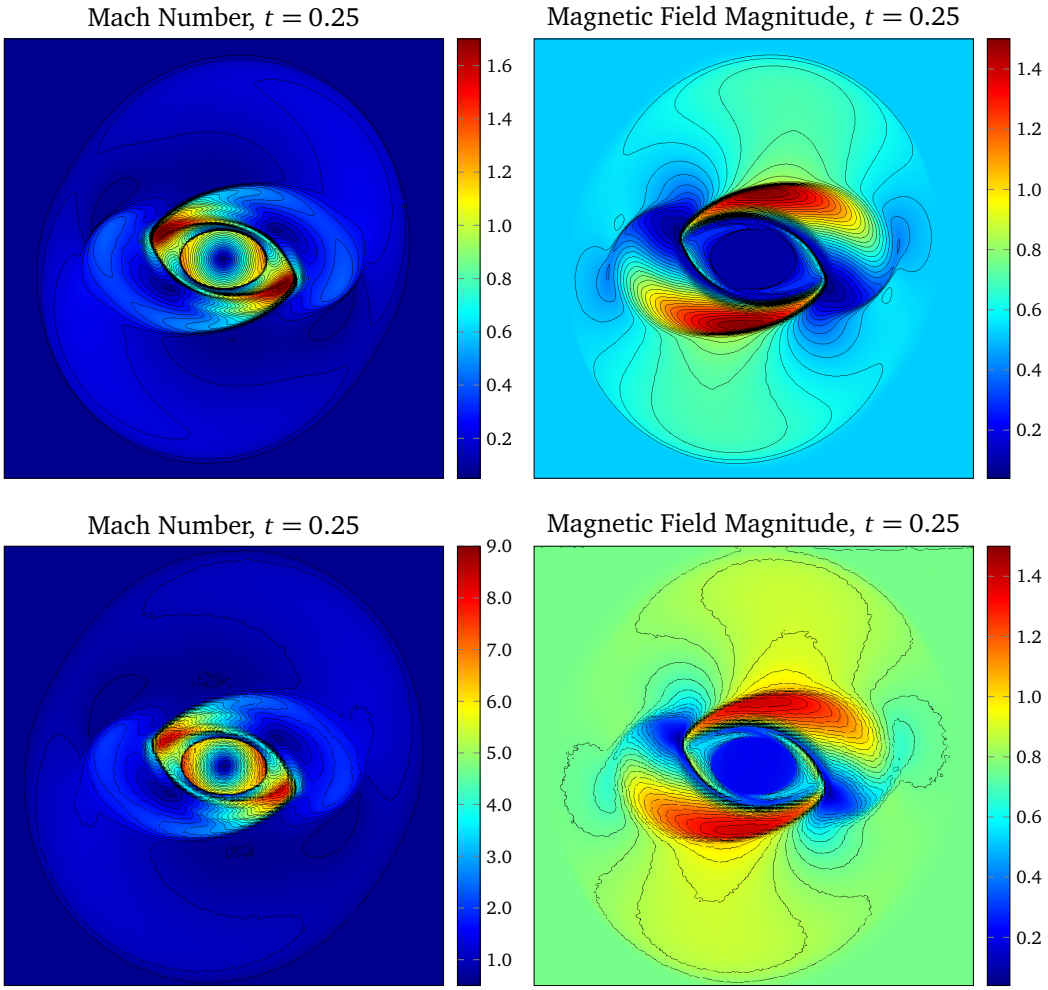

Figure 4.16: Rotor problem. Contour plots of the Mach number and magnetic field magnitude at time $t = 0.25$. The computations were obtained with a RKFV-WENO7 scheme (top), and the RKDG with $N = 5$ and hybrid DG/FV-WENO3 shock capturing (bottom). The computational domain is given by the box $[0,1] \times [0,1]$.

gular speed. For the RKDG scheme is also plotted the mesh and the FV subcells where the hybrid DG/FV-WENO3 is acting as shock capturing approach. The RKFD and RKFV provide the best resolution for this problem, and also the best stability. We observe the appearance of some oscillations in the plots obtained from the computation with the RKDG scheme. In the figure 4.17 are plotted slices of the x and y components of the magnetic field at $x = 0.5$ and $y = 0.5$, respectively, for different numerical methods (RKFD, RKFV, and RKDG), mesh resolutions (600×600 for the RKFD and RKFV schemes, and 120×120 for the RKDG scheme) and reconstruction operators (WENO5 and WENO7 for the RKFD and RKFV), or polynomial degree ($N = 5$ for the RKDG method). We observe the lack of oscillations in these plots, and also the very good agreement for the RKFD and RKFV schemes, with a light difference with the RKDG scheme.

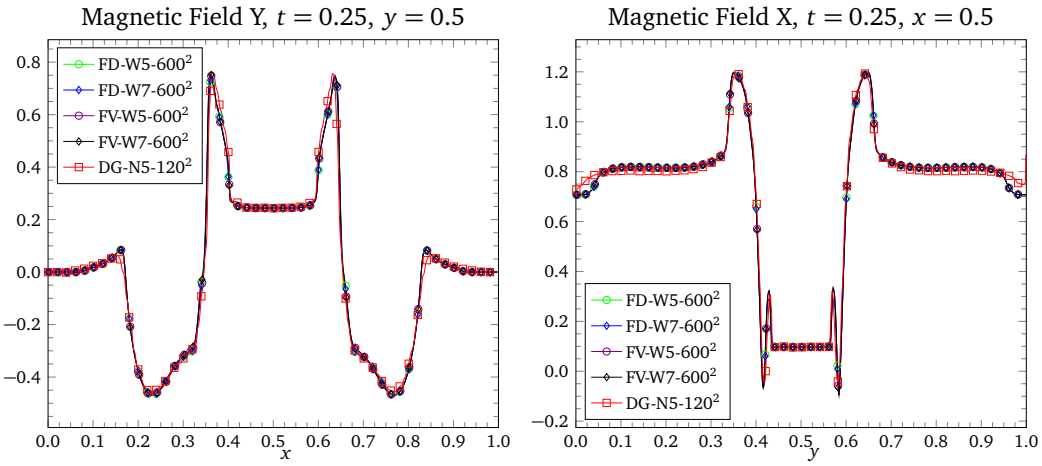

Figure 4.17: Rotor problem. Slices of the x and y components of the magnetic field at $x = 0.5$ and $y = 0.5$, respectively, for the RKFD, RKFV, and RKDG schemes, with different mesh resolutions, and reconstruction operators.

Cloud-Shock Interaction

This problem consists in the interaction of a strong shock wave with a dense cloud. We follow mainly the setup presented by (Tóth 2000), which is basically similar to the discussed by (Dai & Woodward 1994b).

The computational domain is the box $[0, 2] \times [0, 1]$. The discontinuity is located at $x = 1.2$ with the left and right states given by

$$\hat{\boldsymbol{u}}_L = \begin{pmatrix} 3.86859 \\ 0.0 \\ 0.0 \\ 0.0 \\ 167.345 \\ 0.0 \\ 2.1826182 \\ -2.1826182 \end{pmatrix}, \quad \hat{\boldsymbol{u}}_R = \begin{pmatrix} 1.0 \\ -11.2536 \\ 0.0 \\ 0.0 \\ 1.0 \\ 0.0 \\ 0.56418958 \\ 0.56418958 \end{pmatrix}. \tag{4.28}$$

The cloud is assumed to be a high-density cylinder, which center is located at $(1.6, 0.5)$. Its radius is $r = 0.15$, and its density and pressure are $\rho = 10.0$, $p = 1.0$. The cloud is in hydrostatic equilibrium with the ambient gas. An adiabatic equation of state with $\gamma = 5/3$ is considered. At the boundaries of the domain we consider transmissive boundary conditions. The end simulation time is $t = 0.1$, and in the figure 4.18 are depicted the density and gas pressure at time $t = 0.1$, when the MHD equations were solved with the RKFD scheme (top), and RKFV scheme (bottom), both with WENO7 reconstruction on a grid with 600×600 points/cells. The WENO3 as shock capturing was employed in both computations. The CFL condition was set to CFL $= 0.95$. Observe that the numerical results are quite similar each other.

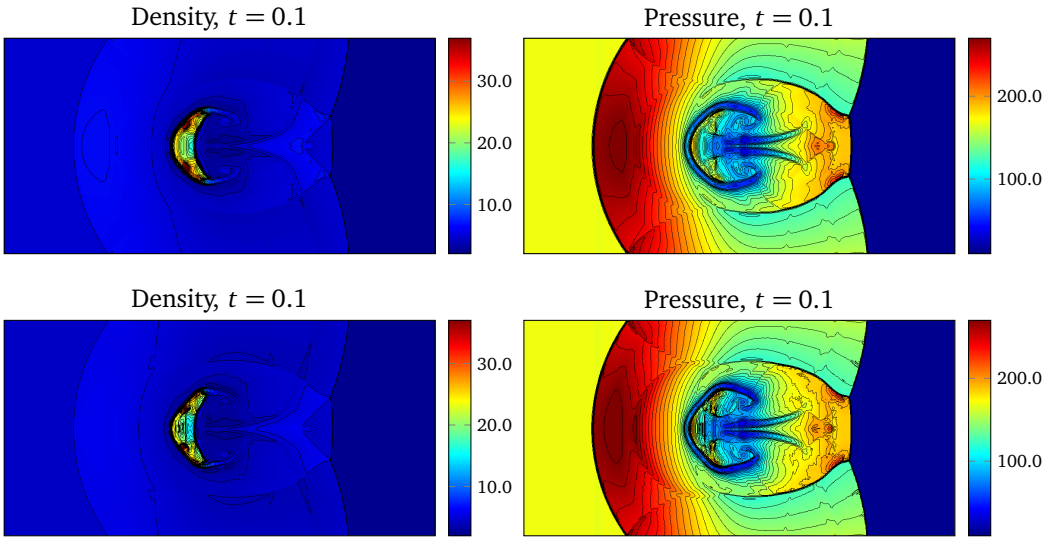

Figure 4.18: Cloud-shock interaction. Contour plots of the density (left) and pressure (right) at time $t = 0.10$. The solutions were calculated with the RKFD-WENO7 and RKFV-WENO7 schemes, both using the WENO3 as shock capturing. The computational domain is the box $[0, 2] \times [0, 1]$, and it is made of 800×400 grid points/cells.

Kelvin-Helmholtz Instability

The Kelvin-Helmholtz instability occurs when a perturbation is introduced to a system with a velocity shear. Here, we run this test problem to demonstrate the algorithm's ability to evolve a linear perturbation into nonlinear magnetohydrodynamic turbulence. As a test of the linear regime, one can compare the growth rate of the instability with the analytic result before the instability becomes nonlinear. A single mode perturbation is needed for such a comparison.

The computational domain is the box $[-0.5, +0.5] \times [-0.5, +0.5]$. The density is set to $\rho = 1.0$ for $|y| \leq 0.25$, and $\rho = 2.0$ for $|y| < 0.25$. We set the pressure uniform in the whole domain, with $p = 2.5$. We set $v_x = 0.5$ if $|y| \leq 0.25$, and $v_x = -0.5$ if $|y| < 0.25$. The shear velocity is given by

$$v_x(x) = \begin{cases} +v_{\text{shear}} + A_0 \sin(2\pi x), & \text{if } y \geq 0.25; \\ -v_{\text{shear}} - A_0 \sin(2\pi x), & \text{if } y < 0.25; \end{cases} \tag{4.29}$$

where $v_{\text{shear}} = 0.5$. The instability is seeded by adding a small perturbation in the transverse component of the velocity,

$$v_y(x) = \begin{cases} +A_0 \sin(2\pi x), & \text{if } y \geq 0.25; \\ -A_0 \sin(2\pi x), & \text{if } y < 0.25; \end{cases} \tag{4.30}$$

where $A_0 = 0.01$ is the perturbation amplitude. The components of the magnetic field are given by $B_x = 0.2$, and $B_y = B_z = 0$. An adiabatic equation of state with $\gamma = 7/5$ is considered. At the boundaries of the domain we consider periodic boundary conditions.

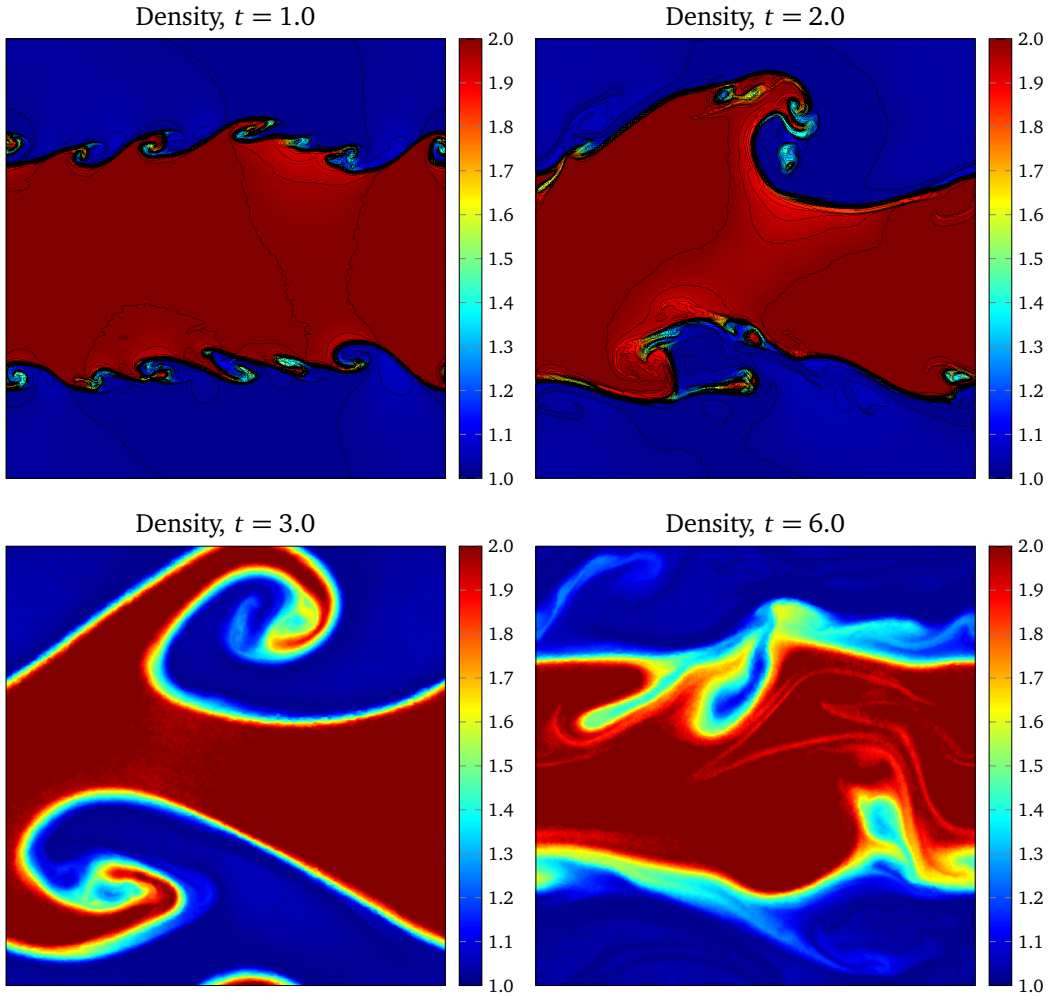

Figure 4.19: Kelvin-Helmholtz instability. Contour plots of the density at times $t = 1.00$, $t = 2.00$, $t = 3.00$, and $t = 6.00$. The calculations were performed with a RKFD-WENO7 scheme (top-left), a RKFV-WENO7 scheme (top-right) on a mesh made of 600×600 grid points/cells, and a RKDG with $N = 5$ and hybrid DG/FV-WENO3 shock capturing on a mesh of 120×120 elements. The computational domain is the box $[-0.5, +0.5] \times [-0.5, +0.5]$.

The computational domain is decomposed into 600×600 cells. The WENO7 reconstruction is used in smooth parts of the flow and the WENO3 in regions with discontinuities. The divergence cleaning of (Dedner et al. 2002) was used. The CFL condition was set to CFL $= 0.95$. The simulation is run until $t = 6.0$, and in the figure 4.19 are depicted the density at times $t \in \{1.0, 2.0, 3.0, 6.0\}$.

CHAPTER 5

Relativistic Hydrodynamics

This chapter covers the extension of the conservative finite difference, finite volume, and discontinuous Galerkin methods to relativistic hydrodynamics. After giving a short introduction on the special relativistic hydrodynamics equations, their spectral decomposition, and the algorithm for dealing with the conservative-to-primitive variables conversion, we present numerical computations obtained with very high-order numerical schemes. Of special interest are the one-dimensional Riemann problems, two-dimensional Riemann problems, the cloud-shock interaction, the relativistic double Mach reflection problem, the relativistic Kelvin-Helmholtz instability, and the propagation of a relativistic jet.

5.1. Introduction

High energy astrophysical phenomena involve, in many cases, relativistic flows. Typical examples are superluminal motion of relativistic jets in extragalactic radio sources, accretion flows around massive compact objects, pulsar winds and gamma-ray bursts. In this work, we are interested in those flows which involve special relativistic hydrodynamics. The modeling of the phenomena mentioned above has prompted the search for efficient and accurate numerical formulations of the special relativistic fluid equations (for an excellent review, see Martí & Müller (2003)). There is now a strong consensus that the so-called High-Resolution Shock-Capturing (HRSC) schemes provide the necessary tools in developing stable and robust relativistic fluid dynamical codes (Schneider et al. 1993; Dolezal & Wong 1995; Martí et al. 1996; Aloy et al. 1999a; Aloy et al. 1999b; Mignone & Bodo 2005; Choi & Ryu 2005; Dönmez & Kayali 2006; Dönmez 2006). One of the fundamental ingredients of such schemes is the exact or approximate solution to the Riemann problem. The solution to the Riemann problem in special relativistic hydrodynamics (SRHD) has been extensively studied in literature, and an exact solution can be found within high degree of accuracy by iterative techniques (see Martí & Müller (1994), Pons et al. (2000), Rezzolla & Zanotti (2001), and Rezzolla et al. (2003)). One of the major differences with the classical counterpart is the velocity coupling introduced by the Lorentz factor and the coupling of the latter with the specific enthalpy. This considerably adds to the computational cost, making the use of an exact solver code prohibitive in a multidimensional Godunov-type code (LeVeque et al. 1998).

The relativistic hydrodynamics have received a lot of attention over the last years from the high-order methods community. Some effort has been put into solving the equations with methods based on the WENO reconstruction procedure, as in, for example, the finite volume code by Tchekhovskoy et al. (2007), the finite difference code by Radice & Rezzolla (2012), or the discontinuous Galerkin by Dumbser et al. (2008) and by Radice & Rezzolla (2011). We have to mention that for DG-based codes there is a lot of work to do, especially for shock capturing methods. The robustness of DG methods is lost when shocks take place in the simulations, and some ideas from the finite volume methods have been implemented in order to tackle this problem.

5.2. Equations

5.2.1. Equations in covariant form

In relativistic hydrodynamics the information on the system is encoded in its thermodynamic properties, i.e., its equation of state. Besides, relativistic hydrodynamics relies on only one assumption: local thermodynamic equilibrium. No other assumption is made concerning the nature of the particles and fields, their interactions, the classical/quantum nature of the phenomena involved (Ollitrault 2008).

Standard thermodynamics is about a system in global thermodynamic equilibrium. This means that intensive parameters (p, T, h) are constant throughout the volume, and also that the system is globally at rest, which means that its total momentum is 0. In this section, we study systems whose pressure and temperature vary with space and time, and which are not at rest. We however request that the system is in *local* thermodynamic equilibrium, which means that pressure and temperature are varying so slowly that for any point, one can assume thermodynamic equilibrium in some neighborhood about that point. There is, however, a general condition for local thermodynamic equilibrium to apply, which is that the mean free path of a particle between two collisions is much smaller than all the characteristic dimensions of the system. The fluid equations derived under the assumption of local thermodynamic equilibrium are called inviscid, or ideal-fluid, equations (Weinberg 1972).

All thermodynamic quantities associated with a fluid element (for example, ρ, p and n) are defined in the rest frame. The rest frame of a fluid element is the Galilean frame in which its momentum vanishes. They are therefore Lorentz scalars by construction. Local thermodynamic equilibrium implies that the fluid element has isotropic properties in the fluid rest frame. This is a very strong assumption. It is, in fact, the only non-trivial assumption of inviscid hydrodynamics.

In non-relativistic fluid dynamics the equation of mass conservation is

$$\frac{\partial \rho}{\partial t} + \nabla \cdot (\rho \boldsymbol{v}) = 0, \tag{5.1}$$

where ρ is the mass density. A relativistic conservation equation must take into account

the Lorentz contraction of the volume by a factor u^0. Recall that the baryon density n is always defined in the fluid rest frame. The baryon density in the moving frame is therefore nu^0. Replacing ρ with nu^0 in the above equation and using $\boldsymbol{u} = u^0\boldsymbol{v}$, one obtains the following covariant equation (Ollitrault 2008)

$$\partial_\mu(nu^\mu) = 0. \tag{5.2}$$

This is a conservation equation for the 4-vector nu^μ. nu^0 is the baryon density, and $n\boldsymbol{u}$ is the baryon flux.

In the rest frame of the fluid, the baryon flux vanishes. In non-relativistic fluid dynamics, this is how the fluid rest frame is defined. In the relativistic case, the baryon flux could in principle be $\neq 0$ in the fluid rest frame, defined as the frame where the momentum density is zero: the momentum of baryons could be compensated by the momentum of baryonless particles (pions, gluons). However, local thermodynamic equilibrium implies isotropy. If there was a non-zero current, it would define a direction in space and isotropy would be lost. The baryon flux therefore vanishes in inviscid hydrodynamics. In relativistic viscous hydrodynamics, which studies deviations from local thermodynamic equilibrium, the baryon flux may be non-zero in the local rest frame: this transport phenomenon is called diffusion.

The conservation of total energy and momentum yields 4 local conservation equations, each of which is analogous to the equation of baryon-number conservation. Baryon conservation gives a conserved current, which is a contravariant 4-vector $J^\mu = nu^\mu$. Energy and momentum are also a contravariant 4-vector, therefore the associated conserved currents can be written as a contravariant tensor $T^{\mu\nu}$, where each value of ν corresponds to a component of the 4-momentum, and each value of μ is a component of the associated current (Misner et al. 1973). Specifically,

- T^{00} is the energy density.
- T^{0j} is the density of the j^{th} component of momentum, with $j = 1, 2, 3$.
- T^{i0} is the energy flux along axis i.
- T^{ij} is the flux along axis i of the j^{th} component of momentum.

In the fluid rest frame, the assumption of local thermodynamic equilibrium strongly constrains the energy-momentum tensor. Isotropy implies that the energy flux T^{i0} and the momentum density T^{0j} vanish. In addition, it implies that the pressure tensor is proportional to the identity matrix, i.e., $T^{ij} = p\delta^{ij}$, where p is the thermodynamic pressure. The energy-momentum in the fluid rest frame is thus

$$T^{\mu\nu}_{(0)} \doteq \begin{pmatrix} \rho & 0 & 0 & 0 \\ 0 & p & 0 & 0 \\ 0 & 0 & p & 0 \\ 0 & 0 & 0 & p \end{pmatrix}, \tag{5.3}$$

where the subscript 0 refers to the fluid rest frame. In order to obtain the energy-momentum tensor in a moving frame, one applies a Lorentz transformation

$$T^{\mu\nu} = \Lambda_{\alpha}{}^{\mu}\Lambda^{\nu}{}_{\beta}T^{\alpha\beta}_{(0)}. \tag{5.4}$$

The components of the momentum-energy tensor are

$$T^{\mu\nu} = (\rho + p)u^{\mu}u^{\nu} + p\eta^{\mu\nu} \tag{5.5}$$

where $\eta^{\mu\nu} \equiv \mathrm{diag}(-1,+1,+1,+1)$ is the Minkowski metric tensor. The symmetry of $T^{\mu\nu}$ is a nontrivial consequence of relativity. In non-relativistic fluid dynamics, the energy flux and the momentum density differ. (Recall that non-relativistic energy does not include mass energy).

The conservation equations of energy and momentum are

$$\partial_{\mu}T^{\mu\nu} = 0. \tag{5.6}$$

Equations (5.2), (5.5) and (5.6) are the equations of inviscid relativistic hydrodynamics. Together with the equation of state of the fluid, they form a closed system of equations.

5.2.2. Equations in conservative form

Considering the Minkowski spacetime with Cartesian coordinates (t,x,y,z), the conservation equations (5.2) and (5.6) form a system of conservation laws which can be written as (see Font et al. (1994), Mignone et al. (2005), and Ryu et al. (2006))

$$\frac{\partial D}{\partial t} + \nabla\cdot(D\boldsymbol{v}) = 0, \tag{5.7a}$$

$$\frac{\partial \boldsymbol{S}}{\partial t} + \nabla\cdot(\boldsymbol{S}\otimes\boldsymbol{v} + p\mathbb{I}) = \boldsymbol{0}, \tag{5.7b}$$

$$\frac{\partial E}{\partial t} + \nabla\cdot\boldsymbol{S} = 0. \tag{5.7c}$$

5.2.3. Variables Transformations

The five conserved quantities D, S_x, S_y, S_z and E are the mass density, the three components of the momentum density, and the total energy density, respectively. They are all measured in the laboratory frame, and are related to quantities in the local rest frame of the fluid (primitive variables (ρ, v_x, v_y, v_z, p)) through

$$D = \rho\Gamma, \tag{5.8a}$$

$$\boldsymbol{S} = \rho h\Gamma^2\boldsymbol{v}, \tag{5.8b}$$

$$E = \rho h\Gamma^2 - p, \tag{5.8c}$$

where $\boldsymbol{v}$ is the three-velocity of the fluid and is related with the four-velocity $\mathbf{u}$ through

$$\mathbf{u} = \Gamma\big(1,\boldsymbol{v}\big) \tag{5.9}$$

where Γ is the Lorentz factor defined by

$$\Gamma = \frac{1}{\sqrt{1-v^2}}, \tag{5.10}$$

ρ is the rest-mass density, p is the isotropic gas pressure and h is the specific enthalpy. The velocity $\boldsymbol{v} = (v_x, v_y, v_z)$ of a fluid element is defined as the velocity of the rest frame of this fluid element with respect to the laboratory frame. The fluid velocity is a function of (t, x, y, z), as are the thermodynamic quantities ρ, p and n. The fluid velocity is also referred to as the "collective" velocity.

The system (5.7) of partial differential equations is closed with an equation of state $h = h(p, \rho)$ or $p = p(\rho, \varepsilon)$. The system (5.7) is hyperbolic for causal equations of state (Anile 1989; Rezzolla & Zanotti 2013), i.e., for those where the local sound speed satisfies $c_s < 1$, where c_s is defined by

$$hc_s^2 = -\rho \frac{\partial h}{\partial \rho} \left(\rho \frac{\partial h}{\partial p} - 1 \right)^{-1}, \tag{5.11}$$

In this work, we employ the most commonly used equation of state, the ideal gas equation of state, which is given by

$$p = (\gamma - 1)(\varepsilon - \rho), \quad \text{or} \quad h = 1 + \frac{\gamma}{\gamma - 1} \frac{p}{\rho}. \tag{5.12}$$

Here $\gamma = c_p/c_v$ is the ratio of specific heats and ε is the sum of the internal and rest-mass energy densities in the local frame and is related to the specific enthalpy as

$$h = \frac{\varepsilon + p}{\rho}. \tag{5.13}$$

In this way, the speed of sound is given by

$$c_s^2 = \frac{\gamma p}{\rho h} \tag{5.14}$$

Algorithm to recover the primitive variables

Compared to the classical hydrodynamics equations, also known as Euler equations, in the relativistic hydrodynamics system, the relation between the primitive and conservative variables is not so simple. In this work two strategies for expressing the primitive variables in terms of the conservative ones were followed: The first one, by solving iteratively an equation for the pressure and then determining the other variables from this (Mignone et al. 2005). The second one, which is most robust, consists in solving a quartic equation on the velocity v (as it outlined in references (Schneider et al. 1993), (Duncan & Hughes 1994), (Ryu et al. 2006)). Though this last one is more computationally expensive, it provides more accurate results and does not have the problem of

the iterative method with the initial guess of the pressure. In our algorithm, we combine both strategies in such way, that when the first one fails to find iteratively a root, we proceed to use the second algorithm. Only in very rare cases, for instance, when strong shocks are involved, the second algorithm is employed. This approach seems to be the most robust even for multidimensional flow simulations.

Solving numerically with Newton-Raphson

Here we follow the approach given by Mignone et al. (2005). The primitive variables (ρ, v_x, v_y, v_z, p) are computed from the conservative quantities

$$D = \rho\Gamma, \tag{5.15a}$$
$$\boldsymbol{S} = \rho h\Gamma^2 \boldsymbol{v}, \tag{5.15b}$$
$$E = \rho h\Gamma^2 - p, \tag{5.15c}$$

by solving with the one-dimensional Newton-Raphson algorithm

$$\frac{\partial f^n(p)}{\partial p}\delta p^{n+1} = f^n(p), \tag{5.16}$$

the implicit equation

$$f(p) = Dh\Gamma - E - p = 0, \tag{5.17}$$

with $f'(p)$ given by

$$\frac{\mathrm{d}f(p)}{\mathrm{d}p} = \frac{\gamma}{\gamma-1}\Gamma^2 - \frac{S^2\Gamma^3}{(E+p)^3}\left(D + \frac{\gamma}{\gamma-1}2p\Gamma\right) - 1, \tag{5.18}$$

where the Lorentz factor is defined by

$$\Gamma_* = \frac{1}{\sqrt{1 - \boldsymbol{v}_* \cdot \boldsymbol{v}_*}}, \tag{5.19}$$

and the components of the velocity are

$$\boldsymbol{v}_* = \frac{\boldsymbol{S}}{E+p}. \tag{5.20}$$

Solving analytically a quartic polynomial on v

Here we follow the approach initially presented in Schneider et al. (1993) and further used by Choi & Ryu (2005) and Ryu et al. (2006). First, we have to derive a quartic polynomial in v starting from the magnitude of the momentum

$$S = \rho h\Gamma^2 v. \tag{5.21}$$

Replacing ρh with the given definition of enthalpy $h(\rho, p)$ and using $D = \rho\Gamma$ we found that

$$S = D\Gamma v + \hat{\gamma} p \Gamma^2 v, \quad \text{with } \hat{\gamma} = \frac{\gamma}{\gamma - 1}. \tag{5.22}$$

Now, using the same trick with the equation of the energy, we can get p as a function of E, D and Γ

$$p = \frac{E - D\Gamma}{\hat{\gamma}\Gamma^2 - 1}. \tag{5.23}$$

From this, the magnitude of the momentum vector becomes

$$S = D\Gamma v + \hat{\gamma}\Gamma^2 v \frac{E - D\Gamma}{\hat{\gamma}\Gamma^2 - 1}, \tag{5.24}$$

and finally readily a quartic polynomial for v is obtained

$$f(v) = \left[\gamma v (E - Sv) - S\left(1 - v^2\right)\right]^2 - \left(1 - v^2\right) v^2 (\gamma - 1)^2 D^2 = 0. \tag{5.25}$$

Schneider et al. (1993) showed that the physically meaningful solution for v is between the lower limit, v_1, and the upper limit, v_2,

$$v_1 = \frac{\gamma E - \sqrt{(\gamma E)^2 - 4(\gamma - 1) S^2}}{2(\gamma - 1) S}, \quad v_2 = \frac{S}{E}, \tag{5.26}$$

and that the solution is unique. Once v is known, the quantities ρ, v_i, and ε can be straightforwardly calculated from the following relations

$$\rho = \frac{D}{\Gamma}, \tag{5.27a}$$

$$v_x = \frac{S_x}{S} v, \tag{5.27b}$$

$$v_y = \frac{S_y}{S} v, \tag{5.27c}$$

$$v_z = \frac{S_z}{S} v, \tag{5.27d}$$

$$\varepsilon = E - S_x v_x - S_y v_y - S_z v_z. \tag{5.27e}$$

that is,

$$p = (\gamma - 1)\left[(E - S_x v_x - S_y v_y - S_z v_z) - \rho\right]. \tag{5.28}$$

5.3. Spectral Decomposition

In this section we will present the spectral decomposition of the Jacobian matrices of the system, $\mathcal{B}_i$, for the relativistic hydrodynamics equations. These matrices are defined by

$$\mathcal{B}_i = \frac{\partial \mathbf{f}_i(\boldsymbol{u})}{\partial \boldsymbol{u}}, \quad (i = x, y, z), \tag{5.29}$$

where the state vector of conservative variables $\boldsymbol{u}$ and the components of the tensor of physical fluxes $\mathbf{f} = [\boldsymbol{f}, \boldsymbol{g}, \boldsymbol{h}]$ in the conservation law

$$\frac{\partial \boldsymbol{u}}{\partial t} + \frac{\partial \boldsymbol{f}(\boldsymbol{u})}{\partial x} + \frac{\partial \boldsymbol{g}(\boldsymbol{u})}{\partial y} + \frac{\partial \boldsymbol{h}(\boldsymbol{u})}{\partial z} = \mathbf{0}, \tag{5.30}$$

are defined as

$$\boldsymbol{u} = \begin{pmatrix} D \\ S_x \\ S_y \\ S_z \\ E \end{pmatrix}, \quad \mathbf{f}_i = \begin{pmatrix} Dv_i \\ S_x v_i + p\delta_{xi} \\ S_y v_i + p\delta_{yi} \\ S_z v_i + p\delta_{zi} \\ S_i \end{pmatrix}, \quad (i = x, y, z). \tag{5.31}$$

We present the spectral decomposition of the Jacobian matrices of the relativistic Euler equations with a ideal gas equation of state in the x-direction, $\mathcal{B}_x$, whereas the cases y and z easily follows from symmetry. The eigenvalues of $\mathcal{B}_x$ are

$$\lambda_- = \frac{1}{1-\boldsymbol{v}^2 c_s^2}\left\{ v_x(1-c_s^2) - c_s\sqrt{(1-\boldsymbol{v}^2)\left[1 - v_x v_x - (\boldsymbol{v}^2 - v_x v_x)c_s^2\right]}\right\} \tag{5.32}$$

$$\lambda_1 = v_x \tag{5.33}$$

$$\lambda_2 = v_x \tag{5.34}$$

$$\lambda_3 = v_x \tag{5.35}$$

$$\lambda_+ = \frac{1}{1-\boldsymbol{v}^2 c_s^2}\left\{ v_x(1-c_s^2) + c_s\sqrt{(1-\boldsymbol{v}^2)\left[1 - v_x v_x - (\boldsymbol{v}^2 - v_x v_x)c_s^2\right]}\right\} \tag{5.36}$$

The eigenvalues represent the five characteristic speeds associated with two sound wave modes (λ_- and λ_+) and three entropy modes ($\lambda_1, \lambda_2, \lambda_3$).

$$\lambda_- < \lambda_1 = \lambda_2 = \lambda_3 < \lambda_+. \tag{5.37}$$

The corresponding complete set of right-eigenvectors is

$$\boldsymbol{r}_1 = \frac{\Gamma^2}{\gamma c_s^2(1-v_x v_x)} \begin{pmatrix} \left[\gamma c_s^2(\boldsymbol{v}^2 - v_x v_x) + (1 - v_x v_x)\right]/h\Gamma \\ \left[2\gamma c_s^2(\boldsymbol{v}^2 - v_x v_x) + (1-\gamma c_s^2)(1 - v_x v_x)\right] v_x \\ \left[\gamma c_s^2(\boldsymbol{v}^2 - v_x v_x) + (1 - v_x v_x)\right] v_y \\ \left[\gamma c_s^2(\boldsymbol{v}^2 - v_x v_x) + (1 - v_x v_x)\right] v_y \\ 2\gamma c_s^2(\boldsymbol{v}^2 - v_x v_x) + (1-\gamma c_s^2)(1 - v_x v_x) \end{pmatrix}, \tag{5.38}$$

$$\boldsymbol{r}_2 = \frac{1}{1-v_x v_x} \begin{pmatrix} v_y/h\Gamma \\ 2v_x v_y \\ 1 - v_x v_x + v_y v_y \\ v_y v_z \\ 2v_y \end{pmatrix}, \tag{5.39}$$

$$\boldsymbol{r}_3 = \frac{1}{1-v_x v_x}\begin{pmatrix} v_z/h\Gamma \\ 2v_x v_z \\ v_y v_z \\ 1-v_x v_x + v_z v_z \\ 2v_z \end{pmatrix}, \tag{5.40}$$

$$\boldsymbol{r}_\pm = \begin{pmatrix} (1-\lambda_\pm v_x)/\Gamma \\ h(1-v_x v_x)\lambda_\pm \\ h(1-\lambda_\pm v_x)v_y \\ h(1-\lambda_\pm v_x)v_z \\ h(1-v_x v_x) \end{pmatrix}, \tag{5.41}$$

The corresponding complete set of left-eigenvectors, which are orthonormal to the right eigenvectors, is

$$\boldsymbol{l}_1 = \begin{pmatrix} h/\Gamma \\ v_x \\ v_y \\ v_z \\ -1 \end{pmatrix}, \tag{5.42}$$

$$\boldsymbol{l}_2 = \begin{pmatrix} -h\Gamma v_y \\ 0 \\ 1 \\ 0 \\ 0 \end{pmatrix}, \tag{5.43}$$

$$\boldsymbol{l}_3 = \frac{W}{h-1}\begin{pmatrix} -h\Gamma v_z \\ 0 \\ 0 \\ 1 \\ 0 \end{pmatrix}, \tag{5.44}$$

$$\boldsymbol{l}_\pm = \frac{1}{\Delta_\pm}\begin{pmatrix} -h(1-\lambda_\pm v_x)(1-\gamma c_s^2)/\Gamma \\ \gamma\lambda_\pm(1-c_s^2\boldsymbol{v}^2) + \lambda_\pm(1+\gamma c_s^2)v_x v_x - (1+\gamma)v_x \\ -(1+\gamma c_s^2)(1-\lambda_\pm v_x)v_y \\ -(1+\gamma c_s^2)(1-\lambda_\pm v_x)v_z \\ (1+\gamma c_s^2\boldsymbol{v}^2) + (1-c_s^2)\gamma v_x v_x - \lambda_\pm(1+\gamma)v_x \end{pmatrix}, \tag{5.45}$$

where $\Delta_\pm$ is defined by

$$\Delta_\pm = h\gamma\left[(\lambda_\pm - v_x)^2\left(1-v_x v_x - (\boldsymbol{v}^2 - v_x v_x)c_s^2\right) + \frac{c_s^2}{\Gamma^2}\right]. \tag{5.46}$$

5.4. Numerical Benchmarking

5.4.1. Smooth Problem

With this test we want to check the order of accuracy of the numerical schemes discussed in this work, namely, the RKFD, the RKFV, and the RKDG methods. For this purpose, we solve a two-dimensional smooth problem with a wave propagating in the physical domain $[0, 2/\sqrt{2}] \times [0, 2]$ at an angle $\theta = 30^\circ$ relative to the horizontal axis. Following He & Tang (2012a), the initial profile is given by

$$\rho = 1 + A\sin\big(2\pi(x\cos\theta + y\sin\theta)\big), \tag{5.47}$$
$$v_x = v_0, \tag{5.48}$$
$$v_y = 0.0, \tag{5.49}$$
$$p = 1.0, \tag{5.50}$$

with $A = 0.2$, and $v_0 = 0.2$. This problem has the exact solution

$$\rho = 1 + A\sin\big[2\pi\big((x\cos\theta + y\sin\theta) - (v_x\cos\theta + v_y\sin\theta)t\big)\big], \tag{5.51}$$
$$v_x = v_0, \tag{5.52}$$
$$v_y = 0.0, \tag{5.53}$$
$$p = 1.0. \tag{5.54}$$

The discretization of the computational domain satisfy $N_y = 2N_x$, and periodic boundary conditions are set all four faces of the domain. In the tables 5.1 and 5.2 are shown the convergence rates for the RKFD, RKFV and RKDG methods. All numerical methods (RKFD, RKFV, and RKDG) converge to the theoretical order of convergence. Observe that for the RKDG method only a few cells were enough to obtain the experimental order of convergence.

5.4.2. One-dimensional Problems

In this section we consider some standard one-dimensional Riemann problems extensively used in relativistic hydrodynamics. The Riemann problem is an initial-value problem for a conservation law defined as

$$\begin{aligned} &\frac{\partial \boldsymbol{u}}{\partial t} + \frac{\partial \boldsymbol{f}(\boldsymbol{u})}{\partial x} = \boldsymbol{0}, \\ &\boldsymbol{u}(x,0) = \begin{cases} \boldsymbol{u}_L(x) & \text{for } x < x_m, \\ \boldsymbol{u}_R(x) & \text{for } x > x_m, \end{cases} \end{aligned} \tag{5.55}$$

where x_m is the position of the initial discontinuity. For all examples here discussed, the one-dimensional domain is the closed interval $[0, 1]$. The membrane is localized in the point $x_m = 0.5$. The initial condition for the Riemann problems is characterized for the two piecewise constant states written in conservative variables $\boldsymbol{u}_L$ and $\boldsymbol{u}_R$ at left and right

Table 5.1: Convergence rates for the SRHD equations with initial condition given by the *smooth flow problem*. The base numerical methods are the RKFD and the RKFV schemes. In these calculations we have employed the Rusanov Riemann solver. Results for L_2 norm error of the rest-mass density are provided, with reconstruction operator WENO3, WENO5 and WENO7. Simulation time was set to $t = 1.0$.

Reconstruction	Cells	L_2 error (FD)	L_2 order (FD)	L_2 error (FV)	L_2 order (FV)
WENO3	40×20	3.837×10^{-4}		2.895×10^{-4}	
	80×40	4.646×10^{-5}	3.045	3.984×10^{-5}	2.861
	160×80	5.387×10^{-6}	3.108	5.278×10^{-6}	2.916
	320×160	6.106×10^{-7}	3.141	6.383×10^{-7}	3.047
WENO5	40×20	4.743×10^{-6}		3.542×10^{-6}	
	80×40	1.331×10^{-7}	5.154	1.123×10^{-7}	4.978
	160×80	3.893×10^{-9}	5.095	3.543×10^{-9}	4.987
	320×160	8.654×10^{-11}	5.491	9.698×10^{-11}	5.191
WENO7	40×20	1.697×10^{-8}		9.274×10^{-8}	
	80×40	2.246×10^{-10}	6.239	6.845×10^{-10}	7.081
	160×80	2.515×10^{-12}	6.480	5.345×10^{-12}	7.000
	320×160	1.769×10^{-14}	7.151	3.856×10^{-14}	7.115

Table 5.2: Convergence rates for the SRHD equations with initial condition given by the *smooth flow problem*. The base numerical scheme is the RKDG method. In these calculations we have employed the Rusanov Riemann solver. Results for L_2 norm error of the rest-mass density are provided, and for polynomial degree $N = 1, 3, 5$. Simulation time was set to $t = 1.0$.

Method	Elements	L_2 error	L_2 order
DGSEM $\mathcal{P}1$	4×4	1.10×10^{-1}	
	8×8	2.10×10^{-2}	2.39
	16×16	3.86×10^{-3}	2.44
	32×32	8.12×10^{-4}	2.24
DGSEM $\mathcal{P}3$	4×4	1.37×10^{-3}	
	8×8	7.08×10^{-5}	4.27
	16×16	6.88×10^{-6}	3.36
	32×32	4.05×10^{-7}	4.08
DGSEM $\mathcal{P}5$	2×2	8.88×10^{-4}	
	4×4	1.38×10^{-6}	6.00
	8×8	6.56×10^{-8}	7.72
	16×16	1.14×10^{-9}	5.84

sides of the membrane, respectively. After the breakup of the membrane, different shock patterns are originated. The problems below discussed have been used as benchmark in most of the relativistic codes found in the literature. We refer to Martí & Müller (2003) for a comprehensive review of relativistic hydrodynamics in special relativity, with a special chapter dedicated to the Riemann problems used here as benchmark, and additionally a detailed literature survey about the numerical methods employed for their solution.

The numerical calculations with high-order schemes are contrasted with the exact solution obtained by using the exact Riemann solver provided by Rezzolla & Zanotti (2001). In the following, we will write all initial states in primitive variables. The left state will be represented by $\hat{\boldsymbol{u}}_L = \big(\rho, v_x, v_y, p\big)_L$ and the right state by $\hat{\boldsymbol{u}}_R = \big(\rho, v_x, v_y, p\big)_R$, where v_y can be interpreted as the tangential velocity in the problem. The computational domain is decomposed into 500 grid points for the RKFD method, 500 cells for the RKFV method and 500 elements for the RKDG method. The numerical results discussed below were obtained with a high-order WENO7 reconstruction for the RKFD and RKFV methods, and with a polynomial $N = 6$ for the RKDG scheme. All computations used the shock capturing strategy outlined in section 3.2, that is, for the RKFD and the RKFV we use the WENO3 reconstruction operator for those regions with shocks, and for the RKDG scheme we use a hybrid DG/FV scheme with WENO3 reconstruction. The exact solution of the Riemann problems is plotted as red lines. The description of the flow patterns is presented below together with some comments regarding the capabilities of the **XTROEM** code for solving relativistic shock-dominated flows.

Riemann Problem 1

We start the benchmarking with a Riemann problem characterized with the left and right states given by

$$\begin{aligned} \hat{\boldsymbol{u}}_L &= \big(1.0, 0.9, 0.0, 1.0\big), \\ \hat{\boldsymbol{u}}_R &= \big(1.0, 0.0, 0.0, 10.0\big). \end{aligned} \tag{5.56}$$

After the breakup of the membrane, one left-going and one right-going shock waves are formed, being separated by a contact discontinuity. We have employed the ideal gas equation of state with adiabatic index $\gamma = 4/3$. Transmissive boundary conditions at both left and right sides of the computational domain are used. For all methods we have set the CFL condition to CFL $= 0.95$. Plots of the rest-mass density, pressure, the x-component of the velocity, and the Lorentz factor at the final simulation time $t = 0.40$ are depicted in the figure 5.1. We point out that in spite of using the Rusanov numerical flux for the RKFV/RKDG methods and the the Lax-Friedrichs splitting for the RKFD method, the results are in good agreement with the exact solution. The contact discontinuity is not very well resolved for all numerical methods because the Riemann solver employed is too diffusive. The RKDG with $N = 6$ and hybrid DG/FV-WENO3 shock capturing presents an outstanding resolution of the solution. In fact, the RKFD and RKFV methods show

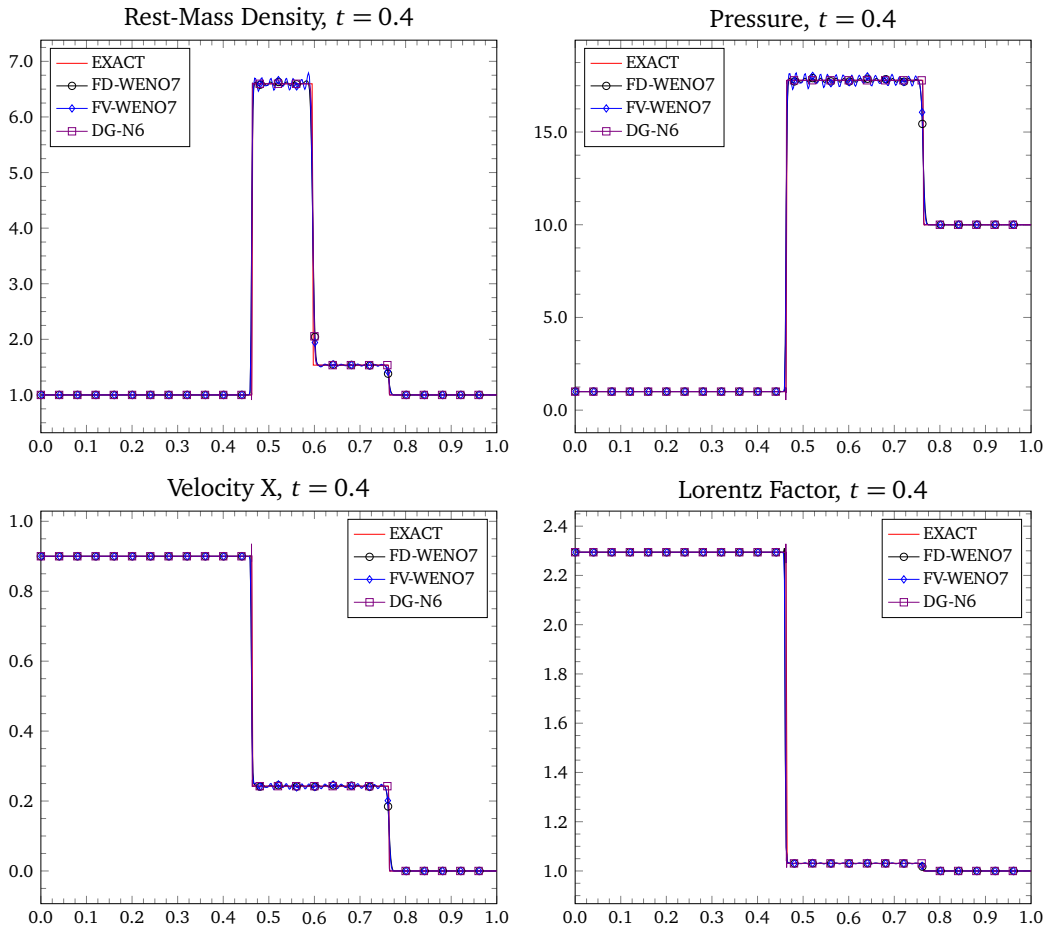

Figure 5.1: Riemann problem 1. The left and right states are given by equation (5.56). The final simulation time is $t = 0.40$. Plots of the rest-mass density, pressure, the x-component of the velocity, and the Lorentz factor are depicted. For the RKFD and RKFV, the WENO7 reconstruction is used in smooth parts of the flow and the WENO3 in regions with shocks. The RKDG is using a polynomial of degree $N = 6$ with the hybrid DG/FV-WENO3 as shock capturing.

many oscillations in the region before the contact discontinuity. The WENO7 operator is responsible for these spurious oscillations.

Riemann Problem 2

In this Riemann problem, the initial condition is determined by the following left and right states

$$\begin{aligned} \hat{\boldsymbol{u}}_L &= \big(1.0, -0.6, 0.0, 10.0\big), \\ \hat{\boldsymbol{u}}_R &= \big(10.0, +0.5, 0.0, 20.0\big). \end{aligned} \tag{5.57}$$

The formed wave pattern includes two rarefaction waves traveling in opposite directions and a contact discontinuity in the middle of these waves. We have utilized the ideal gas equation of state with adiabatic index $\gamma = 5/3$, and set the CFL condition to CFL $= 0.95$

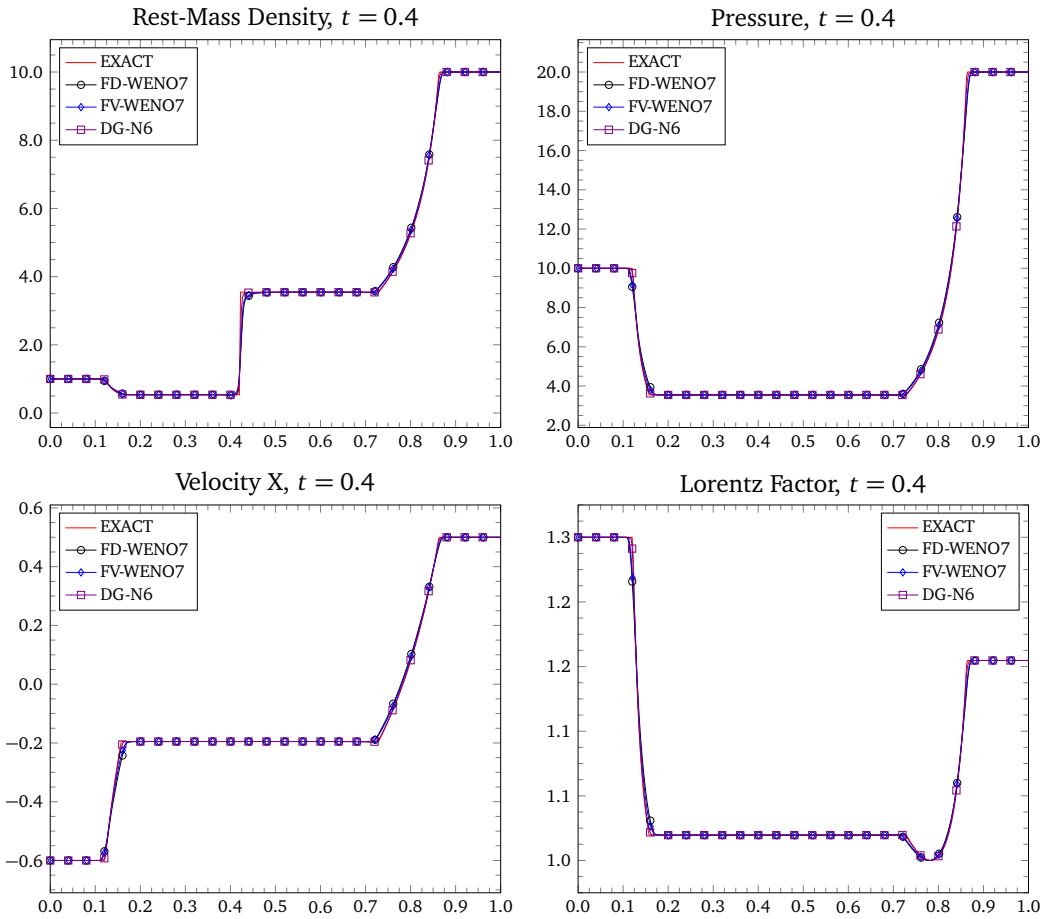

Figure 5.2: Riemann problem 2. The left and right states are given by equation (5.57). The final simulation time is $t = 0.40$. Plots of the rest-mass density, pressure, the x-component of the velocity, and the Lorentz factor are depicted. For the RKFD and RKFV, the WENO7 reconstruction is used in smooth parts of the flow and the WENO3 in regions with shocks. The RKDG is using a polynomial of degree $N = 6$ with the hybrid DG/FV-WENO3 as shock capturing.

for all methods. Transmissive boundary conditions were used at interval edges. Plots of the rest-mass density, pressure, the x-component of the velocity, and the Lorentz factor at simulation time $t = 0.40$ are shown in the figure 5.2. All methods present a very good agreement with the exact solution. The rarefaction waves and the contact discontinuity are very well resolved. There are no spurious oscillations were generated. Due to the subcell resolution of the hybrid DG/FV-WENO3 scheme, this method captures much more better the discontinuities and rarefaction waves than the RKFD and RKFV.

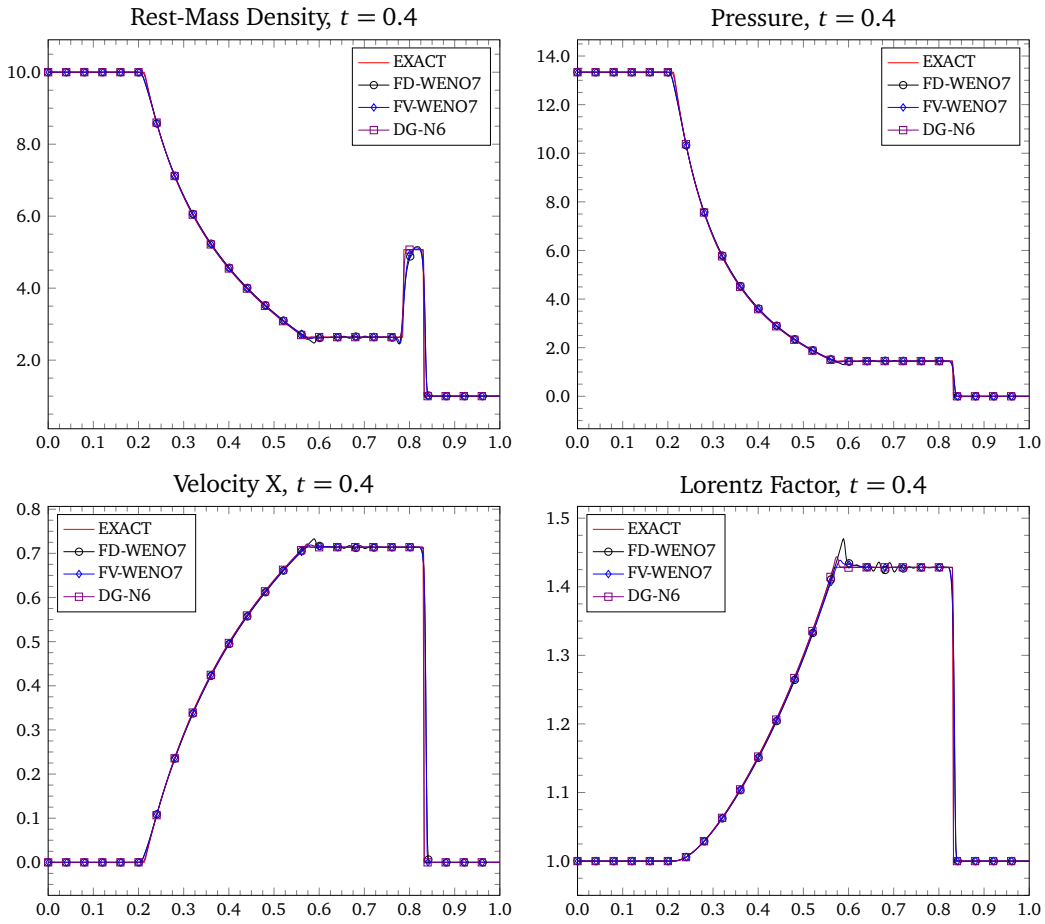

Figure 5.3: Riemann problem 3. The left and right states are given by equation (5.58). The final simulation time is $t = 0.40$. Plots of the rest-mass density, pressure, the x-component of the velocity, and the Lorentz factor are depicted. For the RKFD and RKFV, the WENO7 reconstruction is used in smooth parts of the flow and the WENO3 in regions with shocks. The RKDG is using a polynomial of degree $N = 6$ with the hybrid DG/FV-WENO3 as shock capturing.

Riemann Problem 3: Mildly Relativistic Blast Wave

This test is called also *mildly relativistic blast wave*. The initial condition is determined by the following left and right states

$$\begin{aligned} \hat{\boldsymbol{u}}_L &= \big(10, 0, 0, 40/3\big), \\ \hat{\boldsymbol{u}}_R &= \big(1, 0, 0, 0\big). \end{aligned} \tag{5.58}$$

This test problem has been considered for many authors in the past (Schneider et al. 1993; Martí & Müller 1996; Donat et al. 1998), but it was in Martí & Müller (1994) where an exact solution was first presented. The waves present in this problem are a left-going transonic rarefaction wave, a contact discontinuity and a right-going shock wave. The fluid behind the shock is moving with a mildly relativistic speed $v = 0.72c$ to the right. In this dense shell behind the shock, the fluid is compressed. Because of that, the fluid

is heated to values of the internal energy much larger than the rest-mass energy. This means that the fluid is *thermodynamically* relativistic, but mildly relativistic dynamically. We have employed the ideal gas equation of state with adiabatic index $\gamma = 5/3$. The CFL condition we have used for the computation is CFL $= 0.95$. Transmissive boundary conditions are set at both sides of the interval. The final simulation time is set to $t = 0.4$. In the right state the pressure was set to $2/3 \times 10^{-6}$ for numerical reasons. Plots of the rest-mass density, pressure, and the x-component of the velocity, and the Lorentz factor are depicted in the figure 5.3. Observe that the computation practically lacks oscillations. Only a very small one is clearly visible at $x = 0.57$. All three methods behave excellent for this problem. The employment of the WENO3 operator as shock capturing worked nicely.

Riemann Problem 4: Highly Relativistic Blast Wave

The initial state for the *highly relativistic blast wave* is given by

$$\begin{aligned} \hat{\boldsymbol{u}}_L &= \left(1, 0, 0, 10^3\right), \\ \hat{\boldsymbol{u}}_R &= \left(1, 0, 0, 10^{-2}\right). \end{aligned} \tag{5.59}$$

The decay of the initial discontinuity gives rise to a dense intermediate state located between a right-going shock wave and a rarefaction wave propagating left. The shock wave and the contact discontinuity are very close to each other. The very thin shell is a very challenging feature for any numerical method solving this problem. Actually, in these simulations, and because of the smearing at contact discontinuity, this shell is not well resolved. We have employed the ideal gas equation of state with adiabatic index $\gamma = 5/3$, and CFL number CFL $= 0.95$. Transmissive boundary conditions have been utilized at domain edges. The final simulation time is set to $t = 0.4$. Plots of the rest-mass density, pressure, and the x-component of the velocity, and the Lorentz factor are depicted in the figure 5.4. The RKDG with hybrid DG/FV-WENO3 shock capturing scheme resolved much more better the shock wave and the thin shell. The resolution of this scheme exceeds the provided by the RKFD and RKDG schemes with WENO7 reconstruction.

Riemann Problem 5: Transverse Blast Wave

In the *transverse blast wave* problem, the initial conditions are similar to the Riemann Problem 2, but with the difference that in this problem a non-zero transverse velocity in the right state is introduced. That is, the initial condition is determined by the following left and right states

$$\begin{aligned} \hat{\boldsymbol{u}}_L &= \left(1, 0, 0, 10^3\right), \\ \hat{\boldsymbol{u}}_R &= \left(1, 0, 0.99, 10^{-2}\right). \end{aligned} \tag{5.60}$$

Unlike Newtonian hydrodynamics, where the transverse momentum is not coupled with

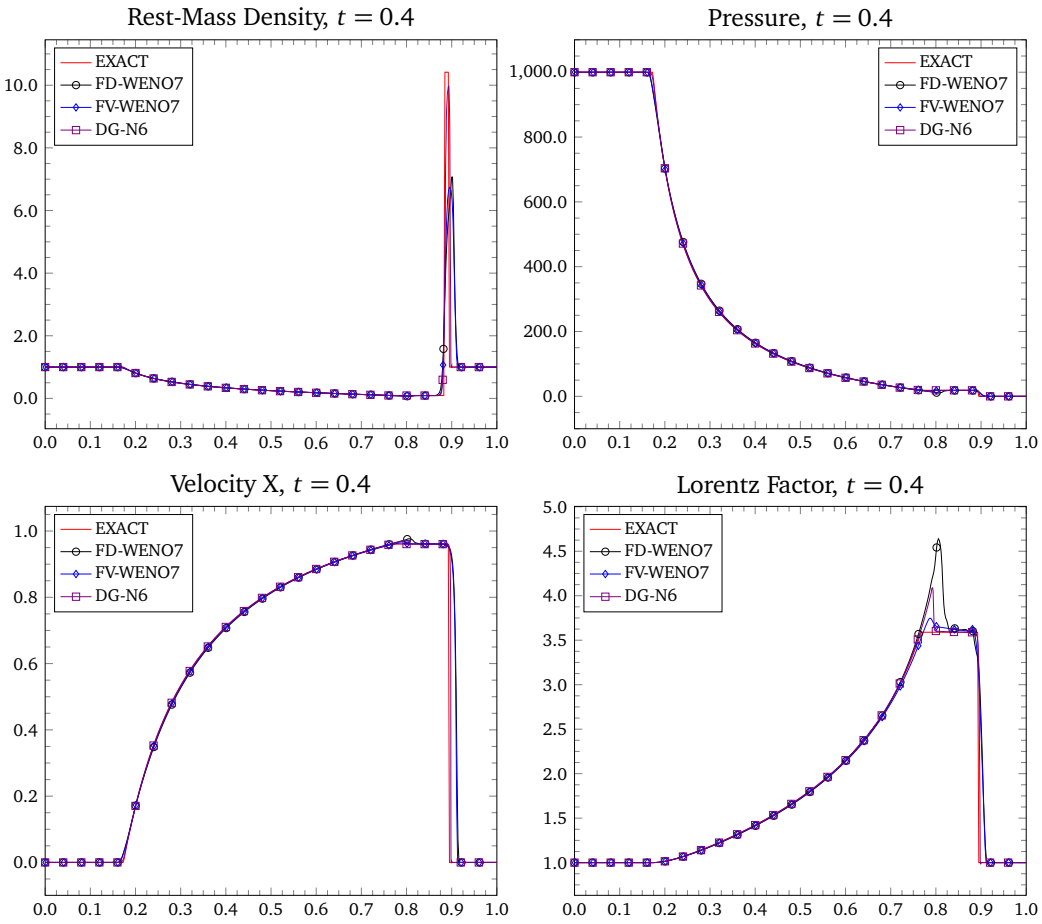

Figure 5.4: Riemann problem 4. The left and right states are given by equation (5.59). The final simulation time is $t = 0.40$. Plots of the rest-mass density, pressure, the x-component of the velocity, and the Lorentz factor are depicted. For the RKFD and RKFV, the WENO7 reconstruction is used in smooth parts of the flow and the WENO3 in regions with shocks. The RKDG is using a polynomial of degree $N = 6$ with the hybrid DG/FV-WENO3 as shock capturing.

the longitudinal one and thus is simply advected, the momentum equations in relativistic hydrodynamics are coupled each other through the Lorentz factor. As consequence of that, a non-zero transverse velocity imprints in the solution of the Riemann problem new physical effects that are not present in classical hydrodynamics (Pons et al. 2000; Rezzolla et al. 2003). An ideal gas equation of state with adiabatic index $\gamma = 5/3$ was used. The CFL number was set to CFL $= 0.95$. Transmissive boundary conditions were imposed at both edges of the interval. The final simulation time is set to $t = 0.4$. Plots of the rest-mass density, pressure, and the x-component of the velocity, and the Lorentz factor are depicted in the figure 5.5. Some overshootings are observed in the numerical solution computed with the RKFD and RKFV schemes. The RKDG presents a very light undershooting in the determination of the shock wave.

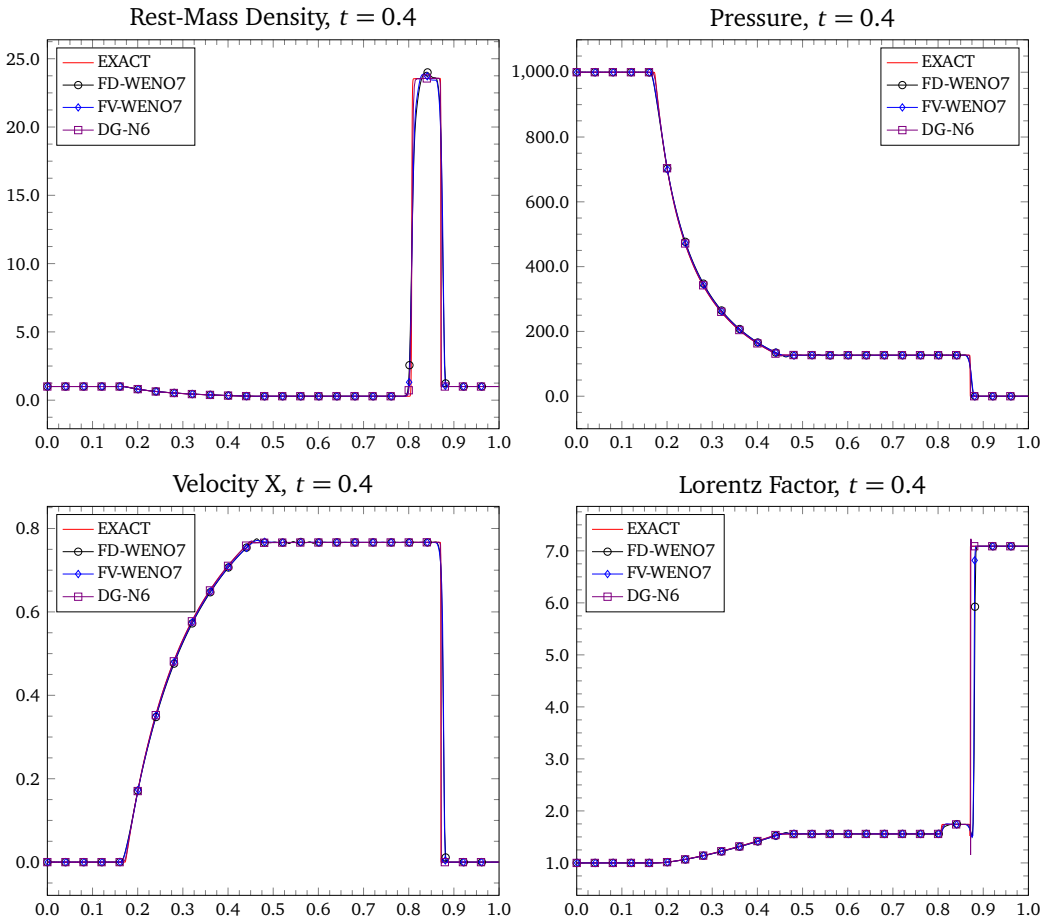

Figure 5.5: Riemann problem 5. The left and right states are given by equation (5.60). The final simulation time is $t = 0.40$. Plots of the rest-mass density, pressure, the x-component of the velocity, and the Lorentz factor are depicted. For the RKFD and RKFV, the WENO7 reconstruction is used in smooth parts of the flow and the WENO3 in regions with shocks. The RKDG is using a polynomial of degree $N = 6$ with the hybrid DG/FV-WENO3 as shock capturing.

Planar Shock Reflection

The *planar shock reflection* consists in an ideal cold fluid colliding a wall, a shock wave propagates backwards, leaving the gas behind at rest. The reflecting wall is located in $x = 1$. At $x = 0$ transmissive boundary conditions are set. The initial state is given by

$$\hat{\boldsymbol{u}} = \big(1, 0.99999, 0, 0.01\big). \tag{5.61}$$

The exact solution of this Riemann problem was first obtained by (Blandford & McKee 1976). We have employed the ideal gas equation of state with adiabatic index $\gamma = 4/3$. We have used CFL $= 0.95$. The final simulation time is set to $t = 1.5$. Plots of the rest-mass density, pressure, and the x-component of the velocity, and the Lorentz factor are depicted in the figure 5.6. We can see that close to the wall ($x = 1$), the numerical solution of the rest-mass density shows an undershooting, which is due to the wall heating phenomenon (Noh 1987).

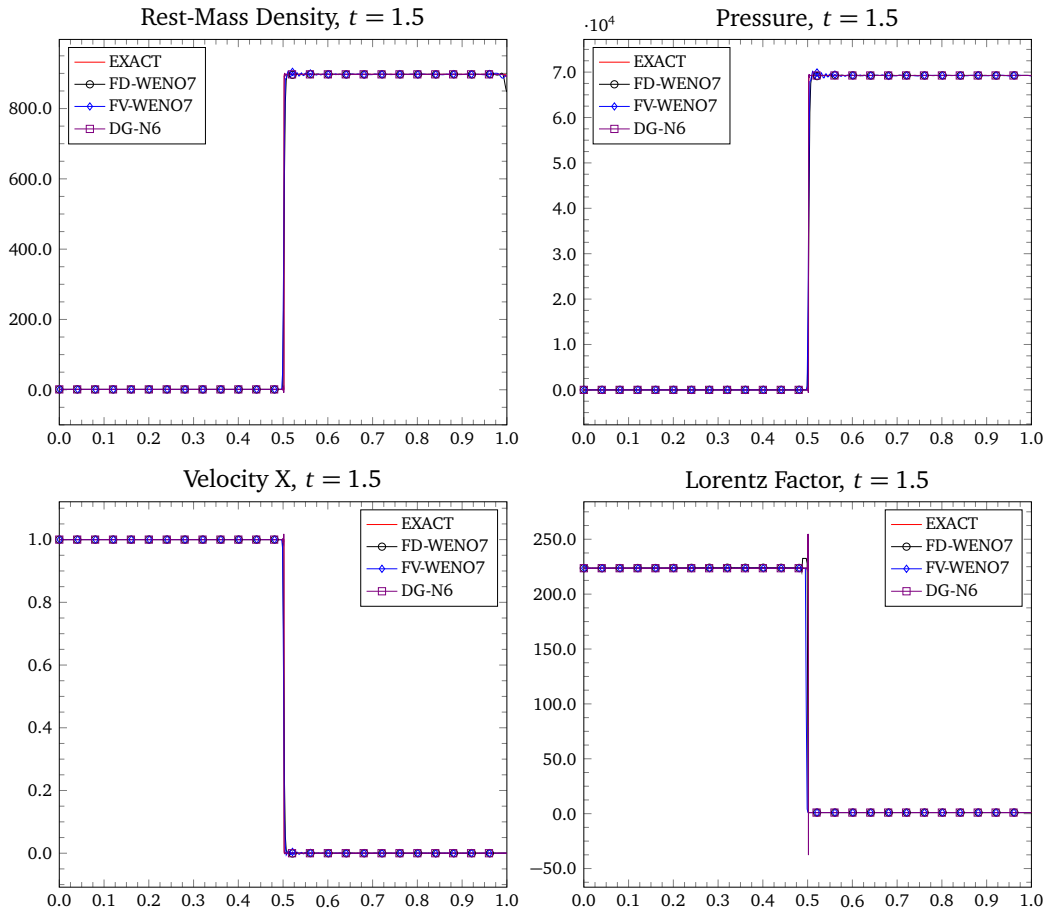

Figure 5.6: Planar shock reflection problem. The left and right states are given by equation (5.61). The final simulation time is $t = 1.5$. Plots of the rest-mass density, pressure, the x-component of the velocity, and the Lorentz factor are depicted. For the RKFD and RKFV, the WENO7 reconstruction is used in smooth parts of the flow and the WENO3 in regions with shocks. The RKDG is using a polynomial of degree $N = 6$ with the hybrid DG/FV-WENO3 as shock capturing.

Sinusoidal Density Perturbation

The last one-dimensional test consists in a perturbed Riemann problem. It was first proposed by Dolezal & Wong (1995), but the version showed here corresponds to the presented in del Zanna & Bucciantini (2002). Here we are interested in the capability of the scheme to transport smooth structures across a discontinuity. The initial condition is given by the following left and right states

$$\begin{aligned} \hat{\boldsymbol{u}}_L &= \big(5.0, 0.0, 0.0, 50.0\big) \\ \hat{\boldsymbol{u}}_R &= \big(2.0 + 0.3\sin 50x, 0.0, 0.0, 5.0\big). \end{aligned} \tag{5.62}$$

We have employed the ideal gas equation of state with adiabatic index $\gamma = 5/3$. For the RKFD and the RKFV methods we have used CFL $= 0.95$. The final simulation time is set to $t = 0.35$. Plots of the rest-mass density, pressure, the x-component of the velocity, and

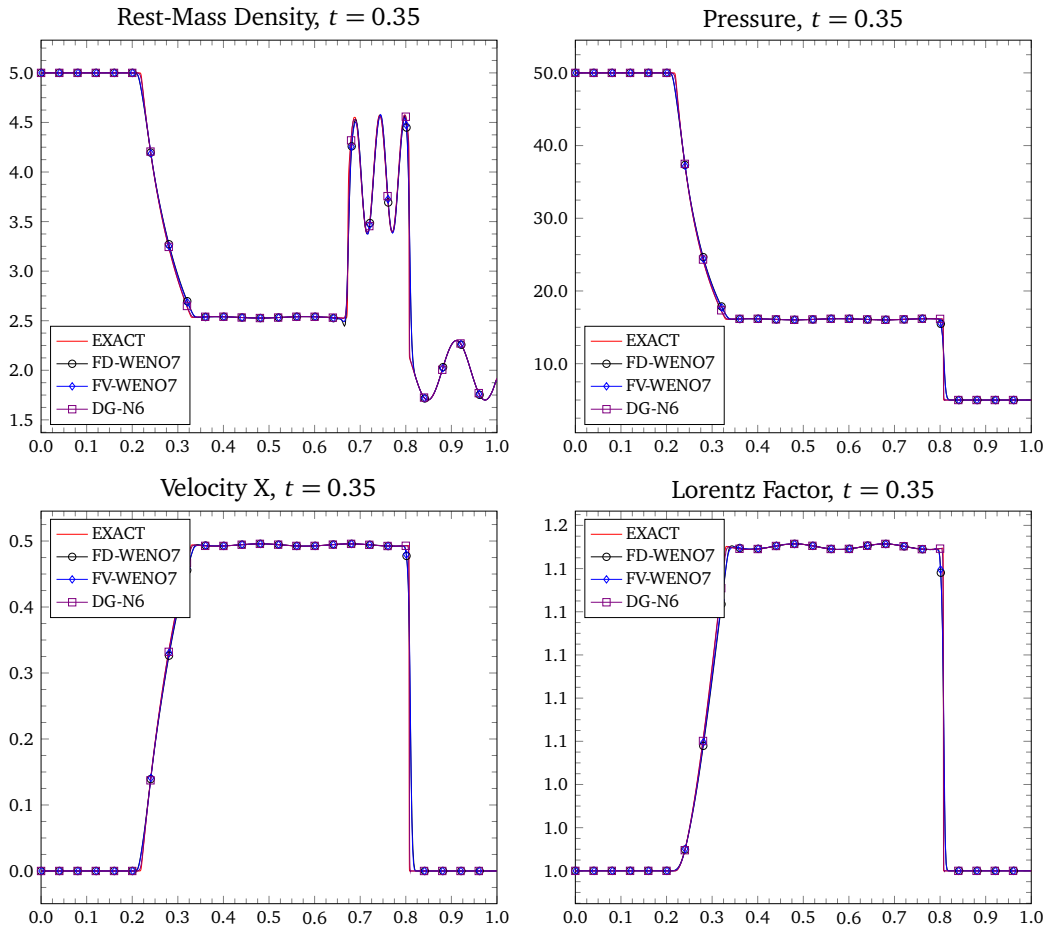

Figure 5.7: Sinusoidal density perturbation. The left and right states are given by equation (5.62). The final simulation time is $t = 0.35$. Plots of the rest-mass density, pressure, the x-component of the velocity, and the Lorentz factor are depicted. For the RKFD and RKFV, the WENO7 reconstruction is used in smooth parts of the flow and the WENO3 in regions with shocks. The RKDG is using a polynomial of degree $N = 6$ with the hybrid DG/FV-WENO3 as shock capturing.

the Lorentz factor are depicted in the figure 5.7. The plotted *exact solution* corresponds actually to a simulation with an RKFD-WENO3 scheme on a grid with 10 000 computational points. We see the very good agreement of the computed solution with high-order methods on a grid composed of only 500 points/cells/elements. For the RKFD and RKFV, the WENO5/WENO7 reconstruction is used in smooth parts of the flow and the WENO3 in regions with shocks. The RKDG is using a polynomial of degree $N = 6$ with the hybrid DG/FV-WENO3 as shock capturing.

5.4.3. Multidimensional Test Problems

In this section we consider multidimensional test problems with different shocks configurations. For the two-dimensional Riemann problems, which initial conditions were

taken from del Zanna & Bucciantini (2002), Tchekhovskoy et al. (2007), and He & Tang (2012a), the computational domain is the box $[-1,1]\times[-1,1]$, divided in four quadrants. The membranes are localized along the lines $x=0$ and $y=0$. These Riemann problems simulate practically all essential features found in a two-dimensional flow, for example, shock reflections, vortex, shock interactions, etc. In the two-dimensional Riemann problems, the initial states are defined in the quadrants $Q1$, $Q2$, $Q3$, and $Q4$, which are the sets

$$\begin{aligned} Q1 &:= \left\{(x,y)\in[-1,1]^2 \,\middle|\, x\geq 0,\, y\geq 0\right\},\\ Q2 &:= \left\{(x,y)\in[-1,1]^2 \,\middle|\, x< 0,\, y\geq 0\right\},\\ Q3 &:= \left\{(x,y)\in[-1,1]^2 \,\middle|\, x< 0,\, y< 0\right\},\\ Q4 &:= \left\{(x,y)\in[-1,1]^2 \,\middle|\, x\geq 0,\, y< 0\right\}. \end{aligned} \tag{5.63}$$

Riemann Problem 1

The box $[-1,1]\times[-1,1]$ is initially filled with a gas with adiabatic index $\gamma=5/3$. This domain is subdivided into four quadrants, where the states in primitive variables are defined by

$$\begin{aligned} \hat{\boldsymbol{u}}_{Q1} &= \big(0.035145216124503, 0.0, 0.0, 0.162931056509027\big),\\ \hat{\boldsymbol{u}}_{Q2} &= \big(0.1, 0.7, 0.0, 1.0\big),\\ \hat{\boldsymbol{u}}_{Q3} &= \big(0.5, 0.0, 0.0, 1.0\big),\\ \hat{\boldsymbol{u}}_{Q4} &= \big(0.1, 0.0, 0.7, 1.0\big). \end{aligned} \tag{5.64}$$

Transmissive boundary conditions are used in all faces of the computational domain. The adiabatic index of the gas is $\gamma=5/3$. The final simulation time is $t=0.8$. Contour plots of the rest-mass density and pressure are depicted in the figure 5.8. After the breakup of the membranes, two contact discontinuities appear on the left and bottom of the domain, and in the first quadrant we can identify two curved front shocks. In the third quadrant it is visible a like-jet structure moving in south-west direction (del Zanna & Bucciantini 2002). The solution was obtained with the RKFD scheme with WENO7 reconstruction on a grid with 600×600 points (top-left), the RKFV scheme with WENO7 reconstruction on a grid of 600×600 cells (top-right), and the hybrid DG/FV-WENO3 method with $N=5$ on a mesh made of 120×120 elements (bottom). The WENO7 reconstruction is used in smooth parts of the flow and the WENO3 in regions with shocks for the RKFD and RKFV schemes. For the RKDG scheme is also plotted the mesh and the FV subcells where the hybrid DG/FV-WENO3 has been used as shock capturing strategy. We set the CFL condition to $\mathrm{CFL}=0.95$. We observe the lack of oscillations in these contour plots, and also the very good agreement for all cases. Since the RKDG scheme used a lower number of cells, the RKFD and RKFV schemes give a better resolution of the flow patterns arose in the simulation.

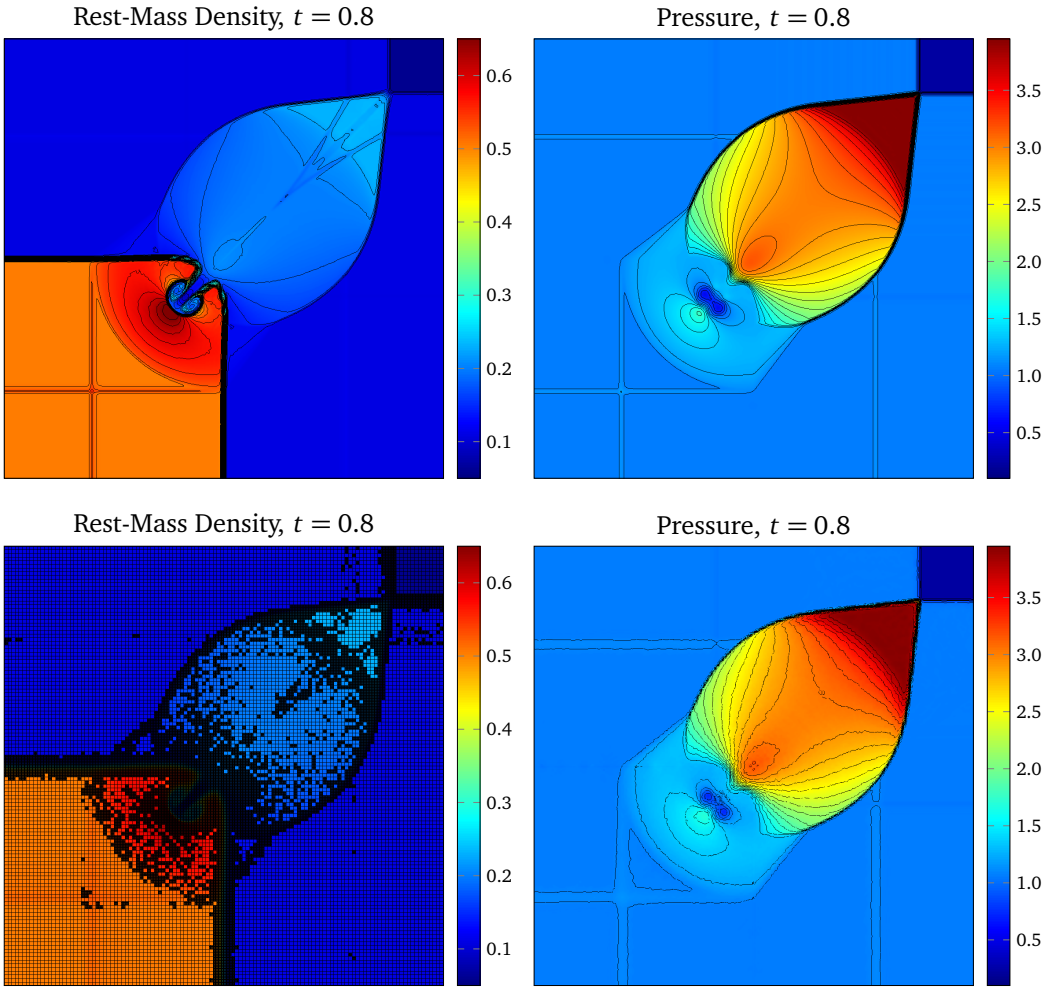

Figure 5.8: Two-dimensional Riemann problem 1. The initial state is given by equation (5.64). Contour plots of the rest-mass density (left) and the pressure (right) at time $t = 0.8$. The calculations were performed with a RKFD scheme with WENO7 reconstruction (top-left) on a grid of 600×600 points, with a RKFV scheme with WENO7 reconstruction (top-right) on a grid of 600×600 cells, and the RKDG with $N = 5$ and hybrid DG/FV-WENO3 shock capturing (bottom).

Riemann Problem 2

The domain is filled with a gas, which initial condition is determined by the following states in primitive variables in the quadrants $Q1$, $Q2$, $Q3$, and $Q4$

$$\begin{aligned}
\hat{\boldsymbol{u}}_{Q1} &= \big(0.5, 0.5, -0.5, 5.0\big), \\
\hat{\boldsymbol{u}}_{Q2} &= \big(1.0, 0.5, 0.5, 5.0\big), \\
\hat{\boldsymbol{u}}_{Q3} &= \big(3.0, -0.5, 0.5, 5.0\big), \\
\hat{\boldsymbol{u}}_{Q4} &= \big(1.5, -0.5, -0.5, 5.0\big).
\end{aligned} \tag{5.65}$$

As in the Riemann problem 1, the adiabatic index of the gas is $\gamma = 5/3$ and the final simulation time is $t = 0.8$. Contour plots of the rest-mass density and the Lorentz factor are depicted in the figure 5.9. Here we can see the interaction of four vortex sheets,

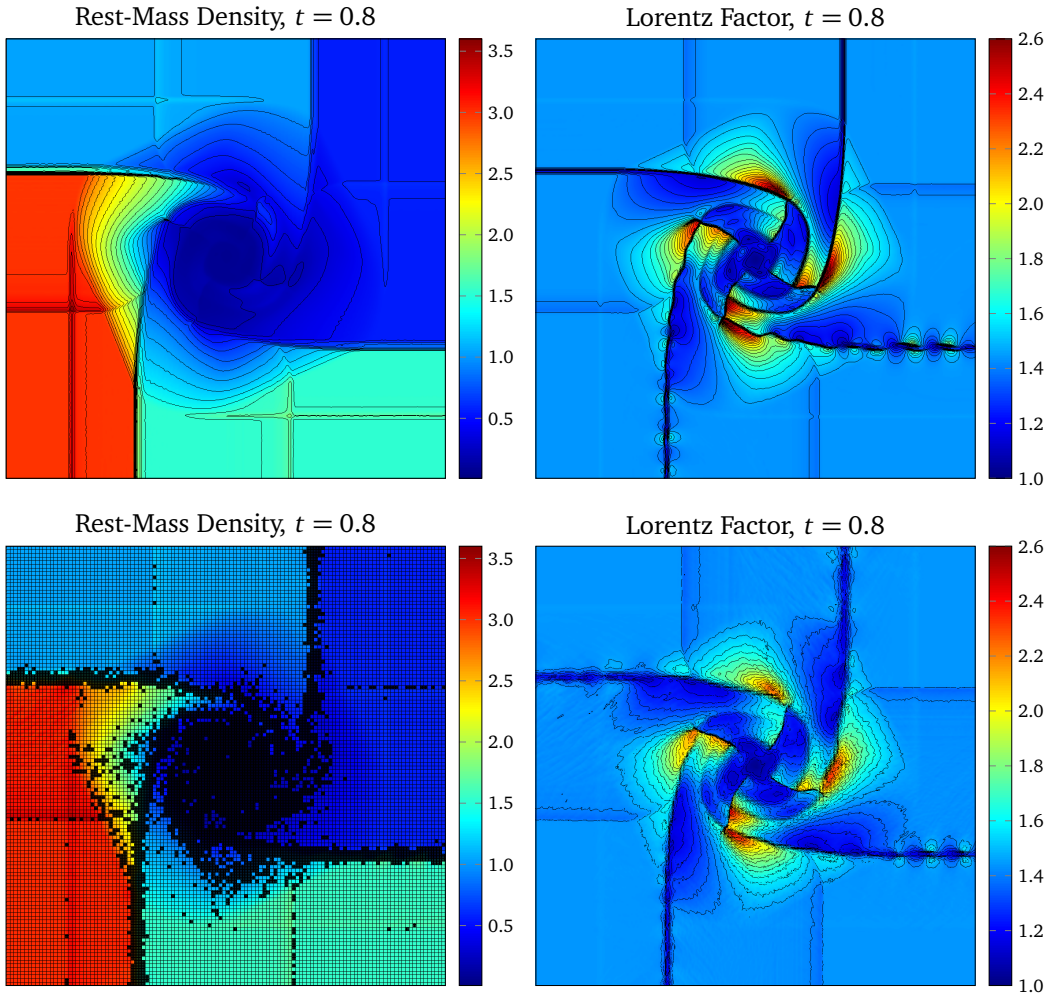

Figure 5.9: Two-dimensional Riemann problem 2. The initial state is given by equation (5.65). Contour plots of the rest-mass density (left) and the Lorentz factor (right) at time $t = 0.8$. The calculations were performed with a RKFD scheme with WENO7 reconstruction (top-left) on a grid of 600×600 points, with a RKFV scheme with WENO7 reconstruction (top-right) on a grid of 600×600 cells, and the RKDG with $N = 5$ and hybrid DG/FV-WENO3 shock capturing (bottom).

forming a spiral with very low rest-mass density in the center of the domain (the typical cavitation in gas dynamics). The solution was obtained with the RKFD scheme with WENO7 reconstruction on a grid with 600×600 points (top-left), the RKFV scheme with WENO7 reconstruction on a grid of 600×600 cells (top-right), and the hybrid DG/FV-WENO3 method with $N = 5$ on a mesh made of 120×120 elements (bottom). The WENO7 reconstruction is used in smooth parts of the flow and the WENO3 in regions with shocks for the RKFD and RKFV schemes. For the RKDG scheme is also plotted the mesh and the FV subcells where the hybrid DG/FV-WENO3 has been used as shock capturing strategy. We set the CFL condition to $\text{CFL} = 0.95$. We observe the very good agreement between all schemes. The RKFD and RKFV schemes provide a better resolution of the flow patterns arose in the simulation than the RKDG scheme, and this is because the

coarse mesh employed in the latter scheme.

Riemann Problem 3

In our last two-dimensional Riemann problem, we set the initial condition as the states in primitive variables in the quadrants $Q1$, $Q2$, $Q3$, and $Q4$ given by

$$\begin{aligned}
\hat{\boldsymbol{u}}_{Q1} &= \big(1.0, 0.0, 0.0, 1.0\big),\\
\hat{\boldsymbol{u}}_{Q2} &= \big(0.5771, -0.3529, 0.0, 0.4\big),\\
\hat{\boldsymbol{u}}_{Q3} &= \big(1.0, -0.3529, -0.3529, 1.0\big),\\
\hat{\boldsymbol{u}}_{Q4} &= \big(0.5771, 0.0, -0.3529, 0.4\big).
\end{aligned} \tag{5.66}$$

The adiabatic index of the gas is $\gamma = 5/3$, and the final simulation time is $t = 0.80$. Contour plots of the rest-mass density, pressure and the Mach number are depicted in the figure 5.10. This problem is about the interaction of planar rarefaction waves. The initial discontinuities evolve into rarefaction waves, interacting each other. This interaction generates two symmetric shock waves in the zone where the rarefaction waves have interplayed. The solution was obtained with the RKFD scheme with WENO7 reconstruction on a grid with 600×600 points (top-left), the RKFV scheme with WENO7 reconstruction on a grid of 600×600 cells (top-right), and the hybrid DG/FV-WENO3 method with $N = 5$ on a mesh made of 120×120 elements (bottom). The WENO7 reconstruction is used in smooth parts of the flow and the WENO3 in regions with shocks for the RKFD and RKFV schemes. For the RKDG scheme is also plotted the mesh and the FV subcells where the hybrid DG/FV-WENO3 has been used as shock capturing strategy. We set the CFL condition to $\mathrm{CFL} = 0.95$. We observe the very good agreement between all schemes. The RKFD and RKFV schemes provide a better resolution of the flow patterns arose in the simulation than the RKDG scheme, and this is because the coarse mesh employed in the latter scheme. additionally, the RKDG solution presents some oscillations, and it required to many FV-subdomains for the shock capturing. This was necessary for the stability of the computation of this problem.

Double Mach Reflection Problem

The double Mach reflection problem was introduced by Woodward & Colella (1984) for Newtonian hydrodynamics. This problem was extended to the equations of relativistic hydrodynamics by Zhang & MacFadyen (2006). The problem consists basically in a shock wave traveling horizontally and collide with an inclined wedge. It is formulated equivalently by sending a shock wave diagonally into a reflecting wall. The computational domain is the box $[0, 4] \times [0, 1]$. We represent the wedge by a reflecting boundary starting at $x = 1/6$ along the x-axis. The strong shock moving initially from the left boundary toward the right makes and 60° angle the x-axis. Due to the original setup of the problem can not be used in the relativistic case, Zhang & MacFadyen (2006) proposed a new initial state that allows the formation of waves patterns present in the Newtonian version.

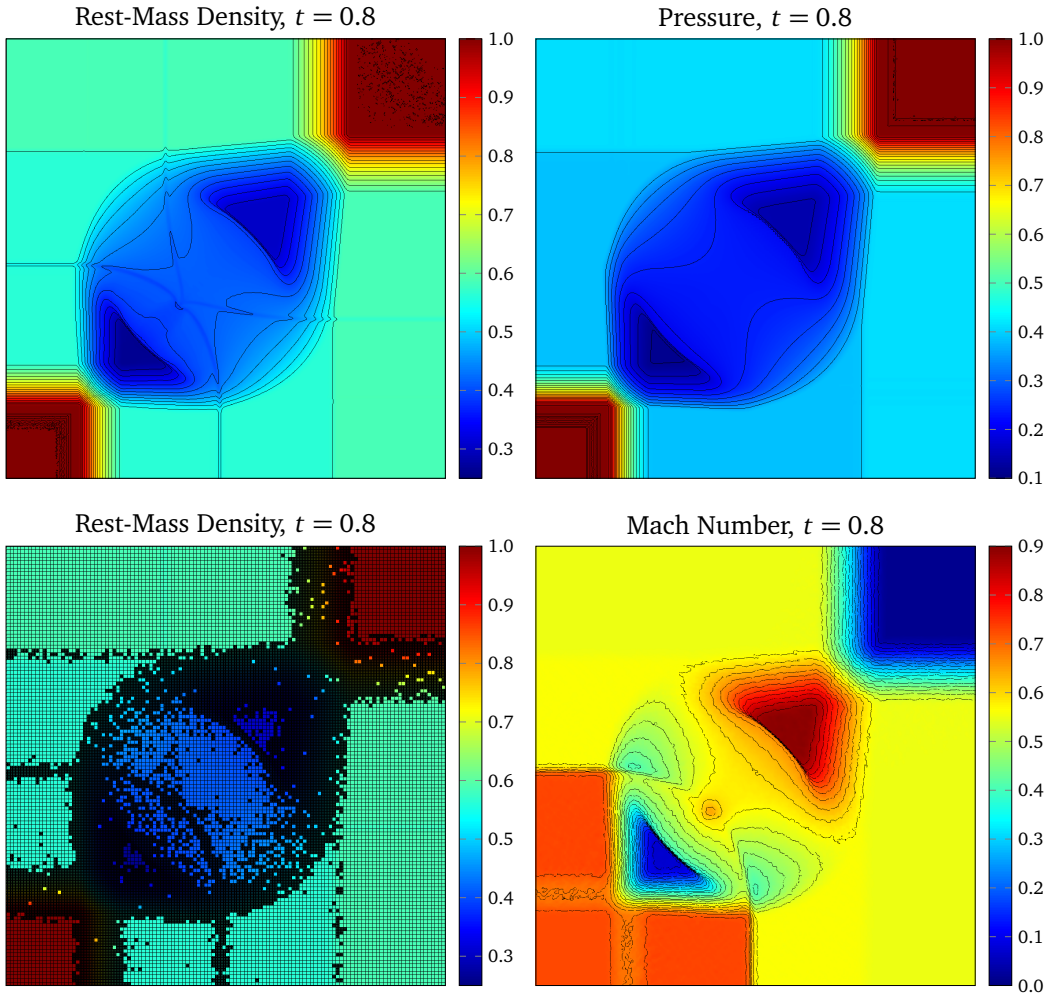

Figure 5.10: Two-dimensional Riemann problem 3. The initial state is given by equation (5.66). Contour plots of the rest-mass density (left), pressure (top-right), and the Mach number (bottom-right) at time $t = 0.8$. The calculations were performed with a RKFD scheme (top-left) on a grid of 600×600 points, with a RKFV scheme (top-right) on a grid of 600×600 cells, and the RKDG with $N = 5$ and hybrid DG/FV-WENO3 shock capturing (bottom).

In fact, they showed that by choosing an ultra-relativistic shock, no Mach reflection is generated. The adiabatic index is set to $\gamma = 1.4$, and the initial state is given by

$$\hat{\boldsymbol{u}}(x,y)\big|_{t=0} = \begin{cases} \hat{\boldsymbol{u}}_L, & \text{for } y > h(x,0), \\ \hat{\boldsymbol{u}}_R, & \text{for } y < h(x,0), \end{cases} \tag{5.67}$$

where the left and right states of the shock wave, and the exact position of the shock at the time t are, respectively (see also He & Tang (2012a)),

$$\begin{aligned} &\hat{\boldsymbol{u}}_L = (8.564, 0.4247\sin 60°, -0.4247\cos 60°, 0.3808), \\ &\hat{\boldsymbol{u}}_R = (1.4, 0.0, 0.0, 0.0025), \\ &h(x,t) = \sqrt{3}\,(x - x_0) - 2v_s t, \quad x_0 = \frac{1}{6}, \quad v_s = 0.4984. \end{aligned} \tag{5.68}$$

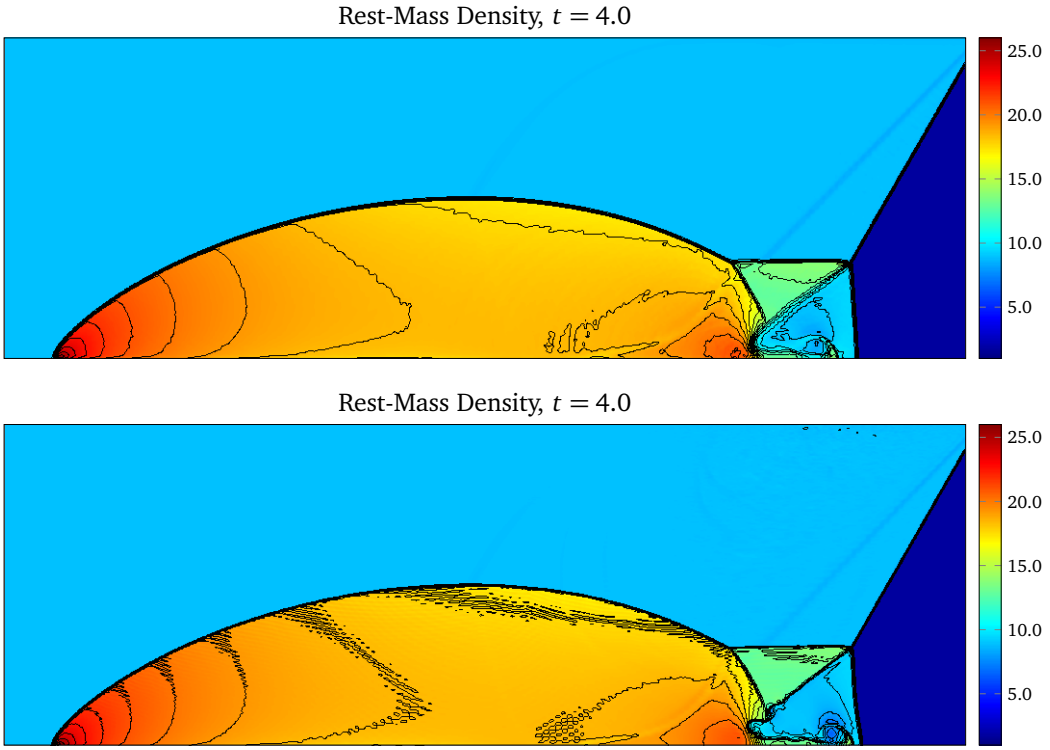

Figure 5.11: Relativistic double Mach reflection problem. The rest-mass density computed with a RKFD-WENO7 scheme (top), and a RKFV-WENO7 scheme (bottom) at simulation time $t = 4.0$. The calculations were performed on a grid of 1600×400 points/cells. The computational domain is the box $[0,4] \times [0,1]$, but only the region $[0,3] \times [0,1]$ is shown.

Regarding the boundary conditions, we set them as follows: A reflecting wall is placed at $x > x_0$, $y = 0$, as we mentioned before. At the top boundary and depending of the position of the shock wave, we set the boundary conditions to either the post-shock state $\hat{\boldsymbol{u}}_L$ or the pre-shock state $\hat{\boldsymbol{u}}_R$. At the right face of the domain the boundary condition is set to the exact pre-shock condition $\hat{\boldsymbol{u}}_R$. For $x < x_0$, the left and part of the bottom boundaries are set to the exact post-shock state $\hat{\boldsymbol{u}}_L$. A contour plot of the rest-mass density at simulation time $t = 4.0$ is depicted in the figure 5.11 for the RKFD and RKFV schemes with WENO7 reconstruction. The computational domain is made of 1600×400 points/cells. In the figure 5.12 is shown the contour plots of the rest-mass density in the region $[2.2, 2.7] \times [0.0, 0.5]$ for both RKFD and RKFV schemes. Observe that the RKFV, for the same resolution and WENO/ reconstruction, provides more details of the small vortices generated, which interact with the second reflected shock wave.

Cloud-Shock Interaction 1

In this example, we will simulate the evolution of a dense spherical cloud as it interacts with a strong shock wave. The interaction of shock waves with density inhomogeneities in the interstellar medium is a very important dynamical process because it may trig-

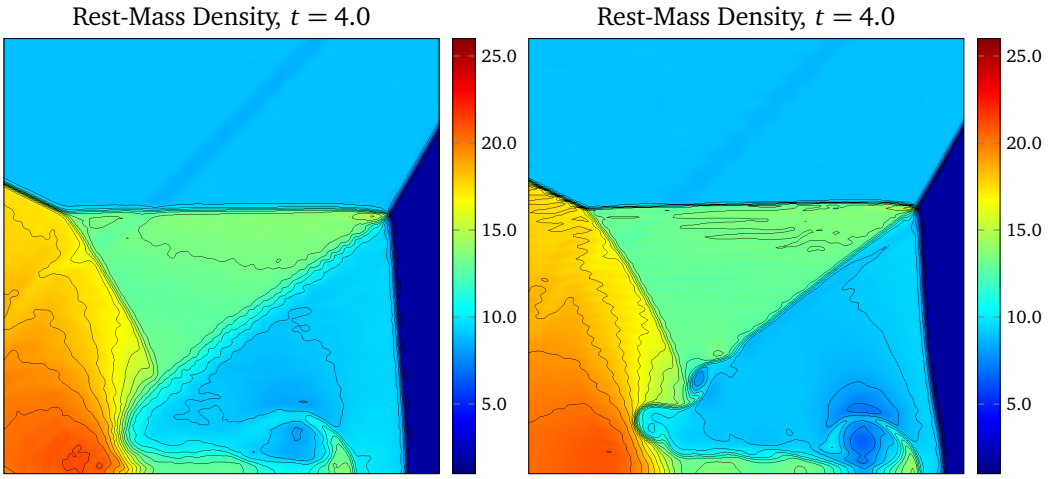

Figure 5.12: Relativistic double Mach reflection problem. The rest-mass density computed with a RKFD-WENO7 scheme (left), and a RKFV-WENO7 scheme (right), in the region $[2.2, 2.7] \times [0.0, 0.5]$ at simulation time $t = 4.0$.

ger gravitational collapse and star formation (Elmegreen & Scalo 2004). The spherical cloud is assumed to be small enough that the effects derived from thermal conduction, radiative cooling, and self-gravity can be ignored. The typical features observed during the numerical simulations of these phenomena in two-dimensional domains are, in first place, a crush of the cloud by the shock wave, and then its complete destruction. In non-relativistic regimes, several studies has been done, for example, in (Chen et al. 2008). The simulation setup is given after He & Tang (2012a): We employ an equation of state with adiabatic index $\gamma = 5/3$. The computational domain is the box $[0, 2] \times [0, 1]$ with transmissive boundary conditions at all faces. The center of the cylindrical cloud is located in the point $(1.4, 0.5)$ and the radius is $r = 0.15$. The initial state for the cloud is $\hat{\boldsymbol{u}}_c = (0.1358, 0, 0, 0.05)$. The left moving shock wave at time $t = 0$ is located at $x = 1.6$, with left and right states given by

$$\begin{aligned} \hat{\boldsymbol{u}}_L &= (1, 0, 0, 0.05), \\ \hat{\boldsymbol{u}}_R &= (1.865225080631180, -0.196781107378299, 0.00, 0.15). \end{aligned} \tag{5.69}$$

Contour plots of the rest-mass density (left) and Mach number (right) at simulation time $t = 3.0$ are depicted in the figure 5.13. For the RKFD scheme (top-left) the computational domain is made of 800×400 grid points; for the RKFV scheme (top-right), the computational domain is decomposed into 800×400 cells; and for the RKDG method (bottom), the domain is subdivided into 160×80 elements. For the RKFD and RKFV, the WENO7 reconstruction is used in smooth parts of the flow and the WENO3 in regions with shocks. The RKDG is using a polynomial of degree $N = 6$ with the hybrid DG/FV-WENO3 as shock capturing. For the RKDG scheme is also plotted the mesh and the FV subcells where the hybrid DG/FV-WENO3 has been used as shock capturing strategy. We set the CFL condition to CFL $= 0.95$. The RKFD and RKFV schemes provide a better

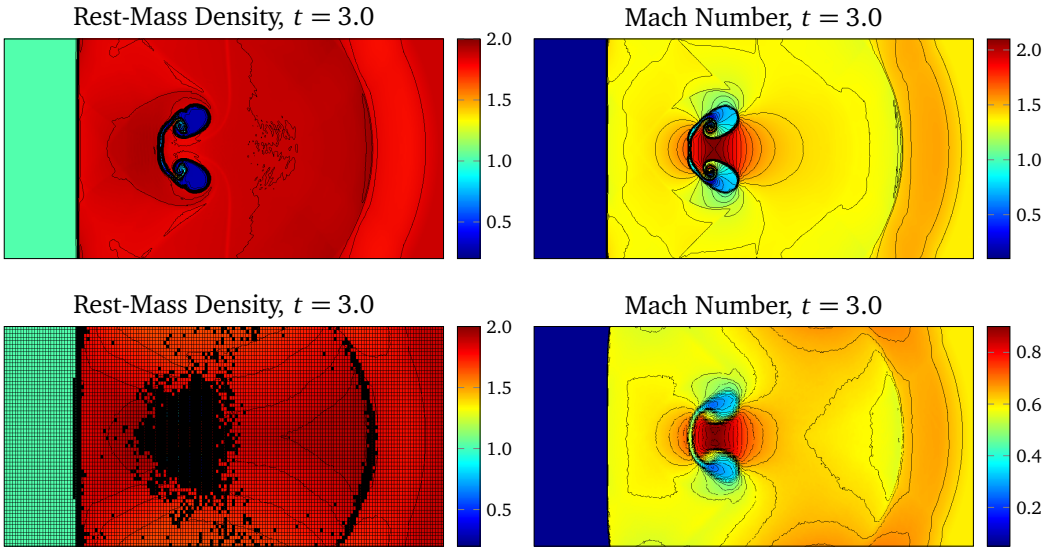

Figure 5.13: Cloud-shock interaction 1. Contour plots of the rest-mass density (left) and the Mach number (right) at time $t = 3.00$. The calculations were performed with a RKFD with WENO7 reconstruction (top-left) on a grid of 800×400 grid points, a RKFV with WENO7 reconstruction (top-right) on a grid of 800×400 cells, and the RKDG scheme with $N = 5$ and hybrid DG/FV-WENO3 shock capturing (bottom).

resolution of the flow patterns arose in the simulation than the RKDG scheme, since the RKDG scheme makes use of a coarser mesh.

Cloud-Shock Interaction 2

This calculation is similar to the previous one, but with the gas in the cloud heavier than the surrounding fluid. The simulation setup is again given after He & Tang (2012a): We employ an equation of state with adiabatic index $\gamma = 5/3$. The computational domain is the box $[0, 2] \times [0, 1]$ with transmissive boundary conditions at all faces. The center of the cylindrical cloud is located in the point $(1.4, 0.5)$ and the radius is $r = 0.15$. The initial state for the cloud is $\hat{\boldsymbol{u}}_c = (3.1538, 0, 0, 0.05)$. The left moving shock wave at time $t = 0$ is located at $x = 1.6$, with left and right states given by

$$\begin{aligned} \hat{\boldsymbol{u}}_L &= (1, 0.0, 0.0, 0.05), \\ \hat{\boldsymbol{u}}_R &= (1.86522508063118, -0.19678110737829, 0.0, 0.15). \end{aligned} \tag{5.70}$$

Contour plots of the rest-mass density (left) and Mach number (right) at simulation time $t = 3.0$ are depicted in the figure 5.14. For the RKFD scheme (top-left) the computational domain is made of 800×400 grid points; for the RKFV scheme (top-right), the computational domain is decomposed into 800×400 cells; and for the RKDG method (bottom), the domain is subdivided into 160×80 elements. For the RKFD and RKFV, the WENO7 reconstruction is used in smooth parts of the flow and the WENO3 in regions with shocks. The RKDG is using a polynomial of degree $N = 6$ with the hybrid DG/FV-

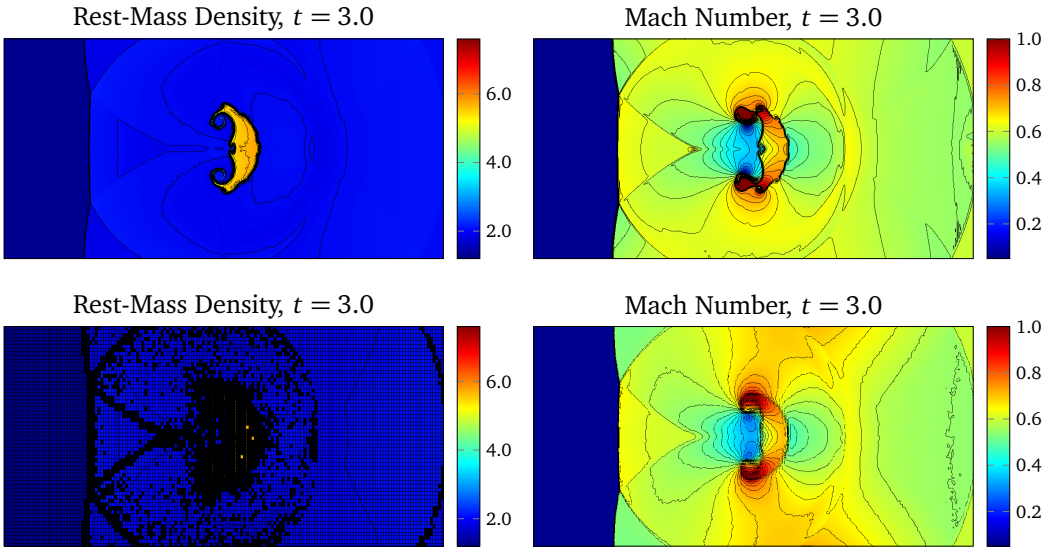

Figure 5.14: Cloud-shock interaction 2. Contour plots of the rest-mass density (left) and the Mach number (right) at time $t = 3.00$. The calculations were performed with a RKFD with WENO7 reconstruction (top-left) on a grid of 800×400 grid points, a RKFV with WENO7 reconstruction (top-right) on a grid of 800×400 cells, and the RKDG scheme with $N = 5$ and hybrid DG/FV-WENO3 shock capturing (bottom).

WENO3 as shock capturing. For the RKDG scheme is also plotted the mesh and the FV subcells where the hybrid DG/FV-WENO3 has been used as shock capturing strategy. We set the CFL condition to CFL $= 0.95$. The RKFD and RKFV schemes provide a better resolution of the flow patterns arose in the simulation than the RKDG scheme, because the RKDG scheme has employed a coarser mesh. Observe the small oscillations in the contour plots obtained with the RKDG solution. The Persson indicator was used in this test for detecting those cells with shocks, in the case of the RKDG computation. The indicator flagged too many elements, making to lose accuracy even in regions where it was not necessary to apply the shock capturing strategy. The RKFD and the RKFV did not suffer that behavior of the indicator, because the Jameson indicator was used instead. Further development consists in implement a more accurate version of the Jameson indicator for the RKDG scheme for relativistic flows.

Kelvin-Helmholtz Instability

The Kelvin-Helmholtz instability occurs when a perturbation is introduced to a system with a velocity shear. Here, we run this test problem to demonstrate the algorithm's ability to evolve a linear perturbation into nonlinear turbulence. As a test of the linear regime, one can compare the growth rate of the instability with the analytic result before the instability becomes nonlinear. The initial conditions are similar to those used by Beckwith & Stone (2011) and Radice & Rezzolla (2012).

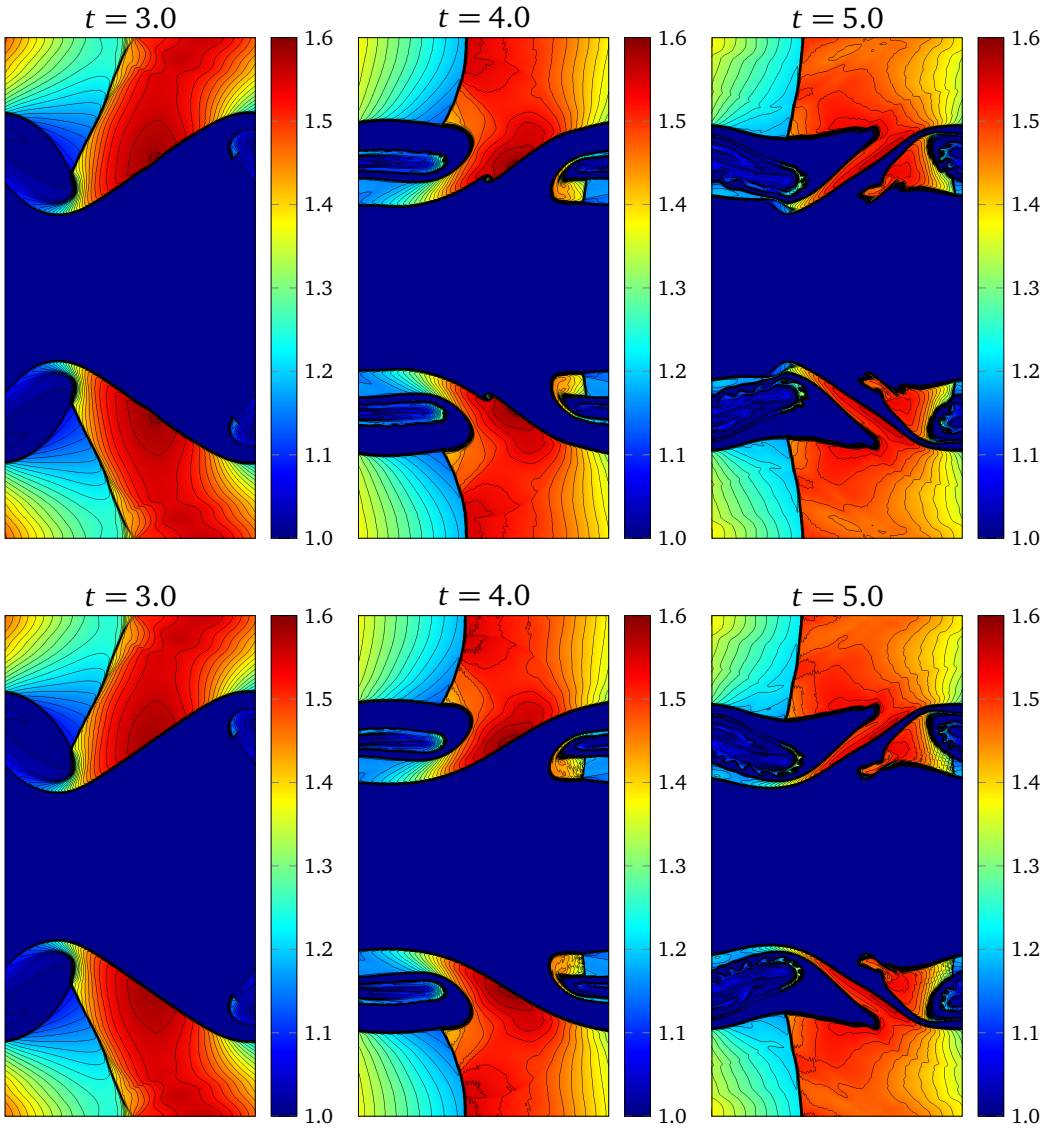

Figure 5.15: Relativistic Kelvin-Helmholtz instability. Contour plots of the rest-mass density at times $t = 3.00$, $t = 4.00$, and $t = 5.00$. The calculations were performed with a RKFD-WENO7 (top), and a RKFV-WENO7 (bottom) schemes on a mesh of 400×800 points/cells. The computational domain is the box $[-0.5, +0.5] \times [-1.0, +1.0]$.

The computational domain is the box $[-0.5, +0.5] \times [-1.0, +1.0]$. The shear velocity is given by

$$v_x(y) = \begin{cases} +v_{\text{shear}} \tanh\big[(y-0.5)/a^2\big], & \text{if } y > 0; \\ -v_{\text{shear}} \tanh\big[(y+0.5)/a^2\big], & \text{if } y \leq 0; \end{cases} \tag{5.71}$$

where $a = 0.1$ is the characteristic size of the shear layer and $v_{\text{shear}} = 0.5$. The instability is seeded by adding a small perturbation in the transverse component of the velocity,

$$v_y(x,y) = \begin{cases} +A_0 v_{\text{shear}} \sin(2\pi x) \exp\big[-(y-0.5)^2/\sigma^2\big], & \text{if } y > 0; \\ -A_0 v_{\text{shear}} \sin(2\pi x) \exp\big[-(y+0.5)^2/\sigma^2\big], & \text{if } y \leq 0; \end{cases} \tag{5.72}$$

where $A_0 = 0.1$ is the perturbation amplitude and $\sigma = 0.1$ its characteristic length scale. The initial pressure is uniform, $p = 1$. The rest-mass density distribution, which is uniform in the x-direction, is instead given by

$$\rho(y) = \begin{cases} \rho_0 + \rho_1 \tanh\left[(y-0.5)/a^2\right], & \text{if } y > 0; \\ \rho_0 - \rho_1 \tanh\left[(y+0.5)/a^2\right], & \text{if } y \leq 0; \end{cases} \tag{5.73}$$

where $\rho_0 = 0.505$ and $\rho_1 = 0.495$, so that $\rho = 1$ in the regions with $v_x = 0.5$ and $\rho = 0.1$ in the regions with $v_x = -0.5$. An adiabatic equation of state with $\gamma = 4/3$ is considered. At the boundaries of the domain we consider periodic boundary conditions. In the figure 5.15 are depicted contour plots of the rest-mass density at times $t = 3.00$ (left), $t = 4.00$ (middle), and $t = 5.00$ (right). The calculations were performed with a RKFD scheme (top), and a RKFV (bottom), both with WENO7 reconstruction operator, on a mesh of 400×800 points/cells. From the simulations we could observe that the linear growth phase of the instability last up to until $t \approx 3$. After that, the evolution of the flow becomes turbulent, with the appearance of large fluctuations in the transverse component of the velocity. The results are quite similar for both numerical methods.

Relativistic Extragalactic Jet

It is widely known that there are three classes of highly collimated and supersonic jets from dense central objects with accretion disks, which depend on the central object, protostars, binary stars, or active galactic nuclei. AGN jets are the largest scale phenomena, and the velocity of the jet beam is highly relativistic, at least close to the central object, see Peterson (1997). The jet, which originates near an accretion disk that surrounds an AGN, can propagate over a long distance, up to a few Mpc, while remaining well collimated. There are two shocks at the end of the jet. One is a bow shock (or a forward shock), which accelerates the ambient gas. The other is a terminal Mach shock (or a reverse shock) at which the beam ends. At the terminal Mach shock, non-thermal particles are accelerated and emit photons through synchrotron radiation and inverse Compton scattering. The gas that crosses the terminal Mach shock into a hot spot is hot and pressurized, and expands laterally, enveloping the beam with the shocked ambient gas, creating a so-called cocoon structure. At the contact discontinuity between the ambient gas and the jet in the cocoon, Kelvin-Helmholtz instabilities develop.

Cygnus A is a suitable object in which to see these features, because it is one of the closest radio galaxies, and the beam propagates perpendicularly to the line of sight. From observations, its size is about 120 kpc, the beam velocity is $\sim 0.4-1c$, and the hot spot's ram pressure advance speed is $0.03c$.

Analytical studies and numerical simulations of the morphology and the dynamics of jets have been performed for the past thirty years. Blandford & Rees (1974) discussed the structure of jets with a theoretical relativistic beam model. The difficulty of numerical relativistic hydrodynamics has delayed the investigation of the relativistic effects on the

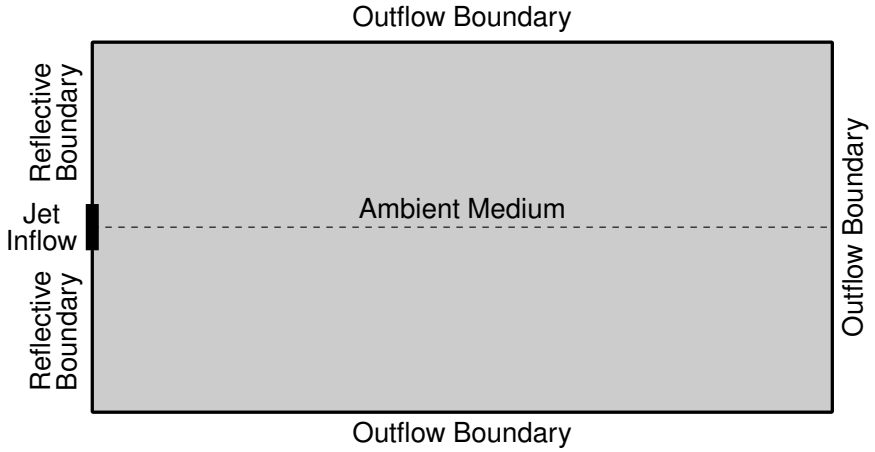

Figure 5.16: Computational domain for the astrophysical jet.

morphology and the dynamics of jets. Only in the past 20 years stable codes, with or without external magnetic fields, have been developed for the ultra-relativistic regime (Duncan & Hughes 1994; Aloy et al. 1999a).

We solve the relativistic hydrodynamic equations (5.7) with our two-dimensional relativistic hydrodynamic code, based on high-order RKFD and RKFV methods. We use a two-dimensional Cartesian computational region. The grid size is uniform, namely $\Delta x = \Delta y =$ constant. We assume that the ambient gas is homogeneous initially. A relativistic beam flow (v_b), is injected at $x = 0$ in the direction of the positive x-axis through a circular nozzle defined by $x^2 + y^2 \leq R_b^2$, where R_b is the beam radius, and is in pressure equilibrium with the ambient medium. Outflow boundary conditions are imposed everywhere except at the plane $x = 0$, where injection is assumed through the nozzle and the rest of the plane has a reflecting boundary. A reflection boundary is imposed $x = 0$ with $x^2 + y^2 > R_b^2$. The boundary condition at $x = 0$ is crucial for dynamics and the outer shape of the jets. The free boundary condition permits the gas to escape at the back side. The radius of the injected beam, R_b, is used as a scaling unit in this study. In the figure 5.16 is outlined the computational domain for the simulation of the relativistic jet. Moreover, the relativistic jet simulation can be fully specified by only setting the following parameters:

- the beam density, ρ_b;
- the beam pressure, p_b;
- the flow speed of the beam, v_b;
- the ratio of the rest mass densities of the beam fluid and the ambient medium, η;
- the ratio of the pressures of the beam fluid and the ambient medium, κ;

For the example considered in this work, the initial parameters are listed in the following. An ideal equation of state with adiabatic index $\gamma = 5/3$. The ratio of the pressures of the beam fluid and the ambient medium is set to $\kappa = 1$. The density and pressure of the beam are $\rho_b = 1.0$ and $p_b = 1.0 \times 10^{-3}$. The speed of the beam is given by $v_b = 0.999c$. The jet nozzle has a radius $r_b = 0.2$. The computational domain has a size $450r_b \times 150r_b$, and it is discretized with 2400×800 grid points and with 3600×1200. The simulations were performed with the WENO5 reconstruction operator for both numerical schemes. According to observations, jets have counterjets that propagate in the opposite direction. We assume the reflective boundary condition so that our calculations begin near the central engine (Aloy et al. 1999a).

From our simulations, we find that the overall morphology and dynamics of the jets are similar to that discussed in previous works in the literature. The figures 5.17 to 5.21 show contour plots of the rest-mass density of the jets simulated with the RKFD-WENO5 and the RKFV-WENO5 schemes at different mesh resolutions. There are some differences in the inner structure of the jets and in the form of the head, mainly because the deceleration phase of the jets, which is caused by the generation and separation of vortices at the head of the jet, is different for the resolutions used in the simulations. All beams remain collimated from the nozzle, where the beam is injected into the computational region, to the head of the jets. It is also important to note that the beam radius does not increase from the nozzle to the head of the jet. At the end of the beam, a strong "terminal Mach shock" is present. One of the most active points is called a "hot spot", into which shocked beam gas enters through the terminal Mach shock at the head of the jet. The pressure in the hot spot is very high, because of the energy dissipation at the terminal Mach shock, and is matched by ambient gas compressed at the bow shock. It is also observed a back flow that creates a shear flow, and the contact surface becomes unstable because of Kelvin-Helmholtz instabilities. The surface between the back flow and the shocked ambient gas flow also becomes unstable and causes the appearance of vortices in the larger cocoon. They are more visible in the figure 5.21, where we have simulated the jet with the highest resolution.

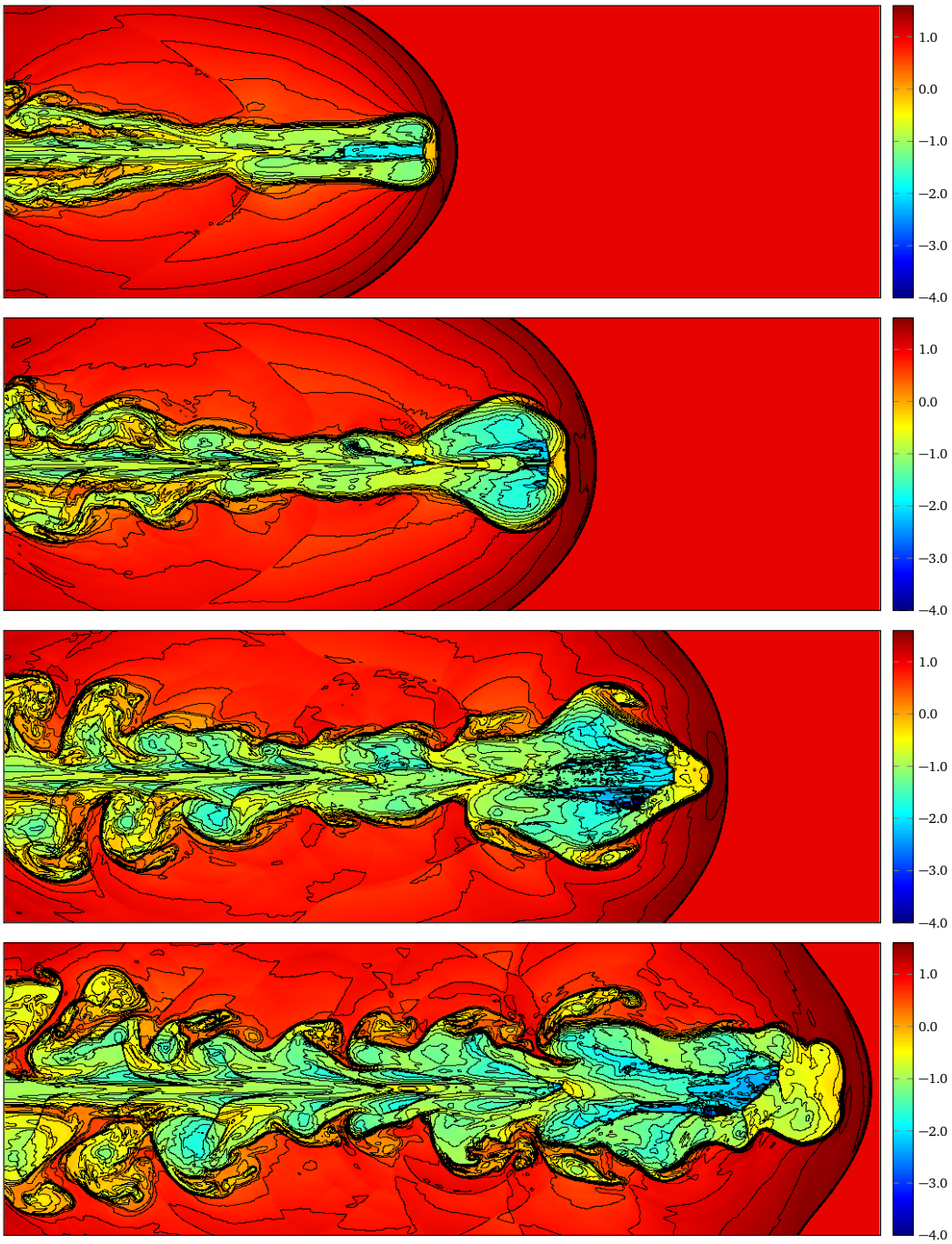

Figure 5.17: Relativistic astrophysical jet simulation. The logarithm of rest-mass density at simulation times $t = 60$, $t = 80$, $t = 100$ and $t = 120$. The RKFD with WENO5 is used in the simulation. The mesh is made of 1800×600 points.

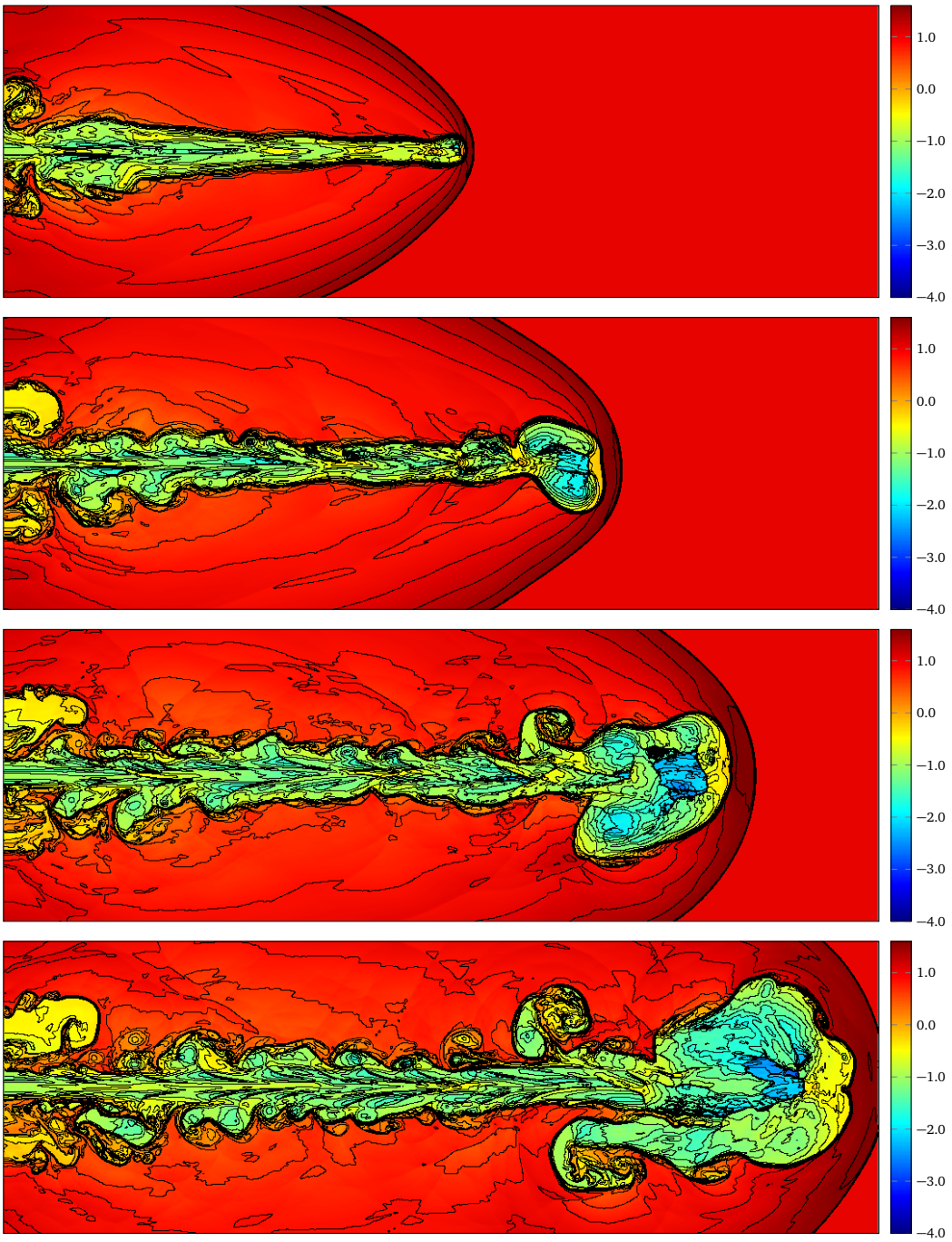

Figure 5.18: Relativistic astrophysical jet simulation. The logarithm of rest-mass density at simulation times $t = 60$, $t = 80$, $t = 100$ and $t = 120$. The RKFD with WENO5 is used in the simulation. The mesh is made of 2400×800 points.

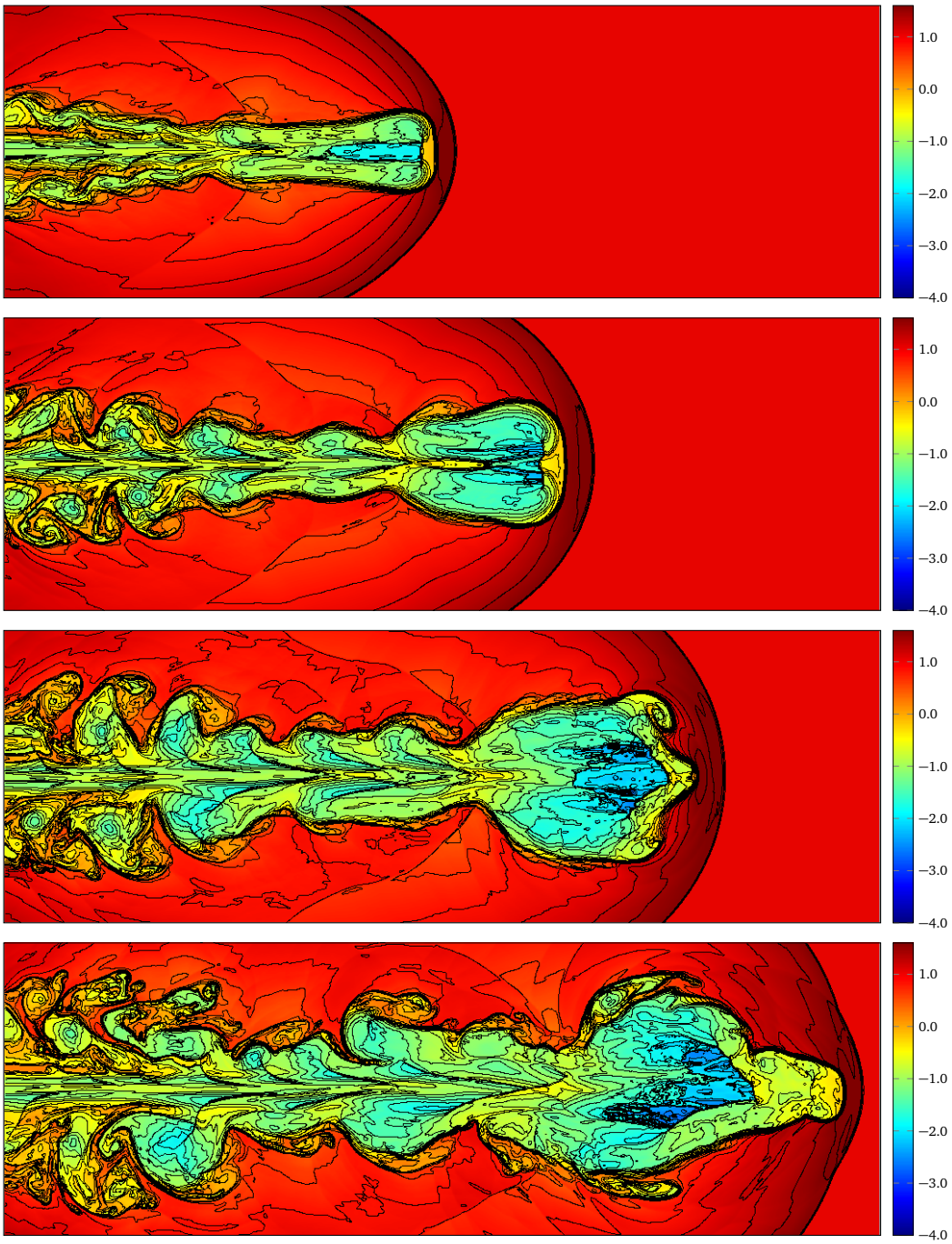

Figure 5.19: Relativistic astrophysical jet simulation. The logarithm of rest-mass density at simulation times $t = 60$, $t = 80$, $t = 100$ and $t = 120$. The RKFV with WENO5 is used in the simulation. The mesh is made of 1800×600 cells.

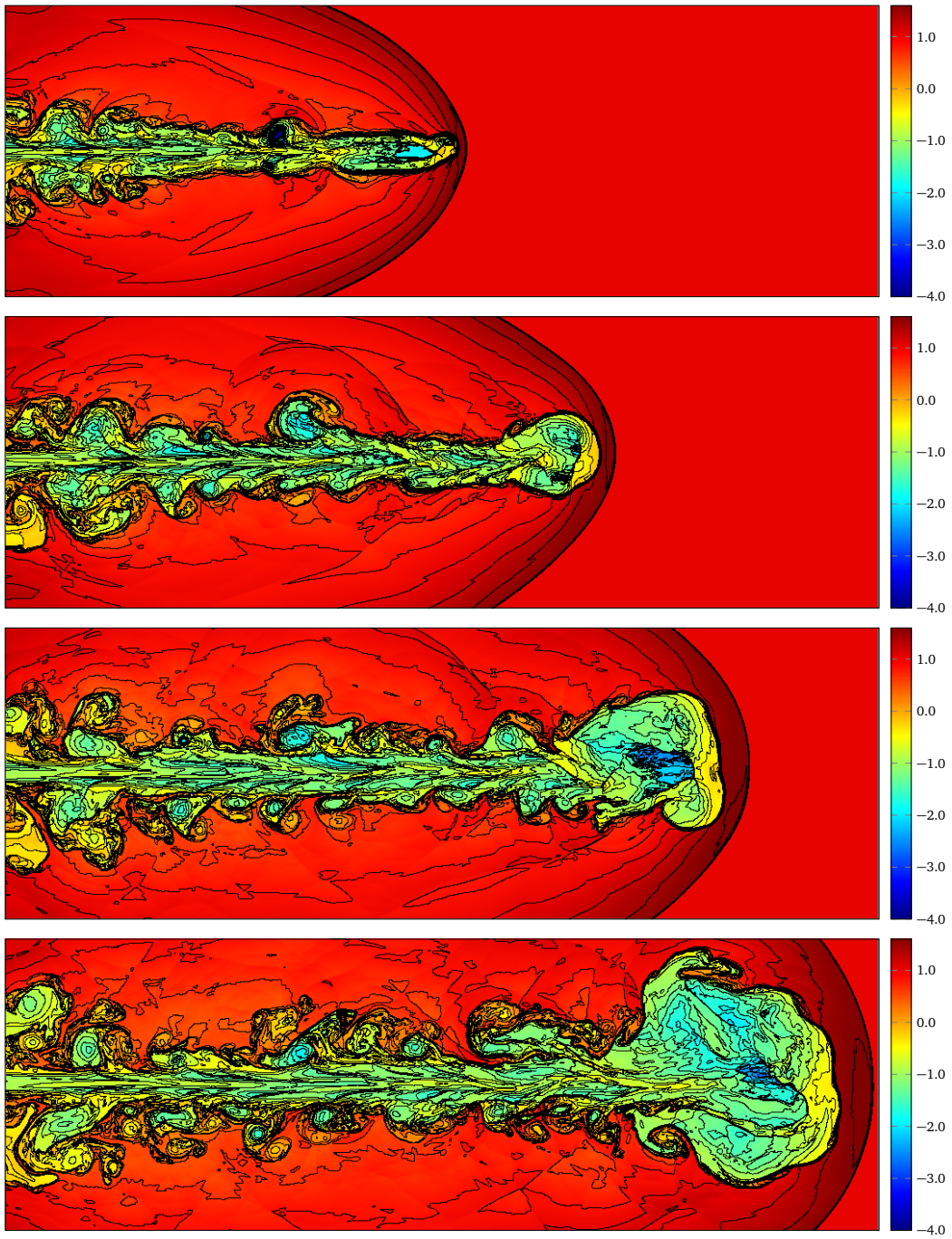

Figure 5.20: Relativistic astrophysical jet simulation. The logarithm of rest-mass density at simulation times $t = 60$, $t = 80$, $t = 100$ and $t = 120$. The RKFV with WENO5 is used in the simulation. The mesh is made of 2400×800 cells.

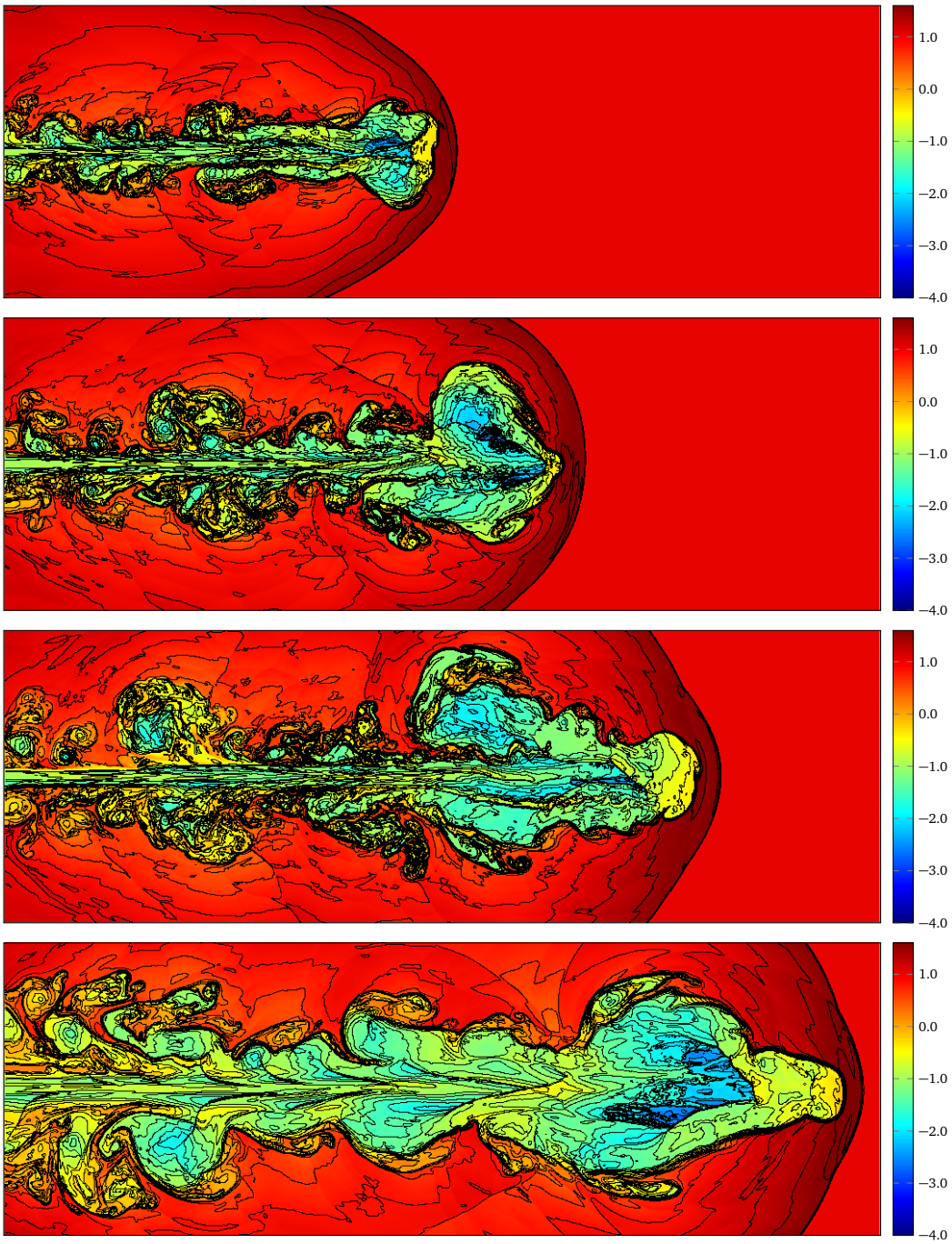

Figure 5.21: Relativistic astrophysical jet simulation. The logarithm of rest-mass density at simulation times $t = 60$, $t = 80$, $t = 100$ and $t = 120$. The RKFD with WENO5 is used in the simulation. The mesh is made of 3600×1200 points.

CHAPTER 6

Relativistic Magnetohydrodynamics

This chapter concerns with the relativistic magnetohydrodynamics equations in special relativity and their numerical solution with the high-order conservative finite difference and finite volume methods. We start with a brief introduction on the relativistic magnetohydrodynamics equations, providing the equations written in conservation form, their eigenstructure, and the algorithm to convert the conservative into primitive variables. An extensive numerical benchmarking is reported, making emphasis on shock-dominated flows, which are solved with efficient and robust very high-order numerical methods.

6.1. Introduction

Special relativistic magnetohydrodynamics provides an accurate description of the underlying dynamics of many astrophysical plasma moving with speeds close to the speed of light. Relativistic magnetohydrodynamics plays a very important role when describing astrophysical jets emerging from super-massive black holes (Begelman et al. 1984). In fact, astronomical observations suggest that astrophysical jets emerging from compact objects involve significant magnetic fields and flows traveling with relativistic speeds. General relativistic effects can be neglected when no strong gravitational fields are involved. The equations of the relativistic magnetohydrodynamics describe the behavior of relativistic, conducting fluids subject to electromagnetic fields. The main assumption is that the mean free-path of the electrons is much smaller than the characteristic length scale of the problem. This leads to a high collisional frequency of the electrons.

The numerical solution of the special relativistic magnetohydrodynamics received a boost with the development of finite volume based codes by Komissarov (1999) and Balsara (2001). The authors used second order TVD schemes for solving the SRMHD equations written in conservation form. Further work for solving these equations has been done for several authors, which enormously improved the quality of the Riemann solvers employed (Mignone & Bodo 2006; Mignone & McKinney 2007; Mignone et al. 2009), implemented high-order reconstruction operator in order to enhance the accuracy of the schemes del Zanna et al. (2003), Anderson et al. (2006), del Zanna et al. (2007), Mignone et al. (2007), and Dumbser et al. (2008), or developed robust adaptive mesh refinement algorithms for SRMHD (Mignone et al. 2012; Keppens et al. 2012).

6.2. Equations

6.2.1. Equations in conservation form

Considering the Minkowski spacetime with Cartesian coordinates (t, x, y, z), the equations of the special relativistic magnetohydrodynamics form a system of conservation laws which can be written as (see Komissarov (1999), and Balsara (2001))

$$\frac{\partial D}{\partial t} + \nabla \cdot (D\boldsymbol{v}) = 0, \qquad \text{(Mass Conservation)} \tag{6.1a}$$

$$\frac{\partial \boldsymbol{S}}{\partial t} + \nabla \cdot (\boldsymbol{S} \otimes \boldsymbol{v} + \mathbb{P}) = \boldsymbol{0}, \qquad \text{(Momentum Conservation)} \tag{6.1b}$$

$$\frac{\partial E}{\partial t} + \nabla \cdot \boldsymbol{S} = 0, \qquad \text{(Energy Conservation)} \tag{6.1c}$$

$$\frac{\partial \boldsymbol{B}}{\partial t} + \nabla \cdot \Big(\boldsymbol{B} \otimes \boldsymbol{v} - \boldsymbol{v} \otimes \boldsymbol{B}\Big) = \boldsymbol{0}, \qquad \text{(Induction Equations)} \tag{6.1d}$$

where we have defined the tensor $\mathbb{P}$ as follows

$$\mathbb{P} = \left(p + \frac{|\boldsymbol{B}|^2}{2\Gamma^2} + \frac{(\boldsymbol{v} \cdot \boldsymbol{B})^2}{2}\right)\mathbb{I} - \left(\frac{\boldsymbol{B}}{\Gamma^2} + (\boldsymbol{v} \cdot \boldsymbol{B})\boldsymbol{v}\right) \otimes \boldsymbol{B}, \tag{6.2}$$

where the quantity in the first bracket is the total pressure (which has contributions from the thermal and magnetic pressure). An equation of state (EOS) is used to close the system. We make use of the ideal gas equation of state with adiabatic exponent γ

$$p = (\gamma - 1)\left(E - \frac{1}{2}\rho\,|\boldsymbol{v}|^2 - \frac{1}{2}\,|\boldsymbol{B}|^2\right). \tag{6.3}$$

The system (6.1) must satisfy an additional constraint: the solenoidal property of the magnetic field,

$$\nabla \cdot \boldsymbol{B} = 0, \tag{6.4}$$

which is the same as in classical magnetohydrodynamics.

6.2.2. Relativistic Magnetohydrodynamics Equations with Divergence Cleaning

Because of the solenoidal constraint of the magnetic field, see equation (6.4), a way to maintain this restriction from the numerical point of view has to be found. Although a very extended approach in the astrophysical community is the constrained transport (Evans & Hawley 1988; Stone & Norman 1992a; Stone & Norman 1992b), we prefer to use the divergence cleaning of Dedner et al. (2002). In this work we use the mixed approach explained in Dedner et al. (2002). Therefore, the equations of the relativistic magnetohydrodynamics together with the Generalized Lagrange Multiplier (GLM) method for the divergence correction are given by

$$\frac{\partial D}{\partial t} + \nabla \cdot (D\boldsymbol{v}) = 0, \qquad \text{(Mass Conservation)} \tag{6.5a}$$

$$\frac{\partial \boldsymbol{S}}{\partial t} + \nabla \cdot (\boldsymbol{S} \otimes \boldsymbol{v} + \mathbb{P}) = \boldsymbol{0}, \qquad \text{(Momentum Conservation)} \tag{6.5b}$$

$$\frac{\partial E}{\partial t} + \nabla \cdot \boldsymbol{S} = 0, \qquad \text{(Energy Conservation)} \tag{6.5c}$$

$$\frac{\partial \boldsymbol{B}}{\partial t} + \nabla \cdot \big(\boldsymbol{B} \otimes \boldsymbol{v} - \boldsymbol{v} \otimes \boldsymbol{B} + \psi \mathbb{I}\big) = \boldsymbol{0}, \qquad \text{(Induction Equations)} \tag{6.5d}$$

$$\frac{\partial \psi}{\partial t} + \nabla \cdot \big(c_h^2 \boldsymbol{B}\big) = -\frac{c_h^2}{c_p^2}\psi. \qquad \text{(Divergence Cleaning)} \tag{6.5e}$$

6.2.3. Variables Transformations

The eight conserved quantities D, S_x, S_y, S_z, E, B_x, B_y, and B_z are the mass density, the three components of the momentum density, the total energy density, and the three components of the magnetic field, respectively. They are all measured in the laboratory frame, and are related to quantities in the local rest frame of the fluid, the so-called primitive variables $(\rho, v_x, v_y, v_z, p, B_x, B_y, B_z)$, through

$$D = \rho\Gamma, \tag{6.6a}$$

$$\boldsymbol{S} = \big(\rho h \Gamma^2 + |\boldsymbol{B}|^2\big)\boldsymbol{v} - (\boldsymbol{v}\cdot\boldsymbol{B})\boldsymbol{B}, \tag{6.6b}$$

$$E = \rho h \Gamma^2 - p + \frac{|\boldsymbol{B}|^2}{2} + \frac{|\boldsymbol{v}|^2 |\boldsymbol{B}|^2}{2} - \frac{(\boldsymbol{v}\cdot\boldsymbol{B})^2}{2}, \tag{6.6c}$$

$$\boldsymbol{B} = \boldsymbol{B}, \tag{6.6d}$$

where $\boldsymbol{v}$ is the three-velocity of the fluid and is related with the four-velocity $\mathbf{u}$ through

$$\mathbf{u} = \Gamma\big(1, \boldsymbol{v}\big), \tag{6.7}$$

with Γ the Lorentz factor, defined by

$$\Gamma = \frac{1}{\sqrt{1 - v^2}}. \tag{6.8}$$

The rest-mass density is the quantity ρ, p is the thermal pressure of the gas, and h is the specific enthalpy. The velocity $\boldsymbol{v} = (v_x, v_y, v_z)$ of a fluid element is defined as the velocity of the rest frame of this fluid element with respect to the laboratory frame. The fluid velocity is a function of (t, x, y, z), as are the thermodynamic quantities ρ, p and n. The fluid velocity is also referred to as the "collective" velocity.

The system (6.1) of partial differential equations is closed with an equation of state $h = h(p, \rho)$ or $p = p(\rho, \varepsilon)$. The system (6.1) is hyperbolic for causal equations of state (Anile 1989; Rezzolla & Zanotti 2013), i.e., for those where the local sound speed satisfies $c_s < 1$, where c_s is defined by

$$h c_s^2 = -\rho \frac{\partial h}{\partial \rho}\left(\rho \frac{\partial h}{\partial p} - 1\right)^{-1}, \tag{6.9}$$

In this work, we employ the most commonly used equation of state, the ideal gas equation of state, which is given by

$$p = (\gamma - 1)(\varepsilon - \rho), \quad \text{or} \quad h = 1 + \frac{\gamma}{\gamma - 1}\frac{p}{\rho}. \tag{6.10}$$

Here $\gamma = c_p/c_v$ is the ratio of specific heats and ε is the sum of the internal and rest-mass energy densities in the local frame and is related to the specific enthalpy as

$$h = \frac{\varepsilon + p}{\rho}. \tag{6.11}$$

In this way, the speed of sound is given by

$$c_s^2 = \frac{\gamma p}{\rho h}. \tag{6.12}$$

Algorithm to recover the primitive variables

Although the numerical scheme evolves the conservative variables $\boldsymbol{u}$, for the calculation of several quantities necessary for the execution of the code (for example, the physical fluxes, the fastest waves, the characteristic variables, etc), the primitive variables have to be calculated at least once every time step. The equations (6.6) express the relation between the conservative variables and the primitive variables. As it is clearly noticed from these equations, such relation is highly nonlinear, and a procedure to find the primitive variables has to be developed. Following the algorithms discussed in Noble et al. (2006) and Mignone & McKinney (2007), we employ in our codes the strategies presented in those works. In this work we solve iteratively an equation for the pressure and then determining the other variables from this (Mignone & McKinney 2007).

Solving numerically with Newton-Raphson

Here we will outline the approach presented by Mignone & McKinney (2007), considering only an ideal equation of state and omitting the more general case when non-relativistic speeds are present (more details can be found in Mignone & McKinney (2007)). Let us write again all equations in (6.6),

$$D = \rho\Gamma, \tag{6.13a}$$

$$\boldsymbol{S} = \left(\rho h\Gamma^2 + |\boldsymbol{B}|^2\right)\boldsymbol{v} - (\boldsymbol{v}\cdot\boldsymbol{B})\boldsymbol{B}, \tag{6.13b}$$

$$E = \rho h\Gamma^2 - p + \frac{|\boldsymbol{B}|^2}{2} + \frac{|\boldsymbol{v}|^2|\boldsymbol{B}|^2}{2} - \frac{(\boldsymbol{v}\cdot\boldsymbol{B})^2}{2}, \tag{6.13c}$$

$$\boldsymbol{B} = \boldsymbol{B}, \tag{6.13d}$$

From these equations, we take in consideration those for the energy and for the square modulus of the momentum. Defining the scalars $\hat{x} = Dh\Gamma$ and $\hat{y} = \boldsymbol{S}\cdot\boldsymbol{B}$, we get

$$E = \hat{x} - p + \frac{1 + |\boldsymbol{v}|^2}{2}|\boldsymbol{B}|^2 - \frac{\hat{y}^2}{2\hat{x}^2}, \tag{6.14}$$

and

$$|\boldsymbol{S}|^2 = \left(\hat{x} + |\boldsymbol{B}|^2\right)^2 |\boldsymbol{v}|^2 - \frac{\hat{y}^2}{\hat{x}^2}\left(2\hat{x} + |\boldsymbol{B}|^2\right). \tag{6.15}$$

From the last equation, one can express $|\boldsymbol{v}|^2$ as a function of the unknown $\hat{x}$

$$|\boldsymbol{v}|^2 = \frac{\hat{y}^2(2\hat{x} + |\boldsymbol{B}|^2) + |\boldsymbol{S}|^2\hat{x}^2}{(\hat{x} + |\boldsymbol{B}|^2)^2\hat{x}^2}. \tag{6.16}$$

The next step is to insert this result into the expression for the energy (6.14)

$$E = \hat{x} - p + \frac{|\boldsymbol{B}|^2}{2} + \frac{|\boldsymbol{B}|^2|\boldsymbol{S}|^2 - \hat{y}^2}{2\left(|\boldsymbol{B}|^2 + \hat{x}\right)^2}. \tag{6.17}$$

This equation will be solved using a Newton-Raphson iterative scheme, where the $(k+1)$-th approximation to $\hat{x}$ is calculated as

$$\hat{x}^{(k+1)} = \hat{x}^{(k)} - \left.\frac{f(\hat{x})}{\mathrm{d}f(\hat{x})/\,\mathrm{d}\hat{x}}\right|_{\hat{x}=\hat{x}^{(k)}}. \tag{6.18}$$

The functional $f(\hat{x})$ is derived from the equation (6.17)

$$f(\hat{x}) = \hat{x} - E - p + \frac{|\boldsymbol{B}|^2}{2} + \frac{|\boldsymbol{B}|^2|\boldsymbol{S}|^2 - \hat{y}^2}{2\left(|\boldsymbol{B}|^2 + \hat{x}\right)^2}. \tag{6.19}$$

Computing the derivative $\mathrm{d}f(\hat{x})/\,\mathrm{d}\hat{x} \equiv \mathrm{d}E/\,\mathrm{d}\hat{x}$, yields

$$\frac{\mathrm{d}E}{\mathrm{d}\hat{x}} = 1 - \frac{\mathrm{d}p}{\mathrm{d}\hat{x}} - \frac{|\boldsymbol{B}|^2|\boldsymbol{S}|^2 - \hat{y}^2}{\left(|\boldsymbol{B}|^2 + \hat{x}\right)^3}. \tag{6.20}$$

Let us assume that $p = p(\rho, \hat{z})$, with

$$\hat{z} \equiv \rho(h-1) = \frac{\rho\Gamma}{\Gamma}(h-1) = \frac{Dh\Gamma - D\Gamma}{\Gamma^2} = \frac{\hat{x} - D\Gamma}{\Gamma^2}. \tag{6.21}$$

Applying the chain rule, we are able to calculate the derivative $\mathrm{d}p/\,\mathrm{d}\hat{x}$,

$$\frac{\mathrm{d}p}{\mathrm{d}\hat{x}} = \left.\frac{\partial p}{\partial \hat{z}}\right|_{\rho} \frac{\mathrm{d}\hat{z}}{\mathrm{d}\hat{x}} + \left.\frac{\partial p}{\partial \rho}\right|_{\hat{z}} \frac{\mathrm{d}\rho}{\mathrm{d}\hat{x}}. \tag{6.22}$$

Calculating the derivatives $\mathrm{d}\hat{z}/\,\mathrm{d}\hat{x}$, $\mathrm{d}\rho/\,\mathrm{d}\hat{x}$, yields

$$\frac{\mathrm{d}\hat{z}}{\mathrm{d}\hat{x}} = \frac{1}{\Gamma^2} - \frac{\Gamma\left(D + 2\hat{z}\Gamma\right)}{2}\frac{\mathrm{d}|\boldsymbol{v}|^2}{\mathrm{d}\hat{x}}, \tag{6.23}$$

and

$$\frac{\mathrm{d}\rho}{\mathrm{d}\hat{x}} = -\frac{D\Gamma}{2}\frac{\mathrm{d}|\boldsymbol{v}|^2}{\mathrm{d}\hat{x}}, \tag{6.24}$$

where

$$\frac{\mathrm{d}|\boldsymbol{v}|^2}{\mathrm{d}\hat{x}} = -\frac{2}{\hat{x}^3}\frac{\hat{y}^2\left[3\hat{x}(\hat{x}+|\boldsymbol{B}|^2)+|\boldsymbol{B}|^4\right]+|\boldsymbol{S}|^2\hat{x}^3}{\left(\hat{x}+|\boldsymbol{B}|^2\right)^3}. \tag{6.25}$$

For the ideal equation of state, we have

$$p(\rho,\hat{z}) = \frac{\gamma-1}{\gamma}\hat{z}. \tag{6.26}$$

From the expression $p(\hat{z},\rho)$ we get easily

$$\frac{\partial p}{\partial \hat{z}} = \frac{\gamma-1}{\gamma}, \quad \frac{\partial p}{\partial \rho} = 0. \tag{6.27}$$

Once $\hat{x}$ has been determined to some accuracy with the Newton-Raphson procedure, we complete the inversion process by computing the velocities from an inversion of equation (6.13b) to obtain

$$v_i = \frac{1}{\hat{x}+|\boldsymbol{B}|^2}\left(S_i + \frac{\hat{y}}{\hat{x}}B_i\right), \tag{6.28}$$

From the velocity, we can calculate the Lorentz factor Γ, and then we get directly $\hat{z}$ from equation (6.21),

$$\hat{z} = \frac{\hat{x}-D\Gamma}{\Gamma^2}. \tag{6.29}$$

The pressure is obtained from the relation

$$p(\rho,\hat{z}) = \frac{\gamma-1}{\gamma}\hat{z}. \tag{6.30}$$

The rest-mass density is obtained from

$$\rho = \frac{D}{\Gamma}, \tag{6.31}$$

and the magnetic field are the same as primitive variables.

6.3. Spectral Decomposition

The characteristic structure of the SRMHD system was first studied by Anile & Pennisi (1987); more details can be found in Anile (1989). These authors derived the eigenvalues and eigenvectors of the associated Jacobian $\mathbf{A}_x(\boldsymbol{u}) = \partial \boldsymbol{f}/\partial \boldsymbol{u}$ by using the covariant notation.

Here we only will show the eigenvalues. For the eigenvectors, we refer to Anile & Pennisi (1987), Anile (1989), Antón et al. (2006), and Antón et al. (2010). These are one entropy wave

$$\lambda_0 = v_x, \tag{6.32}$$

two Alfvén waves

$$\lambda_{\rm A}^{\pm} = \frac{u^x \pm \tilde{b}^x}{u^0 \pm \tilde{b}^0}, \tag{6.33}$$

and four magneto-sonic waves (two fast and two slow waves). These are found by solving the nonlinear quartic equation

$$(1-\varepsilon^2)(u^0\lambda - u^x)^4 + (1-\lambda^2)[(c_s^2(\tilde{b}^0\lambda - \tilde{b}^x)^2 - \varepsilon^2(u^0\lambda - u^x)^2] = 0, \tag{6.34}$$

where $c_s^2 = \Gamma p/w$ is the sound speed squared, $\tilde{b}^\alpha = b^\alpha/\sqrt{w_{\rm tot}}$ ($|\tilde{b}|^2 = \tilde{b}_\alpha \tilde{b}^\alpha = |b|^2/w_{\rm tot}$), and $\varepsilon^2 = c_s^2 + |\tilde{b}|^2 - c_s^2|\tilde{b}|^2$.

6.4. Numerical Benchmarking

6.4.1. One-dimensional Problems

The benchmark for the relativistic magnetohydrodynamics equations involves the solution of one-dimensional Riemann problems. Two fluids with different conditions are separated with a membrane at point x_m. After the membrane is removed, the flow is characterized by the appearance of different shock waves and discontinuities. The solution is computed up to certain end time t. The considered tests are those discussed by Balsara (2001) and Giacomazzo & Rezzolla (2006). For all these tests, we set transmissive boundary conditions. The one-dimensional domain is the closed interval $[0,1]$, and the membrane separating the left and right initial states is localized in the point $x_m = 0.5$. The left state will be represented by $\hat{\boldsymbol{u}}_L = \left(\rho, v_x, v_y, v_z, p, B_x, B_y, B_z\right)_L$ and the right state by $\hat{\boldsymbol{u}}_R = \left(\rho, v_x, v_y, v_z, p, B_x, B_y, B_z\right)_R$. Both states are written in terms of the primitive variables. The exact solution is computed using the exact Riemann solver developed by Giacomazzo & Rezzolla (2006). The computational domain is decomposed into 500 grid points for the RKFD method, and 500 cells for the RKFV method. The numerical results discussed below were obtained with a high-order WENO7 reconstruction for the RKFD and RKFV methods. All computations used the shock capturing strategy outlined in section 3.2, that is, for the RKFD and the RKFV we use the WENO3 reconstruction operator for those regions with shocks. The exact solution of the Riemann problems is plotted as red lines.

Riemann Problem 1

The initial condition is determined by the following left and right states

$$\begin{aligned} \hat{\boldsymbol{u}}_L &= \left(1,0,0,0,1000,1,0,0\right), \\ \hat{\boldsymbol{u}}_R &= \left(0.1,0,0,0,1,1,0,0\right). \end{aligned} \tag{6.35}$$

This initial state will develop into a left-moving fast rarefaction wave, a contact discontinuity and a right-moving fast shock. We have employed the ideal gas equation of

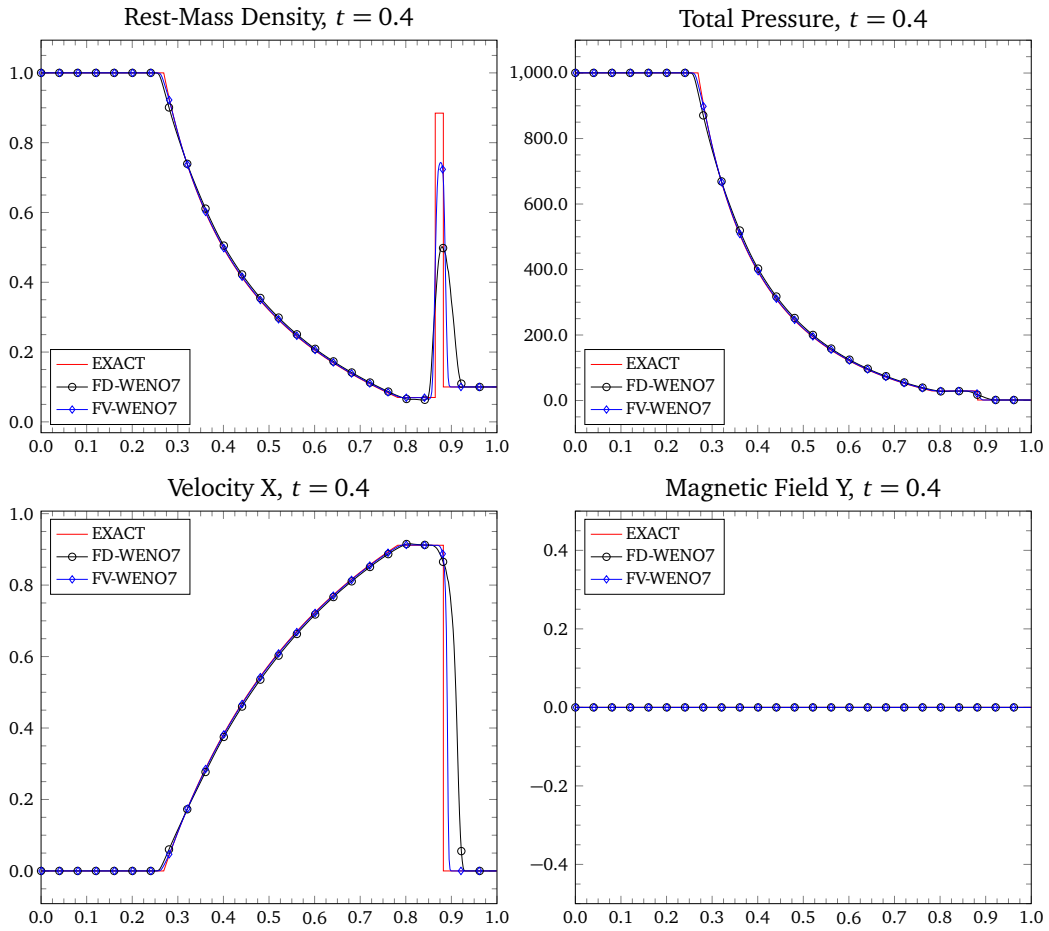

Figure 6.1: Riemann problem 1. The left and right states are given by equation (6.35). The final simulation time is $t = 0.4$. Plots of the rest-mass density, total pressure, the x-component of the velocity, and the y-component of the magnetic field are depicted. For the RKFD and RKFV, the WENO7 reconstruction operator is used in smooth parts of the flow and the WENO3 in regions with shocks.

state with adiabatic index $\gamma = 4/3$. The CFL number used in this simulation is given by CFL $= 0.95$. We set transmissive boundary conditions at both left and right sides of the computational domain. Plots of the rest-mass density, total pressure, x-component of the velocity and the y-component of the magnetic field are depicted in the figure 6.1 at time $t = 0.4$. No oscillations are present around the discontinuities. Both schemes smear the shock wave, especially the RKFD method. The RKFV scheme agrees much more better the shell between the contact discontinuity and the shock wave.

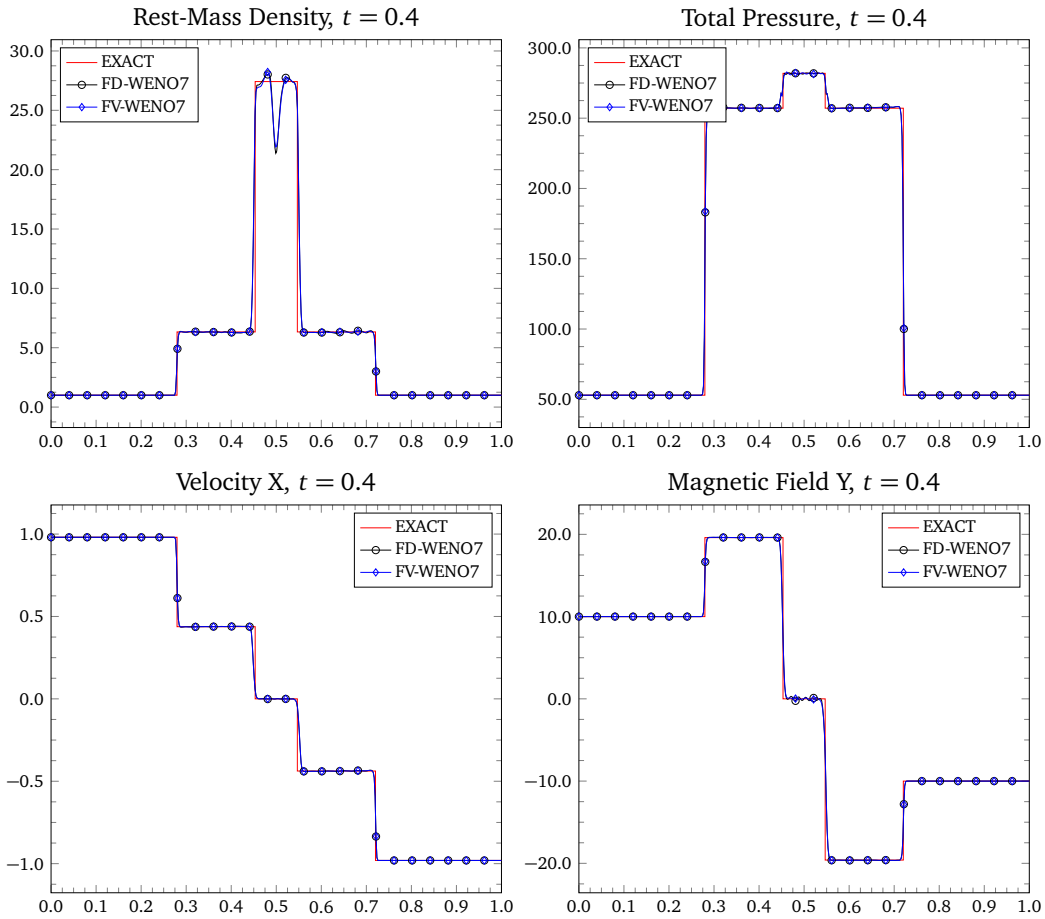

Figure 6.2: Riemann problem 2. The left and right states are given by equation (6.36). The final simulation time is $t = 0.4$. Plots of the rest-mass density, total pressure, the x-component of the velocity, and the y-component of the magnetic field are depicted. For the RKFD and RKFV, the WENO7 reconstruction operator is used in smooth parts of the flow and the WENO3 in regions with shocks.

Riemann Problem 2

The initial condition is determined by the following left and right states

$$\begin{aligned} \hat{\boldsymbol{u}}_L &= \big(1, 5/\sqrt{26}, 0, 0, 1, 10, 10, 0\big), \\ \hat{\boldsymbol{u}}_R &= \big(1, -5/\sqrt{26}, 0, 0, 1, 10, -10, 0\big). \end{aligned} \tag{6.36}$$

This Riemann problem features a left-moving fast shock, a left-moving slow shock, a right-moving slow shock and a right-moving fast shock. We set the adiabatic index $\gamma = 4/3$, for an ideal equation of state. The CFL condition employed in this simulation is $\text{CFL} = 0.95$. We use transmissive boundary conditions at both left and right sides of the computational domain. The z-component of the velocity and magnetic field is zero in the whole domain regions. Plots of the rest-mass density, total pressure, x-component of the velocity and the y-component of the magnetic field are depicted in the figure 6.2

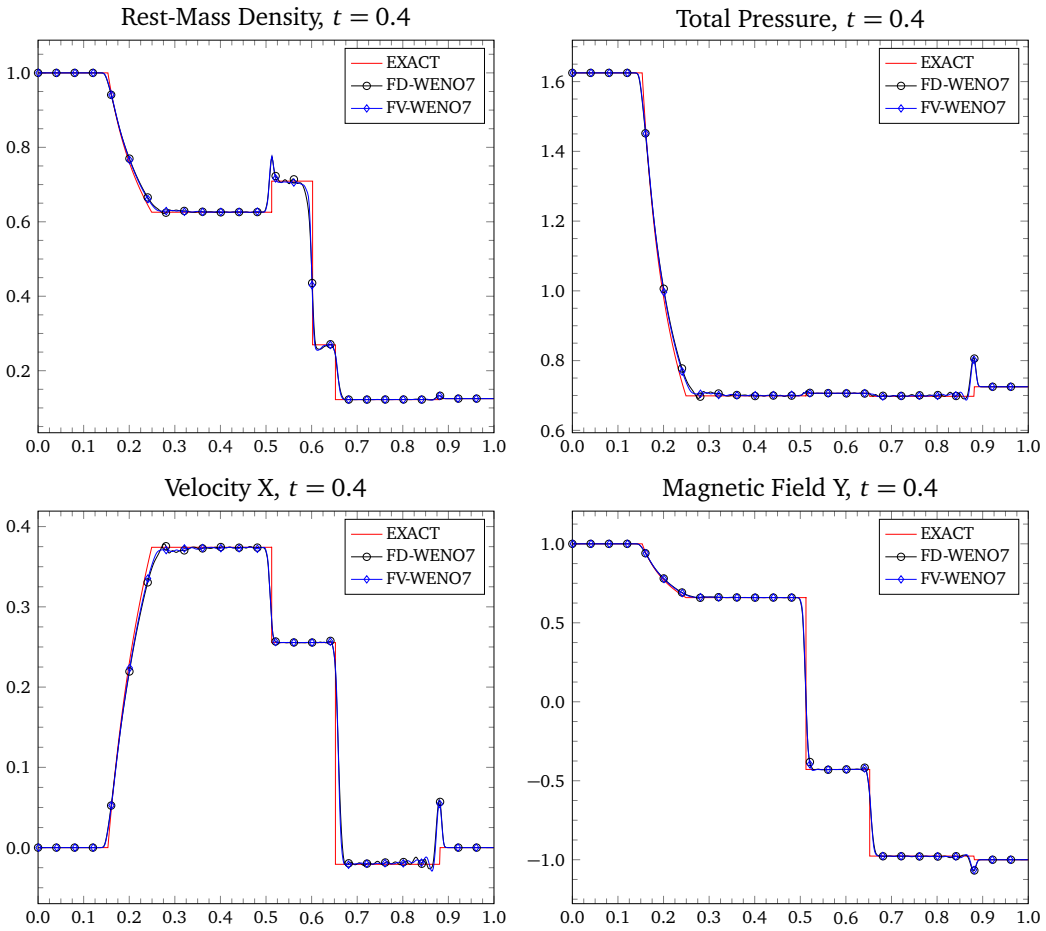

Figure 6.3: Riemann problem 3. The left and right states are given by equation (6.37). The final simulation time is $t = 0.4$. Plots of the rest-mass density, total pressure, the x-component of the velocity, and the y-component of the magnetic field are depicted. For the RKFD and RKFV, the WENO7 reconstruction operator is used in smooth parts of the flow and the WENO3 in regions with shocks.

at time $t = 0.4$. We observe some small oscillations close to the shock waves, for both methods, RKFD and RKFV. It is very appreciable the under-density around $x = 0.5$, and it is because of the solution is affected by the so-called wall-heating effect (Noh 1987).

Riemann Problem 3

The initial condition is determined by the following left and right states

$$\begin{aligned} \hat{\boldsymbol{u}}_L &= \big(1, 0, 0, 0, 1, 0.5, 1, 0\big), \\ \hat{\boldsymbol{u}}_R &= \big(0.125, 0, 0, 0, 0.1, 0.5, -1, 0\big). \end{aligned} \tag{6.37}$$

This test involves the so-called compound structures, that is, structures that involve a shock and a rarefaction of the same wave family moving together. Their existence was first discussed in Brio & Wu (1988) for the classical magnetohydrodynamics equations.

This test involves a left-moving slow compound wave. In the analytic solution, the slow composed wave is absent. Other structures appearing after the breakup of the membrane are two fast rarefactions waves propagating in opposite directions, two slow shocks also propagating in opposite directions, and a contact discontinuity. For this problem we have assumed $\gamma = 2$. We have used CFL $= 0.95$. Transmissive boundary conditions were set at both sides of the interval. Plots of the rest-mass density, total pressure, the x-component of the velocity, and the y-component of the magnetic field are depicted in the figure 6.3 at time $t = 0.4$. Some oscillations are observed in this computation, and also the compound structure. The analytic solution does not show this structure.

Riemann Problem 4

The initial condition is determined by the following left and right states

$$\begin{aligned} \hat{\boldsymbol{u}}_L &= \big(1, 0, 0, 0, 30, 5, 6, 6\big), \\ \hat{\boldsymbol{u}}_R &= \big(1, 0, 0, 0, 1, 5, 0.7, 0.7\big). \end{aligned} \tag{6.38}$$

The solution to this Riemann problem features two left-moving fast and slow rarefactions waves, a contact discontinuity and two right-moving fast and slow shocks. We have employed the ideal gas equation of state with adiabatic index $\gamma = 5/3$. We have used CFL $= 0.95$. We use transmissive boundary conditions at both left and right sides of the computational domain. Plots of the rest-mass density, total pressure, the x-component of the velocity, and the y-component of the magnetic field are depicted in the figure 6.4 at time $t = 0.4$. From the figure, we can see that both high-order schemes have some troubles to capture the shock waves. Besides, the contact discontinuity is smeared by both numerical methods.

Riemann Problem 5

The initial condition is determined by the following left and right states

$$\begin{aligned} \hat{\boldsymbol{u}}_L &= \big(1, 0, 0, 0, 1000, 10, 7, 7\big), \\ \hat{\boldsymbol{u}}_R &= \big(1, 0, 0, 0, 0.1, 10, 0.7, 0.7\big). \end{aligned} \tag{6.39}$$

The solution is composed of two left-moving fast and slow rarefactions waves, a contact discontinuity and two right-moving fast and slow shocks waves. We have employed the ideal gas equation of state with adiabatic index $\gamma = 5/3$. The CFL condition used in this computation was CFL $= 0.95$. Transmissive boundary conditions were set at both left and right sides of the computational domain. Plots of the rest-mass density, total pressure, the x-component of the velocity, and the y-component of the magnetic field are depicted in the figure 6.5 at time $t = 0.4$. A dense intermediate state located between a right-moving shock wave and the contact discontinuity is developed. This feature is very challenging to capture, and both schemes do not resolve very well this shell, especially the RKFD method.

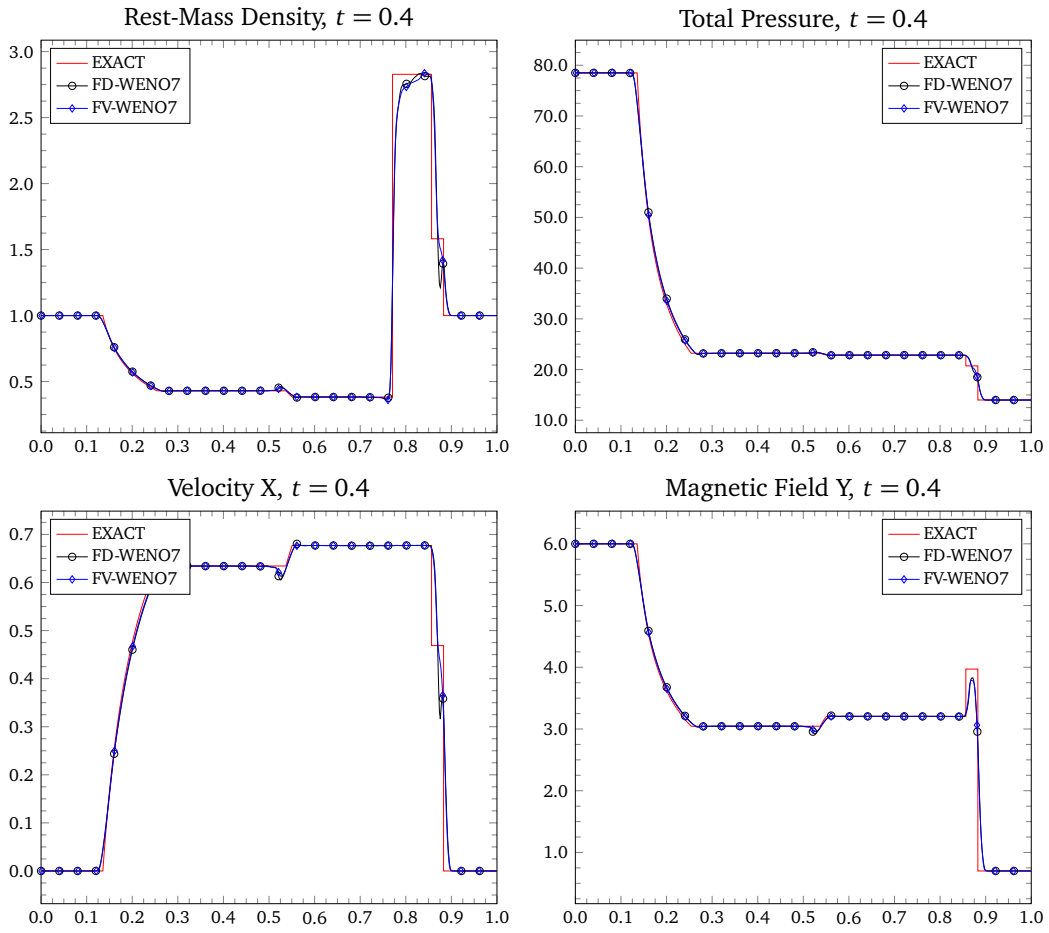

Figure 6.4: Riemann problem 4. The left and right states are given by equation (6.38). The final simulation time is $t = 0.4$. Plots of the rest-mass density, total pressure, the x-component of the velocity, and the y-component of the magnetic field are depicted. For the RKFD and RKFV, the WENO7 reconstruction operator is used in smooth parts of the flow and the WENO3 in regions with shocks.

Riemann Problem 6

The initial condition is determined by the following left and right states

$$\begin{aligned} \hat{\boldsymbol{u}}_L &= \big(1, 0.999, 0, 0, 0.1, 10, 7, 7\big), \\ \hat{\boldsymbol{u}}_R &= \big(1, -0.999, 0, 0, 0.1, 10, -7, -7\big). \end{aligned} \tag{6.40}$$

This Riemann problem features two left-moving fast and slow shocks and two right-moving fast and slow shocks. We have employed the ideal gas equation of state with adiabatic index $\gamma = 5/3$. We have used the CFL number CFL $= 0.95$. Transmissive boundary conditions were set at both left and right sides of the computational domain. Plots of the rest-mass density, total pressure, the x-component of the velocity, and the y-component of the magnetic field are depicted in the figure 6.6 at time $t = 0.4$. In the figure no oscillations are visible. The RKFD and the RKFV have a similar behavior,

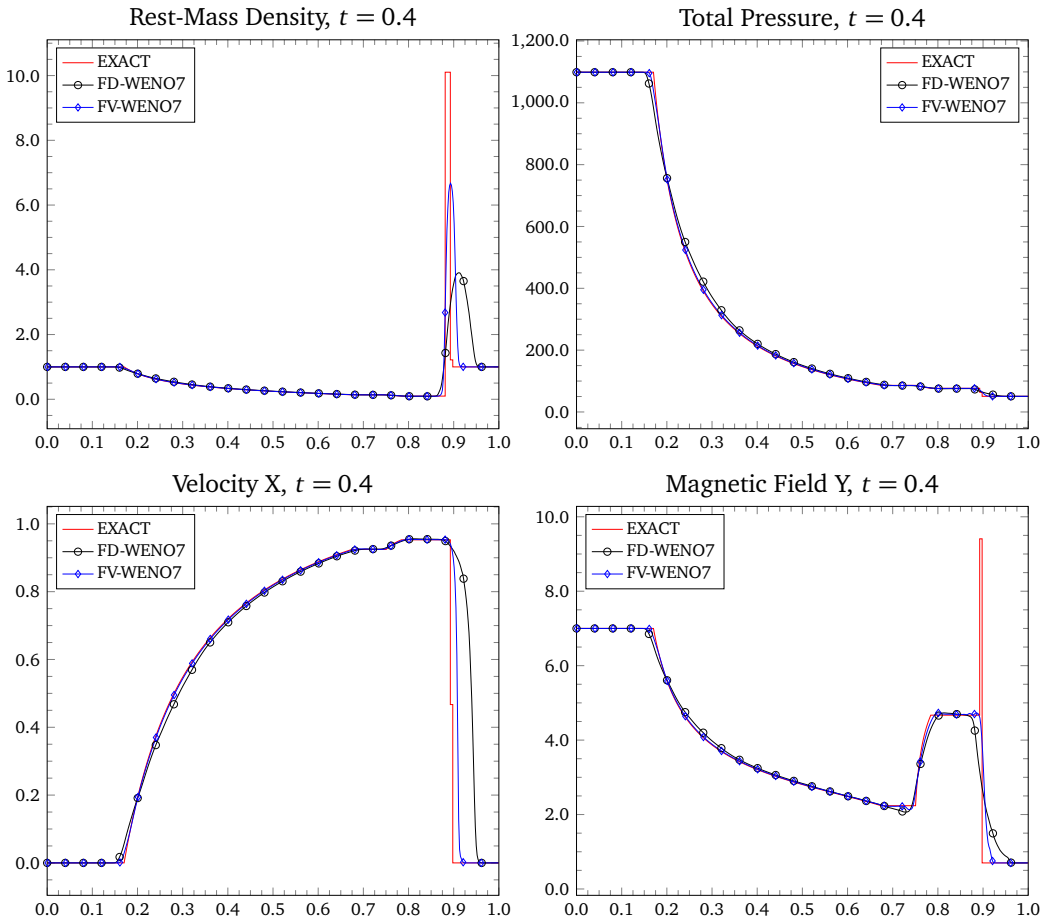

Figure 6.5: Riemann problem 5. The left and right states are given by equation (6.39). The final simulation time is $t = 0.4$. Plots of the rest-mass density, total pressure, the x-component of the velocity, and the y-component of the magnetic field are depicted. For the RKFD and RKFV, the WENO7 reconstruction operator is used in smooth parts of the flow and the WENO3 in regions with shocks.

overlapping each other. Like the Riemann problem 2, this test shows an under-density around $x = 0.5$, and it is due to the wall-heating effect (Noh 1987).

Riemann Problem 7

The initial condition is determined by the following left and right states

$$\begin{aligned} \hat{\boldsymbol{u}}_L &= \big(1.08, 0.4, 0.3, 0.2, 0.95, 2, 0.3, 0.3\big), \\ \hat{\boldsymbol{u}}_R &= \big(1, -0.45, -0.2, 0.2, 1, 2, -0.7, 0.5\big). \end{aligned} \tag{6.41}$$

The solution involves a left-moving fast shock, a left-moving Alfvén discontinuity, a left-moving slow rarefaction, a contact discontinuity, a right-moving slow shock, a right-moving Alfvén discontinuity and a right-moving fast shock. We used an ideal gas equation of state with adiabatic index $\gamma = 5/3$. We have also employed a CFL number CFL $= 0.95$.

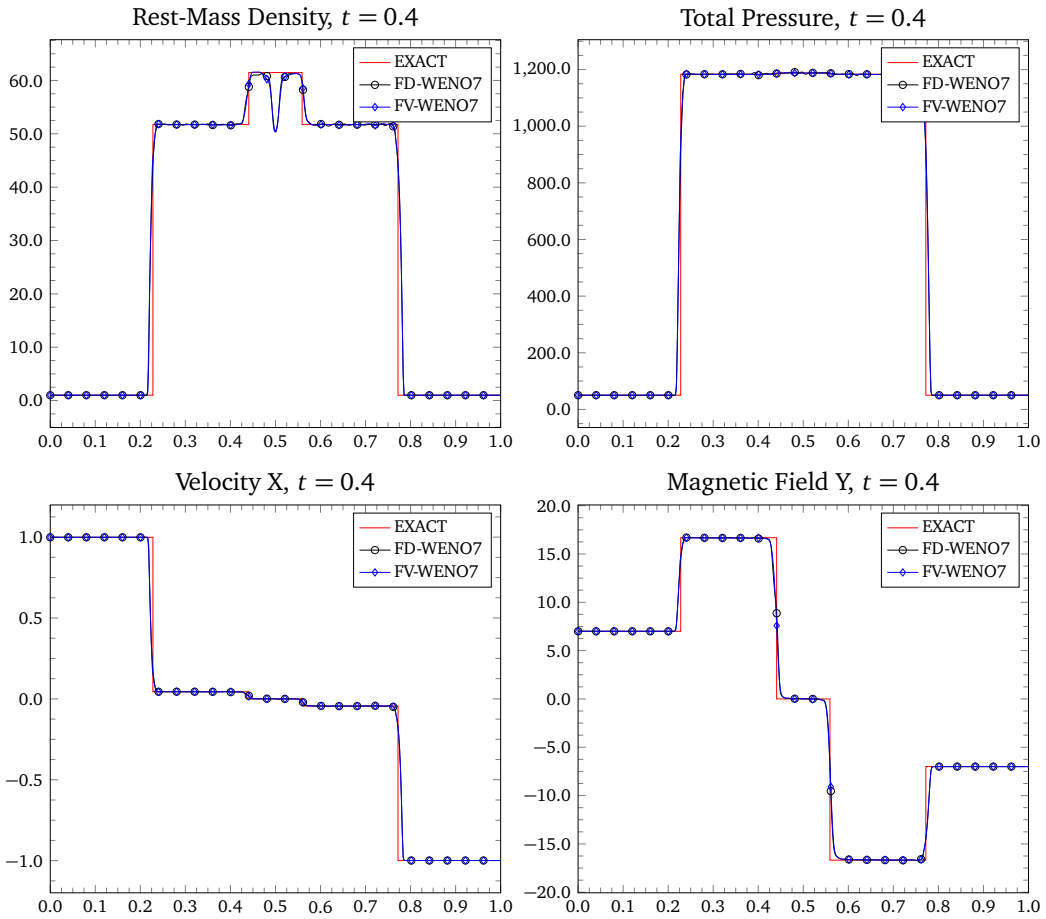

Figure 6.6: Riemann problem 6. The left and right states are given by equation (6.40). The final simulation time is $t = 0.4$. Plots of the rest-mass density, total pressure, the x-component of the velocity, and the y-component of the magnetic field are depicted. For the RKFD and RKFV, the WENO7 reconstruction operator is used in smooth parts of the flow and the WENO3 in regions with shocks.

Transmissive boundary conditions were imposed at both left and right sides of the computational domain. Plots of the rest-mass density, total pressure, the x-component of the velocity, and the y-component of the magnetic field are depicted in the figure 6.7 at time $t = 0.4$. Some oscillations are observed around the left-moving fast shock. An undershooting and smearing of the contact discontinuity is also appreciable from the simulation. The other flow features are very well resolved with the high-order RKFD and RKFV methods.

Riemann Problem 8

The initial condition is determined by the following left and right states

$$\begin{aligned} \hat{\boldsymbol{u}}_L &= \big(1, 0, 0.3, 0.4, 5, 1, 6, 2\big), \\ \hat{\boldsymbol{u}}_R &= \big(0.9, 0, 0, 0, 5.3, 1, 5, 2\big). \end{aligned} \tag{6.42}$$

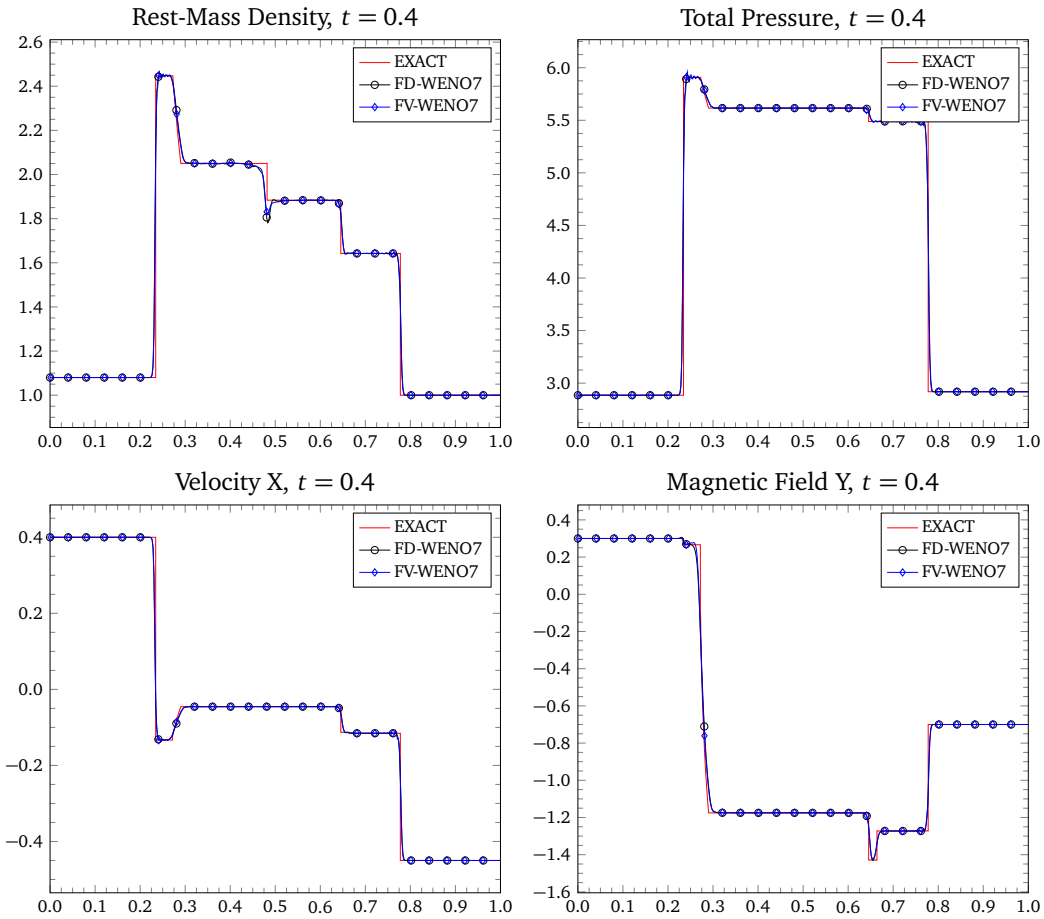

Figure 6.7: Riemann problem 7. The left and right states are given by equation (6.41). The final simulation time is $t = 0.4$. Plots of the rest-mass density, total pressure, the x-component of the velocity, and the y-component of the magnetic field are depicted. For the RKFD and RKFV, the WENO7 reconstruction operator is used in smooth parts of the flow and the WENO3 in regions with shocks.

The solution to this Riemann problem features a left-moving fast rarefaction, a left-moving Alfvén discontinuity, a left-moving slow shock, a contact discontinuity, a right-moving slow shock, a right-moving Alfvén discontinuity and a right-moving fast shock. The gas has adiabatic index $\gamma = 5/3$. The numerical solution is computed assuming CFL $= 0.95$. We use transmissive boundary conditions at both left and right sides of the computational domain. Plots of the rest-mass density, total pressure, the x-component of the velocity, and the y-component of the magnetic field are depicted in the figure 6.8 at time $t = 0.4$. All methods present a very good agreement with the exact solution. The Alvén discontinuities are fairly resolved with both schemes, and some oscillations around the contact discontinuity and the right-moving fast shock are also present in the simulation.

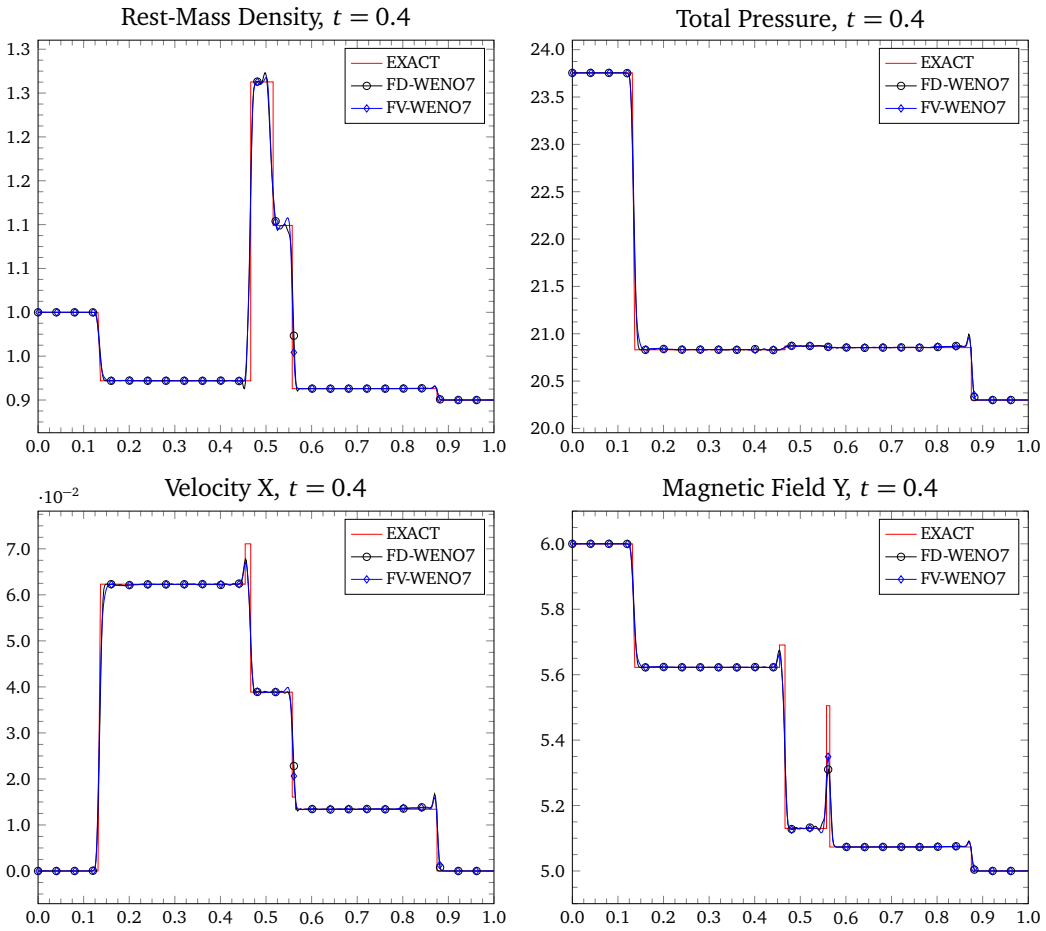

Figure 6.8: Riemann problem 8. The left and right states are given by equation (6.42). The final simulation time is $t = 0.4$. Plots of the rest-mass density, total pressure, the x-component of the velocity, and the y-component of the magnetic field are depicted. For the RKFD and RKFV, the WENO7 reconstruction operator is used in smooth parts of the flow and the WENO3 in regions with shocks.

6.4.2. Multidimensional Test Problems

Magnetic Field Loop Advection

This test has been extensively used for the classical MHD equations. With this one can observe whether the algorithm is able to preserve the condition $\nabla \cdot \boldsymbol{B} = 0$. In this test, a cylindrical current distribution is advected along some direction of the computational domain not aligned with the grid. The magnetic loop remains in magnetostatic balance. For that reason, after some periods, the profile should preserve its form. Multidimensional SRMHD codes that do not include algorithms for preserving the constraint $\nabla \cdot \boldsymbol{B} = 0$, or if they use numerical methods too much diffusive, the magnetic loop will smear over the time (Tóth 2000; Stone et al. 2008; Mignone & Tzeferacos 2010; Beckwith & Stone 2011).

Following the description to this problem given by Beckwith & Stone (2011), the

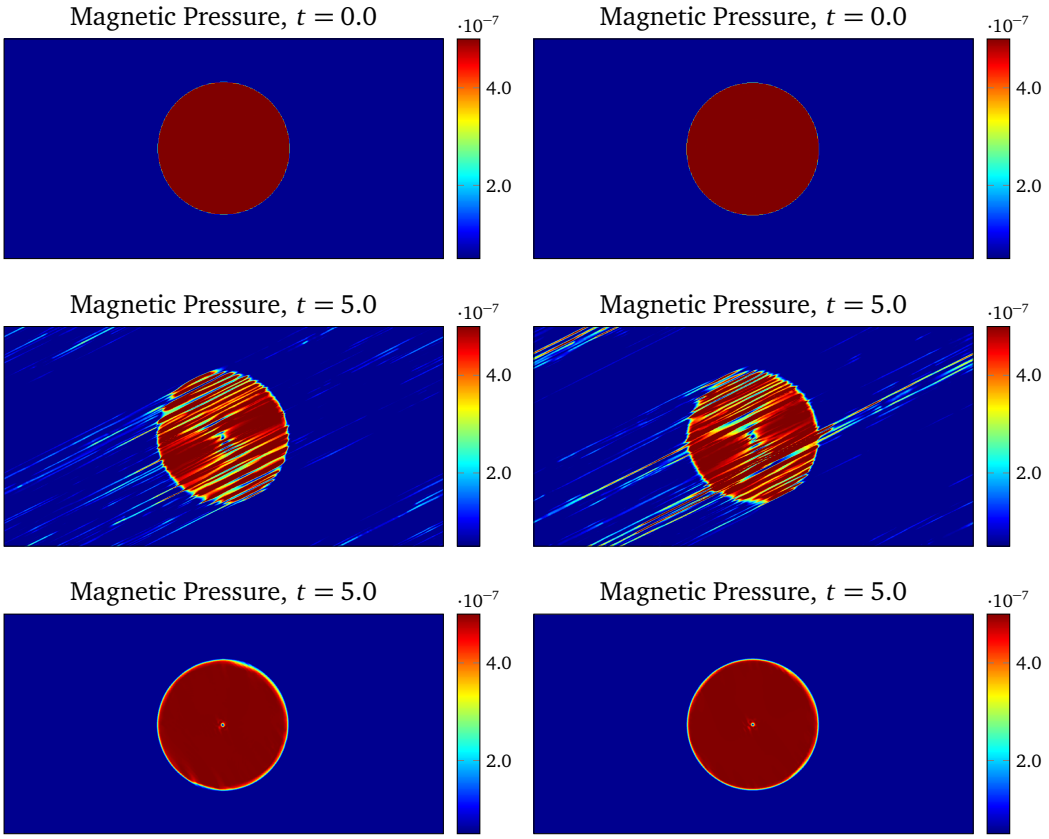

Figure 6.9: Magnetic field loop advection. Contour plots of the magnetic pressure at time $t = 0.0$ without divergence cleaning (top-left) and with divergence cleaning (top-right). Moreover, it is shown contour plots of the magnetic pressure computed with the RKFD-WENO7 scheme at time $t = 5.0$ without divergence cleaning (middle-left) and with divergence cleaning (middle-right). And contour plots of the magnetic pressure computed with the RKFV-WENO7 scheme at time $t = 5.0$ without divergence cleaning (bottom-left) and with divergence cleaning (bottom-right). The computational domain is the box $[-1.0, +1.0] \times [-0.5, +0.5]$, and the calculations were performed on a mesh made of 800×400 points/cells.

computational domain is the box $[-1.0, +1.0] \times [-0.5, +0.5]$. We set the density to $\rho = 1$, and the pressure $p = 1$ in the whole computational domain. The components of the initial velocity satisfy

$$v_x = v_0 n_x, \quad v_y = v_0 n_y, \quad v_z = 0, \tag{6.43}$$

where v_0 is the magnitude of the velocity (we use $v_0 = 2/\sqrt{5}$), n_x and n_y are the components of the unit vector in the direction of movement of the loop (we use $n_x = 2/\sqrt{5}$ and $n_y = 1/\sqrt{5}$). The magnetic field is constant everywhere, except for the loop structure of radius $R = 0.3$). For $r \leq R$ we have

$$B_x = -B_0 y/r, \quad B_y = +B_0 x/r, \quad B_z = 0, \tag{6.44}$$

where $r = \sqrt{x^2 + y^2}$, B_0 is the magnitude of the magnetic field. We use a small value of this quantity in order to keep the magnetic pressure smaller than the gas pressure (we

use $B_0 = 10^{-3}$). An adiabatic equation of state with $\gamma = 5/3$ is considered and closes the system. Periodic boundary conditions are set in all four edges of the computational domain. We run the simulation up to time $t = 5.0$. In the figure 6.9 is depicted the magnetic pressure at times $t \in \{0.0, 5.0\}$. We discretize the computational domain into 800×400 cells. The high-order RKFD and RKFV schemes with WENO7 reconstruction are used. A shock capturing method was not necessary for this test. The divergence cleaning of Dedner et al. (2002) was utilized, with $c_r = 0.18$, and c_h determined by the maximum propagation speed in the system. The profile of the loop is preserved for the methods with a divergence cleaning, but it is smeared and destroyed when the SRMHD equations are solved without a numerical approach for the solenoidal constraint of the magnetic field.

Current Sheet

The current sheet problem was first discussed by Hawley & Stone (1995) for the classical MHD equations, and its extension to SRMHD can be found in Beckwith & Stone (2011). This problem comprises a region which is uniformly filled with a gas at rest. The initial configuration for the magnetic field switches signs at the slices $x = +0.25$ and $x = -0.25$. A perturbation to the system with a sinusoidal velocity function in y is added, which generates nonlinear, linearly polarized Alfvén waves. These Alfvén waves turn into magnetosonic waves because the magnetic pressure does not remain constant. Magnetic reconnection occurs because of the two current sheets at $x = \pm 0.25$. Moreover, since the parameter $\beta < 1$, the magnetic reconnection drives highly over-pressurized regions, which launch magnetosonic waves transverse to the field, causing magnetic energy to be transformed into thermal energy (Hawley & Stone 1995). Close to the place where the magnetic reconnection take place are produced large magnetic field gradients.

The computational domain is the box $[-0.5, +0.5] \times [-0.5, +0.5]$. The rest-mass density and pressure are set uniform in the whole domain, with $\rho = 1.0$, and $p = 0.5\beta$, where the parameter β represents the ratio of gas pressure to magnetic energy density. The velocity has the profile given by $v_y = v_z = 0$, and $v_x = A\sin(2\pi y)$, where the parameter A is used to test robustness of the algorithm (Hawley & Stone 1995). The components of the magnetic field are given by $B_x = B_z = 0$, and $B_y = 1$ for $|x| > 0.25$ and $B_y = -1$ otherwise. In our simulation we set $A = 0.1$ and $\beta = 0.1$. An adiabatic equation of state with $\gamma = 5/3$ is considered. Periodic boundary conditions are used in all faces of the computational domain. The simulation time is $t = 10.0$. The computational domain is decomposed into 600×600 points/cells. The calculations were performed with a RKFD scheme, and a RKFV scheme, both with WENO7 reconstruction operator (only for smooth parts of the flow), along with the WENO3 reconstruction as shock capturing strategy. The divergence cleaning of Dedner et al. (2002) was used, with $c_r = 0.18$, and c_h determined by the maximum propagation speed in the system. In the figures 6.10 and 6.11 are depicted the rest-mass density at simulation times $t \in \{2.5, 5.0, 7.5, 10.0\}$.

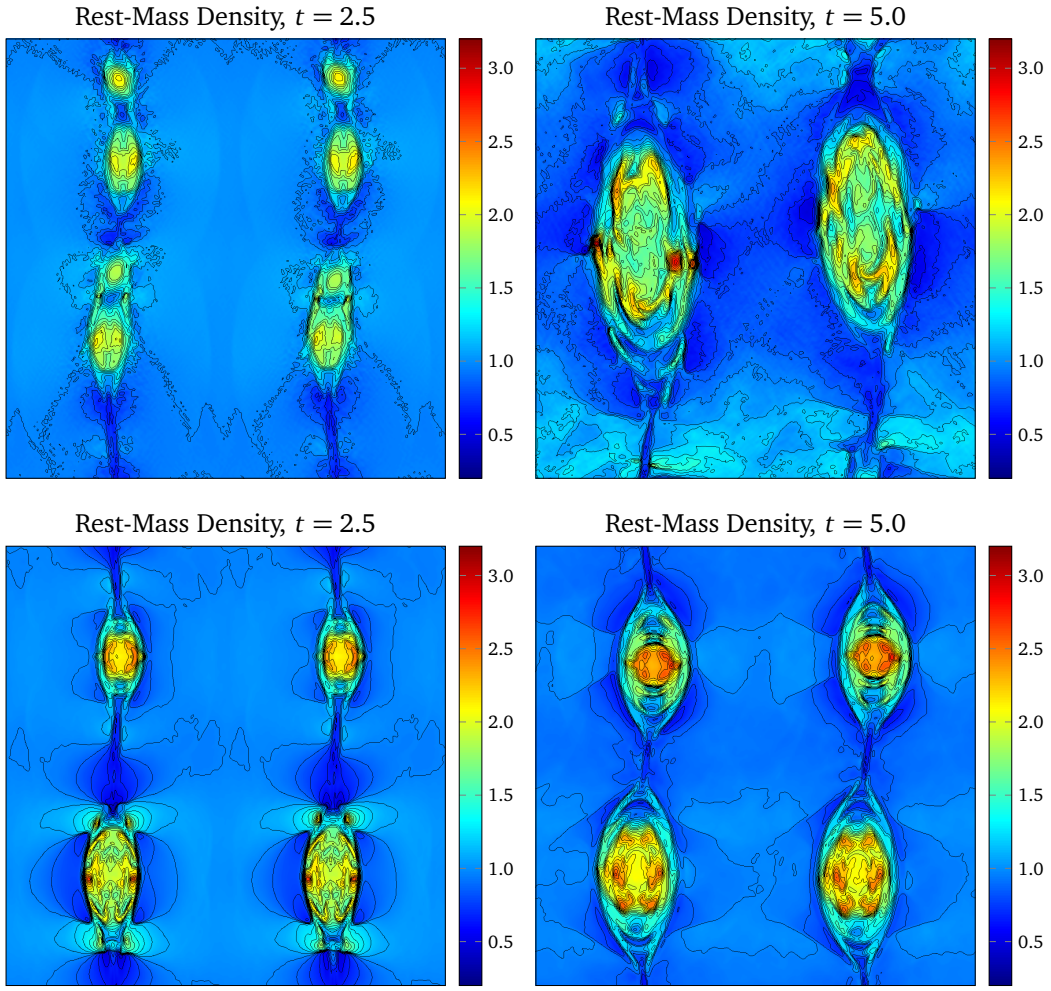

Figure 6.10: Relativistic current sheet problem. Contour plots of the rest-mass density at times $t = 2.5$ (left) and $t = 5.0$ (right). The calculations were performed with a RKFD scheme (top), and a RKFV scheme (bottom), both with WENO7 reconstruction on a mesh of 600×600 points/-cells. The computational domain is the box $[-0.5, +0.5] \times [-0.5, +0.5]$.

The RKFD and RKFV methods were very robust for the very high-order computation of this problem, which again confirms the robustness of the algorithm when very complex flow configurations are tackled. Differences in the evolution at the same time for both schemes is also appreciable, even when both schemes used the most dissipative numerical flux/flux-splitting formula.

Orszag-Tang Vortex

This Orszag-Tang vortex problem was first studied by Orszag & Tang (1979) for the incompressible MHD equations. Many authors have used this problem for the compressible MHD equations in order to know how robust is the used numerical scheme at handling the formation and the interactions of MHD shocks (Zachary et al. 1994; Ryu & Jones

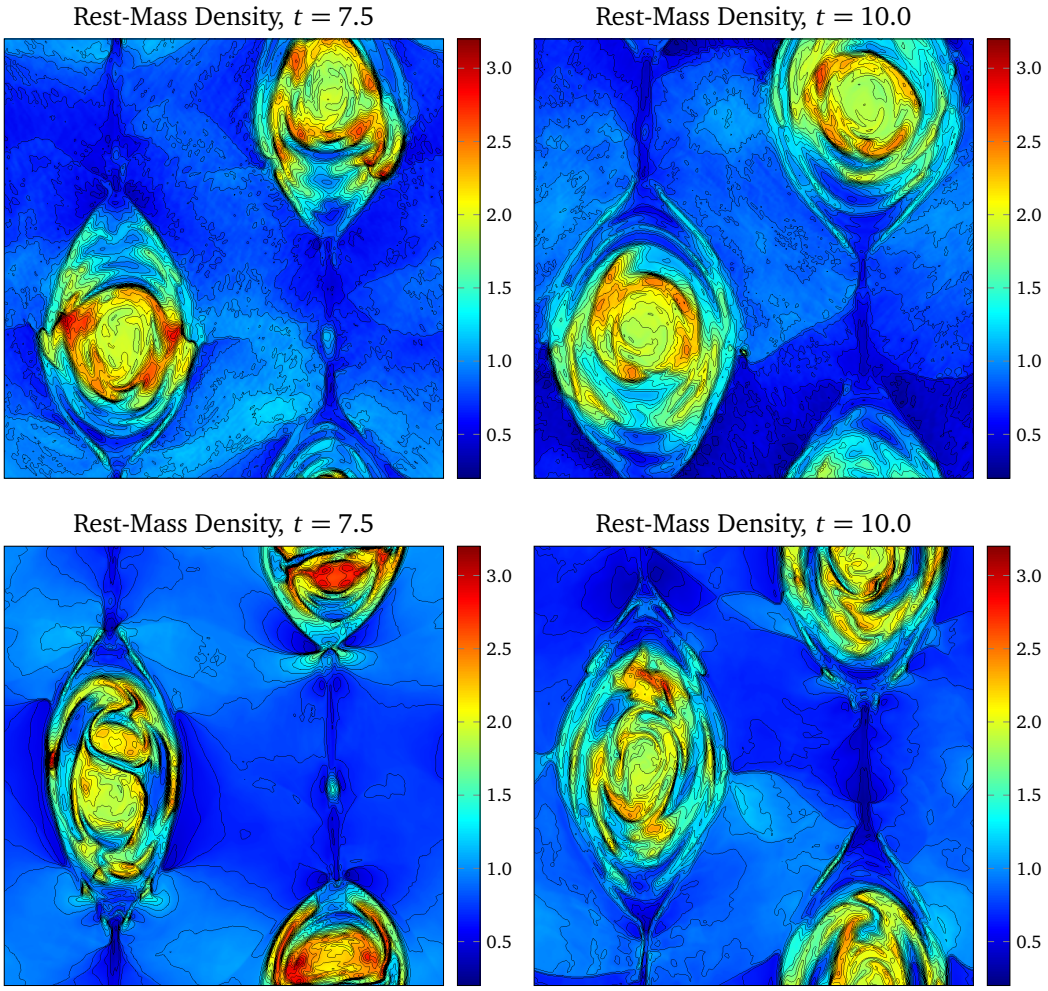

Figure 6.11: Relativistic current sheet problem. Contour plots of the rest-mass density at times $t = 7.5$ (left) and $t = 10.0$ (right). The calculations were performed with a RKFD scheme (top), and a RKFV scheme (bottom), both with WENO7 reconstruction on a mesh of 600×600 points/-cells. The computational domain is the box $[-0.5, +0.5] \times [-0.5, +0.5]$.

1995b; Ryu et al. 1998; Dai & Woodward 1998; Helzel et al. 2011; Jiang & Wu 1999; Tóth 2000; Londrillo & del Zanna 2000). The initial flow profile consists of smooth initial data, and it is obtained by the superposition of a velocity vortex with a magnetic vortex. This initial configuration is highly unstable, which generates a broad range of MHD waves, which interact with each other, making a transition towards turbulence. The extension to relativistic magnetohydrodynamics has been studied by Dumbser et al. (2008) and Beckwith & Stone (2011).

The computational domain is the box $[0.0, +1.0] \times [0.0, +1.0]$. The rest-mass density and pressure are set uniform in the whole domain, with $\rho = \gamma^2$ and $p = \gamma$. With this choice of the density and pressure, the sound speed is $c_s = 1$. The velocity hat the

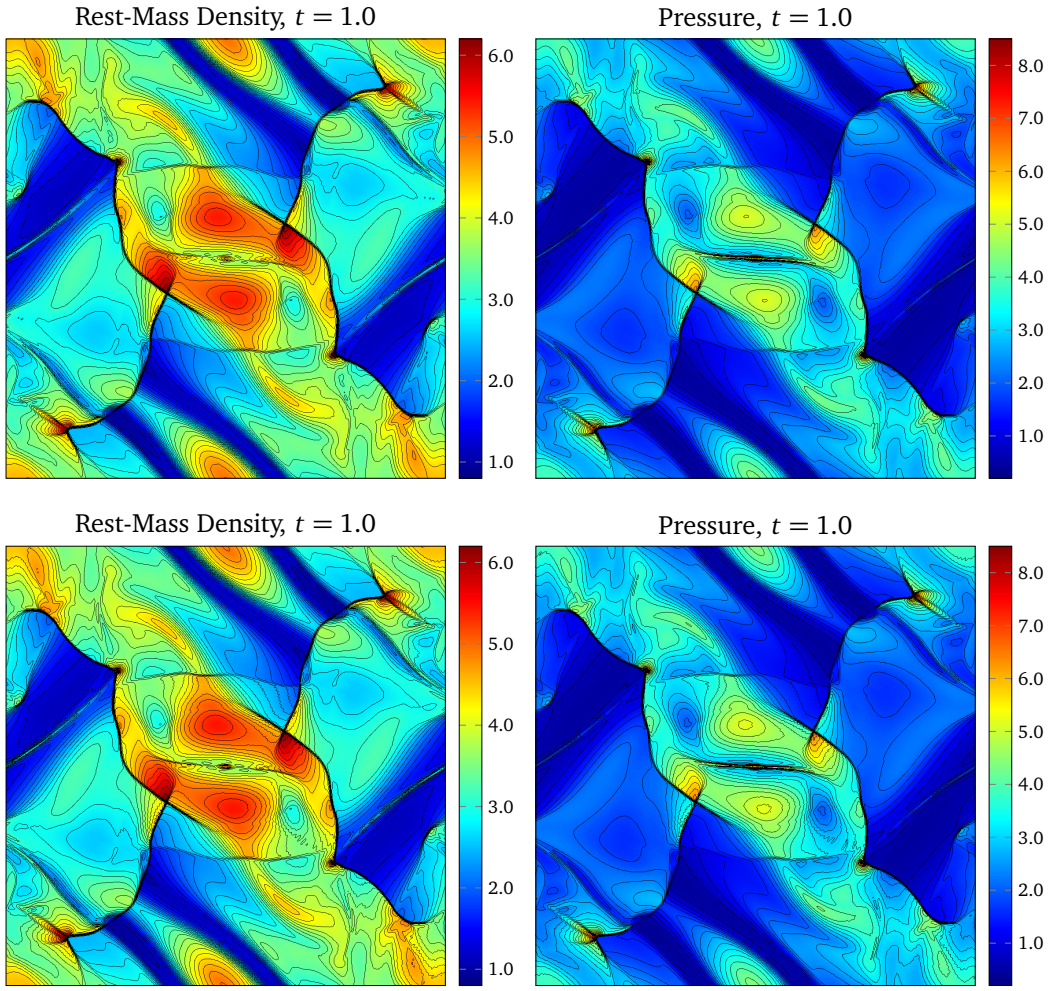

Figure 6.12: Relativistic Orszag-Tang vortex problem. Contour plots of the rest-mass density (left) and the pressure at time $t = 1.00$. The calculations were performed with a RKFD scheme (top), and a RKFV scheme (bottom), both with WENO7 reconstruction on a mesh of 600×600 points/cells. The computational domain is the box $[0.0, +1.0] \times [0.0, +1.0]$.

following profile

$$v_x = -A\sin(2\pi y), \quad v_y = +A\sin(2\pi x), \quad v_z = 0. \tag{6.45}$$

where $A = 0.5$. The magnetic field is given by

$$B_x = -\sin(2\pi y), \quad B_y = +\sin(4\pi x), \quad B_z = 0. \tag{6.46}$$

An adiabatic equation of state with $\gamma = 5/3$ is considered. At the boundaries of the domain we consider periodic boundary conditions. The simulation time is $t = 1.0$, and in the figure 6.12 are depicted the rest-mass density and thermal pressure at time $t = 1.0$. The computational domain is decomposed into 600×600 points/cells. The calculations were performed with a RKFD scheme, and a RKFV scheme, both with WENO7 reconstruction operator (only for smooth parts of the flow), along with the WENO3 reconstruction

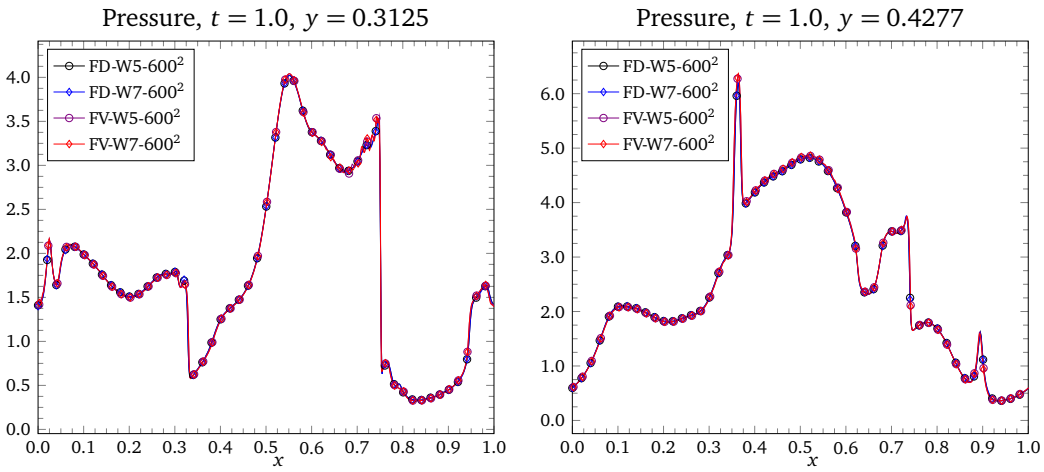

Figure 6.13: Relativistic Orszag-Tang vortex problem. Slices of the pressure at $y = 0.3125$ and $y = 0.4277$ for the RKFD and RKFV schemes, with different mesh resolutions, and reconstruction operators.

as shock capturing strategy. The divergence cleaning of Dedner et al. (2002) was used, with $c_r = 0.18$. We set the CFL condition to CFL $= 0.95$. All schemes used (namely, WENO3, WENO5, and WENO7) are very stable and robust when simulating this very challenging problem. The **XTROEM** was able to capture the shock waves and their interactions with the other flow structures emerging in the evolution of this configuration. In the figure 6.13 is plotted the pressure along the slices $y = 0.4277$ and $y = 0.3125$ at time $t = 1.0$ for the same mesh resolution and with different WENO reconstruction operators. We stress the absence of spurious oscillations in these slices for all WENO reconstructions. The RKFD and RKFV methods for the WENO5 and WENO7 reconstruction operators have also a very good agreement.

Cylindrical Blast Wave

The cylindrical blast wave problem comprises a cylindrical region located in the center of a domain, and filled with a magnetized over-pressured gas. After the system is allowed to evolve, a strong shock wave moving outwards is formed. Because of the formation of unphysical values in quantities like the rest-mass density, the pressure, and the magnitude of the velocity, a very robust shock capturing has to be used in order to stabilize the simulation. Due to the periodic boundary conditions, the interactions of the shock waves lead to very complex configurations (Zachary et al. 1994; Londrillo & del Zanna 2000; Stone et al. 2008; Mignone et al. 2010).

For this problem, the computational domain is given by the box $[0,1]\times[0,1]$. We set the rest-mass density and pressure uniform in the whole domain, with $\rho = 1.0\times10^{-4}$ and $p = 5.0\times10^{-4}$. The pressure in the cylindrical region $(x-x_c)^2+(y-y_c)^2 < R$, with $(x_c, y_c) = (0.5, 0.5)$, and $R = 0.1$, is $p = 1.0$, and the rest-mass density $\rho = 1.0\times10^{-2}$.

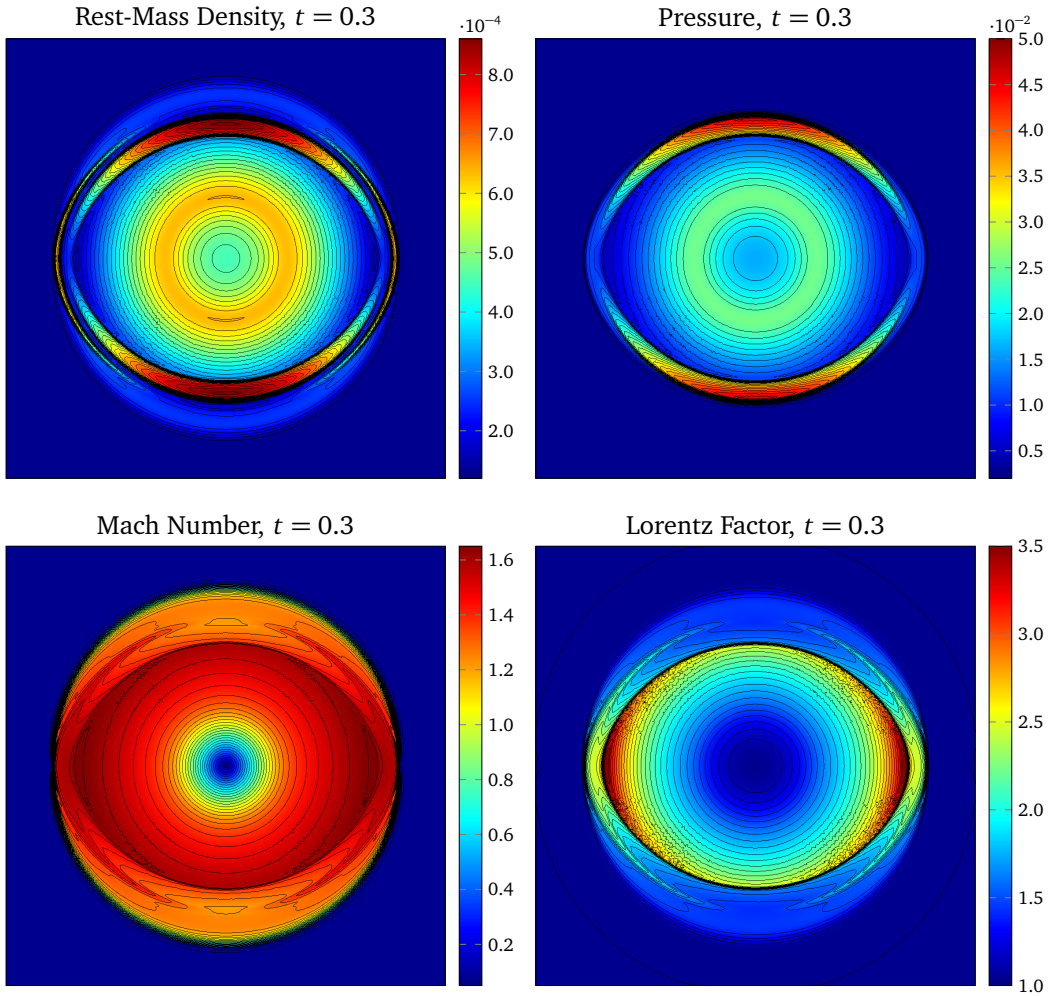

Figure 6.14: Relativistic cylindrical blast wave. Contour plots of the rest-mass density, pressure, Mach number, and Lorentz factor at time $t = 0.30$. The calculations were performed with a RKFD with WENO7 reconstruction on a mesh of 600×600 points. The computational domain is given by the box $[0, 1] \times [0, 1]$.

Initially, the velocity is set to zero, that is $v_x = v_y = v_z = 0$. The magnetic field is set to $B_x = B_y = B_z = 0.1$. An adiabatic equation of state with $\gamma = 4/3$ is considered. We consider periodic boundary conditions. The simulation time is $t = 0.5$, and in the figures 6.14 and 6.15 are depicted the rest-mass density, the pressure, the Mach number, and Lorentz factor at time $t = 0.3$ for the solution computed with the RKFD and RKFV methods. The computational domain is made of 600×600 points/cells. A high-order WENO7 reconstruction is used in smooth parts of the flow, and the WENO3 in regions with shocks, for both RKFD and RKFV schemes. The divergence cleaning of Dedner et al. (2002) was also used. In the figure 6.16 is plotted the pressure along the slices $y = 0.5$ and $x = 0.5$ at time $t = 0.3$ for a mesh resolution of 600×600 points/cells, and different WENO reconstruction operators. Observe the lack of spurious oscillations in these slices for all WENO reconstructions, and the same profile for all methods and orders..

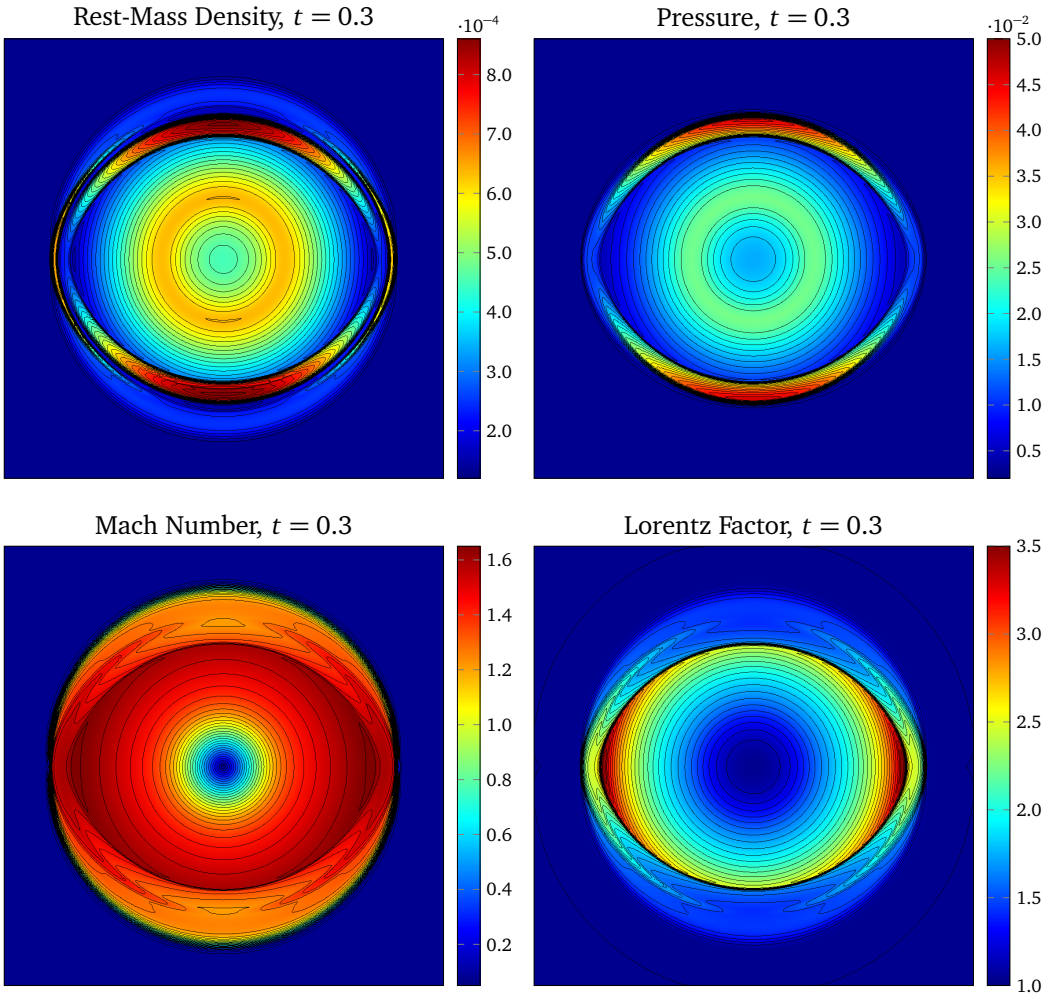

Figure 6.15: Relativistic cylindrical blast wave. Contour plots of the rest-mass density, pressure, Mach number, and Lorentz factor at time $t = 0.30$. The calculations were performed with a RKFV with WENO7 reconstruction on a mesh of 600×600 cells. The computational domain is given by the box $[0,1] \times [0,1]$.

Rotor Problem

The rotor problem was first proposed by Balsara & Spicer (1999a) for classical magnetohydrodynamics. An extension to relativistic magnetohydrodynamics has been considered by del Zanna et al. (2003) and Dumbser et al. (2008). The problem consists of a high-density, rapidly spinning fluid in a low-density fluid. Initially, both fluids are subject to a uniform magnetic field. Torsional Alfvén waves are launched into the fluid at rest because of the rapidly rotating fluid. Then, the rotor decreases its angular momentum.

The computational domain is the square $[-0.5,+0.5] \times [-0.5,+0.5]$. The rest-mass density and the pressure are $\rho = 1.0$ and $p = 1.0$ in the ambient medium. The cylindrical rotor ($0.0 \leq (x - x_c)^2 + (y - y_c)^2 \leq 0.1$, with $(x_c, y_c) = (0.5, 0.5)$), is filled with a fluid with rest-mass density $\rho = 10.0$. The pressure inside the rotor is the same as in

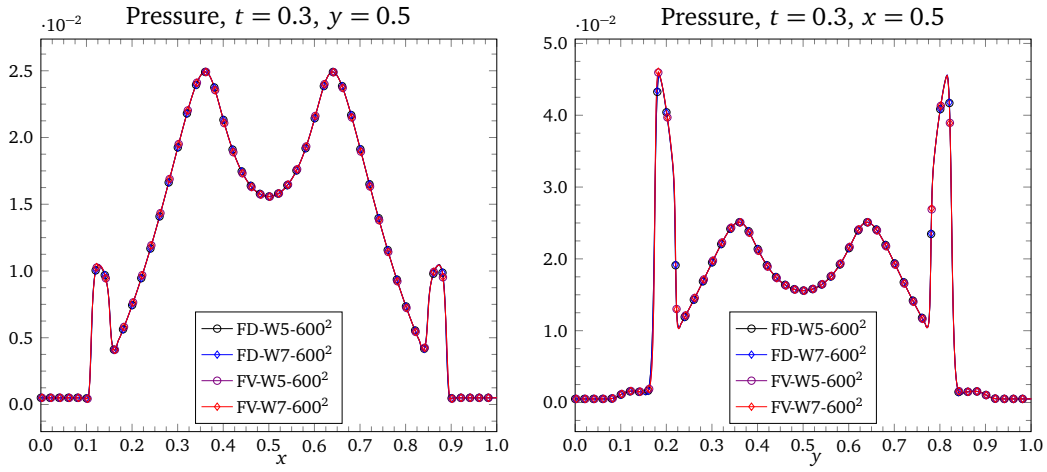

Figure 6.16: Relativistic cylindrical blast wave. Slices of the pressure at $y = 0.5$ and $x = 0.5$, for the RKFD and RKFV schemes, with different mesh resolutions, and reconstruction operators.

the ambient fluid. The ambient fluid is initially at rest, that is $v_x = v_y = v_z = 0$. The rotor has an angular velocity ω such that $v = \omega r = 0.995$ (for the RKFD computation) and ω such that $v = \omega r = 0.9$ (for the RKFV computation), at $r = 0.1$. A linear taper is applied to the velocity and rest-mass density field, however only in a very small range $0 \leq r \leq 1.115$ so that the density and the velocity match those of the ambient fluid at rest at a radius of $R = 1.115$. The magnetic field is given by $B_x = 5.0$, and $B_y = B_z = 0$ in the whole computational domain. An adiabatic equation of state with $\gamma = 7/5$ is considered. We apply periodic boundary conditions at the boundaries of the domain. The computational domain is decomposed into 600×600 cells. The simulation was carried out with a finite volume scheme with WENO7 reconstruction along with WENO3 reconstruction operator in regions with shocks/discontinuities. The divergence cleaning of Dedner et al. (2002) was employed, with $c_r = 0.18$, and c_h determined by the maximum propagation speed in the system. In the figures 6.17 and 6.18 are depicted the rest-mass density, the gas pressure, the Mach number, and the velocity magnitude at simulation time $t = 0.4$, for the solution obtained with the RKFD-WENO7 scheme, and RKFV-WENO7 scheme, respectively. Inside the rotor, the fluid is still in uniform rotation, as it is shown in the Mach number plot.

In the figure 6.19 is plotted the pressure along the slices $y = 0.5$ and $x = 0.5$ at time $t = 0.4$ for different mesh resolutions and different WENO reconstruction operators. Observe the lack of spurious oscillations in these slices for all WENO reconstructions. Observe also that the profile is almost the same for all schemes and resolutions considered in the plot. The RKFD-WENO5 scheme smear the pressure profile, and the RKFD-WENO7 gives a finer resolution of this pressure profile.

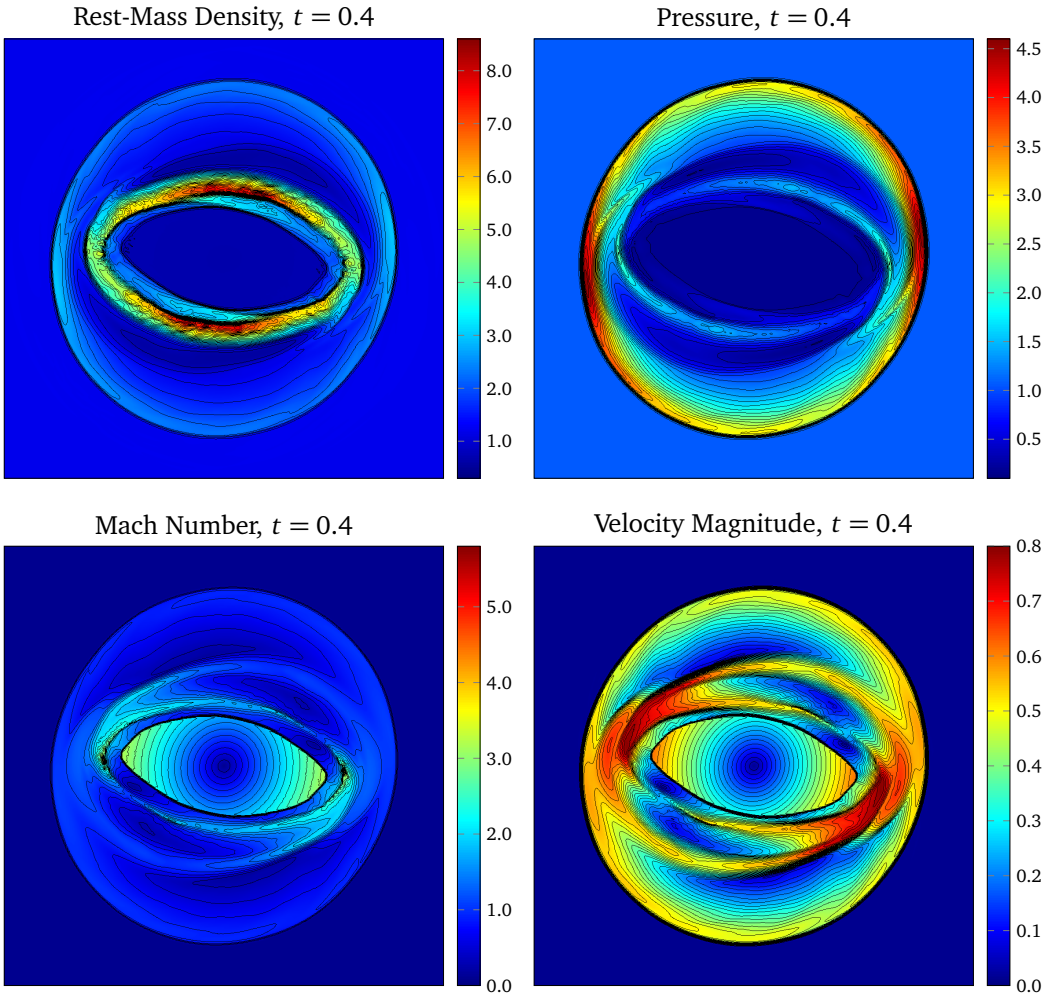

Figure 6.17: Relativistic rotor problem. Contour plots of the rest-mass density, pressure, Mach number, and the velocity magnitude at time $t = 0.4$. The calculations were performed with a RKFD with WENO7 reconstruction on a mesh of 600×600 points. The computational domain is the square $[-0.5, +0.5] \times [-0.5, +0.5]$.

Cloud-Shock Interaction

The cloud-shock interaction problem has been used to simulate the disruption of a high density cloud by a strong shock wave. We follow mainly the setup presented by He & Tang (2012b), which is based on the classical MHD version discussed by Dai & Woodward (1994b) and Tóth (2000). The computational domain is the box $[0.0, +2.0] \times [0.0, +1.0]$. The discontinuity is located at $x = 1.2$ with the left and right states in primitive variables

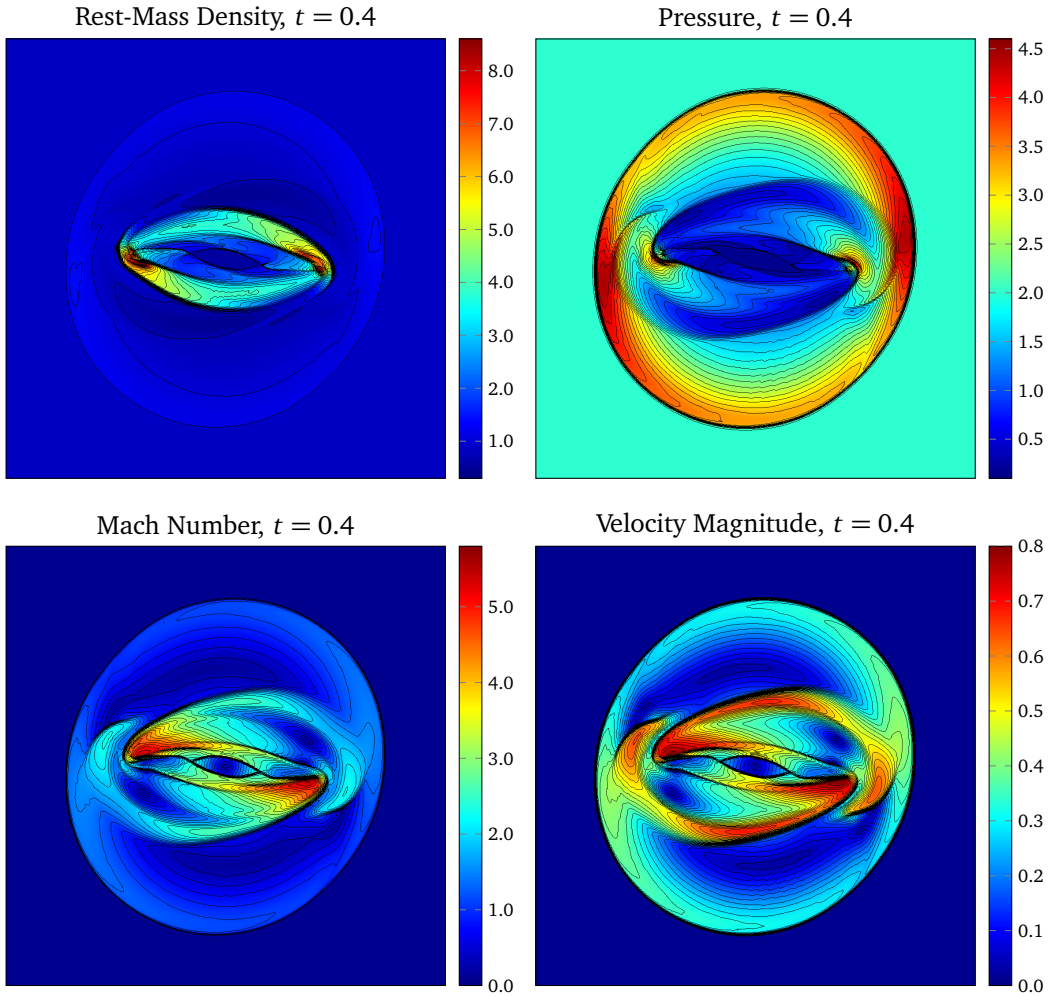

Figure 6.18: Relativistic rotor problem. Contour plots of the rest-mass density, pressure, Mach number, and the velocity magnitude at time $t = 0.4$. The calculations were performed with a RKFV with WENO7 reconstruction on a mesh of 600×600 points. The computational domain is the square $[-0.5, +0.5] \times [-0.5, +0.5]$.

given by

$$\hat{\boldsymbol{u}}_L = \begin{pmatrix} \rho \\ v_x \\ v_y \\ v_z \\ p \\ B_x \\ B_y \\ B_z \end{pmatrix} = \begin{pmatrix} 3.86859 \\ 0.68 \\ 0.0 \\ 0.0 \\ 1.251148954517 \\ 0.0 \\ 0.8498108108786 \\ -0.8498108108786 \end{pmatrix}, \quad \hat{\boldsymbol{u}}_R = \begin{pmatrix} \rho \\ v_x \\ v_y \\ v_z \\ p \\ B_x \\ B_y \\ B_z \end{pmatrix} = \begin{pmatrix} 1.0 \\ 0.0 \\ 0.0 \\ 0.0 \\ 0.05 \\ 0.0 \\ 0.1610642582333 \\ 0.1610642582333 \end{pmatrix}. \tag{6.47}$$

The cloud is represented by a dense cylinder, and it is located at $x = 1.6$, $y = 0.5$. The radius of the cylinder is $r = 0.15$, and its rest-mass density is $\rho = 30.0$. The cloud is in hydrostatic equilibrium with the ambient gas. An adiabatic equation of state with

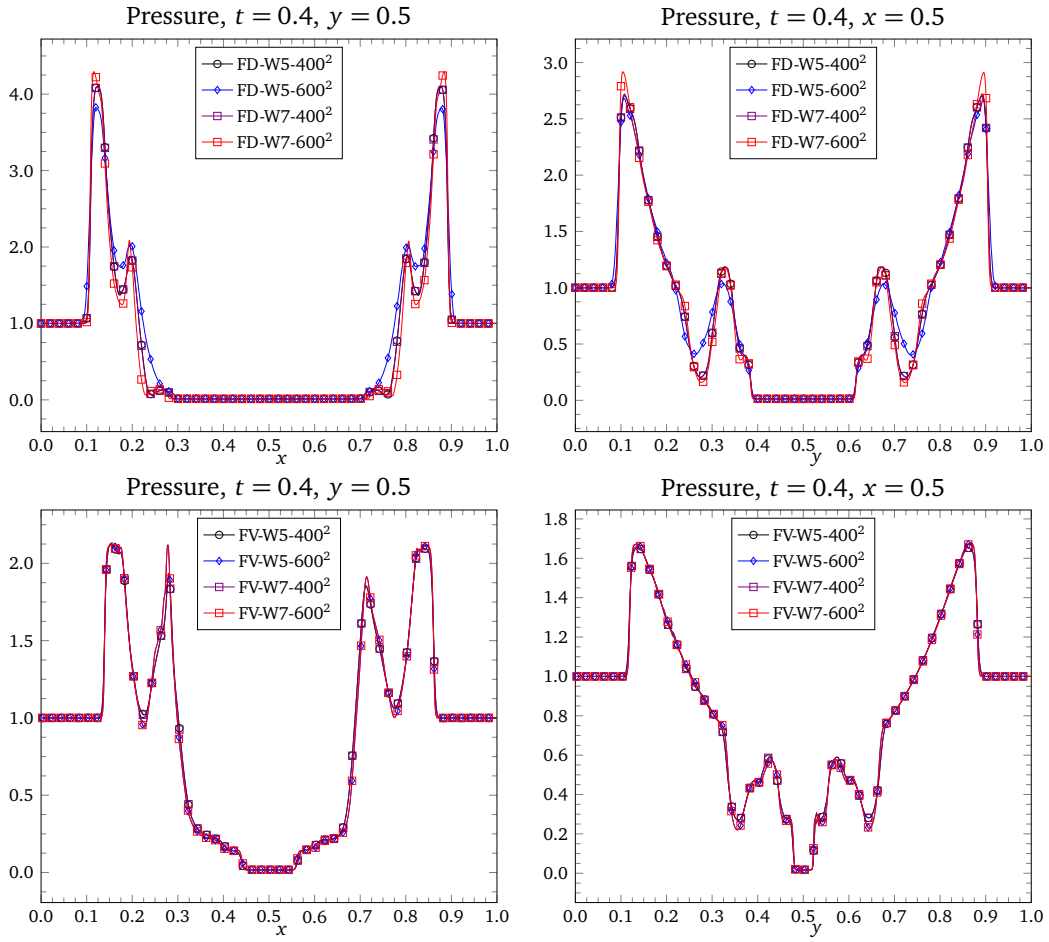

Figure 6.19: Relativistic rotor problem. Slices of the pressure at $y = 0.5$ and $x = 0.5$, for the RKFD and RKFV schemes, with different mesh resolutions, and reconstruction operators.

$\gamma = 5/3$ is considered. Transmissive boundary conditions are applied at the domain boundaries. The simulation time is $t = 2.0$, and in the figure 6.20 are depicted the logarithm of the rest-mass density, the gas pressure, and the Lorentz factor computed with a high-order finite difference scheme and a high-order finite volume scheme with WENO7 reconstruction. The physical domain was decomposed into 800×400 points/cells. The divergence cleaning of Dedner et al. (2002) was used. The CFL condition used in this simulation was CFL $= 0.95$. Observe that the numerical results are quite similar each other.

Kelvin-Helmholtz Instability

For this test, we use the configuration proposed by Beckwith & Stone (2011). The Kelvin-Helmholtz instability consists of a perturbation applied to a system with a velocity shear. Here, we run this test problem to demonstrate the algorithm's ability to evolve a linear perturbation into nonlinear magnetohydrodynamic turbulence (Beckwith & Stone 2011;

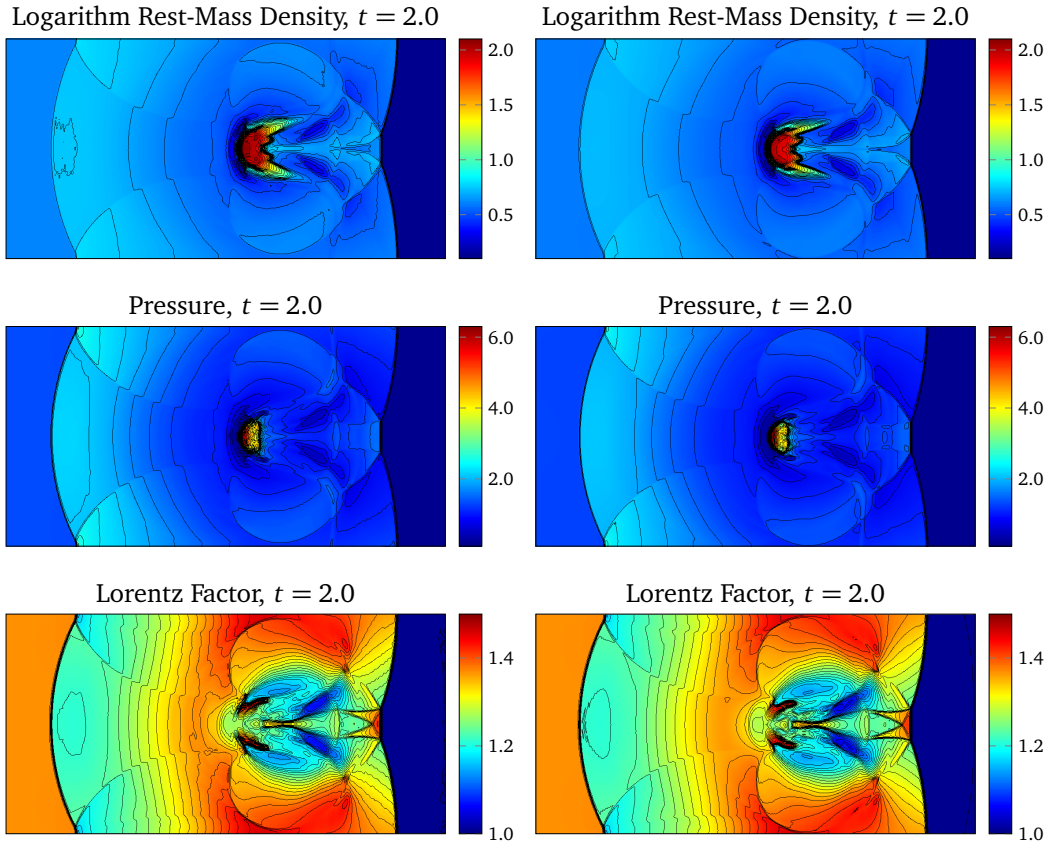

Figure 6.20: Relativistic cloud-shock interaction. Contour plots of the logarithm of the rest-mass density (top), pressure (middle), and Lorentz factor at time $t = 2.0$. The calculations were performed with a RKFD scheme (left) and a RKFV scheme (right) with WENO7 reconstruction on a grid of 800×400 points/cells.

Radice & Rezzolla 2012).

The computational domain is the box $[-0.5, +0.5] \times [-1.0, +1.0]$. The density is set to $\rho = 1.0$ for $|y| \leq 0.25$, and $\rho = 2.0$ for $|y| < 0.25$. The pressure is uniform in the whole domain, with $p = 2.5$. The x-component of the velocity satisfies $v_x = 0.5$ if $|y| \leq 0.25$, and $v_x = -0.5$ if $|y| < 0.25$. The shear velocity is given by

$$v_x(x) = \begin{cases} +v_{\text{shear}} + A_0 \sin(2\pi x), & \text{if } y \geq 0.25; \\ -v_{\text{shear}} - A_0 \sin(2\pi x), & \text{if } y < 0.25; \end{cases} \tag{6.48}$$

where $v_{\text{shear}} = 0.5$. The instability is seeded by adding a small perturbation in the transverse component of the velocity,

$$v_y(x) = \begin{cases} +A_0 \sin(2\pi x), & \text{if } y \geq 0.25; \\ -A_0 \sin(2\pi x), & \text{if } y < 0.25; \end{cases} \tag{6.49}$$

where $A_0 = 0.01$ is the perturbation amplitude. The components of the magnetic field are given by $B_x = 0.2$, and $B_y = B_z = 0$. An adiabatic equation of state with $\gamma = 4/3$ is

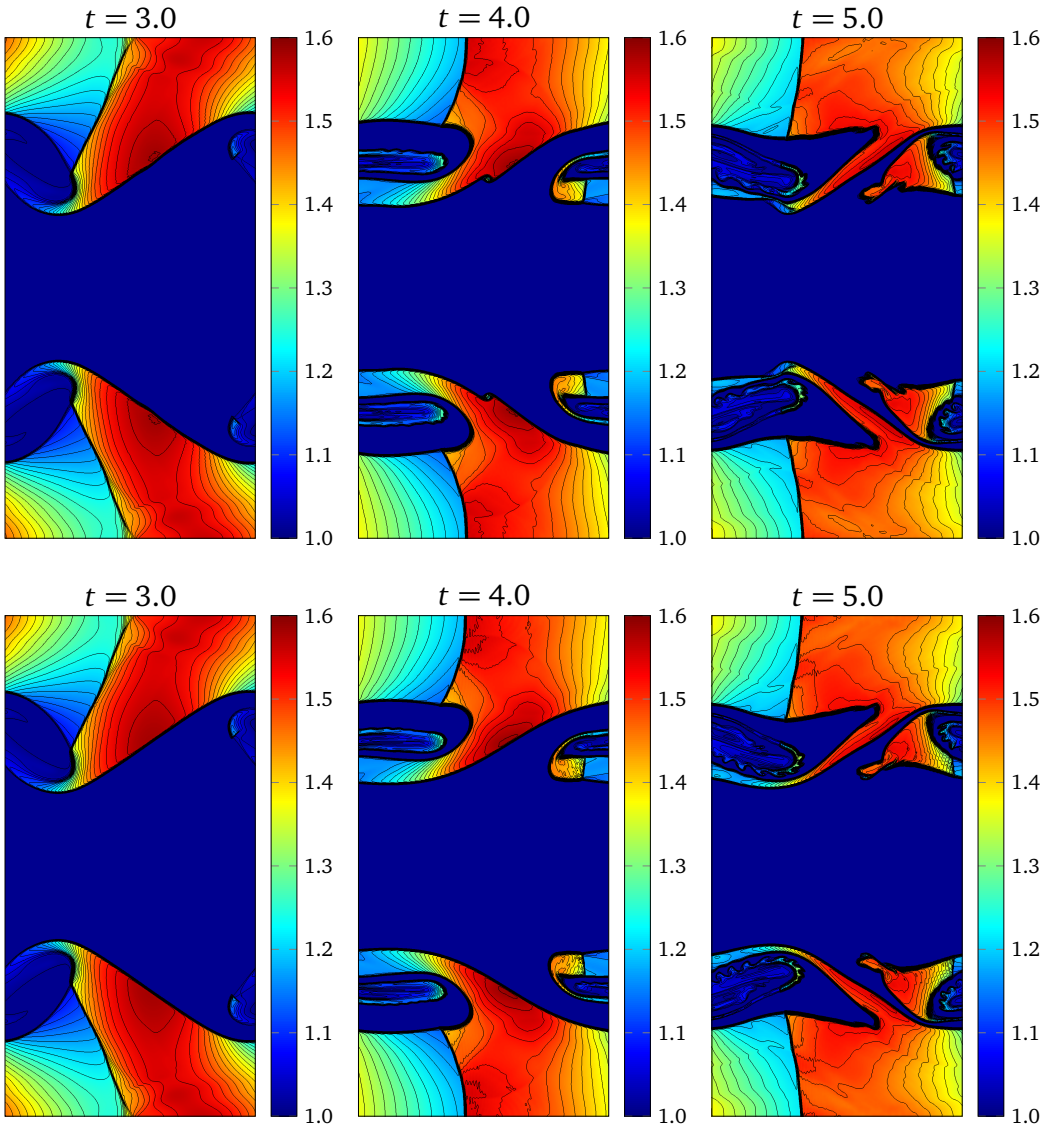

Figure 6.21: Relativistic Kelvin-Helmholtz instability. Contour plots of the rest-mass density at times $t = 3.00$ (left) and $t = 4.00$ (middle), and $t = 5.00$ (right). The calculations were performed with a RKFD-WENO7 scheme (top) and a RKFV-WENO7 scheme (bottom) on a mesh of 400×800 cells.

considered. At the boundaries of the domain we consider periodic boundary conditions. The final simulation time is $t = 5.0$, and in the figure 6.21 is depicted the rest-mass density at times $t \in \{3.0, 4.0, 5.0\}$ obtained with the finite volume WENO7 scheme. The computation was carried out on a mesh made of 400×800 cells.

CHAPTER 7

Conclusions and Outlook

7.1. Conclusions and Outlook

In the present work we have shown the successful development and implementation of the very high-order conservative finite difference, finite volume, and discontinuous Galerkin spectral element methods for the ideal magnetohydrodynamics, relativistic hydrodynamics and relativistic magnetohydrodynamics on Cartesian meshes. The implementation was performed on our own numerical framework, **XTROEM**. In the table 7.1 are summarized the properties of the codes developed as part of this dissertation. Three codes were written using the programming language Fortran 95/2003. For the data output, the library HDF5 was selected and for the parallel implementation, we used the MPI library. Every code has the ability to solve the MHD, SRHD, and SRMHD equations in one-, two-, and three-dimensional spaces.

Our numerical framework has been subject to the standard testbench in computational astrophysics. Numerical results of problems having smooth flows and problems involving supersonic flows are reported. On smooth flows, the DGSEM method is the fastest one (measured as time per-degree-of-freedom), followed by the RKFD and the RKFV methods. When shocks are present in the solution, the RKFD using the Lax-Friedrichs splitting is the most stable, and the discontinuous Galerkin the less stable. When using the stabilization algorithm outlined in the section 3.2, the DGSEM gets a better behavior, it is still faster than the RKFD, but it does have some stabilization problems, as we could see when it was implemented in the relativistic magnetohydrodynamics. Some work has to be done in this point, and probably, the MOOD approach in combination with DG methods as it has been reported by Dumbser et al. (2014), may improve the stabilization of the hybrid DGSEM/FV.

DGSEM schemes can handle complex geometries without compromising the locality of the scheme. In fact, this is one of the most important features of the DG schemes. RKFD and RKFV may also be applied to unstructured geometries, but the accuracy of the scheme is reduced or the complexity of the algorithms and their computational price increases notoriously, especially for parallel computations. Nevertheless, an outstanding behavior for the RKFD and the RKFV is observed when solving really complex flows under extreme conditions, typical in astrophysical fluid dynamics. The combination of a very

Table 7.1: Outline of the capabilities of the **XTROEM** code.

	MHD	**SRHD**	**SRMHD**
	Dimensions of the implemented spatial operator		
RKFD	1D/2D/3D	1D/2D/3D	1D/2D/3D
RKFV	1D/2D/3D	1D/2D/3D	1D/2D/3D
RKDG	1D/2D/3D	1D/2D/3D	Not Fully Implemented
	Order of accuracy on smooth flows		
RKFD	$\mathcal{O}(3)$–$\mathcal{O}(7)$	$\mathcal{O}(3)$–$\mathcal{O}(7)$	$\mathcal{O}(3)$–$\mathcal{O}(7)$
RKFV	$\mathcal{O}(3)$–$\mathcal{O}(7)$	$\mathcal{O}(3)$–$\mathcal{O}(7)$	$\mathcal{O}(3)$–$\mathcal{O}(7)$
RKDG	$\mathcal{O}(3)$–$\mathcal{O}(10)$	$\mathcal{O}(3)$–$\mathcal{O}(10)$	$\mathcal{O}(3)$–$\mathcal{O}(10)$
	Shock capturing strategy		
RKFD	FD-WENO3	FD-WENO3	FD-WENO3
RKFV	FV-WENO3	FV-WENO3	FV-WENO3
RKDG	Hybrid FV-WENO3	Hybrid FV-WENO3	Not Fully Implemented

high-order reconstruction operator for smooth flows and a robust third order WENO for shocks/discontinuities, makes these scheme the most reliable for computational astrophysics. It was noted in our simulations that for this kind of conditions, DGSEM schemes are prone to lose accuracy and stability, in the sense that the computation blows up. In order to improve the capabilities of the DGSEM schemes for tackling flows with shocks, a more exhaustive study of shock sensors/indicators have to be carried out. Additionally, we have to improve the coupling between the DGSEM subdomains and the FV subdomains, making it more robust robust, and keeping in mind the conservative properties of both numerical methods.

Further research involves the implementation of more complex equations systems, like resistive magnetohydrodynamics and its relativistic counterpart, the relativistic resistive magnetohydrodynamics. Additionally, implementation of appropriate time discretization is needed for these equations, like the family of implicit-explicit Runge-Kutta methods, or fully implicit schemes. Moreover, numerical flow simulations with complex and highly dynamical structures require efficient adaptive mesh refinement algorithms. Among the advantages of an adaptive mesh refinement scheme, we can mention the following ones: Saving of computational effort and memory consumption over a static mesh approach. The code is able to control the mesh resolution and resolve the small flow structures in an very efficient way. The combination of adaptive mesh refinement with high-order methods will allow to tackle more efficiently large scale simulations of astrophysical plasmas.

7.2. Summary of Achievements

The main achievements reached within this dissertation are

- Development and implementation of robust high-order finite difference and finite volume WENO schemes on for magnetohydrodynamics, relativistic hydrodynamics and relativistic magnetohydrodynamics on multiple space dimensions.
- Development of hybrid high-order finite volume and discontinuous Galerkin spectral element methods for magnetohydrodynamics and relativistic hydrodynamics in multiple space dimensions, with special emphasis on problems with strong shocks.
- Construction of a high-order accurate hybrid finite volume/discontinuous Galerkin scheme for computational astrophysics. This hybrid scheme allows to solve the smooth parts of the flow with the very efficient discontinuous Galerkin spectral element method, the regions with strong shocks with a robust finite volume method with the WENO3 reconstruction procedure as main building block.
- Simulations of complex astrophysical plasmas with higher-order numerical methods.

Appendix A

Mathematica Notebook for the WENO Reconstruction

In this appendix we will present a Mathematica® notebook for the calculation of the linear weights, oscillation indicators and the polynomials in every stencil for the WENO reconstruction, and for arbitrary polynomial degree N. Remember that for a polynomial degree N, a WENO-$(2N+1)$ scheme is obtained. For a given cell Ω_i, with the following notebook we get the polynomials $u(x)$ at the point $x = x_\alpha$, for α an admisible value, that is, a value that does not generate negative linear weights. For example, along this work we have used $\alpha = i \pm \frac{1}{2}$ and $\alpha = i \pm \frac{1}{2\sqrt{3}}$.

Lagrange Interpolating Polynomial

```
LagrangePolynomial[data_,zz_]/;MatrixQ[data]:=
  Module[{nn=Length[data],xx,yy},{xx,yy}=Transpose[data];
    Sum[Product[(zz-xx[[in]])/(xx[[jn]]-xx[[in]]),
      {in,Complement[Range[nn],{jn}]}]yy[[jn]],{jn,nn}]];

LagrangePolynomial[data_,zz_]/;VectorQ[data]:=
  LagrangePolynomial[Transpose[{Range[Length[data]],data}],zz];

StencilAbscissa[nn_,mm_]:=Δx((i-((nn+1)-(mm-1)))+1/2);
StencilOrdinate[nn_,mm_]:=Sum[Δx(u_{i-kk}),{kk,(nn+1),(nn+1)-(mm-1),-1}];
```

Stencil Generation

```
CreateStencil[nn_]:=Module[{},
  LinearWeights=Table[0,{nn+1}];
  SuperStencil=Table[0,{2 (nn+1)}];
  SmallStencils=Table[0,{nn+1},{nn+2}];
  NodesPolySuperStencil=Table[0,{2 nn+1}];

  Do[Do[SmallStencils[[mii,mjj]]={StencilAbscissa[nn,mjj+(mii-1)],
    StencilOrdinate[nn,mjj+(mii-1)]},{mjj,1,nn+2}],{mii,1,nn+1}];

  Do[SuperStencil[[mii]]={StencilAbscissa[nn,mii],
    StencilOrdinate[nn,mii]},{mii,1,2(nn+1)}];

  Do[NodesPolySuperStencil[[kk]]=u_{i-(nn+1-kk)},{kk,1,2 nn+1}];

  Do[LinearWeights[[kk]]=γ_{kk},{kk,1,nn+1}];

  PolyStencil[xx_,ii_]:=
    FullSimplify[D[LagrangePolynomial[
      SmallStencils[[ii,All]],x],x]/.{x->xx}];
```

```
30
31  PolyStencilDerivatives[xx_,ii_,jj_]:=
32   FullSimplify[D[LagrangePolynomial[
33    SmallStencils[[ii,All]],x],{x,jj+1}]/.{x->xx}];
34
35  PolySuperStencil[xx_]:=
36   FullSimplify[D[LagrangePolynomial[SuperStencil[[All]],x],x]/.{x->xx}];
37
38  CoeffPolySuperStencil[xx_]:=
39   Coefficient[PolySuperStencil[xx],NodesPolySuperStencil];
40
41  SumPolyStencil[xx_]:=
42   Sum[γii PolyStencil[xx,ii],{ii,1,nn+1}];
43
44  CoeffSumPolyStencil[xx_]:=
45   Coefficient[SumPolyStencil[xx],NodesPolySuperStencil];
46
47  LinearWeightsStencil[xx_]:=
48   Solve[CoeffPolySuperStencil[xx]-CoeffSumPolyStencil[xx]==0,
49    LinearWeights][[1]];
50
51  IntDerPolyStencil[ii_,jj_]:=
52   Integrate[Δx^(2ii-1)(D[PolyStencil[x,jj],{x,ii}])^2,
53    {x,(i-1/2)Δx,(i+1/2)Δx}];
54
55  SmoothnessIndicatorStencil[ii_]:=
56   Sum[IntDerPolyStencil[jj,ii],{jj,1,nn}];];
```

Polynomials, Weights and Oscillation Indicators

```
57 ShowPolynomials[xx_,ii_]:=
58  Module[{},Print[Subscript[p,ii],"(",Subscript[x,xx/Δx],")","=",
59   Factor[PolyStencil[xx,ii]]];];
60
61 ShowPolynomialsDerivatives[xx_,ii_,jj_]:=
62  Module[{},Print[Subscript[p,ii],"(",Subscript[x,xx/Δx],")","=",
63   Factor[PolyStencilDerivatives[xx,ii,jj]]];];
64
65 ShowLargePolynomial[xx_]:=
66  Module[{},Print[P,"(",Subscript[x,xx/Δx],")","=",
67   Factor[PolySuperStencil[xx]]];];
68
69 ShowLinearWeights[xx_]:=
70  Module[{},Print[P,"(",Subscript[x,xx/Δx],")","->",
71   LinearWeightsStencil[xx]];];
72
73 ShowSmoothnessIndicator[ii_]:=
74  Module[{},Print[Subscript[β,ii],"=",
75   Factor[SmoothnessIndicatorStencil[ii]]];];
```

Bibliography

Aloy, Miguel Angel, José Antonio Pons & José María Ibáñez. An efficient implementation of flux formulae in multidimensional relativistic hydrodynamical codes. *Computer Physics Communications*, 120(2-3):115–121, 1999

Aloy, Miguel Angel, José María Ibáñez & José María Martí. GENESIS: high-resolution code for three-dimensional relativistic hydrodynamics. *The Astrophysical Journal Supplement Series*, 122:151–166, 1999

Anderson, Matthew, Eric Hirschmann, Steven Liebling & David Neilsen. Relativistic MHD with adaptive mesh refinement. *Classical and Quantum Gravity*, 23(22):6503–6524, 2006

Anile, Angelo. *Relativistic fluids and magnetofluids*. Cambridge University Press, Cambridge, 1989

Anile, Angelo & Sebastiano Pennisi. On the mathematical structure of test relativistic magnetofluiddynamics. eng. *Annales de l'institut Henri Poincaré (A) Physique théorique*, 46(1):27–44, 1987

Antón, Luis, Olindo Zanotti, Juan Antonio Miralles, José María Martí, José María Ibáñez, José Antonio Font & José Antonio Pons. Numerical 3+1 general relativistic magnetohydrodynamics: A local characteristic approach. *The Astrophysical Journal*, 637(1):296–312, 2006

Antón, Luis, Juan Antonio Miralles, José María Martí, José María Ibáñez, Miguel Angel Aloy & Petar Mimica. Relativistic magnetohydrodynamics: Renormalized eigenvectors and full wave decomposition Riemann solver. *The Astrophysical Journal Supplement Series*, 188(1):1–31, 2010

Apostol, Tom. *Calculus: Multi-variable calculus and linear algebra, with applications to differential equations and probability*. John Wiley & Sons, 2nd edition, 1969

Apostol, Tom. *Calculus: One-variable calculus, with an introduction to linear algebra*. John Wiley & Sons, 2nd edition, 1969

Artzi, Matania Ben & Joseph Falcovitz. A second-order Godunov-type scheme for compressible fluid dynamics. *Journal of Computational Physics*, 55(1):1–32, 1984

Ascher, Uri, Steven Ruuth & Raymond Spiteri. Implicit-explicit Runge-Kutta methods for time-dependent partial differential equations. *Applied Numerical Mathematics*, 25(2-3):151–167, 1997

Balbus, Steven & John Hawley. A powerful local shear instability in weakly magnetized disks: I - Linear analysis. *Astrophysical Journal*, 376:214–222, 1991

Balbus, Steven & John Hawley. A powerful local shear instability in weakly magnetized disks: II - Nonlinear evolution. *Astrophysical Journal*, 376:223–233, 1991

Balbus, Steven & John Hawley. Instability, turbulence, and enhanced transport in accretion disks. *Reviews of Modern Physics*, 70:1–53, 1 1998

Balbus, Steven & John Hawley. On the nature of angular momentum transport in nonradiative accretion flows. *The Astrophysical Journal*, 573(2):749, 2002

Balsara, Dinshaw. Total variation diminishing scheme for relativistic magnetohydrodynamics. *The Astrophysical Journal Supplement Series*, 132:83–101, 2001

Balsara, Dinshaw. Second-order-accurate schemes for magnetohydrodynamics with divergence-free reconstruction. *The Astrophysical Journal Supplement Series*, 151:149–184, 2004

Balsara, Dinshaw & Chi-Wang Shu. Monotonicity preserving weighted essentially non-oscillatory schemes with increasingly high order of accuracy. *Journal of Computational Physics*, 160:405–452, 2000

Balsara, Dinshaw & Daniel Spicer. A staggered mesh algorithm using high order Godunov fluxes to ensure solenoidal magnetic fields in magnetohydrodynamic simulations. *Journal of Computational Physics*, 149:270–292, 1999

Balsara, Dinshaw & Daniel Spicer. Maintaining pressure positivity in magnetohydrodynamic simulations. *Journal of Computational Physics*, 148:133–148, 1999

Barth, Timothy & Herman Deconinck, editors. *High-order methods for computational physics*. Springer-Verlag, Berlin, 1999

Beckwith, Kris & James Stone. A second-order Godunov method for multi-dimensional relativistic magnetohydrodynamics. *The Astrophysical Journal Supplement Series*, 193:6–35, 2011

Begelman, Mitchell, Roger Blandford & Martin Rees. Theory of extragalactic radio sources. *Reviews of Modern Physics*, 56:255–351, 2 1984

Biswas, Rupak, Karen Devine & Joseph Flaherty. Parallel, adaptive finite element methods for conservation laws. *Applied Numerical Mathematics*, 14(1-3):255–283, 1994

Blandford, Roger & Christopher McKee. Fluid dynamics of relativistic blast waves. *Physics of Fluids*, 19(8):1130–1138, 1976

Blandford, Roger & Martin Rees. A 'twin-exhaust' model for double radio sources. *Monthly Notices of the Royal Astronomical Society*, 169:395–415, 1974

Blazek, Jiri. *Computational fluid dynamics: Principles and applications*. Elsevier Science, Amsterdam, 2nd edition, 2005

Borges, Rafael, Monique Carmona, Bruno Costa & Wai Sun Don. An improved weighted essentially non-oscillatory scheme for hyperbolic conservation laws. *Journal of Computational Physics*, 227(6):3191–3211, 2008

Boris, Jay & David Book. Flux-corrected transport. I. SHASTA, a fluid transport algorithm that works. *Journal of Computational Physics*, 11(1):38–69, 1973

Brackbill, Jerry & Daniel Barnes. The effect of nonzero $\nabla \cdot \mathbf{B}$ on the numerical solution of the magnetohydrodynamic equations. *Journal of Computational Physics*, 35:426–430, 1980

Bressan, Alberto. *Hyperbolic systems of conservation laws: the one-dimensional Cauchy problem*. Oxford University Press, Oxford, 2000

Brio, Moysey & Cheng-Chin Wu. An upwind differencing scheme for the equations of ideal magnetohydrodynamics. *Journal of Computational Physics*, 75:400–422, 1988

Buchmüller, Pawel & Christiane Helzel. Improved accuracy of high-order WENO finite volume methods on cartesian grids. *Journal of Scientific Computing*:1–26, 2014

Canuto, Claudio, Mohammad Hussaini, Alfio Quarteroni & Thomas Zang. *Spectral methods: fundamentals in single domains*. Springer-Verlag, Berlin, 2006

Carpenter, Mark & Christopher Kennedy. Fourth-order 2N-storage Runge-Kutta schemes. NASA Technical Memorandum (109112). NASA Langley Research Center, 1994.

Casoni, Eva, Jaime Peraire & Antonio Huerta. Un método de captura de choques basado en las funciones de forma para Galerkin discontinuo de alto orden. *Revista Internacional de Métodos Numéricos para Cálculo y Diseño en Ingeniería*, 28(4):204–213, 2012

Casoni, Eva, Jaime Peraire & Antonio Huerta. One-dimensional shock-capturing for high-order discontinuous Galerkin methods. *International Journal for Numerical Methods in Fluids*, 71(6):737–755, 2013

Casper, Jay & Harold Atkins. A finite-volume high order ENO scheme for two dimensional hyperbolic systems. *Journal of Computational Physics*, 106:62–76, 1993

Chen, Guoxian, Huazhong Tang & Pingwen Zhang. Second-order accurate Godunov scheme for multicomponent flows on moving triangular meshes. *Journal of Scientific Computing*, 34(1):64–86, 2008

Choi, Eunwoo & Dongsu Ryu. Numerical relativistic hydrodynamics based on the total variation diminishing scheme. *New Astronomy*, 11(1):116–129, 2005

Chorin, Alexandre. A numerical method for solving incompressible viscous flow problems. *Journal of Computational Physics*, 2(1):12–26, 1967

Chung, T. *Computational fluid dynamics*. Cambridge University Press, Cambridge, 2002

Cockburn, Bernardo & Chi-Wang Shu. TVB Runge-Kutta local projection discontinuous Galerkin finite element method for conservation laws II: General framework. *Mathematics of Computation*, 52(186):411–435, 1989

Cockburn, Bernardo & Chi-Wang Shu. The Runge-Kutta discontinuous Galerkin method for conservation laws V: Multidimensional systems. *Journal of Computational Physics*, 141(2):199–224, 1998

Cockburn, Bernardo & Chi-Wang Shu. Runge-Kutta discontinuous Galerkin methods for convection-dominated problems. *Journal of Scientific Computing*, 16(3):173–261, 2001

Cockburn, Bernardo, San-Yih Lin & Chi-Wang Shu. TVB Runge-Kutta local projection discontinuous Galerkin finite element method for conservation laws III: One-dimensional systems. *Journal of Computational Physics*, 84(1):90–113, 1989

Cockburn, Bernardo, Suchung Hou & Chi-Wang Shu. The Runge-Kutta local projection discontinuous Galerkin finite element method for conservation laws. IV: The multidimensional case. *Mathematics of Computation*, 54(190):pp. 545–581, 1990

Colella, Phillip & Paul Woodward. The piecewise parabolic method (PPM) for gas-dynamical simulations. *Journal of Computational Physics*, 54(1):174–201, 1984

Courant, Richard, Kurt Friedrichs & Hans Lewy. Über die partiellen Differenzengleichungen der mathematischen Physik. German. *Mathematische Annalen*, 100(1):32–74, 1928

Dai, Wenlong & Paul Woodward. Approximate Riemann solver for the ideal magnetohydrodynamics. *Journal of Computational Physics*, 111:354–372, 1994

Dai, Wenlong & Paul Woodward. Extension of the Piecewise Parabolic Method to Multidimensional Ideal Magnetohydrodynamics. *Journal of Computational Physics*, 115:485–514, 1994

Dai, Wenlong & Paul Woodward. On the divergence-free condition and conservation laws in numerical simulations for supersonic magnetohydrodynamic flows. *The Astrophysical Journal*, 494:317–335, 1998

Dedner, Andreas, Friedmann Kemm, Dietmer Kröner, Claus-Dieter Munz, Thomas Schnitzer & Matthias Wesenberg. Hyperbolic divergence cleaning for the MHD equations. *Journal of Computational Physics*, 175(2):645–673, 2002

del Zanna, Luca & Niccolo Bucciantini. An efficient shock-capturing central-type scheme for multidimensional relativistic flows I. Hydrodynamics. *Astronomy & Astrophysics*, 390:1177–1186, 2002

del Zanna, Luca, Niccolo Bucciantini & Pasquale Londrillo. An efficient shock-capturing central-type scheme for multidimensional relativistic flows II. Magnetohydrodynamics. *Astronomy & Astrophysics*, 400:397–413, 2003

del Zanna, Lucca, Olindo Zanotti, Niccolo Bucciantini & Pasquale Londrillo. ECHO: a Eulerian conservative high-order scheme for general relativistic magnetohydrodynamics and magnetodynamics. *Astronomy & Astrophysics*, 473(1):11–30, 2007

Dolezal, Antonin & Samuel Wong. Relativistic hydrodynamics and essentially non-oscillatory shock capturing schemes. *Journal of Computational Physics*, 120:266–277, 1995

Donat, Rosa, José Antonio Font, José María Ibáñez & Antonio Marquina. A Flux-Split algorithm applied to relativistic flows. *Journal of Computational Physics*, 146:58–81, 1998

Dönmez, Orhan. Solving 1-D special relativistic hydrodynamics (SRH) equations using different numerical methods and results from different test problems. *Applied Mathematics and Computation*, 181:256–270, 2006

Dönmez, Orhan & Refik Kayali. Simulation of astrophysical jet using the special relativistic hydrodynamics code. *Applied Mathematics and Computation*, 182:1296–1308, 2006

Dumbser, Michael & Martin Käser. Arbitrary high order non-oscillatory finite volume schemes on unstructured meshes for linear hyperbolic systems. *Journal of Computational Physics*, 221(2):693–723, 2007

Dumbser, Michael & Claus-Dieter Munz. Building blocks for arbitrary high order discontinuous Galerkin schemes. *Journal of Scientific Computing*, 27(1-3):215–230, 2006

Dumbser, Michael, Martin Käser, Vladimir Titarev & Eleuterio Toro. Quadrature-free non-oscillatory finite volume schemes on unstructured meshes for nonlinear hyperbolic systems. *Journal of Computational Physics*, 226(1):204–243, 2007

Dumbser, Michael, Dinshaw Balsara, Eleuterio Toro & Claus-Dieter Munz. A unified framework for the construction of one-step finite volume and discontinuous Galerkin schemes on unstructured meshes. *Journal of Computational Physics*, 227(18):8209–8253, 2008

Dumbser, Michael, Olindo Zanotti, Raphaël Loubère & Steven Diot. A posteriori subcell limiting of the discontinuous Galerkin finite element method for hyperbolic conservation laws. *Journal of Computational Physics*, 278:47–75, 2014

Duncan, Comer & Philip Hughes. Simulations of relativistic extragalactic jets. *The Astrophysical Journal*, 436:L119–L122, 1994

Einfeldt, Bernd. On Godunov-type methods for gas dynamics. *SIAM Journal on Numerical Analysis*, 25(2):294–318, 1988

Elmegreen, Bruce & John Scalo. Interstellar turbulence I: Observations and Processes. *Annual Review of Astronomy and Astrophysics*, 42(1):211–273, 2004

Evans, Charles & John Hawley. Simulation of magnetohydrodynamic flows - A constrained transport method. *The Astrophysical Journal*, 332:659–677, 1988

Font, José Antonio. Numerical hydrodynamics and magnetohydrodynamics in general relativity. *Living Reviews in Relativity*, 11(7), 2008

Font, José Antonio, José María Ibáñez, Antonio Marquina & José María Martí. Multidimensional relativistic hydrodynamics: Characteristic fields and modern high-resolution shock-capturing schemes. *Astronomy & Astrophysics*, 282(1):304–314, 1994

Gerolymos, Georges, Dorothée Sénéchal & Isabelle Vallet. Very-high-order WENO schemes. *Journal of Computational Physics*, 228(23):8481 –8524, 2009

Giacomazzo, Bruno & Luciano Rezzolla. The exact solution of the Riemann problem in relativistic magnetohydrodynamics. *Journal of Fluid Mechanics*, 562:223–259, Sept. 2006

Gibbs, Josiah Willard. Fourier's series. *Nature*, 59(1522):200, 1898

Gibbs, Josiah Willard. Fourier's series. *Nature*, 59(1539):606, 1899

Godlewski, Edwige & Pierre-Arnaud Raviart. *Numerical approximation of hyperbolic systems of conservation laws*. Springer-Verlag, New York, 1996

Godunov, Sergei. A finite difference method for the numerical computation and discontinuous solutions of the equations of fluid dynamics. *Matematicheskii Sbornik*, 47:271–306, 1959

Goedbloed, Hans & Stefaan Poedts. *Principles of Magnetohydrodynamics*. Cambridge University Press, Cambridge, 2004

Gottlieb, Sigal. On high order strong stability preserving Runge-Kutta and multi step time discretizations. *Journal of Scientific Computing*, 25(1):105–128, 2005

Gottlieb, Sigal & Chi-Wang Shu. Total variation diminishing Runge-Kutta schemes. *Mathematics of Computation*, 67:73–85, 1998

Gottlieb, Sigal, Chi-Wang Shu & Eitan Tadmor. Strong stability-preserving high-order time discretization methods. *SIAM Review*, 43:89–112, 2001

Gottlieb, Sigal, David Ketcheson & Chi-Wang Shu. High order strong stability preserving time discretizations. *Journal of Scientific Computing*, 38(3):251–289, 2009

Hairer, Ernst & Gerhard Wanner. *Solving ordinary differential equations II: Stiff and differential-algebraic problems*. Springer-Verlag, Heidelberg, 1996

Hairer, Ernst, Syvert Nørsett & Gerhard Wanner. *Solving ordinary differential equations I: Nonstiff problems*. Springer-Verlag, Heidelberg, 1993

Harten, Amiram. High resolution schemes for hyperbolic conservation laws. *Journal of Computational Physics*, 49(3):357–393, 1983

Harten, Amiram, Peter Lax & Bram van Leer. On upstream differencing and Godunov type methods for hyperbolic conservation laws. *SIAM Review*, 25(1):35–61, 1983

Harten, Amiram, Bjorn Engquist, Stanley Osher & Sukumar Chakravarthy. Uniformly high order accurate essentially non-oscillatory schemes, III. *Journal of Computational Physics*, 71(2):231–303, 1987

Hawley, John & James Stone. MOCCT: A numerical technique for astrophysical MHD. *Computer Physics Communications*, 89(1-3):127–148, 1995

He, Peng & Huazhong Tang. An adaptive moving mesh method for two-dimensional relativistic hydrodynamics. *Communications in Computational Physics*, 11:114–146, 2012

He, Peng & Huazhong Tang. An adaptive moving mesh method for two-dimensional relativistic magnetohydrodynamics. *Computers & Fluids*, 60:1–20, 2012

Helzel, Christiane, James Rossmanith & Bertram Taetz. An unstaggered constrained transport method for the 3D ideal magnetohydrodynamic equations. *Journal of Computational Physics*, 230(10):3803–3829, 2011

Hesthaven, Jan & Tim Warburton. *Nodal discontinuous Galerkin methods: Algorithms, analysis, and applications*. Springer-Verlag, Heidelberg, 2008

Hou, Thomas & Philippe LeFloch. Why nonconservative schemes converge to wrong solutions: error analysis. *Mathematics of Computation*, 62:497–530, 1994

Hu, Changqing & Chi-Wang Shu. Weighted essentially non-oscillatory schemes on triangular meshes. *Journal of Computational Physics*, 150:97–127, 1999

Hundsdorfer, Willem, Steven Ruuth & Raymond Spiteri. Monotonicity-preserving linear multistep methods. *SIAM Journal on Numerical Analysis*, 41(2):605–623, 2003

Jackson, John David. *Classical Electrodynamics*. John Wiley & Sons, New York, 1998

Jameson, Antony, Wolfgang Schmidt & Eli Turkel. Numerical solution of the Euler equations by finite volume methods using Runge-Kutta time-stepping schemes. In *Proceedings of the AIAA 49th Fluid and Plasma Dynamic Conference*. (AIAA 1981-1259) in. Palo Alto, California, June 1981.

Janhunen, Pekka. A positive conservative method for magnetohydrodynamics based on HLL and Roe methods. *Journal of Computational Physics*, 160(2):649–661, 2000

Jiang, Guang-Shan & Chi-Wang Shu. Efficient Implementation of Weighted ENO Schemes. *Journal of Computational Physics*, 126(1):202–228, 1996

Jiang, Guang-Shan & Cheng-Chin Wu. A high-order WENO finite difference scheme for the equations of ideal magnetohydrodynamics. *Journal of Computational Physics*, 150(2):561–594, 1999

Kennedy, Christopher, Mark Carpenter & Robert Lewis. Low-storage, explicit Runge-Kutta schemes for the compressible Navier-Stokes equations. *Applied Numerical Mathematics*, 35(3):177–219, 2000

Keppens, Rony, Zakaria Meliani, Allard-Jan van Marle, Peter Delmont, Alkis Vlasis & Bart van der Holst. Parallel, grid-adaptive approaches for relativistic hydro and magnetohydrodynamics. *Journal of Computational Physics*, 231(3):718–744, 2012

Ketcheson, David. Highly efficient strong stability-preserving Runge-Kutta methods with low-storage implementations. *SIAM Journal on Scientific Computing*, 30(4):2113–2136, 2008

Ketcheson, David. Runge-Kutta methods with minimum storage implementations. *Journal of Computational Physics*, 229(5):1763–1773, 2010

Kolgan, Vladimir. Application of the principle of minimizing the derivative to the construction of finite-difference schemes for computing discontinuous solutions of gas dynamics. *Transactions of the Central Aerohydrodynamics Institute*, 3(6):68–77, 1972. (In Russian)

Komissarov, Serguei. A Godunov-type scheme for relativistic magnetohydrodynamics. *Monthly Notices of the Royal Astronomical Society*, 303:343–366, 1999

Kopriva, David. A conservative staggered-grid Chebyshev multidomain method for compressible flows. II. A semi-structured method. *Journal of Computational Physics*, 128(2):475–488, 1996

Kopriva, David. *Implementing spectral methods for partial differential equations*. Springer-Verlag, Berlin, 2009

Kopriva, David & John Kolias. A conservative staggered-grid Chebyshev multidomain method for compressible flows. *Journal of Computational Physics*, 125(1):244–261, 1996

Krivodonova, Lilia. Limiters for high-order discontinuous Galerkin methods. *Journal of Computational Physics*, 226(1):879–896, 2007

Kröner, Dietmar. *Numerical schemes for conservation laws*. Wiley-Teubner, Chichester, 1997

Kubatko, Ethan, Clint Dawson & Joannes Westerink. Time step restrictions for Runge-Kutta discontinuous Galerkin methods on triangular grids. *Journal of Computational Physics*, 227(23):9697–9710, 2008

Lax, Peter. *Hyperbolic systems of conservation laws and the mathematical theory of shock waves*. SIAM, Philadelphia, 1973

Lax, Peter & Burton Wendroff. Systems of conservation laws. *Communications on Pure and Applied Mathematics*, 13(2):217–237, 1960

LeFloch, Philippe & Pierre-Arnaud Raviart. An asymptotic expansion for the solution of the generalized Riemann problem. Part I: General theory. *Annales de l'institut Henri Poincaré (C) Analyse non linéaire*, 5(2):179–207, 1988

LeVeque, Randall. *Numerical methods for conservation laws*. Birkhäuser, Bern, 2nd edition, 1992

LeVeque, Randall. *Finite-volume methods for hyperbolic problems*. Cambridge University Press, Cambridge, 2002

LeVeque, Randall, D. Mihalas, E. Dorfi & Ewald Müller. *Computational methods for astrophysical fluid flow*. Steiner, O. & A. Gautschy, editors. Springer-Verlag, Berlin, 1998

Liu, Xu-Dong, Stanley Osher & Tony Chan. Weighted essentially non-oscillatory schemes. *Journal of Computational Physics*, 115(1):200–212, 1994

Londrillo, Pasquale & Lucca del Zanna. High-order upwind schemes for multidimensional magnetohydrodynamics. *The Astrophysical Journal*, 530(1):508–524, 2000

Martí, José María & Ewald Müller. The Analytical solution of the Riemann problem in relativistic hydrodynamics. *Journal of Fluid Mechanics*, 258:317–333, 1994

Martí, José María & Ewald Müller. Extension of the piecewise parabolic method to one-dimensional relativistic hydrodynamics. *Journal of Computational Physics*, 123(1):1–14, 1996

Martí, José María & Ewald Müller. Numerical hydrodynamics in special relativity. *Living Reviews in Relativity*, 6(7):1–100, 2003

Martí, José María, José Antonio Font, José María Ibáñez & Ewald Müller. Hydrodynamical simulations of relativistic jets: morphology, dynamics and propagation. In *Energy Transport in Radio Galaxies and Quasars*. Hardee, P., A. Bridle & J. Zensus, editors. Volume 100. In Astronomical Society of the Pacific Conference Series. Boulder, USA, 1996.

Meister, Andreas & Jens Struckmeier. *Hyperbolic partial differential equations: theory, numerics and applications*. Vieweg, Braunschweig, 2002

Merriman, Barry. Understanding the Shu-Osher conservative finite difference form. *Journal of Scientific Computing*, 19(1-3):309–322, 2003

Mignone, Andrea & Gianluigi Bodo. An HLLC Riemann solver for relativistic flows - I. Hydrodynamics. *Monthly Notices of the Royal Astronomical Society*, 364(1):126–136, 2005

Mignone, Andrea & Gianluigi Bodo. An HLLC Riemann solver for relativistic flows - II. Magnetohydrodynamics. *Monthly Notices of the Royal Astronomical Society*, 368(3):1040–1054, 2006

Mignone, Andrea & Jonathan McKinney. Equation of state in relativistic magnetohydrodynamics: variable versus constant adiabatic index. *Monthly Notices of the Royal Astronomical Society*, 378(3):1118–1130, 2007

Mignone, Andrea & Petros Tzeferacos. A second-order unsplit Godunov scheme for cell-centered MHD: The CTU-GLM scheme. *Journal of Computational Physics*, 229(6):2117–2138, 2010

Mignone, Andrea, Tomasz Plewa & Gianluigi Bodo. The piecewise parabolic method for multidimensional relativistic fluid dynamics. *The Astrophysical Journal Supplement Series*, 160(1):199–219, 2005

Mignone, Andrea, Gianluigi Bodo, Silvano Massaglia, Titos Matsakos, Ovidiu Tesileanu, Claudio Zanni & Attilio Ferrari. PLUTO: A Numerical Code for Computational Astrophysics. *The Astrophysical Journal Supplement Series*, 170(1):228–242, 2007

Mignone, Andrea, Marcella Ugliano & Gianluigi Bodo. A five-wave Harten-Lax-van Leer Riemann solver for relativistic magnetohydrodynamics. *Monthly Notices of the Royal Astronomical Society*, 393(4):1141–1156, 2009

Mignone, Andrea, Petros Tzeferacos & Gianluigi Bodo. High-order conservative finite difference GLM-MHD schemes for cell-centered MHD. *Journal of Computational Physics*, 229(17):5896–5920, 2010

Mignone, Andrea, Claudio Zanni, Petros Tzeferacos, Brian van Straalen, Phillip Colella & Gianluigi Bodo. The PLUTO code for adaptive mesh computations in astrophysical fluid dynamics. *The Astrophysical Journal Supplement Series*, 198(1):7, 2012

Misner, Charles, Kip Thorne & John Archibald Wheeler. *Gravitation*. W. H. Freeman and Company, San Francisco, 1973

Munz, Claus-Dieter, Rudolf Schneider, Eric Sonnendrücker & Ursula Voss. Maxwell's equations when the charge conservation is not satisfied. *Comptes Rendus de l'Académie des Sciences - Series I - Mathematics*, 328(5):431–436, 1999

Nitsche, Joachim. Über ein Variationsprinzip zur Lösung von Dirichlet-Problemen bei Verwendung von Teilräumen, die keinen Randbedingungen unterworfen sind. *Abhandlungen aus dem Mathematischen Seminar der Universität Hamburg*, 36(1):9–15, 1971

Noble, Scott, Charles Gammie, Jonathan McKinney & Luca Del Zanna. Primitive variable solvers for conservative general relativistic magnetohydrodynamics. *The Astrophysical Journal*, 641(1):626–637, 2006

Noh, W.F. Errors for calculations of strong shocks using an artificial viscosity and an artificial heat flux. *Journal of Computational Physics*, 72(1):78–120, 1987

Ollitrault, Jean-Yves. Relativistic hydrodynamics for heavy-ion collisions. *European Journal of Physics*, 29:275–305, 2008

Orszag, Steven & Cha-Mei Tang. Small-scale structure of two-dimensional magnetohydrodynamic turbulence. *Journal of Fluid Mechanics*, 90:129–143, 1979

Osher, Stanley & Fred Solomon. Upwind difference schemes for hyperbolic systems of conservation laws. *Mathematics of Computation*, 38(158):339–374, 1982

Pareschi, Lorenzo & Giovanni Russo. Implicit-explicit Runge-Kutta schemes and applications to hyperbolic systems with relaxation. *Journal of Scientific Computing*, 25(1):129–155, 2005

Persson, Per-Olof & Jaime Peraire. Sub-cell shock capturing for discontinuous Galerkin methods. In *Proceedings of the AIAA 44th Aerospace Sciences Meeting and Exhibit*. (AIAA-2006-0112) in. Reno, Nevada, 2006.

Peterson, B. *An introduction to active galactic nuclei*. Cambridge University Press, Cambridge, 1997

Pons, José Antonio, José María Martí & Ewald Müller. The exact solution of the Riemann problem with non-zero tangential velocities in relativistic hydrodynamics. *Journal of Fluid Mechanics*, 422:125–139, 2000

Powell, Kenneth. An approximate Riemann solver for magnetohydrodynamics. Technical report. Institute for Computer Applications in Science and Engineering, NASA Langley Research Center, 1994.

Qiu, Jianxian & Chi-Wang Shu. A comparison of troubled-cell indicators for Runge-Kutta discontinuous Galerkin methods using weighted essentially nonoscillatory limiters. *SIAM Journal on Scientific Computing*, 27(3):995–1013, 2005

Qiu, Jianxian & Chi-Wang Shu. Runge-Kutta discontinuous Galerkin method using WENO limiters. *SIAM Journal on Scientific Computing*, 26(3):907–929, 2005

Quirk, James. A contribution to the great Riemann solver debate. *International Journal for Numerical Methods in Fluids*, 18(6):555–574, 1994

Radice, David & Luciano Rezzolla. Discontinuous Galerkin methods for general-relativistic hydrodynamics: Formulation and application to spherically symmetric spacetimes. *Physical Review D*, 84:024010, 2 2011

Radice, David & Luciano Rezzolla. THC: a new high-order finite-difference high-resolution shock-capturing code for special-relativistic hydrodynamics. *Astronomy & Astrophysics*, 547:A26, 2012

Reddy, Junuthula & Maurice Rasmussen. *Advanced engineering analysis*. Wiley-Interscience, New York, 1982

Reed, William & Thomas Hill. Triangular mesh methods for the neutron transport equation. Technical Report (LA-UR-73-479). Los Alamos Scientific Laboratory, 1973.

Rezzolla, Lucciano & Olindo Zanotti. An improved exact Riemann solver for relativistic hydrodynamics. *Journal of Fluid Mechanics*, 449:395–, 2001

Rezzolla, Luciano & Olindo Zanotti. *Relativistic hydrodynamics*. Oxford University Press, Oxford, 2013

Rezzolla, Luciano, Olindo Zanotti & José Antonio Pons. An improved exact Riemann solver for multidimensional relativistic flows. *Journal of Fluid Mechanics*, 479:199–219, 2003

Roe, Philip. Approximate Riemann solvers, parameter vectors, and difference schemes. *Journal of Computational Physics*, 43(2):357–372, 1981

Ruuth, Steven & Raymond Spiteri. Two barriers on strong-stability-preserving time discretization methods. *Journal of Scientific Computing*, 17:211–220, 1-4 2002

Ryu, Dongsu & Thomas Jones. Numerical magnetohydrodynamics in astrophysics: algorithm and tests for multidimensional flow. *The Astrophysical Journal*, 452:785–796, 1995

Ryu, Dongsu & Thomas Jones. Numerical magnetohydrodynamics in astrophysics: algorithm and tests for one-dimensional flow. *The Astrophysical Journal*, 442:228–258, 1995

Ryu, Dongsu, Francesco Miniati, Thomas Jones & Adam Frank. A divergence-free upwind code for multidimensional magnetohydrodynamic flows. *The Astrophysical Journal*, 509(1):244, 1998

Ryu, Dongsu, Indranil Chattopadhyay & Eunwoo Choi. Equation of state in numerical relativistic hydrodynamics. *The Astrophysical Journal Supplement Series*, 166:410–420, 2006

Schiesser, William. *The numerical method of lines: Integration of partial differential equations*. Academic Press, 1991

Schneider, V, Ulrich Katscher, Dirk Rischke, Béla Waldhauser, Joachim Maruhn & Claus-Dieter Munz. New algorithms for ultra-relativistic numerical hydrodynamics. *Journal of Computational Physics*, 105(1):92–107, 1993

Sebastian, Kurt & Chi-Wang Shu. Multidomain WENO finite difference method with interpolation at subdomain interfaces. *Journal of Scientific Computing*, 19(1-3):405–438, 2003

Shen, Chaopeng, Jing-Mei Qiu & Andrew Christlieb. Adaptive mesh refinement based on high order finite difference WENO scheme for multi-scale simulations. *Journal of Computational Physics*, 230(10):3780–3802, 2011

Shi, Jing, Changqing Hu & Chi-Wang Shu. A technique for treating negative weights in WENO schemes. *Journal of Computational Physics*, 175:108–127, 2002

Shu, Chi-Wang. Total-variation-diminishing time discretizations. *SIAM Journal on Scientific and Statistical Computing*, 9(6):1073–1084, 1988

Shu, Chi-Wang. High order weighted essentially nonoscillatory schemes for convection dominated problems. *SIAM Review*, 51:82–126, 2009

Shu, Chi-Wang & Stanley Osher. Efficient implementation of essentially non-oscillatory shock-capturing schemes. *Journal of Computational Physics*, 77(2):439–471, 1988

Shu, Chi-Wang & Stanley Osher. Efficient implementation of essentially non-oscillatory shock-capturing schemes, II. *Journal of Computational Physics*, 83(1):32–78, 1989

Sonntag, Matthias & Claus-Dieter Munz. Shock capturing for discontinuous Galerkin methods using finite volume subcells. In Fuhrmann, Jürgen, Mario Ohlberger & Christian Rohde, editors, *Finite volumes for complex applications VII-Elliptic, parabolic and hyperbolic problems*. Volume 78, in Springer Proceedings in Mathematics & Statistics, pages 945–953. Springer International Publishing, 2014

Spiteri, Raymond & Steven Ruuth. A new class of optimal high-order strong-stability-preserving time discretization methods. *SIAM Journal on Numerical Analysis*, 40(2):469–491, 2002

Spiteri, Raymond & Steven Ruuth. Non-linear evolution using optimal fourth-order strong-stability-preserving Runge-Kutta methods. *Mathematics and Computers in Simulation*, 62(1-2):125–135, 2003

Stone, James & Michael Norman. ZEUS-2D: A radiation magnetohydrodynamics code for astrophysical flows in two space dimensions. I - The hydrodynamic algorithms and tests. *The Astrophysical Journal Supplement Series*, 80:753–790, 1992

Stone, James & Michael Norman. ZEUS-2D: A radiation magnetohydrodynamics code for astrophysical flows in two space dimensions. II. The magnetohydrodynamic algorithms and tests. *The Astrophysical Journal Supplement Series*, 80:791, 1992

Stone, James, Thomas Gardiner, Peter Teuben, John Hawley & Jacob Simon. Athena: A new code for astrophysical MHD. *The Astrophysical Journal Supplement Series*, 178(1):137, 2008

Suresh, Ambady & Hung Huynh. Accurate monotonicity-preserving schemes with Runge-Kutta time stepping. *Journal of Computational Physics*, 136(1):83–99, 1997

Susanto, Andree, Lucian Ivan, Hans De Sterck & Clinton Groth. High-order central ENO finite-volume scheme for ideal MHD. *Journal of Computational Physics*, 250:141–164, 2013

Taube, Arne, Michael Dumbser, Dinshaw Balsara & Claus-Dieter Munz. Arbitrary high-order discontinuous Galerkin schemes for the magnetohydrodynamic equations. *Journal of Scientific Computing*, 30(3):441–464, 2007

Tchekhovskoy, Alexander, Jonathan McKinney & Ramesh Narayan. WHAM: a WENO-based general relativistic numerical scheme - I. Hydrodynamics. *Monthly Notices of the Royal Astronomical Society*, 379(2):469–497, 2007

Titarev, Vladimir & Eleuterio Toro. ADER: Arbitrary high order Godunov approach. *Journal of Scientific Computing*, 17(1):609–618, 2002

Titarev, Vladimir & Eleuterio Toro. Finite-volume WENO schemes for three-dimensional conservation laws. *Journal of Computational Physics*, 201:238–260, 2004

Titarev, Vladimir & Eleuterio Toro. ADER schemes for three-dimensional non-linear hyperbolic systems. *Journal of Computational Physics*, 204:715–736, 2005

Toro, Eleuterio, editor. *Godunov methods: Theory and applications*. Springer-Verlag, Berlin, 2001

Toro, Eleuterio. *Riemann solvers and numerical methods for fluid dynamics*. Springer-Verlag, Berlin, 3rd edition, 2009

Toro, Eleuterio, Michael Spruce & William Speares. Restoration of the contact surface in the HLL-Riemann solver. *Shock Waves*, 4:25–34, 1 1994

Torrilhon, Manuel. Uniqueness conditions for Riemann problems of ideal magnetohydrodynamics. *Journal of Plasma Physics*, 69:253–276, 03 Apr. 2003

Tóth, Gábor. The $\nabla \cdot \mathbf{B} = 0$ constraint in shock-capturing magnetohydrodynamics codes. *Journal of Computational Physics*, 161(2):605–652, 2000

Touil, Hatem, Mohammad Hussaini & Mark Sussman. Tracking discontinuities in hyperbolic conservation laws with spectral accuracy. *Journal of Computational Physics*, 225(2):1810–1826, 2007

van Leer, Bram. Towards the ultimate conservative difference scheme I. The quest of monotonicity. In Cabannes, Henri & Roger Temam, editors, *Proceedings of the Third International Conference on Numerical Methods in Fluid Mechanics*. Volume 18, in Lecture Notes in Physics, pages 163–168. Springer-Verlag, 1973

van Leer, Bram. Towards the ultimate conservative difference scheme. II. Monotonicity and conservation combined in a second-order scheme. *Journal of Computational Physics*, 14(4):361–370, 1974

van Leer, Bram. Towards the ultimate conservative difference scheme. III. Upstream-centered finite-difference schemes for ideal compressible flow. *Journal of Computational Physics*, 23(3):263–275, 1977

van Leer, Bram. Towards the ultimate conservative difference scheme. IV. A new approach to numerical convection. *Journal of Computational Physics*, 23(3):276–299, 1977

van Leer, Bram. Towards the ultimate conservative difference scheme. V. A second-order sequel to Godunov's method. *Journal of Computational Physics*, 32(1):101–136, 1979

van Leer, Bram. An introduction to the article "Reminiscences about difference schemes" by S. K. Godunov. *Journal of Computational Physics*, 153(1):1–5, 1999

Wang, Zhi-Jian. High-order methods for the Euler and Navier-Stokes equations on unstructured grids. *Progress in Aerospace Sciences*, 43:1–41, 2007

Wang, Zhi-Jian, editor. *Adaptive high-order methods in computational fluid dynamics*. World Scientific Publishing, Singapore, 2011

Wang, Zhi-Jian, Krzysztof Fidkowski, Rémi Abgrall, Francesco Bassi, Doru Caraeni, Andrew Cary, Herman Deconinck, Ralf Hartmann, Koen Hillewaert, Hung Huynh, Norbert Kroll, Georg May, Per-Olof Persson, Bram van Leer & Miguel Visbal. High-order CFD methods: current status and perspective. *International Journal for Numerical Methods in Fluids*, 72:811–845, 2013

Weinberg, Steven. *Gravitation and cosmology: principles and applications of the general theory of relativity*. John Wiley & Sons, New York, 1972

Williamson, James. Low-storage Runge-Kutta schemes. *Journal of Computational Physics*, 35(1):48–56, 1980

Wilson, J. & G. Mathews. *Relativistic numerical hydrodynamics*. Cambridge University Press, Cambridge, 2003

Woodward, Paul & Phillip Colella. The numerical simulation of two-dimensional fluid flow with strong shocks. *Journal of Computational Physics*, 54(1):115–173, 1984

Zachary, Andrew & Phillip Colella. A higher-order Godunov method for the equations of ideal magnetohydrodynamics. *Journal of Computational Physics*, 99(2):341–347, 1992

Zachary, Andrew, Andrea Malagoli & Phillip Colella. A higher-order Godunov method for multidimensional ideal magnetohydrodynamics. *SIAM Journal on Scientific Computing*, 15(2):263–284, 1994

Zel'dovich, Yakov & Yuri Raizer. *Physics of shock waves and high-temperature hydrodynamic phenomena*. Academic Press, New York, 1967

Zhang, Weiqun & Andrew MacFadyen. RAM: A relativistic adaptive mesh refinement hydrodynamics code. *The Astrophysical Journal Supplement Series*, 164(1):255, 2006

Zhong, Xinghui & Chi-Wang Shu. A simple weighted essentially nonoscillatory limiter for Runge-Kutta discontinuous Galerkin methods. *Journal of Computational Physics*, 232(1):397–415, 2013

Zhu, Jun, Jianxian Qiu, Chi-Wang Shu & Michael Dumbser. Runge-Kutta discontinuous Galerkin method using WENO limiters II: Unstructured meshes. *Journal of Computational Physics*, 227(9):4330–4353, 2008

Zhu, Jun, Xinghui Zhong, Chi-Wang Shu & Jianxian Qiu. Runge-Kutta discontinuous Galerkin method using a new type of WENO limiters on unstructured meshes. *Journal of Computational Physics*, 248:200–220, 2013

Ziegler, Udo. A central-constrained transport scheme for ideal magnetohydrodynamics. *Journal of Computational Physics*, 196(2):393–416, 2004

List of Tables

List of Figures

Index

Curriculum Vitae

18.12.1983	Born in Cartagena, Colombia
1990–1992	Colegio Latinoamericano. Cartagena, Colombia
1993–1994	Ciudad Escolar Comfenalco. Cartagena, Colombia
1995–1998	Colegio Ciudad Escolar Comfenalco. Cartagena, Colombia
1999–2000	Colegio Nacional José María Córdoba. Montería, Colombia
2001–2006	Bachelor of Science in Physics
	Universidad de Córdoba. Montería, Colombia
2006–2008	Master of Science in Astronomy
	Observatorio Astronómico Nacional
	Universidad Nacional de Colombia. Bogotá, Colombia
2009–2014	Research Assistant
	Institute of Aerodynamics and Gas Dynamics
	University of Stuttgart. Stuttgart, Germany
2014	Dissertation: *High-Order Methods for Computational Astrophysics*

30th December 2014

Jonatan Núñez-de la Rosa
Stuttgart, Germany